UNIVERSITY OF CAPE TOWN

DEPARTMENT OF MECHANICAL ENGINEERING

RONDEBOSCH, CAPE TOWN, SOUTH AFRICA

Passenger Comfort during Formation Flight within Atmospheric Turbulence

Submitted in partial fulfilment of the requirements for the Master of Science in Mechanical Engineering degree

AUTHOR: BIZINOS, NICHOLAS (BZNNIC001)

SUPERVISOR: Prof. C. Redelinghuys

DATE: 25June 2012

COURSE CODE: MEC5010Z

Declaration

I know the meaning of plagiarism and declare that all of the work in the dissertation, save for that which is properly acknowledged, is my own

Nicholas Bizinos

BZNNIC001

Abstract

Formation flight is currently being investigated as a means to reduce drag and improve fuel efficiency in commercial aviation. In light of this, the potential for passenger discomfort due to the formation flying through free air turbulence was considered in this study. In an attempt to approximately ascertain the increase in discomfort, a simple formation flight aerodynamic model for two aircraft in formation was developed. The wing trailing vortices were assumed to shift in an ideal fashion within atmospheric turbulence resulting in aerodynamic disturbance loads acting on the trailing aircraft. As the sensitivity of the human body to vibrations is frequency dependent, spectral representation of atmospheric turbulence was incorporated. Monte Carlo simulations were done for various levels of turbulence intensity. The predicted acceleration responses of the trailing aircraft were used to determine the passenger comfort levels by applying the criteria of ISO Standard 2631-1, and compared with comfort levels experienced in an aircraft flying in isolation in the same turbulent atmosphere. A significant increase in discomfort was predicted for lateral separations corresponding to optimum drag benefit. The discomfort for lateral separations outboard of wing-tip to wing-tip flight was only slightly greater than that experienced in isolation. Surprisingly, it was found that in formation, seating in front of the aircraft may be less comfortable than in the rear, which opposes the trend for flight in isolation. Seating locations forward and inboard (closer to the lead aircraft) of the mass centre showed the greatest increase in discomfort.

Acknowledgements

First and foremost, I would like to extend my sincere thanks and gratitude to my supervisor and Head of Mechanical Engineering Department, Prof Chris Redelinghuys for his guidance, advice and wonderful demeanour throughout the project. I would also like to express thanks to Jordan Adams, Drewan Sanders and William Norton for there advice and assistance.

I wish to thank Andy Williams, Ian Marr, David Ravenscroft along with Prof Norman Wood for there invaluable input.

The financial support by Airbus and the National Aerospace Centre of the University of the Witwatersrand, Johannesburg, along with the financial assistance provided by the University of Cape Town is acknowledged and indeed much appreciated.

Finally, I wish to thank Caitlin Bergh for her input and advice directly related to my research as well as the support and love she gave in ample abundance over the last few years. I am deeply grateful.

Contents

List of Figures

List of Tables

List of Symbols

AR	Aspect ratio
C	Subjective comfort index
C_D	Drag coefficient in the stability frame
C_L	Lift coefficient in the stability frame
C_{L_j}	Lead aircraft lift coefficient
C_{L_k}	Trail aircraft lift coefficient
$C_{L_{kw}}$	Trail aircraft wing lift coefficient
C_{L_α}	$\partial C_L/\partial\alpha$
$C_{L_{\delta e}}$	$\partial C_L/\partial\delta_e$
C_l	Rolling moment coefficient
C_{l_β}	$\partial C_l/\partial\beta$
$C_{l_{\delta_a}}$	$\partial C_l/\partial\delta_a$
$C_{l_{\delta_r}}$	$\partial C_l/\partial\delta_r$
C_m	Pitching moment coefficient
C_{m_k}	Trail aircraft pitching moment coefficient
C_{m_0}	Pitching moment coefficient about wing aerodynamic centre
C_{m_α}	$\partial C_m/\partial\alpha$
$C_{m_{\delta e}}$	$\partial C_m/\partial\delta_e$
C_n	Yawing moment coefficient
C_{n_β}	$\partial C_n/\partial\beta$
$C_{n_{\delta_a}}$	$\partial C_n/\partial\delta_a$
$C_{n_{\delta_r}}$	$\partial C_n/\partial\delta_r$
C_S	Sideforce coefficient in the stability frame
C_T	Thrust coefficient
C_x	Longitudinal force coefficient in body frame
C_y	Sideforce coefficient in body frame
C_{y_β}	$\partial C_y/\partial\beta$
$C_{y_{\delta_a}}$	$\partial C_y/\partial\delta_a$
$C_{y_{\delta_r}}$	$\partial C_y/\partial\delta_r$
C_z	Vertical force coefficient in body frame
D	Drag
E	Expected value operator

H_{uu}	Transfer function to transform white noise to longitudinal atmospheric turbulence
H_{vv}	Transfer function to transform white noise to lateral atmospheric turbulence
H_{ww}	Transfer function to transform white noise to vertical atmospheric turbulence
$H_{w_x w_x}$	Transfer function to transform white noise to atmospheric turbulence pitch rate
$H_{v_x v_x}$	Transfer function to transform white noise to atmospheric turbulence yaw rate
I_x, I_y, I_z	Moments of inertia about XYZ
I_{xy}, I_{yz}, I_{xz}	Products of inertia about XYZ
L	Lift; Longitudinal length scale (L_u)
L_j	Lead aircraft lift
$\widetilde{L}_k$	Trail aircraft roll moment
L_T	Tailplane lift
L_u	Longitudinal turbulence scale
L_v	Lateral turbulence scale
L_w	Vertical turbulence scale; Wing lift
N	Magnitude of subjective response
N_{k_w}	Trail aircraft yaw moment on wing
M	Mach number; Pitch moment
M_0	Pitch moment about wing aerodynamic centre
Q	Dynamic pressure
$\boldsymbol{R}$	Rotation matrix
R_{uu}	Longitudinal autocorrelation
S	Wing area; Sideforce
S_f	Tailfin area
T	Time duration
U	Axial velocity
$\boldsymbol{V}$	Velocity vector
V	Steady forward velocity (V_E)
V_E	Steady forward velocity in inertial frame
$V_{A/W}$	Velocity of aircraft w.r.t. the wind
V_∞	Freestream velocity
$V\langle t \rangle$	Instantaneous velocity w.r.t. atmosphere
V_θ	Tangential velocity
$\bar{V}_T$	Tailplane volume ratio
$\bar{V}_f$	Tailfin volume ratio
W_i	Frequency weighting at frequency i
X	Longitudinal body axis; Stimulus input of psychophysical function

Y	Lateral body axis
Z	Vertical body axis
$\boldsymbol{a}$	Linear acceleration vector
a	Atmospheric turbulence constant = 1.339
a_v	Overall vibration value
a_{v_s}	Seat translational vibration value
a_{v_r}	Seat rotational vibration value
a_k	Amplitude at frequency k
a_i	Acceleration at frequency band i
a_w	Frequency weighted acceleration
a_1	2-D taiplane lift coefficient gradient; VM2 core scale
a_2	VM2 core scale
b	Wing span
b_v	Bound vortex span
b_f	Tailfin double span
b_{f_v}	Tailfin bound vortex span
b_h	Tailplane span
b_{h_v}	Tailplane bound vortex span
c	Unit conversion factor of psychophysical function
$\bar{c}$	Mean geometric chord
$\bar{c}_f$	Tailfin mean geometric chord
$c.g.$	Center of gravity
c_{l_α}	2-D Wing lift coefficient gradient
$c_{l_{\alpha_f}}$	2-D tailfin lift coefficient gradient
$\boldsymbol{dl}$	Vortex filament segment
f_i	Centre frequency of one third octave band
f_{i_n}	Lower frequency bound of one third octave band
$f_{i_{n+1}}$	Upper frequency bound of one third octave band
g	Gravitational acceleration
h	C.G. position on reference chord; Perpendicular distance from vortex filament to influence point
h_0	Aerodynamic centre position on reference chord
k_u, k_v, k_w	Translational component weighting factors
k_p, k_q, k_r	Rotational component weighting factors
l_T	Tailplane moment arm to c.g.
l_f	Tailfin moment arm to c.g.
m	Aircraft mass

p	Roll rate
q	Pitch rate
$\boldsymbol{r}$	Displacement vector
r	Yaw rate; Radius
r_c	Core radius
r_2	Radius at which the total circulation is almost attained
$\bar{r}$	Dispersion radius
r_{eff}	Effective core radius
r_{roll}	Rolling moment radius
r_i	Inner core radius used with VM2 profile
r_o	Outer core radius used with VM2 profile
s	Laplace transform operator
t	Time
t^*	Non-dimensional time
t'	Reference time
u	Forward velocity
v	Lateral velocity
$\boldsymbol{v}_{rel}$	Relative velocity vector
v_{jk_f}	Induced sidewash on trail tailfin
w	Vertical velocity
w'	Downwash along portion of the wing span equal to tailplane span
w_{jk}	Induced downwash on trail wing
x	Longitudinal displacement
y	Lateral displacement
y_c	Lateral displacement of vortex centre
z	Vertical displacement
z_c	Vertical displacement of vortex centre
z_v	Vertical displacement from aircraft longitudinal axis to tailfin root
Γ	Circulation
Γ_j	Lead wing circulation
Γ_k	Trail wing circulation
Δ	Prefix to denote total change due to influence of lead trailing vortices
$\Delta C_{Di,k}$	Trail aircraft change in induced drag coefficient
$\Delta C_{L,k}$	Trail aircraft change in lift coefficient
$\Delta C_{L,w_h}$	Trail aircraft change in wing portion lift coefficient over span equal to tailplane span
$\Delta C_{l,k}$	Trail aircraft change in roll moment coefficient
$\Delta C_{m,k}$	Trail aircraft change in pitch moment coefficient
$\Delta C_{n,k}$	Trail aircraft change in yaw moment coefficient
$\Delta C_{n,k_w}$	Trail aircraft change in yaw moment coefficient on wing

$\Delta C'_{n,k_f}$	Trail aircraft change in yaw moment coefficient due to tailfin referred to wing area
$\Delta C_{y,k_f}$	Trail aircraft change in tailfin sideforce coefficient
$\Delta C'_{y,k_f}$	Trail aircraft change in tailfin sideforce coefficient referred to wing area
$\Delta C'_{y,k}$	Trail aircraft change in sideforce coefficient
Δx	Longitudinal separation
Δy	Lateral separation
Δy_{eff}	Effective lateral separation
Δz	Vertical separation
Δz_{eff}	Effective vertical separation
Δt	Sampling period
$\Delta \boldsymbol{x}$	Change of displacement vector
Φ	Spectral density
Φ_{uu}	Spectral density of longitudinal gust velocity
Φ_{vv}	Spectral density of lateral gust velocity
Φ_{ww}	Spectral density of vertical gust velocity
$\Phi_{w_y w_y}$	Spectral density of atmospheric turbulence roll rate
$\Phi_{w_x w_x}$	Spectral density of atmospheric turbulence pitch rate
$\Phi_{v_x v_x}$	Spectral density of atmospheric turbulence yaw rate
Φ_{WN}	Spectral density of white noise
Ω_u	Longitudinal spatial frequency
$\bar{\alpha}$	Difference between geometric angle of attack and zero lift angle of attack
α	Geometric angle of attack
α_T	Tailplane angle of attack
α_{geom}	Geometric angle of attack
$\alpha_{L=0}$	Zero lift angle of attack
β	Sideslip angle; Power factor of psychophysical function
δ	Prefix to denote change in deflection angle or disturbance orientation angle
δ_α	Change in steady state angle of attack
δ_β	Change in steady state sideslip angle
δ_1	Angle from influence point to end of vortex filament
δ_2	Angle from influence point to end of vortex filament
δ_a	Aileron deflection angle
$\delta\delta_a$	Change in aileron deflection angle
δ_e	Elevator deflection angle
$\delta\delta_e$	Change in elevator deflection angle
δ_k	All control deflections
δ_r	Rudder deflection angle
$\delta\delta_r$	Change in rudder deflection angle

δ_{th}	Thrust control deflection
$\delta\alpha_i$	Change in induced angle of attack due to the presence of the lead aircraft trailing vortices
ϵ	Induced downwash angle on tailplane due to wing
ζ	Dimensionless vertical separation referred to b
ζ_{eff}	Dimensionless effective vertical separation referred to b
ζ_f	Dimensionless tailfin double span referred to b
ζ_v	Dimensionless vertical displacement from aircraft longitudinal axis to tailfin root referred to b
η	Dimensionless lateral separation referred to b
η_{eff}	Dimensionless effective lateral separation referred to b
η_T	Tailplane incidence angle
η_h	Dimensionless tailplane span referred to b
θ	Pitch angle
ι	VM2 profile factor
κ	Ratio of standard deviation of accelerations in formation flight to standard deviation of accelerations in isolated flight
λ	Longitudinal wavelength
μ	Dimensionless core radius referred to b
ν	Kinematic viscosity
ξ	Dimensionless longitudinal separation referred to b
ρ	Air pressure
σ	Standard deviation
σ_{jk}	Downwash influence factor
σ_{jk_f}	Sidewash influence factor on tailfin
σ_{jkwh}	Downwash influence factor on wing portion equal to span of tailplane bound vortex
σ_u	Longitudinal turbulence intensity magnitude
σ_v	Lateral turbulence intensity magnitude
σ_w	Vertical turbulence intensity magnitude
σ_{form}	Standard deviation in formation flight
σ_{isol}	Standard deviation in isolated flight
τ	Time separation
τ_{jk}	Moment influence factor
τ_{jk_f}	Moment influence factor on tailfin
ψ	Yaw angle
ϕ	Roll angle
φ	Quarter chord sweep angle
$\boldsymbol{\omega}$	Angular velocity vector
ω	Temporal frequency; Angular velocity

Superscripts

B	Body frame
I	Inertial frame
$\hat{}$	Dimensionless

Subscripts

0	Steady
B	Burnham Hallock profile
H	Helmholtz profile
$approx$	Approximation, ignoring influence of bound vortex
$bound$	Bound vortex filament
cg	Center of gravity
d	Disturbance
eff	Effective
far	Far trailing vortex filament
$form$	Formation
f	Formation
g	Gust
$isol$	Isolation
j	Lead aircraft
k	Trail aircraft
$near$	Near trailing vortex filament
p	Passenger
r	Reference condition
w	Frequency weighted

1 Introduction

1.1 Background

Close formation flight allows an increase in range or endurance via induced drag reduction. Wind tunnel tests have shown the decrease in drag to be between 10% and 30% depending on the configuration [1, 2, 3]. This drag benefit is a consequence of the upwash field created by a lead aircraft which essentially rotates the lift vector of the trail aircraft forward, thereby reducing the induced drag.

Beukenberg and Hummel [4] showed that significant power reductions are obtainable for the rear aircraft in a two ship formation using analytical studies along with flight tests results which yielded power reductions of 10%. The error margin w.r.t. the optimum location within the upwash field is however very small (approximately one quarter wing span vertically and laterally) with steep changes marginally inboard [5]. Furthermore, very large rolling moments are experienced due to the wake vortex of a lead aircraft [6](see chapter 2).

Results from a wind tunnel test of two tailless delta wing aircraft in close proximity showed that the maximum induced rolling moment corresponded to 100% control deflection [3]. Bradley [7] reported on a number of large aircraft which incurred unsatisfactory handling characteristics during aerial refuelling tests conducted at the tanker wing drogue position (mid-wing span). Other handling problems identified included a short period pitching motion and yaw oscillations that required large rudder deflections. Due to these destabilizing influences and other safety concerns, close formation flight is avoided in commercial aviation.

The aerodynamic interference effects due to formation flight and the associated difficulty in flight control has spurred a large research interest in the field of automated formation flight control. Most current research investigates aerial refuelling and UAV formation flight. With the advent of improved automated flight control systems providing increased flight path precision coupled with the ever increasing research interest in formation flight control, the question is raised whether commercial aviation can exploit the benefits of formation flight. An analyses of the potential benefit of formation flight in a realistic commercial scenario demonstrated that a 13% reduction in fuel burn is achievable [8]. Ning et al. [9] conducted studies to investigate the potential of formation flight in the far wake-field, as a solution to reduce the risk of collision, and concluded that significant drag savings can still

be made from 10 to 40 spans in low to moderately low turbulence.

Conversely, a number of feasibility questions are introduced. Aside from the handling characteristics mentioned earlier, the interaction of atmospheric turbulence with the vortex generated flow field, particularly near the core of the vortex results in changing aerodynamic loads which may cause unacceptable passenger comfort levels in a trailing aircraft.

1.2 Objectives and Outline of the Research

It is the objective of the current study to ascertain the comfort levels experienced by a passenger onboard a large passenger airliner flying in formation. The study focuses on passenger comfort in the trailing aircraft of a two ship formation as it is understood that a trailing aircraft would be more severely affected by the trailing vortices of a lead aircraft.

In order to determine passenger comfort, the passenger accelerations and frequency of these accelerations are required [10]. These accelerations are determined by: the position of the passenger from the mass centre as well as the forces and the moments about the mass centre. To determine the irregular motion of an aircraft flying through a disturbed atmosphere, two principal factors need to be analysed:

1. Disturbance loads due to the turbulence.

2. Compensatory control inputs by the pilot or autopilot.

In the current study, focus is placed on analysing item 1 only or more specifically the effect of turbulence on the aerodynamic loads on the aircraft.

It is further recognized that simplifying assumptions will be made to obtain approximate models capable of representing the dominant physical effects. The intention is to develop a simple model capable of approximately accounting for the effects of turbulence intensity and frequency content on aerodynamic loads. The comfort levels are investigated for different levels of atmospheric turbulence intensity and various seating locations within the aircraft.

The lead aircraft wing is modelled as a single horseshoe vortex responsible for the formation influence effects on the trailing aircraft. The three primary lifting surfaces of the trailing aircraft, i.e. wing, tailplane and tailfin, are also modelled as single horseshoe vortices which interact with the lead horseshoe trailing vortices. The Burnham-Hallock vortex velocity profile, which allows for a solid vortex core, is used to model the flow field of the vortex.

The lead aircraft trailing vortices are assumed to move in an ideal fashion in atmospheric turbulence, i.e. the direction of the trailing vortex is parallel to the instantaneous velocity vector with respect to the air. These disturbed horseshoe vortices alter the effective sepa-

ration between the aircraft and thus change the induced aerodynamic loads caused by the trailing vortices.

The induced forces and moments due to the trailing vortices are derived in Chapter 3. A very non-linear relationship exists between the induced forces and moments and the effective separation with steep changes particularly near optimum separation. A time based simulation is therefore necessary to obtain the frequency content of the accelerations.

The atmospheric turbulence model plays a key role in ultimately generating the induced forces and moments. The von Karman turbulence model, bearing a close relationship to measured data, is used to model atmospheric turbulence. Chapter 4 details the method and assumptions used to determine the effect of the atmospheric turbulence on the trailing vortices. Linearised equations of motion used to model the trailing aircraft are derived in Chapter 5. A Monte Carlo type simulation is implemented using the stochastic nature of atmospheric turbulence to generate psuedo random input data necessary for this type of simulation. The comfort levels are determined via comparison to ISO 2631-1 [10], where the passenger accelerations are weighted according to their frequency and thus necessitate the need for frequency dependent acceleration spectra. A discussion of the turbulence input data along with and the method used to determine the passenger comfort is discussed in chapter 6.

Results and discussion are found in Chapter 7 followed by conclusions and recommendations in Chapters 8 and 9 respectively.

2 Background and Literature Review

2.1 Wing Tip Vortices

Tip vortices are formed because the pressure differential between the bottom and top surfaces of a wing (pressure and suction surfaces) drives fluid around the wing tip resulting in a strong vortex. A spanwise flow is generated toward the wing tip on the pressure surface and toward the fuselage on the suction surface showing a different sense of direction at the wing trailing edge. Thus, a free shear layer or vortex sheet develops [11]. The flow field immediately downstream of the trailing edge, up to one chord length, is characterised by the formation of highly concentrated vortices downstream of all wing surface discontinuities and rapid upward motion of the tip vortices [12, 13]. Through self induction, the vortex sheet begins to roll up immediately leading to two, well defined, counter-rotating vortices. Roll up is essentially complete within a few spans downstream of the wing trailing edge [14]. Jacquin et al. [15] observe that at a downstream distance of nine wing spans all the secondary vortices, generated by discontinuities on the wing surface, have merged into a fully formed single vortex in each half-plane. This region is known as the extended near-wake field and is limited to ten to twelve wing spans downstream [12]. The far wake-field, stretching from 10 to 100 wing spans, is the region where the vortex pair descends in the atmosphere without undergoing any major change. Atmospheric turbulence and the level of stratification have a significant influence on the distance/longevity of this region. Immediately following this far-field, the onset of rapid decay occurs and the vortex structure breaks down quickly exhibiting fast decay of circulation [16].

2.1.1 Wing Wake Turbulence

Spalart [13] lists different types of turbulence that may be found in the wake of a wing together with the sources and length scales (table 2.1) and notes that interaction of different types of turbulence usually requires their length and time scales to be of the same order of magnitude. Experimental evidence for the presence of turbulence within the vortex core has been given by Green and Acosta [17] who observed unsteadiness in the core. Chow et al. [18] observed elevated velocity fluctuations in the core of a wing tip vortex generated in a wind tunnel. Their vortex showed r.m.s. fluctuations of 19% of the freestream velocity at Reynolds numbers of around one million and are likely to be present at typical aircraft wing scales (Reynolds numbers of 40 million). In an experimental study of a trailing vortex

Table 2.1: Types of turbulence in the wing wake, reprinted from [13].

Source	$\frac{\Delta V}{V_e}$	$\frac{L}{b}$	Extent
Boundary layers	1	0.001	To trailing edge
Viscous wakes	0.1	0.01	A span
Vortex sheet	0.1	0.01	A few spans
Rolled-up vortex	1	0.1	Possibly many spans
Atmosphere	0.01	10	Everywhere

up to 25 chord lengths, Beninati and Marshall [19] found the turbulent length scales to range from 2% to 100% of the core diameter. Nearly all of the turbulence energy measured outside of the core was found to be small-scale turbulence (length scales of 2% to 10% of the core diameter) and the larger scale fluctuations were only apparent within the vortex core. The maximum magnitude of this turbulent kinetic energy was shown to decay with downstream distance where the peak turbulent kinetic energy decreased by about two thirds from 4 chord lengths to 25 chord lengths.

Investigations have also shown that trailing vortices exhibit a low frequency meander/wander in wind tunnels where the vortex core drifts about a mean point in a plane normal to the streamwise flow [12, 17, 20, 21]. The origin of these perturbations is not well understood. The source of the meandering was originally attributed to wind tunnel freestream turbulence and considered an experimental artefact [21, 22]. Jacquin et al. [12] suggest three other possible causes: turbulence in the surrounding shear layer as it rolls up around the core, interactive instabilities between the trailing vortex and other vortices in the flow, and propagation of unsteadiness originating from the vortex generating model. Beresh et al. [23] show that the vortex meander is also partially due to wall boundary layer turbulence. This influence of the nearby wall on vortex meander is expected to be greater with low aspect ratio lifting surfaces as opposed to a vortex shed from an aircraft wing whose tip is much further away from a wall. No conclusive evidence is given to suggest that one source of this meander is dominant.

Experimental evidence of a laminar core can be found in the measurements of Devenport et al. [21] and Heyes et al. [24], which show little or no velocity fluctuations within the vortex core up to stream-wise distances of 23 chords behind the wing. Results, corrected for vortex wandering indicated, that the vortex core is laminar and the apparent unsteadiness in the uncorrected data is entirely due to wandering [24].

Heyes et al. show that the variation in rms wandering magnitude decreases with increasing vortex strength indicating that the vortex is responding to an external influence, for

example free-stream turbulence, and that it becomes less susceptible as the vortex strength is increased. Heyes et al., Beninati and Marshall conclude that the variation in wandering magnitude increases with streamwise distance. Heyes et al., however, suggest that the upstream turbulence intensity does not affect the final wandering amplitude and that, whilst wandering increases with stream-wise distance, it is also a function of the local turbulence intensity.

2.1.2 Vortex Velocity Profile and Core Radius

In the extended near field and far field, a two-dimensional model of the wake flow is justified since the roll up process takes place gradually enough [14, 25] and yet rapidly enough that viscous effects can be neglected [14]. The tangential velocity in a two-dimensional plane normal to the vortex filament is given by a number of different theoretical profiles. The Biot Savart Helmholtz velocity profile is the most basic profile of vortex velocity where the tangential velocity is inversely proportional to the radius and the flow is potential at every point except on the vortex filament itself.

$$V_\theta(r) = \frac{\Gamma}{2\pi r} \tag{2.1}$$

This profile, however, does not allow for viscous effects at the core and generates an infinite velocity at the centre. There are a number of profiles which account for the viscous effects at the core and in turn remove the singularity.

The Rankine solid body profile assumes that the vorticity is confined to a solid core which rotates about the centre while the flow outside of the core is still potential. A discontinuity in the velocity profile is realised where $r = r_c$ and r_c is the core radius.

$$V_\theta(r) = \begin{cases} \frac{\Gamma}{2\pi r} & \text{for } r > r_c \\ \frac{\Gamma}{2\pi}\frac{r}{r_c^2} & \text{for } r < r_c \end{cases} \tag{2.2}$$

The Rankine solid body profile is simple and easily integrated but yields multiple solutions and experimental evidence has shown this model to be a poor approximation [14].

The Lamb-Oseen vortex model considers that the vorticity follows a Gaussian distribution of standard deviation $\sqrt{2\nu\tau}$, where ν is the kinematic viscosity of the air and τ is the age of the vortex. The circumferential velocity of the Lamb-Oseen vortex is given in [26].

$$V_\theta(r) = \frac{\Gamma}{2\pi r}\left(1 - e^{-\frac{r^2}{4\nu\tau}}\right) \tag{2.3}$$

Near the centre of the vortex, the motion quickly becomes a solid body rotation due to viscosity effects. The vortex core size, $r_c = 2.24\sqrt{2\nu\tau}$, increases with time due to viscous diffusion and exhibits a conical structure.

Spalart [13] states that the Rankine model is an over simplified model and asserts that the real circulation at r_c is less than 30% of the total, compared with 100% as per the Rankine model and 72% for the Lamb Oseen profile.

Kurylowich [27] developed an alternate form of the Lamb-Oseen vortex model, rewriting the exponential term as a function of the core radius:

$$V_\theta(r) = \frac{\Gamma}{2\pi r}\left(1 - e^{-1.2526\frac{r}{r_c}^2}\right) \tag{2.4}$$

This allowed adaptation of the core radius to match experimental data. The modified form of r_c was given as:

$$r_c = 36.2\sqrt{\frac{\nu\tau}{\cos\varphi}} \tag{2.5}$$

where φ is the wing quarter chord sweep angle.

Burnham and Hallock [28] developed the Burnham Hallock profile which has been shown to correlate well with experimental data [29], is easily integrated, and yields a single solution.

$$V_\theta(r) = \frac{\Gamma}{2\pi}\frac{r}{r^2 + r_c^2} \tag{2.6}$$

Donaldson [30] developed an approximation of the Betz distribution profile which was shown to agree well with experimental data. The Betz profile is derived from an analysis of the roll-up of the vorticity shed by a wing with an elliptic loading. Three basic assumptions are made: All the vorticity shed by each half of the wing is found rolled up in the trailing vortex behind the same half wing; The centre of gravity of the vorticity distribution remains at a constant lateral distance from the plane of symmetry i.e. $\frac{\pi b}{8}$ for an elliptical lift distribution; The moment of inertia of the vorticity is a constant about its centre of gravity, hence an axisymmetric rolled-up wake is assumed [30].

The modified Betz velocity profile developed by Donaldson [30] is given as:

$$V_\theta(r) = \begin{cases} \frac{\Gamma}{2\pi r}\left(6\frac{r}{b} - 9\left(\frac{r}{b}\right)^2\right)^{\frac{1}{2}} & \text{for } 0 < \frac{r}{b} < \frac{1}{3} \\ V_\theta(r) = \frac{\Gamma}{2\pi r} & \text{for } \frac{1}{3} < \frac{r}{b} \end{cases} \tag{2.7}$$

The Betz model does not require an assumption of the core radius but a programmer must ensure that control points do not fall on the vortex centreline or risk undefined solutions.

Jacquin et al. [12] discuss the various core radii used in literature today. The predominant physical description of the core radius, r_c, is given as the distance from the vortex centre where the tangential velocity, V_θ, is maximum for a fully rolled up vortex. An external core radius, r_2, is used to denote the radius at which the total circulation is almost attained and the region within r_2 still contains vorticity surrounding the internal core, r_c. A "dispersion" radius is also discussed which, as the name suggests, provides an evaluation

of the vorticity field dispersion in the plane normal to the streamwise flow:

$$\bar{r}^2 = \frac{1}{\Gamma}\int_{-\infty}^{\infty} dz \int_{0}^{\pm\infty} dy \left[\left((y-y_c)^2 + (z-z_c)^2\right)\omega\right]$$

Here y_c and z_c are the coordinates of the vortex centroid. Widnall et al. [31] introduces the "effective core radius" which includes an axial component and is defined as:

$$r_{eff} = r^2 e^{(\frac{1}{4}-A+C)}$$

where $A = \left(\frac{2\pi}{\Gamma}\right)^2 \int_0^{r_2} V_\theta^2 \langle r\rangle r\, dr$, $C = 2\left(\frac{2\pi}{\Gamma}\right)^2 \int_0^{r_2} U^2 \langle r\rangle r\, dr$, V_θ is the tangential velocity component and U is the axial velocity deficit. For an elliptical loading, this leads to an estimation of the effective core radius, $r_{eff} = 0.11b$. Jacquin et al. [12] also highlights a final definition of the core size, being the "rolling moment radius" which is used for evaluating the hazard that a vortex wake represents for a following aircraft.

$$r_{roll} = \frac{1}{\Gamma}\int_{-\infty}^{\infty} dz \int_{0}^{\pm\infty} dy \left[\sqrt{(y-y_c)^2 + (z-z_c)^2}\omega\right]$$

Devenport et al. [21] conducted wind tunnel tests with a rectangular NACA 0012 wing of 0.2 m chord and 0.88 m semi-span at 5° angle of attack and Reynolds number of 5.3×10^5. Results, corrected for vortex wandering, show the peak tangential velocity of $0.236V_\infty$ at $r_c = 0.036\bar{c}$ thirty chords downstream. A growth in the core radius was observed for streamwise distances of five to thirty chords, however, this was attributed to uncertainty in their wandering correction method. Heyes et al. [24] present data showing the core radius does increase and to be much larger. A linear increase of 41% was found from 1 to 23 chord lengths downstream. This increase is greater than that predicted for a Lamb Oseen vortex undergoing viscous diffusion. At 23 chords, results showed r_c between 0.025 and 0.03 wing spans and peak tangential velocity of $0.285V_\infty$. This data was corrected for wandering using direct measurement as opposed to the statistical method used by Devenport et al.. Results from Bailey and Tavoularis [32] show the maximum tangential velocity at 10 chord lengths downstream to be at a radial distance of approximately $0.04\bar{c}$ or $0.007b$ (based on wing geometry) from the vortex centre after correcting for vortex wandering using a two point direct mesurement method. Bailey and Tavoularis conclude that the core radius does not change with streamwise distance or freestream turbulence. Both Heyes et al. and Bailey and Tavoularis indicate that the maximum tangential velocity decreases with increasing streamwsie distance and with increasing free-stream turbulence. It should be noted, however, that the relative freestream turbulence length scales (length scale/wing span) were small. Bailey and Tavoularis used a NACA 0012 wing of 177.8 mm chord and 520.7 mm semi-span with grid turbulence generators of 25.4 mm and 50.8 mm grid size. Heyes et al. generated similar relative turbulence length scales. The length scale of

atmospheric turbulence at high altitudes is given as 762 m [33] and the wing span of a typical large airliner is approx 60 m, thus, the real relative length scale is far greater. Devenport et al., Heyes et al. and Bailey and Tavoularis used the same wing profile with similar angle of attack and Reynolds numbers of the same order of magnitude.

Burnham and Hallock [28] observed the core size to be small with aircraft which had no wing mounted engines while large aircraft with 4 wing mounted engines had much larger core radii. Blake and Multhopp [5] used a core radius of 3% of the wingspan of the wake generating vehicle while Hinton and Tatnall [34] used a core radius of 5%. Gerz, Holzapfel and Darracq [35] assumed a value of 4.12%. In a study of the vortex wake in the far field, Holzapfel et al. [16] used a vortex core radius of 6.7% span to represent the vortex wake of a Boeing 747.

Ning et al. [9] discuss the use of referencing the core radius to the wingspan. It is shown that irregular wing loadings compared to an elliptical wing loading may result in core sizes which are not representative of the actual core size, e.g. the core size of a wing with a large aspect ratio and a flat lift distribution would be over-predicted. Ning et al. used the vortex radius, r_2, as defined by Spalart [13] to overcome this concern.

Jacquin et al. [12] conducted wind tunnel tests on a 1:100 Airbus A300 model with wing span of 448 mm, geometric chord of 58.2 mm and a lift coefficient of 0.7 at 4° angle of attack for the clean configuration with a freestream velocity of 50 m/s. From the results obtained Jacquin et al. [12] proposed a multiple scale velocity profile with three distinct regions for the 'clean' aircraft case. The internal core is very small ($r_i \leq 0.01b$) and increases linearly to the maximum tangential velocity. From r_i, the tangential velocity decreases with $r^{-0.57}$ to an outer core radius, $r_o \approx 0.1b$, before it follows the potential flow law of r^{-1}. The velocity profile recorded by Jacquin et al. for streamwise distances of 3, 5 and 9 wing spans is shown in Fig. 2.1. Fabre and Jacquin [36] later developed a smooth profile accounting for the multiple scale deduced from experimental data and named it the VM2 profile:

$$V_\theta(r) = \frac{\Gamma}{2\pi a_1^2}\left(\frac{a_1}{a_2}\right)^{1-\iota} \frac{r}{[1+\left(\frac{r}{a_1}\right)^4]^{1+\iota}[1+\left(\frac{r}{a_2}\right)^4]^{1-\iota}} \tag{2.8}$$

Jacquin et al. go on to show the peak tangential velocity to be approximately $0.15V_\infty$ for the clean configuration at $r_i \approx 0.01b$. This is much lower than results obtained from Devenport et al., Heyes et al. and Bailey and Tavoularis. Figure 2.2 shows a comparison of different vortex velocity profiles.

2.1.3 Vortex Decay

Since the early 1970s, a large number of theoretical, numerical and experimental studies have focused on the study of wake vortex decay. A number of different vortex decay

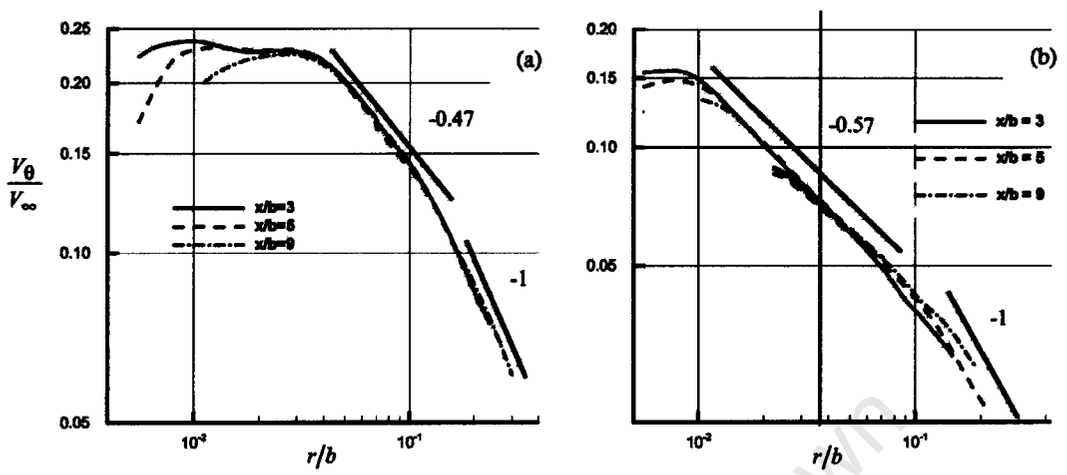

Figure 2.1: Tangential velocity $\frac{V_\theta}{V_\infty}$ versus the radius from experimental data of A300 model for the (a) high lift configuration and (b) clean configuration on log-log plot, reprinted from Jacquin et al. [12].

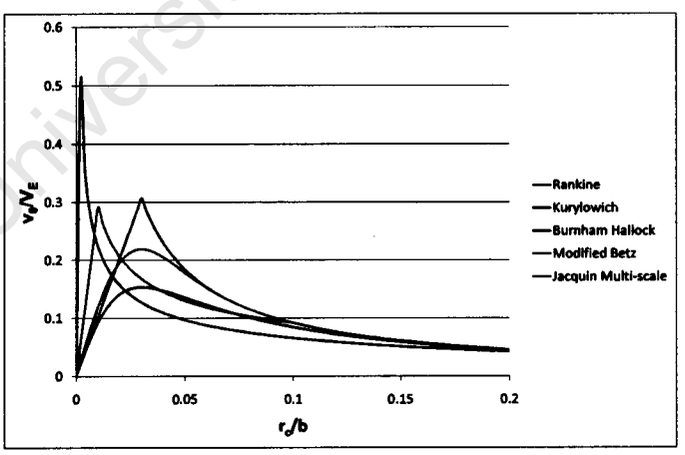

Figure 2.2: Comparison of vortex velocity profiles.

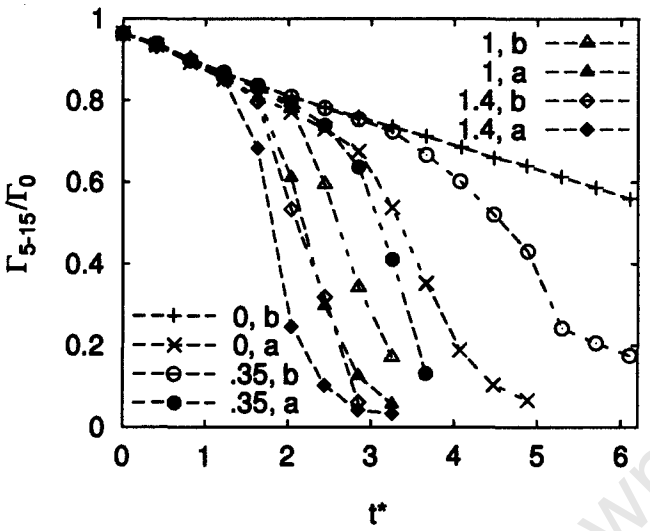

Figure 2.3: Data representing two phase vortex decay for different levels of stratification (N=0, 0.35, 1, 1.4) and turbulence where case(b) represents aircraft boundary layer turbulence only and case(a) includes light to moderate atmospheric turbulence. Reprinted from Holzapfel et al. [16].

very different to one in the clean configuration. Investigations of vortex encounters at high altitudes are not as common.

Bradley [7] reports on handling characteristics during aerial refuelling tests with various large receiver and tanker aircraft. Trials to investigate refuelling from the wing drogue position (approximately midspan on the tanker wing) were undertaken with various large receiver aircraft. Approaching a Tristar tanker drogue position, a Hercules aircraft required full aileron deflection to hold the wings level eventually having to terminate the approach. Tests were repeated at higher speeds with two large turbojet receiver aircraft where large aileron and rudder deflections were necessary to hold station. Several large receiver aircraft experienced additional yaw oscillations approaching the drogue from the same outboard position. In most cases this yaw oscillation was countered effectively with rudder deflections but a Nimrod aircraft behind a Victor tanker experienced unacceptable handling characteristics because of an undamped yawing oscillation. Longitudinal handling problems identified included marked changes in pitch moment and a short period pitching oscillation that required moderate elevator deflections. Once again it was found that the pitching oscillation was more pronounced behind the Victor tanker. No conclusions were drawn as to why the Victor tanker generated worse handling characteristics on the receiver aircraft. The Victor has a very large wing area and lower wing loading compared with the other tankers (VC 10 and Tristar) which have wing shapes (loading) similar to those found

on most typical airliners.

Hansen and Cobleigh [48] and Vachon et al. [49] report on flight tests conducted by NASA Dryden Flight Research Centre with two F-18 aircraft to investigate autonomous formation flight and optimum relative separation for performance benefits. In general, the induced moments experienced were well within the control authority available to the pilot. For zero vertical separation, the maximum positive rolling moment occurred at approximately 15% wingspan overlap which is equivalent to the separation for maximum drag benefit. This compares favourably with 22% overlap given by a horseshoe vortex of an elliptically loaded wing. Both the rolling moment and yawing moment had large rates of change further inboard and near 25% overlap both moments became negative. Pilots found the handling unpredictable or, "squirrelly", in this region. The pilots further noted that they did not have any difficulty adapting to the pitching moments.

2.2.2 Modelling the Effects of Formation Flight

The interference effects of an aircraft wake on a following aircraft have been modelled using numerous methods, including both lifting line theory and vortex lattice methods. The single horseshoe vortex offers a simple yet close approximation of two counter rotating fully rolled up trailing vortices. It, however, does not offer an adequate representation of the vortex sheet undergoing roll up. In studies relating to aerial refuelling, Bloy et al. [50] and Bloy et al. [51] investigated the lateral and longitudinal dynamic stability and control of a large receiver aircraft by using a horseshoe vortex to represent the trailing vortices from a tanker wing and calculated the aerodynamic interference effects via an extended form of Prandtl's lifting line theory developed by Kuchemann [52].

Bloy and Trochalidis [53, 54] and Bloy et al. [55] used horseshoe vortex pairs and the vortex lattice method to calculate the aerodynamic interference effects. Fairly good agreement was found between predictions and results from wind tunnel tests, however, small differences were noted and the pitching moments were not predicted well. Incomplete roll up of the trailing vortices was highlighted as one of the main causes for the differences observed. This effect was demonstrated by comparing the experimental data with theoretical results obtained using the horseshoe vortex and the vortex sheet representation of the vortex wake. The differences were found to be greatest for the rolling moment where the experimental data was found to lie between the theoretical results obtained from the horseshoe vortex model, which over predicts the effect, and the results obtained from the vortex sheet model. In further studies, Bloy et al. [56] used a vortex sheet and later, Bloy and Jouma'a [57] used a rolled-up vortex sheet model to represent a tanker wing and used the vortex lattice method to determine the aerodynamic loads on a receiver aircraft. In both cases, the

predictions compared favourably with experimental data obtained from wind tunnel tests.

Bloy and colleagues [50, 51, 56, 57] also studied many of the positional stability derivatives. Negative/divergent stability results if the wake induced forces tend to drive the trail aircraft away from its original position when disturbed. Simulations revealed divergent oscillations in pitch, roll and yaw at certain relative separations, primarily for the receiver astern and below the tanker. It was observed that pitching oscillations would occur if the receiver was displaced vertically while a yaw displacement would results in a loss of directional control. This was confirmed when compared with flight tests where pilots constantly had to apply aileron deflections and small elevator and rudder deflections during aerial refuelling. The change in rolling moment due to lateral displacement was noted as the most significant handling characteristic. Large sideforce and yaw moment increments were also observed with lateral displacement.

Blake and Multhopp [5] used single horseshoe vortex models with viscous cores to represent aircraft of different weight and size in a formation of more than two aircraft in order to analyse the performance benefits of different formation flight configurations. The results were found to be consistent with results obtained from the HASC95 planar vortex lattice code [58].

Hoganson [59] expanded the single horseshoe vortex model in order to develop a more realistic lift distribution of a tanker wing in an analytical study of the effects during aerial refuelling where the receiver was modelled as a rectangular wing. Two further linear lift distribution models were introduced: The triangular "tent" distribution and modified linear distribution which can be seen to approximate an elliptical lift distribution in Fig. 2.4. Hoganson reports that the results obtained via use of the analytical approach showed qualitative agreement with data from the Douglas Aircraft Company on the KC-10. The method was noted to be "a good place to start to get an approximate idea of the flow field" and showed that the changes in the tanker's lift distribution significantly influences the induced downwash which was generally over-estimated by 25-30%. Hoganson also applied a vortex lattice method in the same study and reported predictions of induced downwash within 5-10% of Douglas KC-10 data. The study neglected the effects of the fuselages, wing camber, and wake roll up and did not consider the induced rolling moment.

Beukenberg and Hummel [4] used the horseshoe vortex, vortex sheet, and rolled up vortex sheet model to investigate the achievable power savings and showed that power reductions of 15% are obtainable for the rear aircraft in a two ship formation of equal aircraft. Beukenberg and Hummel found that the horseshoe vortex method predicted a smaller power reduction than the flat or rolled up vortex sheet while the shape of the vortex sheet with roll up was generated by an iterative procedure which was observed to

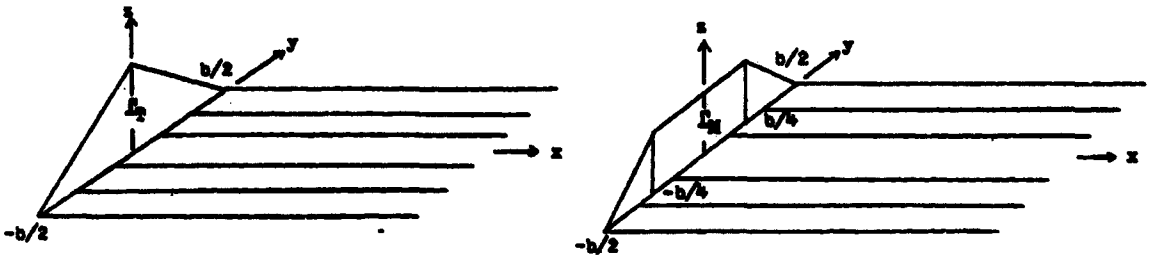

(a) Tent distribution.

(b) Modified tent distribution.

Figure 2.4: Alternative linear circulation distributions. Reprinted from Hoganson [59].

be "extremely laborious". Flight test results of a DO-228 (lead) and Do-28 (trail) aircraft in formation using a formation flight controller yielded power reductions of 10% measured on the trail aircraft over a 2.5 minute interval comparing well with the predicted savings. Beukenberg and Hummel showed the aileron and rudder deflections for the compensation of the corresponding moments to be of moderate size.

In an effort to simplify the aerodynamic calculations for the simulation of formation flight, Myatt and Blake [1] and Blake [6] conducted wind tunnel experiments of F-18 aircraft and compared the results with theoretical results obtained via the HASC95 vortex lattice code [58]. Except for over predictions of peak values, good agreement of trends was found. Results showed that the forces and moments are highly non linear functions of relative separation. Aside from the induced drag, the aerodynamic force and moment increments on the trailing aircraft are adequately modelled as functions of the relative separation and lift coefficient of the vortex generating aircraft (lead). This suggests that the trailing aircraft angle of attack and sideslip angle do not significantly affect the induced forces and moments (excluding induced drag). The induced drag was found to be a significant function of the trailing aircraft lift coefficient along with relative separation and lead lift coefficient. The largest effect was on rolling moment which required large aileron deflections to trim, while the yawing moment and sideforce were significant, but only required small control deflections to trim. The pitching moment was found to be insignificant. Myatt and Blake [1] found reduced pitch stability and yaw stability an order of magnitude less on a trailing aircraft at certain relative separations behind the lead. The dihedral effect (roll due to sideslip) was also significantly reduced.

Blake and Gingras [3] conducted wind tunnel tests of two tailless delta wing aircraft in close formation flight and compared results with predictions from the HASC95 vortex lattice code [58]. The pitching and rolling moments were well predicted, however, the induced drag reduction was over predicted by an average of 15% over the relative separation investigated.

The discrepancy was attributed to flow separation at the trailing aircraft wing tip caused by the induced upwash. It was found that the experimentally identified stable and unstable regions of three positional stability derivatives (change in lift and pitching moment with height, and change in roll moment with lateral separation) within the trefftz plan were in good agreement with predictions. It should be noted that the aircraft studied had no tailplane nor any tailfin, hence, the pitching moment, yaw moment and side force data gathered in this study may not be characteristic of a typical aircraft configuration.

Dogan et al. [60] developed a novel approach to calculating the induced forces and moments. "The non uniform vortex induced wind and wind gradients acting on the trail aircraft are approximated as effective uniform wind and wind gradients". This method, therefore, allows the very non-linear induced forces and moments as functions of the relative separation to be approximated as linear functions which can then be incorporated into the standard equations of motion. Results from this approximate method were compared with wind tunnel data and reasonable agreement was found with the incremental force and moment coefficients.

Ning et al. [9] conducted studies to investigate the potential of formation flight in the far wake-field and concluded that significant drag savings can still be made from 10 to 40 spans in low to moderately low turbulence. Tracking error was found to be the largest source of fluctuations in induced drag savings, hence, it was concluded that higher levels of turbulence would make formation flight impractical at these streamwise distances.

2.3 Passenger Comfort

The evaluation of passenger ride comfort is not a straightforward undertaking since human perception of comfort is subjective and depends on environmental conditions (vibration, temperature, humidity, noise level, pressure), aircraft maneuvers (roll, pitch, deceleration, climb/descent, compound manoeuvres) and seating (seat width, leg room) as well as personal conditions such as health, physiology and psychological attitude [61, 62].

With reference to passenger comfort due to ride quality, Jacobson et al. [63] developed a method to predict passenger satisfaction with the ride quality of transportation vehicles. This model generates a subjective comfort factor (C index) as a function of the angular velocities, linear accelerations and their derivatives. There are many different simplified forms of the C index, but the common theme is to integrate the joint probability density function for the motion variables, $\mathrm{f}(a_x, a_y, a_z, ...\dot{\omega}_z)$ over the motion space and arrive at a probability function for the passenger's comfort level. This would yield the probability that the comfort rating is less than or equal to some value C. The final step relates the derived comfort rating to a value judgement taken to be passenger satisfaction with the

ride. Jacobson and Lapins [61] went on to relate local manoeuvres, environmental events and the subjective ride comfort levels for these events to the overall comfort and satisfaction for the entire trip. They note that a memory decay occurs whereby events at the beginning of a flight tend to become less important than events near the end and latter portions of the flight will have a stronger impact on the passenger's evaluation. It was further discovered that negative normal acceleration from a negative pitch rate was to a large extent the primary cause of discomfort in a set of complex manoeuvres involving turns, deceleration, pitch over and steady descent.

Brindisi and Concilio [62] discuss the human perception of comfort, indicating that the subjective response is largely dependent on health, physiology and psychological attitude and notes that approaches for predicting passengers' judgements about comfort should take into account environmental as well as personal conditions affecting the highly non linear human judgement process.

Stevens [64] developed a psychophysical function which is a basic power law function for relating stimulus for many sensory modalities to the magnitude of the subjective response, N.

$$N = cX^{\beta} \tag{2.9}$$

where X is the magnitude of the stimulus raised to the power β and c is a constant factor which scales the function based on the choice of units. Many investigators have determined different β values for various whole body vibration stimuli.

Hiramatsu and Griffin [65] conducted experiments to determine the exponents of the psychophysical function for the discomfort produced by whole-body vertical vibration. An exponent value of 0.96 was reported after subjects were exposed to accelerations of 0.5 to 2.5 m/s^2 at 8 Hz. Howarth and Griffin [66] investigated both horizontal and vertical motion using a sinusoidal signal of 0.04 to 0.4 m/s^2 over a frequency range of 4 to 63 Hz. The psychophysical function exponent was found to vary from 1.04 to 1.47 for vertical motion and from 0.68 to 1.99 for horizontal motion. Changes in frequency were found to have insignificant effects in the vertical orientation, however, for horizontal motion, the exponent increased with increasing frequency.

ISO 2631-1 [10] provides a quantitative method for determining passenger comfort due to vibration and incorporates various features not found in the Jacobson et al. method. High peak values are considered separately from the root mean square method which tends to under predict their effect on passenger comfort while distributed frequency weightings are applied to account for the way human perception changes as a function of frequency. ISO 2631-1 [10] also considers the effect of vibration on health and the effect of lower frequency vibrations on motion sickness. Vibrations with high peak values are considered

by investigating crest values which are defined as the modulus of the ratio of the maximum instantaneous peak value of the frequency weighted acceleration signal to its r.m.s. value, $\left\| \frac{a_w\langle t \rangle}{a_w} \right|$. For crest factors less than 9, use of the root-mean-square (r.m.s) value is suggested:

$$a_{w_{rms}} = \left[\frac{1}{T} \int_0^T a_w^2 \langle t \rangle \, dt \right]^{\frac{1}{2}} \tag{2.10}$$

or

$$a_w = \left[\sum_i (W_i a_i)^2 \right]^{1/2} \tag{2.11}$$

where $a_w\langle t \rangle$ is the instantaneous frequency weighted acceleration and T is the duration of measurement. For crest factors greater than 9, the use of a root-mean-quad (r.m.q) measure,

$$a_{w_{rmq}} = \left[\frac{1}{T} \int_0^T a_w^4 \langle t \rangle \, dt \right]^{\frac{1}{4}} \tag{2.12}$$

or of a vibration dose value (VDV) is recommended,

$$VDV = \left[\int_0^T a_w^4 \langle t \rangle \, dt \right]^{\frac{1}{4}} \tag{2.13}$$

since the 4th power methods are more sensitive to peaks than the r.m.s. method. In order to provide guidance to the investigator, ISO 2631-1 [10] gives approximate indications of likely reactions to various magnitudes of overall vibration values in public transport but also notes that reactions at various magnitudes depend on many factors specific to each application.

In a study to investigate the potential reduction of passenger discomfort in a large capacity civil aircraft applying active control of flexible modes , Kubica and Madelaine [67] use ISO 2631-1 [10] for passenger comfort evaluation. Simulations run over 3 minutes in strong turbulence revealed an increase in the predicted percentage of ill passengers for further aft seating position, being minimum at the front of the fuselage (Fig. 2.5).

2.4 Atmospheric Turbulence

Out of boundary layer effects at higher altitudes, numerous types of turbulence are known to exist, which are frequently grouped into two categories: convective turbulence in and around clouds, and 'CAT', which is an acronym for Clear Air Turbulence. The mechanism of turbulence is an incredibly varied and complicated process which can only be managed by statistical methods [68]. The analytical discreet gust model which later evolved into

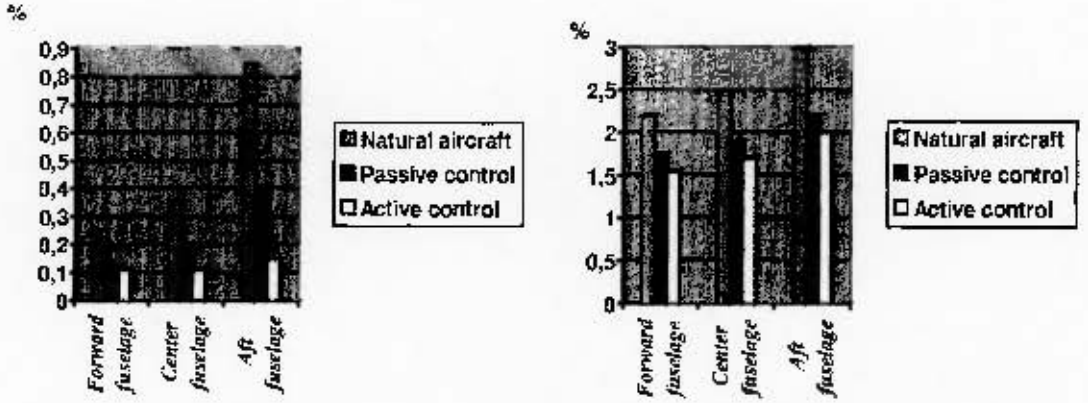

(a) Lateral axis.

(b) Vertical axis.

Figure 2.5: Percentage of ill passengers in turbulence. Reprinted from Kubica and Madelaine [67].

the 'one-minus-cosine' discreet gust model which is used for simplicity, investigates only one particular wavelength, expected to produce the most significant response on a typical aircraft configuration. In order to investigate all possible wavelengths, and the gust magnitudes associated with these wavelengths, power spectral techniques were developed for application with atmospheric turbulence. After considerable data had been collected, various assumptions were made to simplify the continuous gust model. Atmospheric turbulence is considered stationary and homogeneous which imply that the statistical characteristics are assumed to be invariant with respect to the time and position in the turbulence and the direction through the turbulence [69].

Houbolt et al. [69] note that there appears to be some degree of stationarity and homogeneity present even in severe storm turbulence. It is further suggested that large-scale patterns of air motion which exhibit stationarity and homogeneity might be expected within regions of approximately 100 miles and time durations of approximately an hour. From measured data in a thunderstorm, homogeneous and stationary characteristics were only evident for a time duration of about 5 minutes in a storm of about 21 miles in diameter. With reference to the extent of turbulence patches, Houbolt [70] notes that results obtained by different investigators differ considerably. Data presented by Houbolt suggests that the majority of turbulence patches are reasonably shallow (less than 1000 feet).

From the assumption that turbulence is stationary and homogeneous, it is also, subsequently, considered ergodic. The time averages are therefore the same as the ensemble average [71]. Both Houbolt et al. [69] and Etkin [72] agree that a Gaussian distribution of the turbulence appears reasonable for many practical purposes.

Wang and Frost [73] and Houbolt et al. [69] investigated both the von Karman and

Dryden analytical models and compared these models with flight measurements of random atmospheric turbulence (Fig. 2.6). The von Karman model was found to provide an excellent fit of the data for both the autocorrelation function and the spectrum. By comparison, the Dryden model did not fit very well where conflict arose between fitting of spectrum data and best fit of the correlation function, by adapting the integral scale, L_u (see equation (2.19)). The Dryden model is, however, easier to handle mathematically and was developed from wind tunnel data varying in proportion to ω^{-2} at high frequencies while the von Karman model varies in proportion to $\omega^{-\frac{5}{3}}$ [69, 72]. The Global Atmospheric Sampling Program (GASP) obtained temperature and velocity spectra from over 6000 commercial aircraft flights between 1975 and 1979. From this data, Nastrom and Gage [74] concluded that the spectral slopes followed a $\omega^{-\frac{5}{3}}$ relationship for large wavelengths (greater than 2.6 km) and are independent of latitude, season and location in the troposphere or stratosphere. From spectral data deduced with measurements taken by a light aircraft (Piper Cherokee), Houbolt [70] was able to verify the validity of the von Karman spectral form for high frequency atmospheric turbulence components (Fig. 2.7). The von Karman model considers

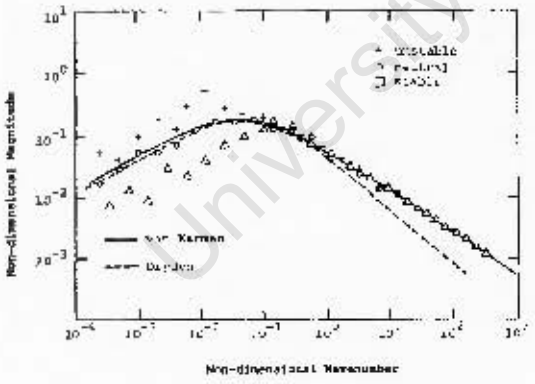

Figure 2.6: Comparison of von Karman and Dryden spectral shapes with measured data. Adapted from Wang and Frost [73].

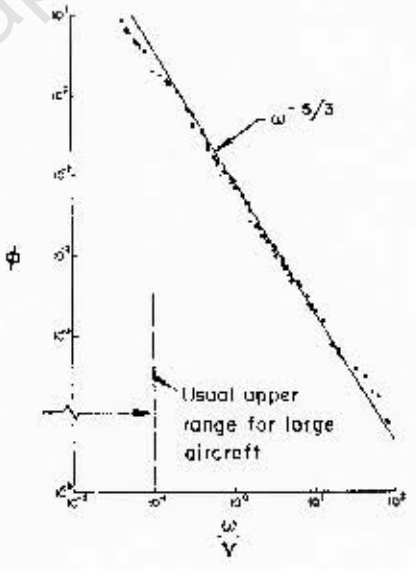

Figure 2.7: Spectral shape of atmospheric turbulence at high frequencies. Reprinted from Houbolt [70].

the turbulence to be isotropic which assumes that the statistical properties at a point are independent of the orientation of the axes [71]. The mean square velocity components are therefore:

$$\sigma^2 = E[u^2] = E[v^2] = E[w^2] \tag{2.14}$$

where $E[x]$ is the expected value of x. The von Karman one dimensional linear spectra are defined as functions of spatial frequency by [72, 69, 70]:

$$\Phi_{vv}(\Omega_u) = \Phi_{ww}(\Omega_u) = \frac{\sigma^2 L}{\pi} \frac{1 + \frac{8}{3}(aL\Omega_u)^2}{[1 + (aL\Omega_u)^2]^{\frac{11}{6}}} \tag{2.15}$$

$$\Phi_{uu}(\Omega_u) - \frac{\sigma^2 L}{\pi} \frac{1}{[1 + (aL\Omega_u)^2]^{\frac{5}{6}}} \tag{2.16}$$

while the Dryden spectra are defined as [69]:

$$\Phi_{vv}(\Omega_u) = \Phi_{ww}(\Omega_u) = \frac{\sigma^2 L}{\pi} \frac{1 + 3(L\Omega_u)^2}{[1 + (L\Omega_u)^2]^2} \tag{2.17}$$

$$\Phi_{uu}(\Omega_u) = \frac{2\sigma^2 L}{\pi} \frac{1}{1 + (L\Omega_u)^2} \tag{2.18}$$

where σ^2 is the total area under the complete spectrum or the initial value of the autocorrelation function of the gust velocity and the constant a is defined by Houbolt et al. [69] as $a = 1.339$. The numerical value of σ represents the intensity of the turbulence, being equal to zero in still air and large in the presence of a thunderstorm. The σ rms velocity parameter is established as a probability of exceedance, usually as a function of altitude. Houbolt [70] notes that atmospheric turbulence, in contrast to typical random processes, can exhibit peak velocities in the order of 20 times the rms value, though usually peaks of 4σ to 5σ are typical. L is the longitudinal turbulence scale given by:

$$L = L_u = \frac{1}{\sigma^2} \int_0^\infty R_{uu}(\Delta x)\, d\Delta x \tag{2.19}$$

The integral scale, also known as length scale, L, of equation 2.19 in atmospheric turbulence is interpreted physically as a measure of the longest distance that two points in a turbulent field may be separated before the velocity correlation becomes zero. Houbolt et al. [69] indicates that this scale, L, is approximately 3000 feet (1524 m) in clear atmospheric turbulence out of boundary layer effects while MIL-F-8785C [33] and Schaeffer et al. [75] specify an integral scale of 2500 feet (762 m). Houbolt [70] later suggests that the the integral scale could in fact be much smaller, in the range of 500 to 750 feet, particularly in the case of lower intensity turbulence while larger integral scales are expected in more severe turbulence.

2.5 Summary

Following from Ning et al. [9] who suggest that the commercial application of formation flight is most probable at longitudinal separations of 10 to 40 spans, the current study

considers the same longitudinal separations. At longitudinal separations of 10 spans, the trailing vortex is shown to be fully rolled up [12]. In this case, the basic single horseshoe vortex which models two fully rolled up counter rotating vortices and has been shown to have reasonable agreement with experiment and flight data [5, 59], is considered adequate for an approximate analysis of the effects due to formation flight. The work of Blake and Multhopp [5] provides the basis from which to develop induced flow, force and moment equations. Further Development is required to incorporate the effects of the tailplane and tailfin which were not considered by Blake and Multhopp.

Blake and Multhopp apply the Burnham Hallock vortex velocity profile which provides a very simple solution to implement and can be integrated analytically. It also represents a reasonable approximation of the Jacquin and Fabre [42] model, albeit with a reduced peak tangential velocity, and the van Jaarsveld et al. [40] model. The results of Jacquin et al. [12] and the VM2 profile developed from these results [42] may be more representative of the shorter longitudinal separations considered while the proposed model by van Jaarsveld et al. [40] may be more representative of the vortex flow at longer streamwise separations (+40 spans).

It is evident that an analysis of the induced effects over a large range of vertical and lateral relative separations (greater than 20% span) will yield non linear functions with respect to these separations [5, 6, 3]. A simulation may be necessary to genetate response data from both atmospheric turbulence and the trailing vortices.

ISO 2631-1 [10] will be used to predict the passenger comfort from accelerations determined via analysis of the aircraft response.

3 Aerodynamic Forces and Moments Induced by Formation Flight

3.1 Single Horseshoe Vortex

The Biot Savart law gives the change in velocity due to the circulation of an incremental length of vortex filament represented by the following equation:

$$d\boldsymbol{V} = \frac{\Gamma}{4\pi}\frac{d\boldsymbol{l} \times \boldsymbol{r}}{|\boldsymbol{r}|^3} \tag{3.1}$$

Integration of equation (3.1) over the length of the vortex filament yields:

$$V_\theta = \frac{\Gamma}{4\pi h}(cos\delta_2 - cos\delta_1) \tag{3.2}$$

Where h is the perpendicular distance from the vortex axis and δ_2 and δ_1 are the angles to the filament ends shown in Fig. 3.1.

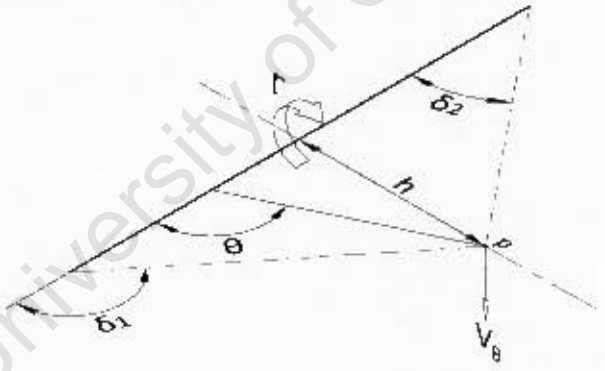

Figure 3.1: Velocity induced at point P due to a finite, straight vortex filament.

From the Kutta-Joukowski theorem, a bound vortex will experience a force $L = \rho V_E \Gamma$. The finite wing of span b is replaced with a bound vortex of strength Γ extending from $y = -\frac{b}{2}$ to $y = \frac{b}{2}$. To satisfy the Helmholtz theorem, two free vortices extend downstream from the bound vortex ends to infinity. The single horseshoe vortex is shown in Fig. 3.2. These free trailing vortices induce a flow field which change the local angle of attack and sideslip angle. For a wing of span b with an elliptical lift distribution, it can be shown that a single horseshoe vortex of equivalent circulation will have a bound vortex with a span of $\frac{\pi}{4}b$.

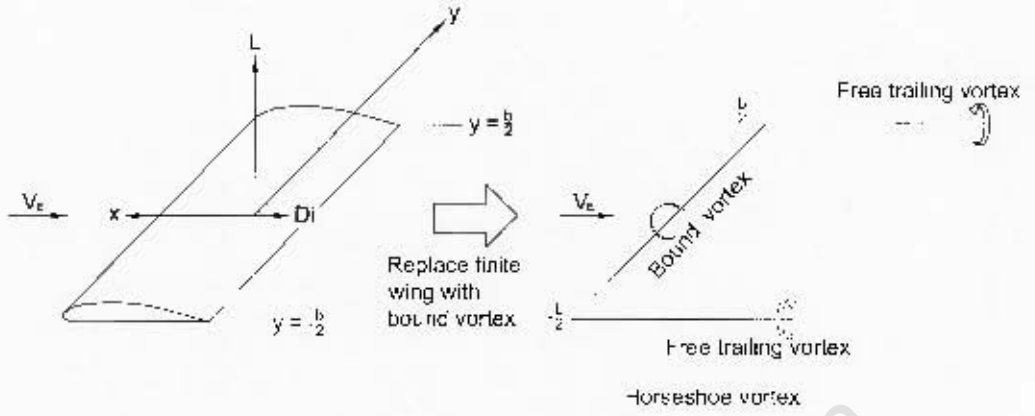

Figure 3.2: Horseshoe vortex representation - adapted from Anderson [76].

3.2 Induced Downwash on a Following Wing

Two identical aircraft are considered in a right echelon formation. The aircraft, therefore, share the same span, b, lift distribution and aspect ratio, AR. One significant difference is that only the lead aircraft main wing, represented by a single horseshoe vortex, is modelled while the trailing aircraft consists of a main wing, tailplane and tailfin. The co-ordinate axes are shown in Fig. 3.3. Note that the aircraft are assumed to fly straight and level, thus, the influence effects are considered in the inertial frame. The following aircraft's lifting surfaces will experience an induced flow field due to the lead aircraft's free trailing vortices. The downwash w_{jk} on the rear aircraft lifting surfaces due to the horseshoe vortex filaments of the lead aircraft using the Helmholtz vortex velocity profile is given by equation (3.2) (refer to Fig. 3.1). Subscript jk refers to the influence of the lead aircraft (j) on the trailing aircraft (k). As was discussed in chapter 2, the Burnham Hallock and the Lamb-Oseen (Kurylowich) profiles offer reasonable approximations with greatest ease of implementation. Following from the work of Blake and Multhopp [5] where reasonable agreement was found with the HASC95 vortex lattice code, the Burnham Hallock profile is chosen, as noted in Section 2.5. Furthermore, it is believed that it is somewhat easier to implement.

$$V_\theta = \frac{\Gamma_j}{4\pi} \frac{h}{h^2 + r_c^2} (cos\delta_1 - cos\delta_2)$$

Equation (A.11) in Appendix A gives the downwash on a wing from both free trailing vortices but excludes the bound vortex portion. This is shown to have a negligible effect. However, the simple Biot-Savart Helmholtz vortex velocity profile is used in equation

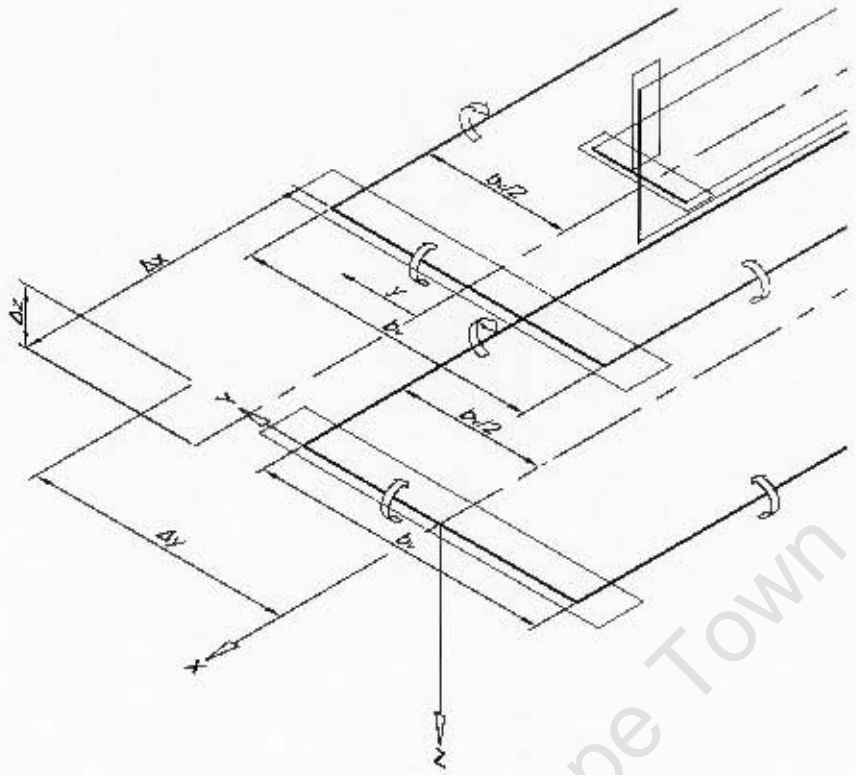

Figure 3.3: Horseshoe vortices in right echelon formation.

(A.11). This profile does not consider viscous effects and results in a singularity at $\eta = \frac{\pi}{4}$. Introducing a viscous core, r_c, into equation (A.11) using the Burnham Hallock profile yields:

$$\left(\frac{4\pi}{\Gamma_j}\right) w_{jk\,approx_B} = -\frac{y + \Delta y - \frac{b_v}{2}}{(y + \Delta y - \frac{b_v}{2})^2 + \Delta z^2 + r_c^2}(2) + \frac{y + \Delta y + \frac{b_v}{2}}{(y + \Delta y + \frac{b_v}{2})^2 + \Delta z^2 + r_c^2}(2) \tag{3.3}$$

The induced distribution along the elliptical planform is approximated by a distribution over a rectangular planform of span equal to the bound vortex and constant c_{l_α}. This is done in order to obtain a basic analytical equation for implementation in the simulation, since the elliptical distribution is not analytically integrable. The result of this approximation is compared with results obtained from a numerical integration over the full span of an elliptical planform in Fig. B.1.

A "σ" influence factor is introduced, defined as:

$$\sigma_{jk\,approx_B} = \left(\frac{4\pi}{\Gamma_j}\right) \int_{-\frac{b_v}{2}}^{\frac{b_v}{2}} w_{jk\,approx_B}\, dy \tag{3.4}$$

which integrates the induced downwash due to the lead horseshoe trailing vortices along the span of the trailing bound vortex ($\frac{-b_v}{2}$ to $\frac{b_v}{2}$). The details of the integration along

with conversion to dimensionless separation, ξ, η and ζ, with respect to the span, b, where $\Delta x = b\xi$, $\Delta y = b\eta$ and $\Delta z = b\zeta$ is shown in Appendix A. Incorporating this influence factor and converting to dimensionless units, the integration yields:

$$\sigma_{jk\,approx_B} = \ln \left| \frac{\left((\eta - \frac{\pi}{4})^2 + \zeta^2 + \mu^2\right)\left((\eta + \frac{\pi}{4})^2 + \zeta^2 + \mu^2\right)}{\left(\eta^2 + \zeta^2 + \mu^2\right)^2} \right| \tag{3.5}$$

where $\mu = \frac{r_c}{b}$. A comparison of $\sigma_{jk\,approx_H}$ using the Helmholtz profile and $\sigma_{jk\,approx_B}$ using

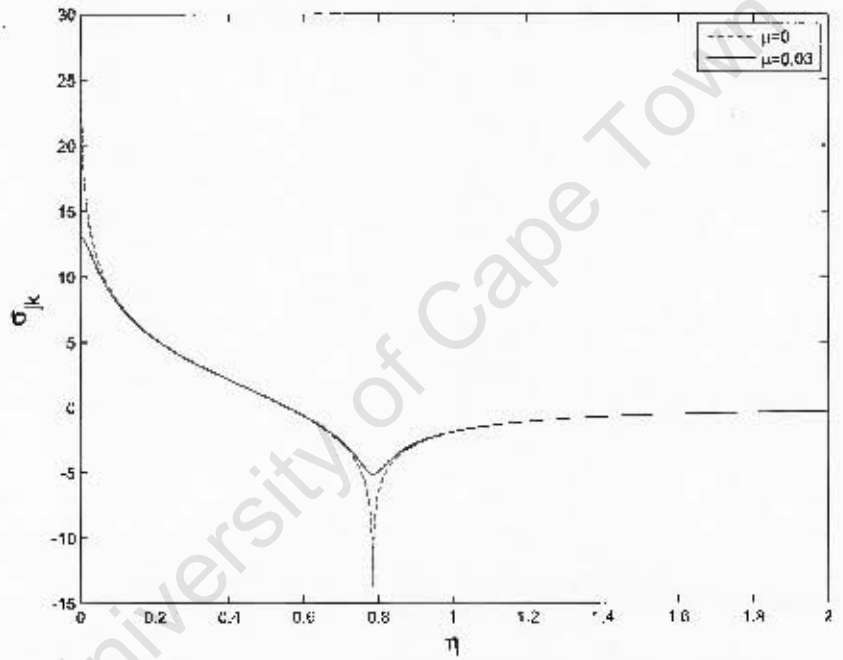

Figure 3.4: Comparison of $\sigma_{jk\,approx_H}$ using the Biot-Savart Helmholtz profile ($\mu = 0$) with $\sigma_{jk\,approx_B}$ using the Hallock Burnham profile ($\mu = 0.03$) where $\xi = -10$ and $\zeta = 0$.

the Burnham profile with $\mu = 0.03$ is depicted in Fig. 3.4. A contour map of $\sigma_{jk\,approx_B}$ for changes in η and ζ is shown in Fig. 3.5. Henceforth, the effect of the lead horseshoe vortex is represented by a combination of the approximation of $\Delta x \to \infty$ and a solid vortex core, r_c, equal to 3% of the wingspan. Other influence factors, τ_{jk}, σ_{jk_f} and τ_{jk_f} are introduced later in this report, however, they all use the same two aforementioned assumptions and are also functions of the separation alone. Following from this assumption and in order to reduce the length of the subscript, $jk\,approx_B$, all terms with subscript jk infers the use of the approximate method and Burnham Hallock profile, aside from sections A.1 and A.2 in appendix A which derives the downwash influence factor using the Helmholtz profile.

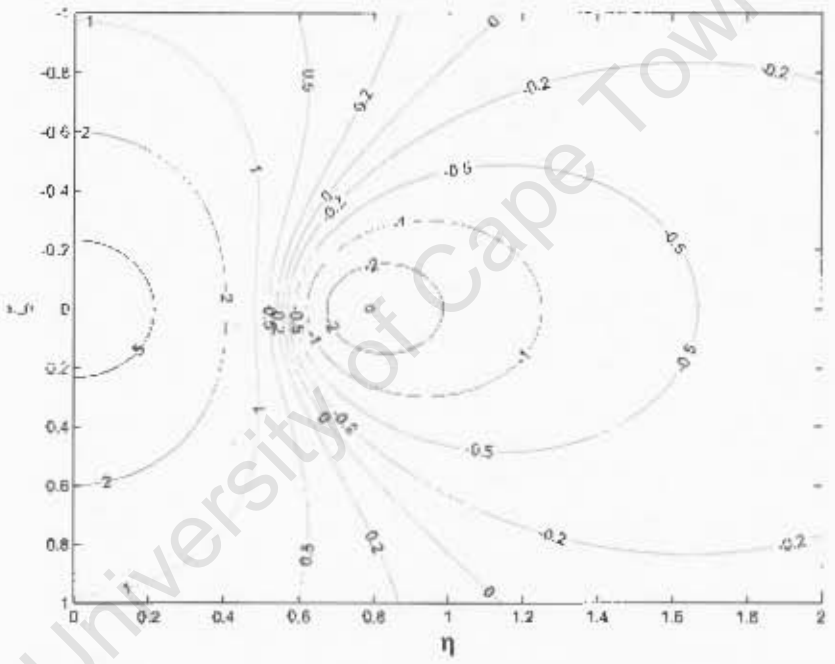

Figure 3.5: Contour map of $\sigma_{jk\,approx_D}$ using the Hallock Burnham profile for changes in η and ζ where $\xi = -10$ and $\mu = 0.03$.

3.3 Downwash and Sidewash Influence Factors

The lift and drag increments are considered a result of the induced downwash on the wing alone. Thus the influence factor, σ_{jk}, is used. The induced rolling moment is dependent on the downwash distribution along the wing. An influence factor which integrates the downwash together with the moment arm along the wing is required. This will be referred to as the moment influence factor, τ_{jk}. The induced yawing moment is dependent on both the downwash distribution along the wing, requiring $\tau_j k$, and the sidewash on the tailfin. The induced sideforce is considered a result of the induced sidewash on the tailfin only. The influence factor representing the sidewash on the tailfin is referred to as σ_{jk_f} where the subscript f refers to the tailfin. The pitching moment increment is partly caused by an induced downwash on the wing over a span equal to the tailplane span. Here, the influence factor is named $\sigma_{jk_{wh}}$.

3.3.1 Downwash Distribution Along the Wing

The distribution of downwash along the wing is obtained by multiplying the downwash by the moment arm from the c.g. and integrating over the bound vortex which yields τ_{jk}.

$$\tau_{jk} = \frac{4\pi}{\Gamma_j b} \int_{-\frac{b_w}{2}}^{\frac{b_w}{2}} w_{jk} y \, dy \tag{3.6}$$

Recalling equation (3.3) and multiplying by the moment arm y gives:

$$\left(\frac{4\pi}{\Gamma_j}\right) w_{jk} y = -\frac{2y\left(y + \Delta y - \frac{b_w}{2}\right)}{(y + \Delta y - \frac{b_w}{2})^2 + \Delta z^2 + r_c^2} + \frac{2y\left(y + \Delta y + \frac{b_w}{2}\right)}{(y + \Delta y + \frac{b_w}{2})^2 + \Delta z^2 + r_c^2} \tag{3.7}$$

Integration and conversion to dimensionless units with respect to b yields (see Appendix A.5):

$$\begin{aligned}\tau_{jk} = &-2\sqrt{\zeta^2 + \mu^2}\left[\tan^{-1}\left(\frac{\eta - \frac{\pi}{4}}{\sqrt{\zeta^2 + \mu^2}}\right) + \tan^{-1}\left(\frac{\eta + \frac{\pi}{4}}{\sqrt{\zeta^2 + \mu^2}}\right) - 2\tan^{-1}\left(\frac{\eta}{\sqrt{\zeta^2 + \mu^2}}\right)\right] \ldots \\ &- \eta \ln\left|\frac{\left((\eta - \frac{\pi}{4})^2 + \zeta^2 + \mu^2\right)\left((\eta + \frac{\pi}{4})^2 + \zeta^2 + \mu^2\right)}{\left(\eta^2 + \zeta^2 + \mu^2\right)^2}\right| - \frac{\pi}{8}\ln\left|\frac{(\eta + \frac{\pi}{4})^2 + \zeta^2 + \mu^2}{(\eta - \frac{\pi}{4})^2 + \zeta^2 + \mu^2}\right|\end{aligned} \tag{3.8}$$

Investigation of Figs. 3.6 and 3.7 show the limits at $\eta = \frac{\pi}{8}$ and $\eta = \frac{\pi}{4}$. At $\eta = \frac{\pi}{8}$ and $\zeta = 0$ the trailing aircraft longitudinal axis is coincident with the lead aircraft's near trailing vortex, hence resulting in upwash on the outboard and downwash on the inboard wing. This is likely to create a a strong negative rolling moment (toward the lead aircraft). At $\eta = \frac{\pi}{4}$ and $\zeta - 0$ the induced upwash on the inboard wing is far greater than the induced upwash on the outboard wing which is more distant from the trailing vortex filaments. Here, a maximum positive rolling moment is expected, i.e. away from the lead aircraft.

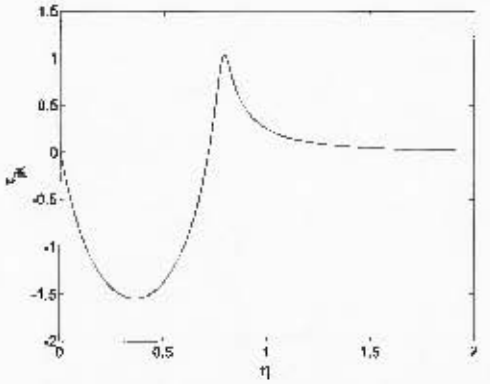

Figure 3.6: τ_{jk} using the Hallock Burnham profile where $\xi = -10$, $\zeta = 0$ and $\mu = 0.03$.

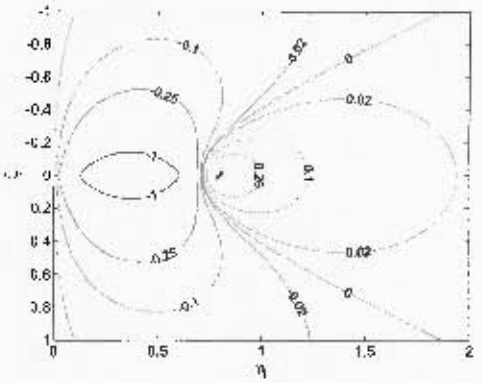

Figure 3.7: Contour map of τ_{jk} using the Hallock Burnham profile where $\xi = -10$ and $\mu = 0.03$.

Furthermore, a sharp change is shown between lateral separations of $\eta - \frac{\pi}{8}$ and $\eta - \frac{\pi}{4}$ (see section 3.5.1 for further discussion and derivation of rolling moment).

3.3.2 Sidewash on Tailfin

Recalling the method used to obtain equation (3.3), the same method can be used to obtain v_{jkf}, the sidewash at a point z_0 on the tailfin of the trailing aircraft due to the trailing vortices of the lead aircraft. The tailfin is assumed to be a semi-wing with a horseshoe vortex in the vertical xz plane centred on the tailfin root and extending to $\frac{\pi}{4}$ times the tailfin height (see Fig. 3.9). The lead bound vortex has no effect on the sidewash at the tailfin. The sidewash at the tailfin due to the near and far trailing vortices after simplifying, by letting $\Delta x \to \infty$, becomes:

$$\left(\frac{4\pi}{\Gamma_j}\right) v_{jk_f} = \frac{2(\Delta z \mid z_v \mid z)}{(\Delta y - \frac{b_y}{2})^2 \mid (\Delta z \mid z_v \mid z)^2 \mid r_c^2} - \frac{2(\Delta z + z_v \mid z)}{(\Delta y \mid \frac{b_y}{2})^2 \mid (\Delta z + z_v + z)^2 \mid r_c^2} \tag{3.9}$$

z_v is the vertical distance from the bottom of the tailfin, (centre of tailfin bound vortex), to the aircraft longitudinal centreline which is in plane with the wing. Introducing a sidewash influence factor σ_{jk_f}:

$$\sigma_{jk_f} \equiv \frac{4\pi}{\Gamma_j} \int_{-\frac{b_{fin}}{2}}^{0} v\langle z \rangle \, dz \tag{3.10}$$

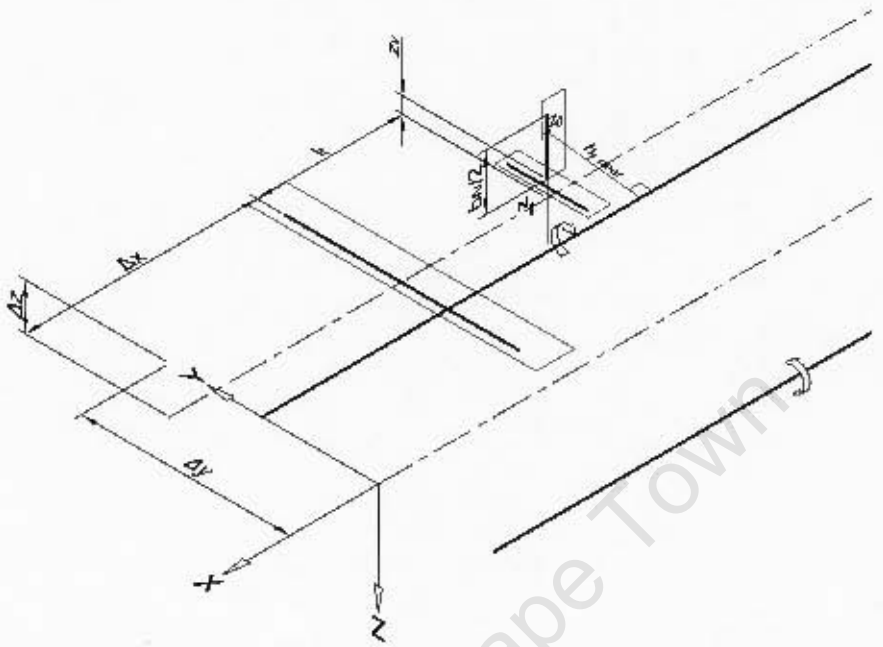

Figure 3.8: Schematic of aircraft arrangement and dimensions to calculate sidewash on tailfin.

Integration across the upper half of the tailfin bound vortex and conversion to dimensionless units obtains (see Appendix A.6):

$$\sigma_{jk_f} = \ln\left|\frac{(\eta - \frac{\pi}{8})^2 + (\zeta + \zeta_v - \frac{\pi}{8}\zeta_f)^2 + \mu^2}{(\eta - \frac{\pi}{8})^2 + (\zeta + \zeta_v)^2 + \mu^2}\right| - \ln\left|\frac{(\eta + \frac{\pi}{8})^2 + (\zeta + \zeta_v - \frac{\pi}{8}\zeta_f)^2 + \mu^2}{(\eta + \frac{\pi}{8})^2 + (\zeta + \zeta_v)^2 + \mu^2}\right| \quad (3.11)$$

Where $\zeta_f = \frac{b_f}{b}$. In order to represent equation (3.11) graphically, the necessary parameters were obtained from a typical large airliner, i.e. Boeing 747 (see section G). The sidewash on the tailfin due to the lead aircraft's trailing vortices is depicted in Figs. 3.10 and 3.11. Note that the maximum induced sidewash on the tailfin occurs at a lateral separation of $\eta = \frac{\pi}{8}$, where the trailing aircraft nose is marginally inboard of the lead aircraft's wing tip, and a small positive vertical separation (trailing aircraft below lead aircraft). The contour plot shows that for a further increase in the vertical separation, a rapid change in the sidewash occurs from an initially negative sidewash in the y direction to a positive sense. It can be immediately extrapolated that the yawing moments in this region would be highly unpredictable. A further discussion and derivation of the induced yawing moment follows in section 3.5.3.

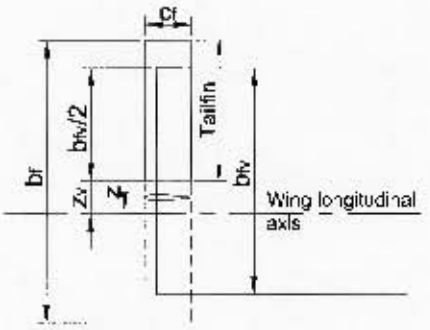

Figure 3.9: Representation of tailfin

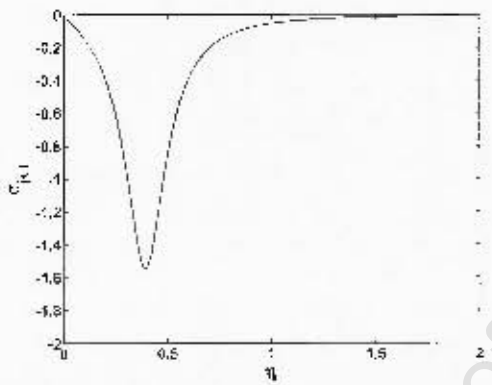

Figure 3.10: σ_{jk_f} using the Hallock Burnham profile where $\xi = -10$, $\zeta = 0$ and $\mu = 0.03$.

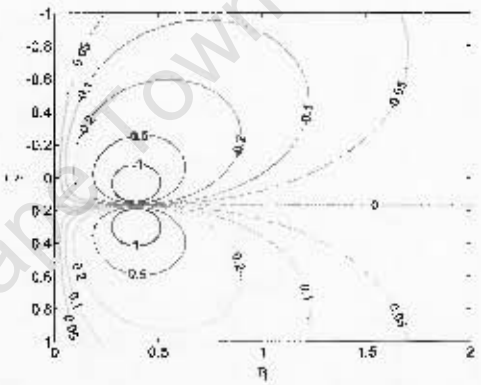

Figure 3.11: Contour map of σ_{jk_f} using the Hallock Burnham profile where $\xi = -10$ and $\mu = 0.03$.

3.4 Induced Forces

3.4.1 Change in Induced Lift and Drag

The derivations below closely follow those contained in reference [5]. At any spanwise position, y, the local downwash, $w(y)$, due to the presence of the lead aircraft causes a reduction in angle of attack equal to $\frac{w(y)}{V_E}$, where small angles are assumed. An approximation of the change in lift due to the induced downwash is given by:

$$\Delta C_{L,k} = -\frac{c_{l\alpha}}{V_E b} \int_{-b_c/2}^{b_c/2} w_{jk}\, dy \tag{3.12}$$

where the integration is taken along the bound vortex. From basic aerodynamic relationships, the circulation of the lead horseshoe vortex can be converted to a function of the lead

aircraft coefficient of lift $C_{L,j}$.

$$\Gamma_j = \frac{L_j}{\rho V_E b_v} = \frac{2V_E b}{\pi AR} C_{L,j} \tag{3.13}$$

With the dimensionless influence factor σ_{jk} given by equation (3.5) and substituting equation (3.13), we get:

$$\Delta C_{L,k} = \frac{-c_{l_\alpha} C_{L,j}}{2\pi^2 AR} \sigma_{jk} \tag{3.14}$$

A full derivation is found in Appendix B.1. Equation (3.14) can be simplified further using the result of thin airfoil theory, $c_{l_\alpha} = 2\pi$. Thus, the total change in lift is found by calculating the local change in lift due to the change in local angle of attack and integrating this change over the bound vortex. The change in lift is a direct function of σ_{jk}. If the lead aircraft is assumed to follow an ideal control law by which the circulation remains constant then it can be seen that the change in lift will be directly proportional to the separation. A comparison is made in Fig. B.1c where results obtained from integrating over the bound vortex is compared with results obtained by numerical integration over an elliptical wing. Figure B.2c shows a contour plot of the change in induced lift as a function of lateral and vertical separation. Additional experimental data and results using vortex lattice methods from other studies are shown in Fig. B.3.

The change in drag is found by means of the Kutta-Joukowski theorem, where the downwash will induce a change in drag at any spanwise position given by:

$$\delta C_{Di,k} = \frac{2w(y)\Gamma_k dy}{V_E^2 S}$$

Integrating along the bound vortex filament and using equations (3.13) and (3.4), we find the total change in drag:

$$\begin{aligned} \Delta C_{Di,k} &= \frac{4C_{L,k}}{\pi V_E b} \int_{-b_v/2}^{b_v/2} w_{jk}\, dy \\ &= \frac{2C_{L,j}C_{L,k}}{\pi^3 AR} \sigma_{jk} \end{aligned} \tag{3.15}$$

It can be seen that $\Delta C_{Di,k}$ is a function of the trail aircraft coefficient of lift and σ_{jk}, indicating that, if the lead and trailing aircraft are assumed to follow an ideal control law, then the change in induced drag will be directly proportional to the separation (see Fig. B.1a). These results agree with the findings of Myatt and Blake [1] and Blake [6] who suggested that, aside from the induced drag, aerodynamic force and moment increments on the trailing aircraft can be modelled as functions of the relative separation and lift coefficient of the vortex generating aircraft (lead), while the induced drag can be modelled as a function of the separation and the lift coefficients of both the lead and trailing aircraft.

It will be shown that the following changes in aerodynamic forces and moments are indeed functions of the relative separation and lead aircraft lift coefficient, except for the change in yaw moment which considers the distribution of induced drag along the wing (see Figs. B.1a and B.2a).

3.4.2 Induced Sideforce

The sideforce induced on the tailfin is considered as the total sideforce for the aircraft while the effect of the sidewash over the fuselage is ignored. This sideforce is derived in a similar way to that in which the change in lift on the wing was found. The lead trailing vortex generates a local sidewash on the trailing aircraft tailfin and therefore a local sideslip angle $\beta = \frac{v}{V}$. The sideforce coefficient created by the tailfin due to this local sideslip is:

$$\delta C_{yk_f} = c_{l_{\alpha_f}} \frac{v}{V_E}$$

Assuming the tailfin to be a semi-wing as discussed in section 3.3.2 and shown in Fig. 3.9, integration along the upper half of the tailfin bound vortex gives:

$$\Delta C_{yk_f} = \frac{2}{b_f} \int_{\frac{-b_{f_v}}{2}}^{0} c_{l\alpha_f} \left(\frac{v}{V_E}\right) \, dz \tag{3.16}$$

where b_f is twice the tailfin span, symmetric about an axis at the bottom of the tailfin and ΔC_{yk_f} is referred to the tailfin area $S_f = \bar{c}_f \frac{b_f}{2}$. Recalling the dimensionless influence factor σ_{jk_f} of equation (3.10), equation 3.16 becomes:

$$\Delta C_{yk_f} = \frac{2c_{l\alpha_f}}{b_f} \frac{\Gamma_j}{4\pi} \frac{\sigma_{jk_f}}{V_E}$$

The dimensionless term, $\zeta_f = \frac{b_f}{b}$, is used from which $b_{f_v} = \frac{\pi}{4}\zeta_f b$. Γ_j is converted to C'_{L_j} using equation (3.13). Applying the result of airfoil theory, $c_{l\alpha_f} = 2\pi$, to the tailfin, the solution for the change in sideforce coefficient becomes:

$$\Delta C_{yk_f} = \frac{2C_{L_j}}{\pi A R \zeta_f} \sigma_{jk_f} \tag{3.17}$$

Referring ΔC_{yk_f} to the wing area S, the coefficient for the total sideforce is found:

$$\Delta C_{yk} = \Delta C_{yk_f}{}' = \frac{S_f}{S} \frac{2C_{L_j}}{\pi A R \zeta_f} \sigma_{jk_f} \tag{3.18}$$

The induced sideforce, modelled as solely dependent on the tailfin, only exhibits significant change near $\eta = \frac{\pi}{8}$ where the tailfin is close to the lead aircraft's near trailing vortex filament. The sidewash on the tailfin, and hence the induced sideforce, changes rapidly with vertical separation, especially near $\eta = \frac{\pi}{8}$. Figure B.1b shows the induced sideforce for lateral separation and $\zeta = 0$ while Fig. B.2b shows the dependence on vertical separation.

3.5 Induced Moments

3.5.1 Roll

The induced rolling moment is considered to be a result of the distribution of lift along the wing alone. The distribution of lift and sideforce along the tailplane and tailfin respectively is assumed to be negligible and ignored. The rolling moment due to a wing section is:

$$\delta\bar{L}_k - \delta L_k y - \overline{qc} c_{l_\alpha} \frac{w}{V_E} y dy$$

Here, $\bar{L}$ represents rolling moment and L represents lift. Integration along the trailing wing bound vortex and conversion to dimensionless coefficient, $\delta C_{lk} = \frac{\delta\bar{L}_k}{\bar{q}Sb}$, yields:

$$\Delta C_{lk} = \frac{c_{l_\alpha}}{b^2} \int_{-\frac{b_c}{2}}^{\frac{b_y}{2}} \frac{w}{V_E} y \, dy \tag{3.19}$$

The moment influence factor of equation (3.6) is introduced and from equation (3.13), equation (3.19) becomes:

$$\Delta C_{lk} = \frac{c_{l_\alpha} C_{L,j}}{2\pi^2 AR} \tau_{jk} \tag{3.20}$$

Integrating over the bound vortex with constant geometric chord and constant $c_{l_\alpha} = 2\pi$ yields a positive peak rolling moment at optimum separation which represents an inflated peak value compared to the induced rolling moment of a wing with an elliptical lift distribution (see Fig. B.1d). The peak positive rolling moment of the approximation is, however, well within the same order of magnitude albeit with a steeper gradient. Furthermore, the results obtained from the approximation will be conservative. The approximation is therefore considered adequate for the current study.

3.5.2 Pitch

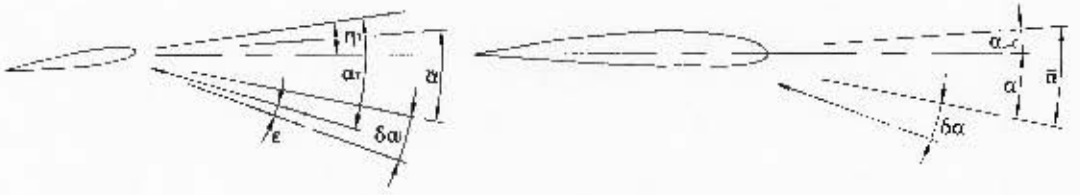

Figure 3.12: Wing tailplane flow geometry.

Figure 3.12 shows the various contributions to angle of attack at the main wing and the tailplane. For the wing, $\bar{\alpha}$ is the combined geometric angle of attack and angle of attack

corresponding to zero lift, i.e. $\bar{\alpha} = \alpha_{geom} - \alpha_{L=0}$ while $\delta\alpha_i$ is the change in induced angle of attack due to the presence of the lead aircraft trailing vortices. The angle of attack on the tailplane is hence,

$$\alpha_T = \bar{\alpha} + \delta\alpha_i - \varepsilon + \eta_T$$
$$\text{and } \bar{\alpha} + \delta\alpha_i - \varepsilon = (\bar{\alpha} + \delta\alpha_i)\left(1 - \frac{d\varepsilon}{d\alpha}\right)$$

For steady flight in isolation i.e. no effect due to the lead trailing vortices, $\bar{\alpha} = \frac{C_{Lk_w}}{a_{l_\alpha}}$ where a_{l_α} is the wing lift coefficient slope. When considering the effect due to the lead trailing vortices, It is assumed that $\delta\alpha_i = -\frac{w'}{V}$, where w' represents the downwash along a portion of the wing span equal to the span of the tailplane bound vortex, due to the presence of the lead aircraft trailing vortices. The tailplane angle of attack is thus approximated as:

$$\alpha_T = \left(\frac{C_{Lk_w}}{a} - \frac{w'}{V_E}\right)\left(1 - \frac{d\varepsilon}{d\alpha}\right) + \eta_T \tag{3.21}$$

To calculate the change in coefficient of pitching moment, δC_{mk}, it follows from Fig. 3.13

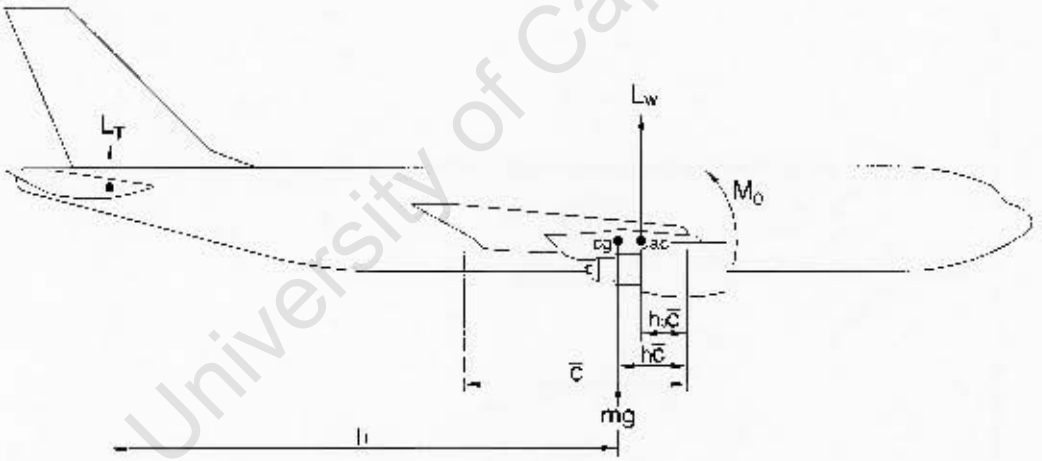

Figure 3.13: Pitch moment model.

that:

$$M = M_0 + L_w(h - h_0)\bar{c} - L_T l_T \tag{3.22}$$

Substituting equation (3.21) into equation (3.22) and converting to dimensionless form:

$$C_{mk} = C_{m_0} + (C_{Lk_w} + \Delta C_{L,k})(h - h_0) - \overline{V}_T\left(a_1\left(\frac{C_{Lk_w}}{a} - \frac{w'}{V_E}\right)\left(1 - \frac{d\varepsilon}{d\alpha}\right) + a_1\eta_T\right)$$

$\bar{V}_T$ is the tailplane volume ratio and $\Delta C_{L,k}$ is the change in wing lift coefficient given by equation (3.14). The change in aircraft pitching moment coefficient due to the presence of the lead aircraft trailing vortices is thus:

$$\begin{aligned}\Delta C_{m\,k} &= -\Delta C_{L,k}(h - h_0) - \overline{V}_T a_1 \frac{w'}{V_E}\left(1 - \frac{d\varepsilon}{d\alpha}\right) \\ &= \Delta C_{L,k}(h - h_0) - \overline{V}_T \Delta C_{L\,w_h}\left(1 - \frac{d\varepsilon}{d\alpha}\right)\end{aligned} \tag{3.23}$$

where $\Delta C_{L\,w_h} = -a_1 \frac{w'}{V_E}$. a_1 is the tailplane lift coefficient slope.

To find the total change in pitching moment coefficient, $\Delta C_{m\,k}$, $\frac{w'}{V_E}$ is required which involves integration along a portion of the wing of which the span is equal to the span of the tailplane bound vortex $\frac{-b_{h_w}}{2}$ to $\frac{b_{h_w}}{2}$. The derivation of $\Delta C_{L\,w_h}$ follows:

$$\Delta C_{L\,w_h} = -a_1 \frac{w'}{V} = -\frac{a_1}{b_{h_w}} \int_{\frac{-b_{h_w}}{2}}^{\frac{b_{h_w}}{2}} \frac{w}{V_E}\, dy \tag{3.24}$$

Introducing the influence factor $\sigma_{jk\,wh}$ (see Appendix A.4)

$$\sigma_{jk\,wh} \equiv \frac{4\pi}{\Gamma_j} \int_{\frac{-b_{h_w}}{2}}^{\frac{b_{h_w}}{2}} w\, dy$$

and following the same approach used to obtain equation (3.14), equation (3.24) becomes

$$\Delta C_{L\,wh} = \frac{-2a_1 C_{l_r,j}}{\pi^3 A R \eta_h} \sigma_{jk\,wh} \tag{3.25}$$

where $\eta_h = \frac{b_h}{b_r}$. $\sigma_{jk\,wh}$ is given as (see Appendix A.4):

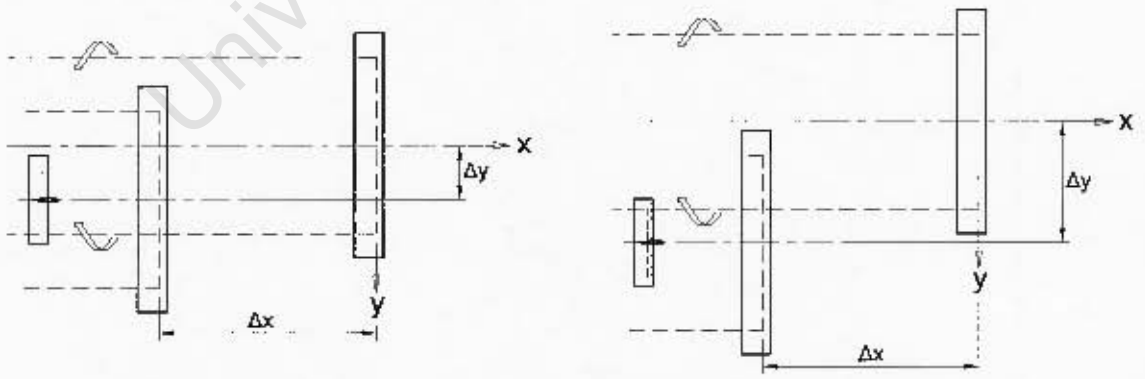

(a) Separation for maximum nose up induced pitching moment.

(b) Separation for maximum nose down induced pitching moment.

Figure 3.14: Graphic indicating relative lateral separations for maximum nose up/down induced pitching moments

$$\sigma_{jk_{wh}} = \ln \left| \frac{\left(\zeta^2 + \left(\eta - \frac{\pi}{8} - \frac{\pi}{8}\eta_h\right)^2 + \mu^2\right)\left(\zeta^2 + \left(\eta + \frac{\pi}{8} + \frac{\pi}{8}\eta_h\right)^2 + \mu^2\right)}{\left(\zeta^2 + \left(\eta - \frac{\pi}{8} + \frac{\pi}{8}\eta_h\right)^2 + \mu^2\right)\left(\zeta^2 + \left(\eta + \frac{\pi}{8} - \frac{\pi}{8}\eta_h\right)^2 + \mu^2\right)} \right| \tag{3.26}$$

Figures B.1e and B.2e show the predicted pitching moment coefficient for lateral and

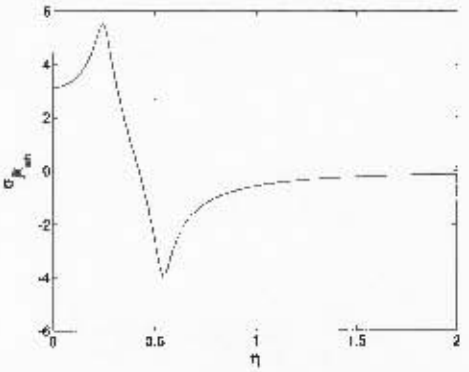

Figure 3.15: $\sigma_{jk_{wh}}$ using the Hallock Burnham profile where $\xi = -10$, $\zeta = 0$ and $\mu = 0.03$.

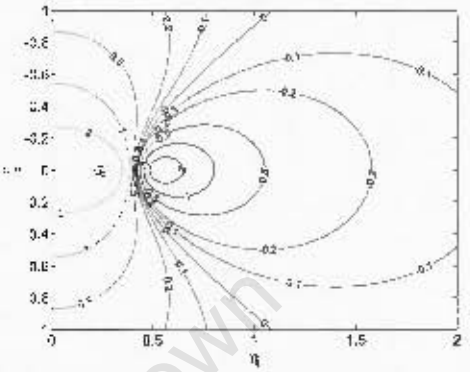

Figure 3.16: Contour map of $\sigma_{jk_{wh}}$ using the Hallock Burnham profile where $\xi = -10$ and $\mu = 0.03$.

vertical separation. The model predicts maximum positive pitching moment for the tailplane directly inboard of the lead aircraft's near trailing vortex and maximum nose down pitching moment for the tailplane directly outboard of the near trailing vortex. This effect is akin to experiencing an upward/downward gust. The aircraft will tend to 'weathercock' into the upwash/downwash.

3.5.3 Yaw

The induced yawing moment is driven by both the induced sidewash on the tailfin and the induced drag distribution along the wing. From the Kutta-Joukowski theorem, the downwash will induce a change in drag of varying magnitude along the wing dependent on the magnitude of the local downwash at a spanwise location, y. This varying induced drag acts about the c.g. and will generate a yawing moment. The moment arm of the yawing moment due to the sideforce on the tailfin is given by the distance from the CG to the tailfin centre of pressure parallel with the x-axis in the body frame, given by l_f.

The yawing moment due to the local drag at a spanwise position, y, is given by:

$$\delta N_{k_w} = \delta D_{ik}\, y = \rho w\langle y\rangle \Gamma_k y dy$$

Conversion to dimensionless coefficient and integration along the wing bound vortex gives:

$$\Delta C_{nk_w} = \frac{2\Gamma_k}{V_E^2 S b} \int_{-b_v/2}^{b_v/2} w_{jk} y \, dy$$

Using τ_{jk} as defined by equation (3.6) and converting Γ_k to $C_{L,k}$ using equation (B.2), we arrive at the equation to describe the change in yaw coefficient due to the drag distribution along the wing:

$$\Delta C_{n\,k_w} = \frac{2C_{L,k}C_{L,j}}{\pi^3 AR}\tau_{jk} \tag{3.27}$$

The yaw moment coefficient due to the tailfin is simply calculated by taking the sideforce on the tailfin and multiplying by the moment arm. Recalling equation (3.17) and introducing the tailfin volume ratio, $\bar{V}_f = \frac{S_f l_f}{Sb}$:

$$\Delta C_{n\,k_f}{}' = -\bar{V}_f \frac{2C_{L,j}}{\pi AR\zeta_f}\sigma_{jk_f} \tag{3.28}$$

The total yaw moment coefficient is hence after summing equations (3.27) and (3.28):

$$\Delta C_{n,k} = \frac{2C_{L,j}C_{L,k}}{\pi^3 AR}\tau_{jk} - \bar{V}_f \frac{2C_{L,j}}{\pi AR\zeta_f}\sigma_{jk_f} \tag{3.29}$$

The combined effect is shown in Figs. B.1f and B.2f where two peaks are revealed for lateral separation and $\zeta = 0$. At $\eta = \frac{\pi}{4}$, the dominant effect is due to the drag distribution along the wing while at $\eta = \frac{\pi}{8}$, the effect due to sidewash on the tailfin dominates. From Fig. 3.11, the sidewash influence factor σ_{jk_f} exhibits a large dependence on vertical separation. Thus, changes in vertical separation near $\eta = \frac{\pi}{8}$ will yield significant changes in the yawing moment.

3.6 Induced Forces and Moments versus Control Authority

In order to gain a clearer insight into the magnitudes of the effects due to the lead trailing vortices on the aerodynamic coefficients, the change in aerodynamic coefficients are calculated and compared with the angle of attack, sideslip angle and control deflection angles required to trim the aircraft at a particular separation. A right echelon formation of two large identical passenger airliners is considered using aircraft data from Appendix G and converting to the model representation required.

From equations (C.2) and (C.4), the steady state trim orientation angles and control surface deflection angles are obtained. The change in orientation angles over a lateral separation of $0 \geq \eta \leq 2$ are shown in Fig. 3.17. Figure 3.17 shows maximum $\delta\alpha$ at $\eta = 0$ where the maximum downwash is encountered and minimum $\delta\alpha$ at $\eta = \frac{\pi}{4}$ where the single horseshoe vortex model predicts maximum increase in lift coefficient and reduction in drag coefficient. Figure 3.18 shows the change in elevator and rudder control deflections as a metric of maximum allowable control deflection for $\zeta - 0$ and $\eta = 0 \ldots 2$ (Physical aircraft data from Appendix G). The maximum predicted rudder and elevator deflections due

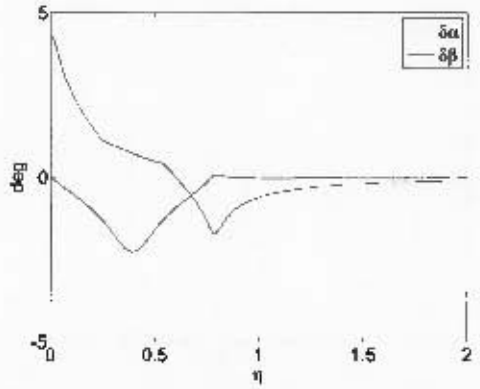

Figure 3.17: Change in steady state angle of attack and sideslip angle due to lead aircraft trailing vortices for lateral separation.

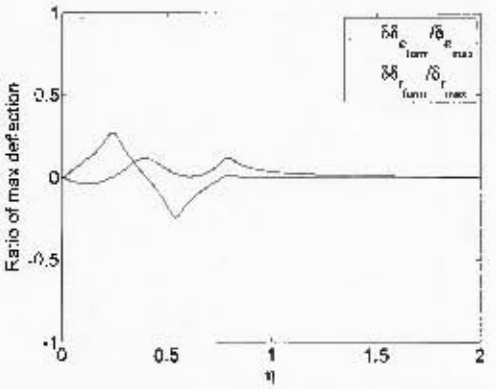

Figure 3.18: Change in steady state elevator and rudder deflection angles due to formation flight. Deflections given as metric of maximum deflections (see Appendix G).

to formation flight are well within the maximum allowable deflection angles. The rudder deflection angle shows two distinct positive spikes at $\eta = \frac{\pi}{8}$ and $\eta = \frac{\pi}{4}$. At $\eta = \frac{\pi}{8}$, the dominant effect is due the sidewash on the tailfin while at $\eta = \frac{\pi}{4}$, the primary cause for the required rudder deflection is due to the downwash distribution along the wing (Fig. 3.20). At $\eta = \frac{\pi}{4}$, the change in yaw moment coefficient is less than half of that encountered at $\eta = \frac{\pi}{4}$ yet the peak rudder deflection angles are both similar at these spanwise separations. It appears that the coupling of the change in yaw moment coefficient with the maximum positive change in roll moment coefficient requires a similar rudder deflection angle at $\eta = \frac{\pi}{4}$ to the deflection angle at $\eta = \frac{\pi}{8}$.

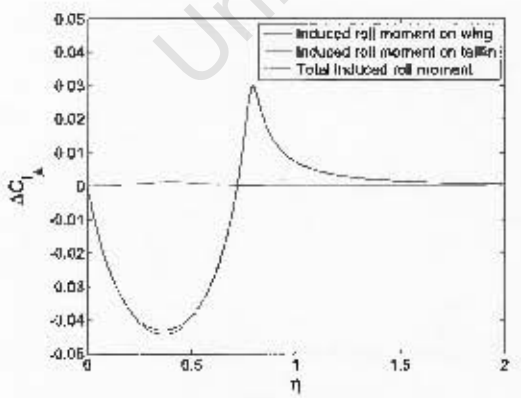

Figure 3.19: The combined influence of the downwash along the wing and sidewash along the tailfin on the roll moment.

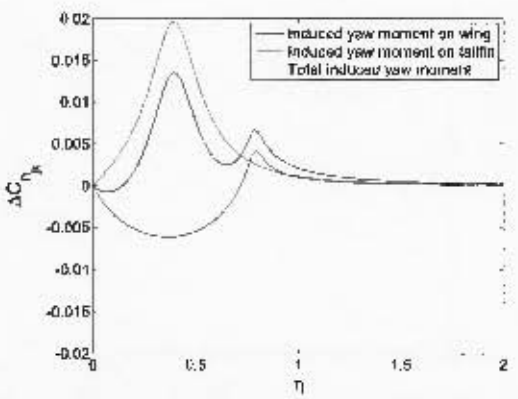

Figure 3.20: The combined influence of the downwash along the wing and sidewash on the tailfin on the yaw moment.

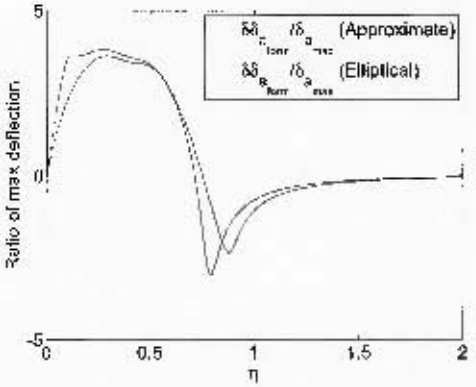

Figure 3.21: Change in steady state aileron deflection due to formation flight.

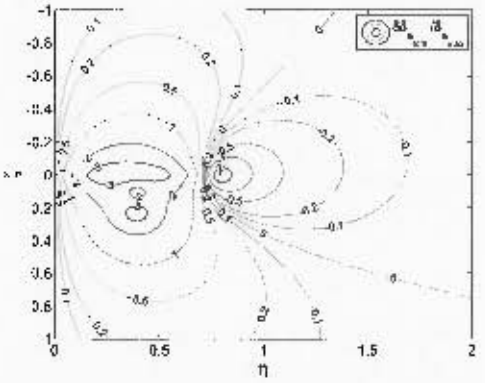

Figure 3.22: Contour plot of aileron deflection angle for lateral and vertical separation.

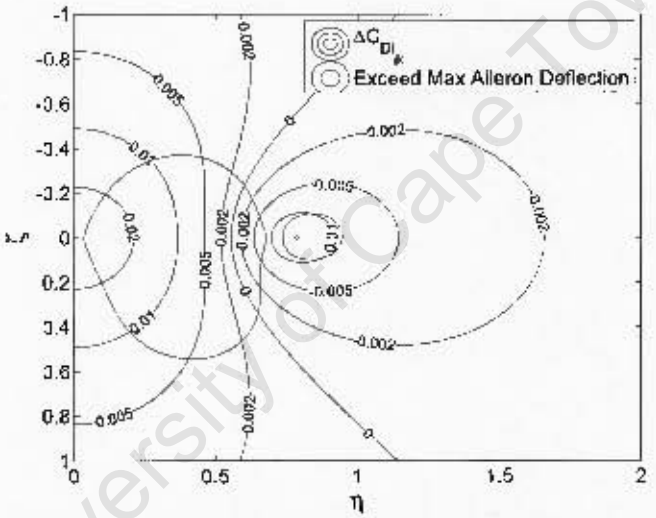

Figure 3.23: Change in drag due to formation flight for lateral and vertical separation with aileron exceedance contour superimposed.

Figures 3.21 and 3.22 show the required aileron deflections well above the available control deflection angle for various ranges of η with $\zeta = 0$ including $\eta = \frac{\pi}{4}$ for optimum drag efficiency. It is clearly evident that the primary cause of the large aileron deflections is due to the change in the roll moment coefficient. Figure 3.19 shows the influence on the roll moment due to the sidewash on the tailfin is negligible, hence, the primary effect on the induced roll moment, and subsequently, the aileron deflection, is due to the downwash along the wing. Figure 3.23 gives an indication of the maximum drag benefit obtainable with respect to the limiting factor of the aileron control authority as predicted by the basic single horseshoe vortex model.

4 Modelling The Effect of Atmospheric Turbulence on Formation Flight

4.1 Simplifying Assumptions on the Effects of Atmospheric Turbulence on Aircraft in Formation

Atmospheric turbulence is modelled as stationary, homogeneous, isotropic, Gaussian turbulence [69, 72]. The two aircraft are modelled as two points considered to be vanishingly small with respect to the wavelengths of all significant spectral components. Etkin [72] shows that the dominant wavelength is defined by:

$$\lambda_{u_{peak}} = \frac{2\pi}{\Omega_{u_{peak}}} = 4.7L \tag{4.1}$$

indicating that the wavelengths are large compared to the size of a typical large airliner. The lateral and vertical relative separations between the lead and trail aircraft are also considered small, thus, only the longitudinal separation is considered. The longitudinal separation is written as a function of the time separation where, $\Delta x = V_E \tau$.

A further assumption is made in order to simplify the model. It is assumed that the gust velocity experienced by the lead aircraft will remain frozen until the trailing aircraft has reached the same streamwise location. As a measure to limit the divergence of this assumption, the longitudinal separation is limited to 10 spans. The one-dimensional correlations and spectral densities given in the literature [69, 72] can subsequently be applied.

Schaeffer et al. [75] note that although a cross spectrum has been found to exist between longitudinal and vertical gust velocities, it has been concluded that the cross spectrum only has a significant magnitude at frequencies too low to be important. Etkin [77] used a power series approximation to generate atmospheric turbulence power spectra and cross spectra of the gust components up to second order derivatives of the components. 14 different non-zero power spectra were identified. Three zero-order, Φ_{uu}, Φ_{vv} and Φ_{ww}, and four first order, $\Phi_{uu_x}, \Phi_{uv_y}, \Phi_{vv_x}$ and Φ_{ww_x} , non-zero spectra were found where only one was a cross-spectrum involving two different velocity components, i.e. Φ_{uv_y} where $v_y = \frac{\partial v}{\partial y}$. Etkin goes on to state that "in a first-order theory, this remains as the only cross-term between velocity components and if it is neglected, complete statistical separation of the response to the three components of the turbulence results".

MIL-F-8785C [33] specifies that, u_g, v_g, w_g and p_g should be considered uncorrelated

while q_g is correlated with w_g and r_g is correlated with v_g. Hence, it is assumed that there is effectively no correlation between any of the linear gust velocity components.

4.2 Atmospheric Turbulence Spectra and Parameters

The von Karman model one dimensional spectra are defined in MIL-F-8785C [33] and Schaeffer et al. [75] as functions of temporal frequency.

$$\Phi_{uu}\langle\omega\rangle = \frac{\sigma^2 L}{\pi V_e}\frac{1}{[1+(aL\frac{\omega}{V_e})^2]^{\frac{5}{6}}} \tag{4.2}$$

$$\Phi_{vv}\langle\omega\rangle = \Phi_{ww}(\omega) = \frac{\sigma^2 L}{\pi V_e}\frac{1+\frac{8}{3}(aL\frac{\omega}{V_e})^2}{[1+(aL\frac{\omega}{V_e})^2]^{\frac{11}{6}}} \tag{4.3}$$

The turbulence gust gradients are considered equivalent in effect to the aircraft angular velocities. These gust gradients are approximated by:

$$p_g = -\frac{\partial w_g}{\partial y} + \frac{\partial v_g}{\partial z} \quad q_g = -\frac{\partial w_g}{\partial x} + \frac{\partial u_g}{\partial z} \quad r_g = \frac{\partial u_g}{\partial y} - \frac{\partial v_g}{\partial x}$$

The spectral densities of the gust velocity gradients are given as:

$$\Phi_{w_y w_y} = \frac{\sigma^2}{V_e L}\frac{0.8\left(\frac{2\pi L}{4b}\right)^{\frac{1}{3}}}{1+\left(\frac{4b\omega}{\pi V_e}\right)^2} \tag{4.4}$$

$$\Phi_{w_x w_x} = \frac{\left(\frac{\omega}{V_e}\right)^2}{1+\left(\frac{4b\omega}{\pi V_e}\right)^2}\Phi_{ww}\langle\omega\rangle \tag{4.5}$$

$$\Phi_{v_x v_x} = \frac{\left(\frac{\omega}{V_e}\right)^2}{1+\left(\frac{3b\omega}{\pi V_e}\right)^2}\Phi_{vv}\langle\omega\rangle \tag{4.6}$$

The recommended rms magnitude of atmospheric turbulence intensity at medium/high altitude is given by MIL-F-8785C as a function of altitude and probability of exceedance, reprinted in Fig. 4.1. At 40000 feet, an rms magnitude of 4.7 m/s is given for severe turbulence while 1.3 m/s is given for moderate turbulence. The data on light turbulence is less clear. A minimum value of 0.9 m/s is recommended by MIL-HDBK-1797 [78] for simulations of aircraft encountering atmospheric turbulence. This value is however very close to the 1.3 m/s for moderate turbulence at 40000 feet. Extrapolation of the data in MIL-F-8785C indicates that the rms magnitude for light turbulence at 40000 feet is 0 where the nearest data point gives 0.2 m/s at 33000 feet. For the purposes of the current study to obtain a comparison of formation flight and isolated flight in different levels of atmospheric turbulence, an rms magnitude of 0.2 m/s is chosen for light turbulence.

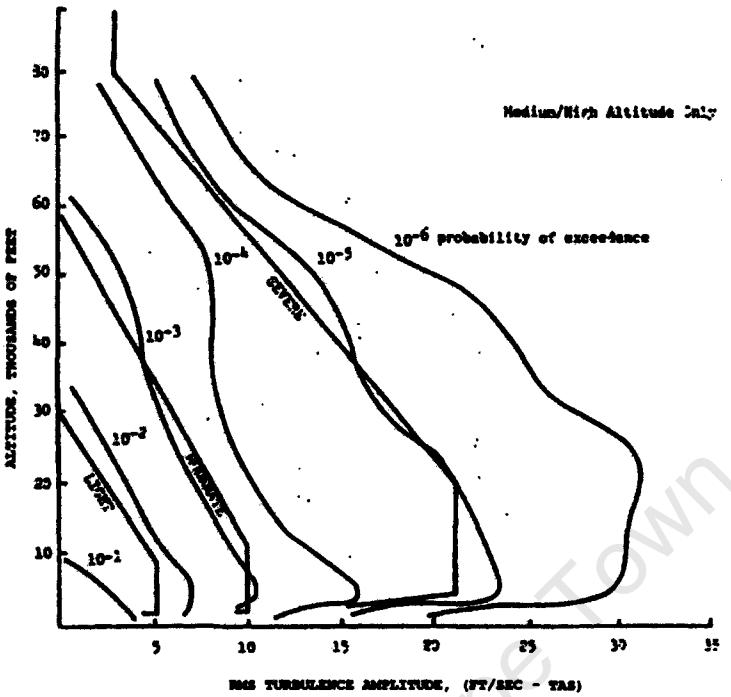

Figure 4.1: RMS turbulence intensity amplitude (feet/sec) as a function of altitude (feet) and probability of exceedance, reprinted from MIL-F-8785C [33].

As prescribed by MIL-F-8785C [33] and Schaeffer et al. [75], an integral scale of L_u = 2500 feet or 762 m is used with the von Karman spectral densities in the current study. A secondary investigation of L_u = 152 m are considered for light and moderate turbulence intensities following from indications by Houbolt [70] that mean length scales of 500 to 700 feet may prevail in turbulence of lighter severity.

4.3 Effective Aircraft Separation

The principle perturbations on the trailing aircraft stem from the assumption that the lead aircraft's trailing vortices are assumed to move in an ideal fashion in atmospheric turbulence. i.e. shift with the lateral and vertical gust velocities. Both vortices are assumed to move identically and thus the relative spacing between the two trailing vortices are maintained. Figure 4.2 describes the ideal movement assumed in a lateral gust.

In order to calculate the effective separation, the direction of the trailing vortex is considered parallel to the local instantaneous velocity vector with respect to the air as shown in Figs. 4.3 and 4.4. These disturbed horseshoe vortices alter the effective separation between the aircraft and thus change the induced aerodynamic loads caused by the trailing

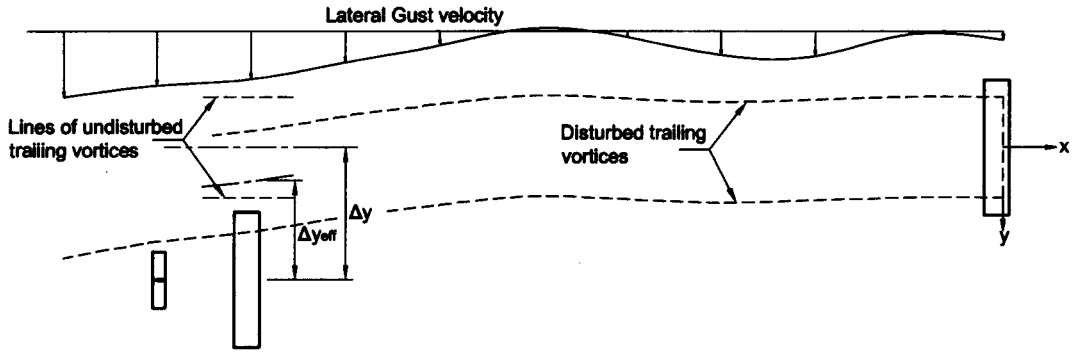

Figure 4.2: Illustration of assumption used to model the disturbed trailing vortices due to lateral gusts causing a change in effective lateral separation.

vortices.

It is assumed that the lead aircraft does not experience vertical acceleration by satisfying an ideal control law which ensures a constant lift. A vertical component of turbulent velocity will change the effective vertical separation, Δz_{eff}, or in dimensionless form, ζ_{eff}. Similarly, in the case of the turbulent lateral velocity, v_g, Δy will become Δy_{eff} or in dimensionless form η_{eff} as shown in Fig. 4.4. A stronger gust velocity or greater streamwise separation will increase the difference between geometric separation and effective separation. The effective

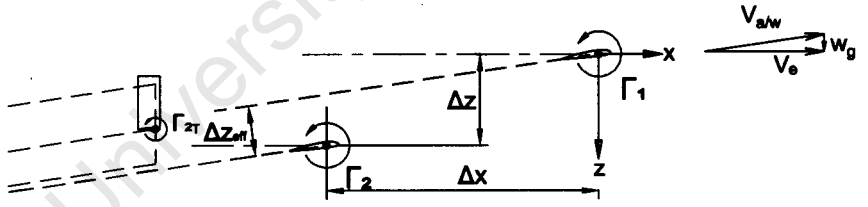

Figure 4.3: Side view of formation in vertical turbulence.

aircraft separation is defined as a function of the gust velocities, v_g and w_g, freestream velocity and geometric separation:

$$\Delta y_{eff} = \sqrt{\Delta x^2 + \Delta y^2} \sin\left(\tan^{-1}\left(\frac{\Delta y}{-\Delta x}\right) - \tan^{-1}\left(\frac{v_g}{V}\right)\right)$$

$$\Delta z_{eff} = \sqrt{\Delta x^2 + \Delta z^2} \sin\left(\tan^{-1}\left(\frac{\Delta z}{-\Delta x}\right) - \tan^{-1}\left(\frac{w_g}{V}\right)\right)$$

Converting to dimensionless units and assuming small angles for v_g and w_g with respect to

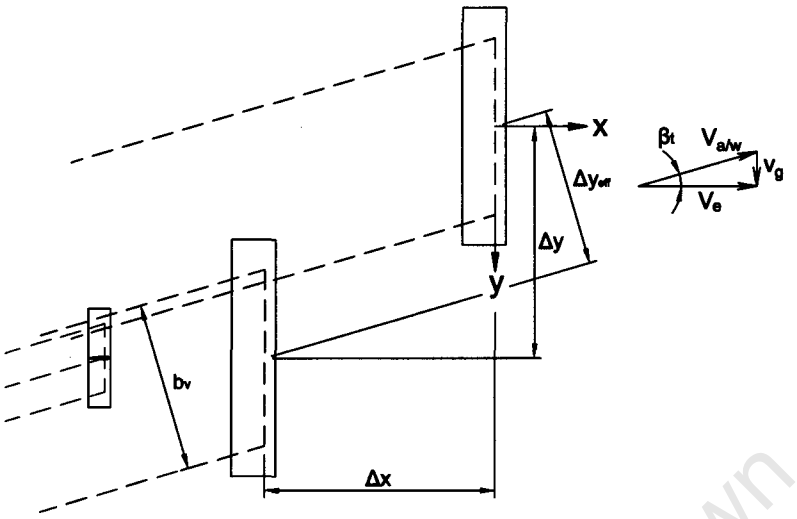

Figure 4.4: Top view of formation in lateral turbulence.

V:

$$\eta_{eff} = \sqrt{\xi^2 + \eta^2} \sin\left(\tan^{-1}\left(\frac{\eta}{-\xi}\right) - \left(\frac{v_g}{V}\right)\right) \tag{4.7}$$

$$\zeta_{eff} = \sqrt{\xi^2 + \zeta^2} \sin\left(\tan^{-1}\left(\frac{\zeta}{-\xi}\right) - \left(\frac{w_g}{V}\right)\right) \tag{4.8}$$

The aerodynamic disturbance loads encountered by the trailing aircraft due to the lead aircraft trailing vortices are therefore defined by substituting η_{eff} and ζ_{eff} for η and ζ into the equations defining the change in aerodynamic load and moment coefficients. The trim condition is set for the loads and moments due to a given separation in zero atmospheric turbulence and thus, in the current study, the difference between η_{eff} and η along with ζ_{eff} and ζ is what ultimately generates the disturbance loads due to the trailing vortices. The gust velocities are defined as stochastic processes by the von Karman spectral densities and assumed to remain frozen for the time it takes the trailing aircraft to cover the longitudinal separation.

Referring to Section 3.6 and Appendix B.7, the gradients displayed in Figs. 3.18 to 3.22 and Figs. B.1a to B.1f give an indication of the disturbance magnitude that a gust would impose. Figure 3.21 is reprinted here for convenience as Fig. 4.5. Considering the steep slope of aileron deflection over lateral separation as an example, a lateral gust of 1% freestream velocity of 236 m/s at 40000 feet (M=0.8), 2.36 m/s, in a formation with longitudinal, lateral and vertical relative separation of 10, 0.785 and 0 spans respectively, would change the effective lateral separation to 0.685 spans. Ignoring unsteady effects, this would result in a change of roll moment requiring the equivalent of 150 ° of aileron

deflection. This example is in no way a realistic description of the roll response over this range of aileron deflection nor of the physical behaviour of the aircraft, but it does provide some indicatation as to the severity of such a condition.

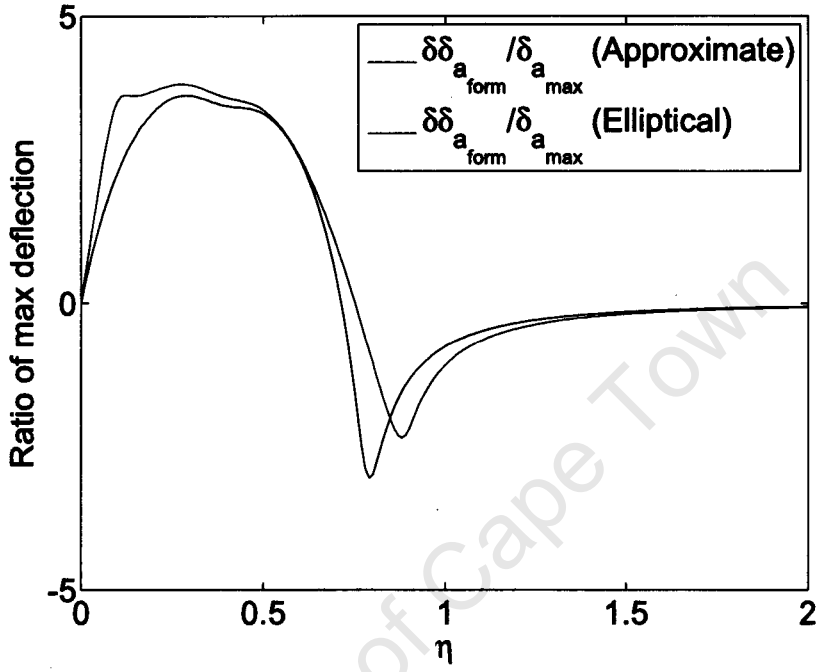

Figure 4.5: Change in steady state aileron deflection due to formation flight. Reprinted from section 3.6

5 Development of the Perturbed Equations of Motion in Formation Flight

In order to obtain the acceleration response and consequently, the acceleration spectra, from a simulation, a set of equations are required to approximate the motion of the aircraft. This chapter summarizes the derivation in Appendix D which yields the equations of motion implemented in the simulation of chapter 6. The current chapter arrives at a fully linearised set of equations of motion for a trailing aircraft of a two ship formation flying through atmospheric turbulence. These are adapted for use in the simulation accounting for the non-linear responses with respect to change in separation. The linearised set of equations aid understanding and shed light on the coupling of the longitudinal and lateral DOF by way of the gust velocities.

The six-degree-of-freedom equations of motion for a rigid body, with origin at the CG are given by equations (D.1) to (D.6), reprinted here for convenience, where the body is symmetrical with respect to the xz plane [79].

$$\begin{aligned} m\left(\dot{u} - vr + wq\right) &= -mg\sin\theta + D + T \\ m\left(\dot{v} + ur - wp\right) &= mg\sin\phi\cos\theta + S \\ m\left(\dot{w} - uq + vp\right) &= mg\cos\phi\cos\theta + L \\ I_x\dot{p} - \left(I_y - I_z\right)qr - I_{xz}\left(pq + \dot{r}\right) &= \tilde{L} \\ I_y\dot{q} - \left(I_z - I_x\right)pr - I_{xz}\left(r^2 - p^2\right) &= M \\ I_z\dot{r} - \left(I_x - I_y\right)pq - I_{xz}\left(\dot{p} - qr\right) &= N \end{aligned}$$

In steady trimmed formation flight, the body frame is slightly rotated with respect to its orientation during steady flight in isolation. The orientation angle $\psi_{0_f}^{BI}$ of the body frame in formation with reference to the inertial frame is non zero and the pitch angle $\theta_{0_f}^{BI}$ is at a different angle. It is assumed that the roll angle, $\phi_{0_f}^{BI}$ is trimmed to zero in formation flight. The transformation due to $\psi_{0_f}^{BI}$ and $\theta_{0_f}^{BI}$ in steady formation flight follows from Fig. 5.1.

$$\begin{aligned} \boldsymbol{u}_{0_f}^{B} &= \boldsymbol{R}_{BI}\boldsymbol{u}_{0_f}^{I} \\ \begin{Bmatrix} u_{0_f} \\ v_{0_f} \\ w_{0_f} \end{Bmatrix}^{B} &= \begin{bmatrix} \cos\theta_{0_f}^{BI}\cos\psi_{0_f}^{BI} & \cos\theta_{0_f}^{BI}\sin\psi_{0_f}^{BI} & -\sin\theta_{0_f}^{BI} \\ -\sin\psi_{0_f}^{BI} & \cos\psi_{0_f}^{BI} & 0 \\ \sin\theta_{0_f}^{BI}\cos\psi_{0_f}^{BI} & \sin\theta_{0_f}^{BI}\sin\psi_{0_f}^{BI} & \cos\theta_{0_f}^{BI} \end{bmatrix} \begin{Bmatrix} u_{0_f} \\ v_{0_f} \\ w_{0_f} \end{Bmatrix}^{I} \end{aligned} \tag{5.1}$$

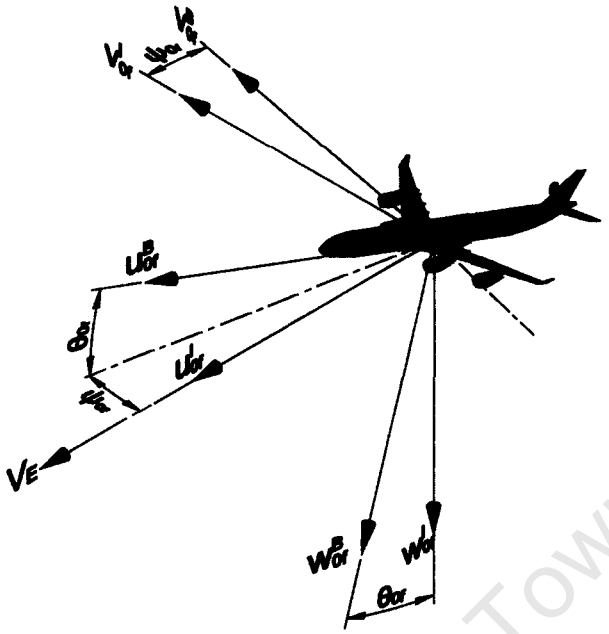

Figure 5.1: Illustration of Axes.

Using these steady state orientation angles and introducing small perturbations, to all parameters, $\dot{u} \ldots \psi$, the linearised perturbed equations of motion can be generated. All disturbance perturbations are assumed to be small. The reference state orientation angle, ϕ_{0_f} is zero while ψ_{0_f} as well as the reference state velocity, v_{0_f}, can be assumed to be small since they represent the change due to formation flight and are zero in steady, symmetric flight in isolation. All 'small' second order terms are considered negligible. Furthermore, for steady flight, $p_{0_f} = q_{0_f} = r_{0_f} = 0$. The terms relating to steady flight alone, i.e. all reference state terms which are not functions of time, are inherently satisfied and fallout from the equations without losing generality. The perturbed equations of motion are therefore reduced to:

$$m\left(\dot{u}_d\langle t\rangle + w_{0_f} q_d\langle t\rangle\right) = -mg\theta_d\langle t\rangle + X_d\langle t\rangle \tag{5.2}$$

$$m\left(\dot{v}_d\langle t\rangle + u_{0_f} r_d\langle t\rangle - w_{0_f} p_d\langle t\rangle\right) = mg\phi_d\langle t\rangle + Y_d\langle t\rangle \tag{5.3}$$

$$m\left(\dot{w}_d\langle t\rangle - u_{0_f} q_d\langle t\rangle\right) = Z_d\langle t\rangle \tag{5.4}$$

$$I_x\dot{p}_d\langle t\rangle - I_{xz}\dot{r}_d\langle t\rangle = \tilde{L}_d\langle t\rangle \tag{5.5}$$

$$I_y\dot{q}_d\langle t\rangle = M_d\langle t\rangle \tag{5.6}$$

$$I_z\dot{r}_d\langle t\rangle - I_{xz}\dot{p}_d\langle t\rangle = N_d\langle t\rangle \tag{5.7}$$

The forces and moments can be written as functions of the non-dimensional stability deriva-

tives. For example:

$$Z_d = \frac{1}{2}\rho V^2 C_{z_d}$$

where $V = \left((u_{0_f} + u_d)^2 + (v_{0_f} + v_d)^2 + (w_{0_f} + w_d)^2\right)^{\frac{1}{2}}$. While noting v_{0_f}, u_d, v_d and w_d are small, $V = \left(u_{0_f}^2 + 2u_{0_f}u_d + w_{0_f}^2 + 2w_{0_f}w_d\right)^{\frac{1}{2}}$.

The aerodynamic force and moment coefficients for steady flight in isolation (equations (D.20) to (D.25)) are combined with the force and moment coefficients due to steady formation flight in zero wind:

$$\begin{aligned}
C^I_{D_{0_f}} =& C^I_{D_0}\langle\alpha,\beta,M\rangle + \sum C^I_{D_0}\langle\delta_k,\alpha,M\rangle \\
&+ \Delta C^I_D\langle\eta,\zeta\rangle + C^I_D\langle\delta\alpha,\delta\beta,M\rangle + \sum C^I_D\langle\delta\delta_k,\alpha,M\rangle && (5.8)\\
C^I_{S_{0_f}} =& C^I_{S_0}\langle\alpha,\beta,M\rangle + \sum C^I_{S_0}\langle\delta_k,\alpha,M\rangle \\
&+ \Delta C^I_S\langle\eta,\zeta\rangle + C^I_S\langle\delta\alpha,\delta\beta,M\rangle + \sum C^I_S\langle\delta\delta_k,\alpha,M\rangle && (5.9)\\
C^I_{L_{0_f}} =& C^I_{L_0}\langle\alpha,\beta,M\rangle + \sum C^I_{L_0}\langle\delta_k,\alpha,M\rangle \\
&+ \Delta C^I_L\langle\eta,\zeta\rangle + C_L\langle\delta\alpha,\delta\beta,M\rangle + \sum C^I_L\langle\delta\delta_k,\alpha,M\rangle && (5.10)\\
C^I_{l_{0_f}} =& C^I_{l_0}\langle\alpha,\beta,M\rangle + \sum C^I_{l_0}\langle\delta_k,\alpha,M\rangle \\
&+ \Delta C^I_l\langle\eta,\zeta\rangle + C_l\langle\delta\alpha,\delta\beta,M\rangle + \sum C^I_l\langle\delta\delta_k,\alpha,M\rangle && (5.11)\\
C^I_{m_{0_f}} =& C^I_{m_0}\langle\alpha,\beta,M\rangle + \sum C^I_{m_0}\langle\delta_k,\alpha,M\rangle \\
&+ \Delta C^I_m\langle\eta,\zeta\rangle + C_m\langle\delta\alpha,\delta\beta,M\rangle + \sum C^I_m\langle\delta\delta_k,\alpha,M\rangle && (5.12)\\
C^I_{n_{0_f}} =& C^I_{n_0}\langle\alpha,\beta,M\rangle + \sum C^I_{n_0}\langle\delta_k,\alpha,M\rangle \\
&+ \Delta C^I_n\langle\eta,\zeta\rangle + C_n\langle\delta\alpha,\delta\beta,M\rangle + \sum C^I_n\langle\delta\delta_k,\alpha,M\rangle && (5.13)
\end{aligned}$$

where subscript 0 represents steady flight in isolation and subscript 0_f represents steady flight in formation. These coefficients are aligned with the free stream velocity vector and are therefore directed along the inertial frame and not the local wind frame (zero average wind is assumed). The change in coefficients due to steady formation flight are denoted with the prefix Δ while the orientation and deflection angle changes due to steady formation flight are denoted with the prefix δ. The change in angle of attack $\theta_{0_f} + \delta\alpha$ and the change in sideslip angle $\delta\beta$ represents the change in the angles between the x_B axis in formation and the free stream velocity. The orientation angles, $\delta\alpha$ and $\delta\beta$, are solved using equations (C.2) and (C.4) from Appendix C.

The force and moment coefficients are transformed to the body frame using $\boldsymbol{R}_{BI}$ from

equation (5.1) where θ_{0_f} and ψ_{0_f} are considered to be small.

$$\begin{Bmatrix} C^B_{x_{0_f}} - C^B_{T_{0_f}} \\ C^B_{y_{0_f}} \\ C^B_{z_{0_f}} \end{Bmatrix} = \mathbf{R}_{BI} \begin{Bmatrix} -C^I_{D_{0_f}} \\ C^I_{S_{0_f}} \\ -C^I_{L_{0_f}} \end{Bmatrix} \tag{5.14}$$

$$\begin{Bmatrix} C^B_{l_{0_f}} \\ C^B_{m_{0_f}} \\ C^B_{n_{0_f}} \end{Bmatrix} = \mathbf{R}_{BI} \begin{Bmatrix} C^I_{l_{0_f}} \\ C^I_{m_{0_f}} \\ C^I_{n_{0_f}} \end{Bmatrix} \tag{5.15}$$

It is now assumed that the formation encounters atmospheric turbulence, resulting in the trailing aircraft being perturbed from its trimmed state. Figures 5.2 and 5.3 describe the disturbance angle of attack and sideslip angle.

$$\alpha_d\langle t\rangle = \frac{w_d\langle t\rangle - w^B_g\langle t\rangle}{u_{0_f} + u_d\langle t\rangle - u^B_g\langle t\rangle}$$
$$\beta_d\langle t\rangle = \frac{v_d\langle t\rangle - v^B_g\langle t\rangle}{u_{0_f} + u_d\langle t\rangle - u^B_g\langle t\rangle}$$

The longitudinal component, $u_{0_f} + u_d\langle t\rangle - u_g\langle t\rangle^B$ is approximated by the free stream

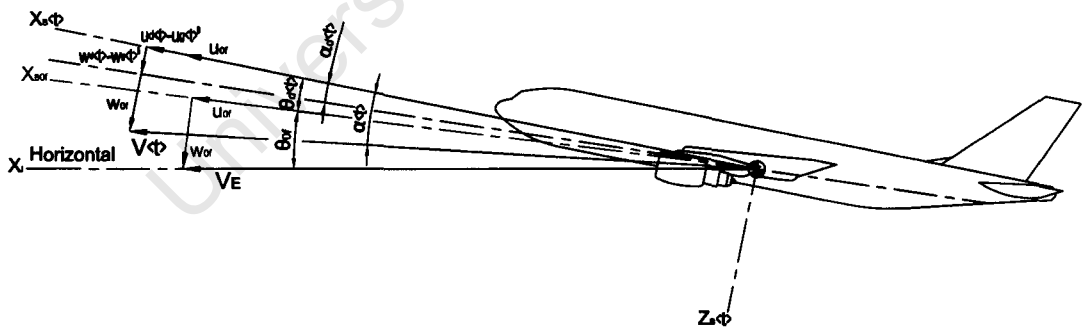

Figure 5.2: Disturbance Angle of Attack.

velocity V_E since the disturbance velocity and gust disturbances are small compared to u_{0_f} while the orientation angles, θ_{0_f} and ψ_{0_f}, are also considered small. The flight regime considered is one at cruise flight (M = 0.8) at 40000 feet. For a typical large passenger airliner, in the specified flight regime, the steady state angle of attack in isolated flight, $\alpha_0 = \theta_0$, can also be considered small. The gust velocities, specified in the inertial frame,

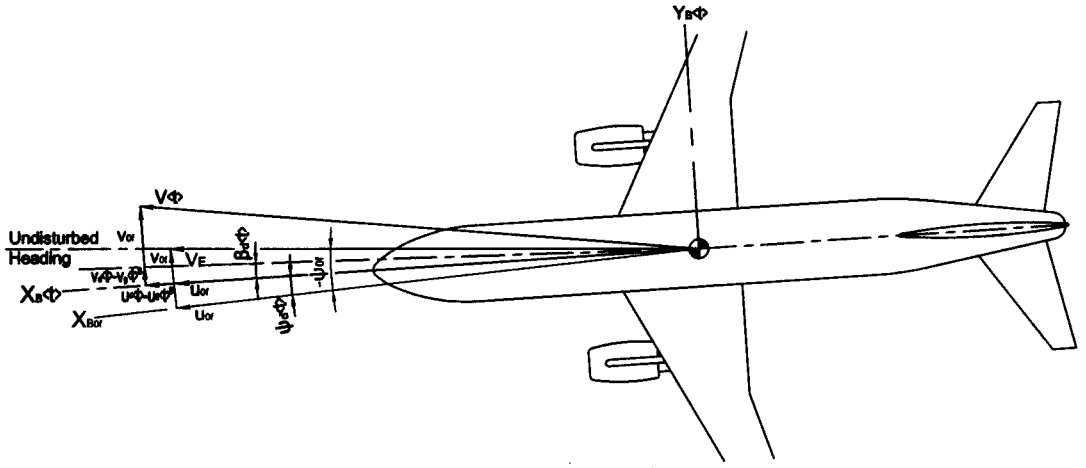

Figure 5.3: Disturbance Sideslip Angle.

are transferred to the body frame with the direction cosine matrix:

$$\mathbf{u}_g^B = \mathbf{R}_{B_dI}\mathbf{u}_g^I$$

$$\mathbf{u}_g^B = \begin{bmatrix} 1 & \psi_{0_f} + \psi_d & -\theta_{0_f} - \theta_d \\ -\psi_{0_f} - \psi_d & 1 & \phi_d \\ \theta_{0_f} + \theta_d & -\phi_d & 1 \end{bmatrix} \mathbf{u}_g^I$$

The trailing vortices of the lead aircraft are displaced by gusts as was discussed in section 4.3. Hence the effective relative position of the trailing aircraft is given by equations (4.7) & (4.8). Assuming $\xi >> |\eta|$ and v_g to be small compared to V_E, equations (4.7) & (4.8) can be simplified to:

$$\eta_{eff}\langle t\rangle = \eta + \xi\left(\frac{v_g\langle t\rangle}{V_E}\right) \tag{5.16}$$

$$\zeta_{eff}\langle t\rangle = \zeta + \xi\left(\frac{w_g\langle t\rangle}{V_E}\right) \tag{5.17}$$

Representing $C_x, C_y, C_z, C_l, C_m, C_n$ as C_i and $\delta\delta_k$ as the change in control inputs while noting that, to first order, $\Delta V\langle t\rangle^2 = 2u_{0_f}\left(u_d\langle t\rangle - u_g\langle t\rangle\right)$, the first order approximations of the aerodynamic loads are given below.

$$\begin{aligned} C_i\langle t\rangle =& C_{i_{0_f}} + C_{i_d}\langle t\rangle \\ C_{i_d}\langle t\rangle =& C_i|_r \frac{2\left(u_d\langle t\rangle - u_g\langle t\rangle\right)}{V} + \frac{\partial C_i}{\partial\alpha}|_r\left\{\frac{w_d\langle t\rangle - w_g^B\langle t\rangle}{V_E}\right\} + \frac{\partial C_i}{\partial\beta}|_r\left\{\frac{v_d\langle t\rangle - v_g^B\langle t\rangle}{V_E}\right\}\cdots \\ &+ \frac{\partial C_i}{\partial\hat{p}}|_r\frac{pb}{2V_E} + \frac{\partial C_i}{\partial\hat{q}}|_r\frac{q\bar{c}}{2V_E} + \frac{\partial C_i}{\partial\hat{r}}|_r\frac{rb}{2V_E} + \frac{\partial C_i}{\partial\delta\delta_k}|_r\delta\delta_k\cdots \\ &+ \frac{\partial C_i}{\partial\eta_{eff}}|_r\left\{\xi\left(\frac{v_g\langle t\rangle}{V_E}\right)\right\} + \frac{\partial C_i}{\partial\zeta_{eff}}|_r\left\{\xi\left(\frac{w_g\langle t\rangle}{V_E}\right)\right\} \end{aligned} \tag{5.18}$$

The first term on the RHS of equation (D.42) is only considered in the x and z components. The last two terms on the RHS of equation (5.18) represent new derivatives due to forma-

tion flight and are not present in conventional aircraft small disturbance stability analysis. These terms therefore vanish for an aircraft flying in isolation. Due to the very non-linear relationship between effective separation and the induced loads and moments, these last two terms may have to be replaced with higher order approximations, particularly if the trailing aircraft is positioned at the optimum separation. The simulation is designed so that it solves the equations by replacing these terms with nonlinear functions as defined in chapter 3. A further standard assumption for small disturbances is:

$$p_d\langle t\rangle = \dot{\phi}_d\langle t\rangle$$
$$q_d\langle t\rangle = \dot{\theta}_d\langle t\rangle$$
$$r_d\langle t\rangle = \dot{\psi}_d\langle t\rangle$$

Substituting equations (D.42) into equations (D.14) to (D.19) and rearranging into matrix form gives the desired set of linearised equations of motion for a trailing aircraft of a two ship formation flying through turbulence.

$$
\begin{bmatrix}
m & 0 & 0 & 0 & 0 & 0 & 0 & 0 & 0 \\
0 & m & 0 & 0 & 0 & 0 & 0 & 0 & 0 \\
0 & 0 & m & 0 & 0 & 0 & 0 & 0 & 0 \\
0 & 0 & 0 & I_x & 0 & -I_{xz} & 0 & 0 & 0 \\
0 & 0 & 0 & 0 & I_y & 0 & 0 & 0 & 0 \\
0 & 0 & 0 & -I_{xz} & 0 & I_z & 0 & 0 & 0 \\
0 & 0 & 0 & 0 & 0 & 0 & 1 & 0 & 0 \\
0 & 0 & 0 & 0 & 0 & 0 & 0 & 1 & 0 \\
0 & 0 & 0 & 0 & 0 & 0 & 0 & 0 & 1
\end{bmatrix}
\begin{Bmatrix}
\dot{u} \\ \dot{v} \\ \dot{w} \\ \dot{p} \\ \dot{q} \\ \dot{r} \\ \dot{\phi} \\ \dot{\theta} \\ \dot{\psi}
\end{Bmatrix} \cdots
$$

$$
= \begin{bmatrix}
\frac{2C_x\bar{q}S}{V_E} & \frac{\bar{q}S}{V_E}\frac{\partial C_x}{\partial \beta} & \frac{\bar{q}S}{V_E}\frac{\partial C_x}{\partial \alpha} & 0 & \frac{\bar{q}S\bar{c}}{2V_E}\frac{\partial C_x}{\partial \hat{q}} - mw_{0_f} & 0 & 0 & -mg & 0 \\
0 & \frac{\bar{q}S}{V_E}\frac{\partial C_y}{\partial \beta} & 0 & \frac{\bar{q}Sb}{2V_E}\frac{\partial C_y}{\partial \hat{p}} + mw_{0_f} & 0 & \frac{\bar{q}Sb}{2V_E}\frac{\partial C_y}{\partial \hat{r}} + mu_{0_f} & mg & 0 & 0 \\
\frac{2C_x\bar{q}S}{V_E} + \frac{\bar{q}S}{V_E}\frac{\partial C_x}{\partial \hat{u}} & \frac{\bar{q}S}{V_E}\frac{\partial C_x}{\partial \beta} & \frac{\bar{q}S}{V_E}\frac{\partial C_x}{\partial \alpha} & 0 & \frac{\bar{q}S\bar{c}}{2V_E}\frac{\partial C_x}{\partial \hat{q}} + mu_{0_f} & 0 & 0 & 0 & 0 \\
0 & \frac{\bar{q}Sb}{V_E}\frac{\partial C_l}{\partial \beta} & 0 & \frac{\bar{q}Sb^2}{2V_E}\frac{\partial C_l}{\partial \hat{p}} & 0 & \frac{\bar{q}Sb^2}{2V_E}\frac{\partial C_l}{\partial \hat{r}} & 0 & 0 & 0 \\
\frac{\bar{q}S\bar{c}}{V_E}\frac{\partial C_m}{\partial \hat{u}} & 0 & \frac{\bar{q}S\bar{c}}{V_E}\frac{\partial C_m}{\partial \alpha} & 0 & \frac{\bar{q}S\bar{c}^2}{2V_E}\frac{\partial C_m}{\partial \hat{q}} & 0 & 0 & 0 & 0 \\
0 & \frac{\bar{q}Sb}{V_E}\frac{\partial C_n}{\partial \beta} & 0 & \frac{\bar{q}Sb^2}{2V_E}\frac{\partial C_n}{\partial \hat{p}} & 0 & \frac{\bar{q}Sb^2}{2V_E}\frac{\partial C_n}{\partial \hat{r}} & 0 & 0 & 0 \\
0 & 0 & 0 & 1 & 0 & 0 & 0 & 0 & 0 \\
0 & 0 & 0 & 0 & 1 & 0 & 0 & 0 & 0 \\
0 & 0 & 0 & 0 & 0 & 1 & 0 & 0 & 0
\end{bmatrix}
\begin{Bmatrix}
u \\ v \\ w \\ p \\ q \\ r \\ \phi \\ \theta \\ \psi
\end{Bmatrix} \cdots
$$

$$
- \begin{bmatrix}
\frac{2C_x\bar{q}S}{V_E} & \frac{\bar{q}S}{V_E}\left(\frac{\partial C_x}{\partial \beta} - \xi\frac{\partial C_x}{\partial \eta_{eff}}\right) & \frac{\bar{q}S}{V_E}\left(\frac{\partial C_x}{\partial \alpha} - \xi\frac{\partial C_x}{\partial \zeta_{eff}}\right) & 0 & \frac{\bar{q}S\bar{c}}{2V_E}\frac{\partial C_x}{\partial \hat{q}} & 0 \\
0 & \frac{\bar{q}S}{V_E}\left(\frac{\partial C_y}{\partial \beta} - \xi\frac{\partial C_y}{\partial \eta_{eff}}\right) & -\frac{\bar{q}S}{V_E}\xi\frac{\partial C_y}{\partial \zeta_{eff}} & \frac{\bar{q}Sb}{2V_E}\frac{\partial C_y}{\partial \hat{p}} & 0 & \frac{\bar{q}Sb}{2V_E}\frac{\partial C_y}{\partial \hat{r}} \\
\frac{2C_x\bar{q}S}{V_E} + \frac{\bar{q}S}{V_E}\frac{\partial C_x}{\partial \hat{u}} & \frac{\bar{q}S}{V_E}\left(\frac{\partial C_x}{\partial \beta} - \xi\frac{\partial C_x}{\partial \eta_{eff}}\right) & \frac{\bar{q}S}{V_E}\left(\frac{\partial C_x}{\partial \alpha} - \xi\frac{\partial C_x}{\partial \zeta_{eff}}\right) & 0 & \frac{\bar{q}S\bar{c}}{2V_E}\frac{\partial C_x}{\partial \hat{q}} & 0 \\
0 & \frac{\bar{q}Sb}{V_E}\left(\frac{\partial C_l}{\partial \beta} - \xi\frac{\partial C_l}{\partial \eta_{eff}}\right) & -\frac{\bar{q}Sb}{V_E}\xi\frac{\partial C_l}{\partial \zeta_{eff}} & \frac{\bar{q}Sb^2}{2V_E}\frac{\partial C_l}{\partial \hat{p}} & 0 & \frac{\bar{q}Sb^2}{2V_E}\frac{\partial C_l}{\partial \hat{r}} \\
\frac{\bar{q}S\bar{c}}{V_E}\frac{\partial C_m}{\partial \hat{u}} & -\frac{\bar{q}S\bar{c}}{V_E}\xi\frac{\partial C_m}{\partial \eta_{eff}} & \frac{\bar{q}S\bar{c}}{V_E}\left(\frac{\partial C_m}{\partial \alpha} - \xi\frac{\partial C_m}{\partial \zeta_{eff}}\right) & 0 & \frac{\bar{q}S\bar{c}^2}{2V_E}\frac{\partial C_m}{\partial \hat{q}} & 0 \\
0 & \frac{\bar{q}Sb}{V_E}\left(\frac{\partial C_n}{\partial \beta} - \xi\frac{\partial C_n}{\partial \eta_{eff}}\right) & -\frac{\bar{q}Sb}{V_E}\xi\frac{\partial C_n}{\partial \zeta_{eff}} & \frac{\bar{q}Sb^2}{2V_E}\frac{\partial C_n}{\partial \hat{p}} & 0 & \frac{\bar{q}Sb^2}{2V_E}\frac{\partial C_n}{\partial \hat{r}}
\end{bmatrix}
\begin{Bmatrix}
u_g \\ v_g \\ w_g \\ p_g \\ q_g \\ r_g
\end{Bmatrix}^B \cdots
$$

$$
+ \begin{bmatrix}
1 & \frac{\partial C_x}{\partial \delta_a} & \frac{\partial C_x}{\partial \delta_e} & \frac{\partial C_x}{\partial \delta_r} \\
0 & \frac{\partial C_y}{\partial \delta_a} & 0 & \frac{\partial C_y}{\partial \delta_r} \\
0 & 0 & \frac{\partial C_x}{\partial \delta_e} & 0 \\
0 & \frac{\partial C_l}{\partial \delta_a} & 0 & \frac{\partial C_l}{\partial \delta_r} \\
\frac{\partial M}{\partial \delta_T} & 0 & \frac{\partial C_m}{\partial \delta_e} & 0 \\
0 & \frac{\partial C_l}{\partial \delta_a} & 0 & \frac{\partial C_l}{\partial \delta_r}
\end{bmatrix}
\begin{Bmatrix}
\delta\delta_T \\ \delta\delta_a \\ \delta\delta_e \\ \delta\delta_r
\end{Bmatrix}
$$

(5.19)

6 Development of Formation Flight Model for Simulation

A study which includes the perturbed state variables can only be undertaken subsequent to the implementation of a formation flight control algorithm. The development of such an algorithm falls outside the scope of the current study. To obtain a first impression of the challenge the autopilot will have to deal with, the comparative effects of a turbulence affected wake flow field on aircraft acceleration are examined here by a) including the aerodynamic loads and moments due to the change in the induced flow field, as a function of atmospheric turbulence, and the direct effect of the atmospheric gust velocities, versus b) including only the direct effect of atmospheric turbulence without the effect of the change in induced flow due to the trailing vortices. As an idealization, the average state variables are kept at there nominal values while the disturbance state variables tend to zero implying perfect autopilot and control surface response.

Due to the extensive information available to the public, the Boeing 747-100 characteristics are used in the simulations to represent both the lead and trailing aircraft in formation flight. It is also used to represent a single aircraft in isolated flight for the purpose of comparison (see Appendix G).

6.1 Generation of the Gust Velocities

The random turbulence signals are fed into the equations of motion by way of a Monte Carlo type simulation. The linear and angular gust velocities can be generated by a number of methods described by Schaeffer et al. [75] and MIL-HDBK-1797 [78]. One basic method involves summing a suitably large collection of continuous sinusoidal signals varying in frequency and amplitude where the amplitude is a function of the frequency obtained from the von Karman power spectral densities [33, 75]. A random phase shift with a uniform probability density of 1 from 0 to 2π is applied to these sinusoidal signals. This random phase shift creates the necessary stochastic nature. For a frequency band ω_1 to ω_2, the amplitude is given as:

$$a_k = \left(2 \int_{\omega_1}^{\omega_2} \Phi(\omega)\, d\omega\right)^{\frac{1}{2}}$$

Another common method is to pass band limited white noise through forming filters or transfer functions derived from the von Karman spectral densities. This method offers high computational speed, however, when white noise is generated digitally, a non-zero sampling period is required and the simulation extends over a finite total period. The spectrum, therefore, is only approximately flat and limits the white noise from having unity power. The output spectral density will therefore have reduced variance. Schaeffer et al. suggest multiplying the output signal by a restoring coefficient equal to $\sqrt{\frac{2\pi}{\Delta t}}$ where Δt is the sample period. This is done using MATLAB Simulink where a white noise signal with Gaussian distribution and unity variance is passed through forming filters. The restoring coefficient is then applied to the output.

Following the result of random vibration theory for a single input, the transfer functions derived from the spectral densities can be obtained:

$$\Phi_{uu}\langle\omega\rangle = |H_{11}\langle\omega\rangle|^2 \Phi_{WN}\langle\omega\rangle$$

$$H_{uu}\langle\omega\rangle = \sqrt{\frac{\Phi_{uu}\langle\omega\rangle}{\Phi_{WN}}}$$

where the spectral density of white noise, Φ_{WN}, is 1. The von Karman spectral densities however contain exponents of frequency that are non even integers and it is therefore not possible to produce linear transfer functions. An approximation is developed by Schaeffer et al..

$$H_{uu}\langle s\rangle = \sigma_u \sqrt{\frac{L_u}{\pi V_E}} \frac{1 + 0.25\frac{L_u}{V_E}s}{1 + 1.357\frac{L_u}{V_E}s + 0.1987\left(\frac{L_u}{V_E}\right)^2 s^2} \tag{6.1}$$

$$H_{vv}\langle s\rangle = \sigma_v \sqrt{\frac{L_v}{2\pi V_E}} \frac{1 + 2.7478\frac{L_v}{V_E}s + 0.3398\left(\frac{L_v}{V_E}\right)^2 s^2}{1 + 2.9958\frac{L_v}{V_E}s + 1.9754\left(\frac{L_v}{V_E}\right)^2 s^2 + 0.1539\left(\frac{L_v}{V_E}\right)^3 s^3} \tag{6.2}$$

$$H_{ww}\langle s\rangle = \sigma_w \sqrt{\frac{L_w}{2\pi V_E}} \frac{1 + 2.7478\frac{L_w}{V_E}s + 0.3398\left(\frac{L_w}{V_E}\right)^2 s^2}{1 + 2.9958\frac{L_w}{V_E}s + 1.9754\left(\frac{L_w}{V_E}\right)^2 s^2 + 0.1539\left(\frac{L_w}{V_E}\right)^3 s^3} \tag{6.3}$$

The transfer functions for the turbulence velocity gradients of the longitudinal change in vertical gust velocity and the longitudinal change in lateral gust velocity are approximated as:

$$H_{w_x w_x}\langle s\rangle = \frac{-\frac{s}{V_E}}{\left(1 + \frac{4l_T}{\pi V_E}\right)s} H_{ww}\langle s\rangle \tag{6.4}$$

$$H_{v_x v_x}\langle s\rangle = \frac{\frac{s}{V_E}}{\left(1 + \frac{4l_T}{\pi V_E}\right)s} H_{vv}\langle s\rangle \tag{6.5}$$

Schaeffer et al. conclude that the the rolling moment due to the change in vertical gust velocity along the wingspan will generally be insignificant compared to the rolling moment caused by the lateral component of turbulence.

Figure 6.1 shows the spectral density estimates of the turbulence signals generated by passing band limited white noise through the transfer functions (6.1) to (6.5) versus the von Karman spectral densities as provided by references [33, 69, 75, 78].

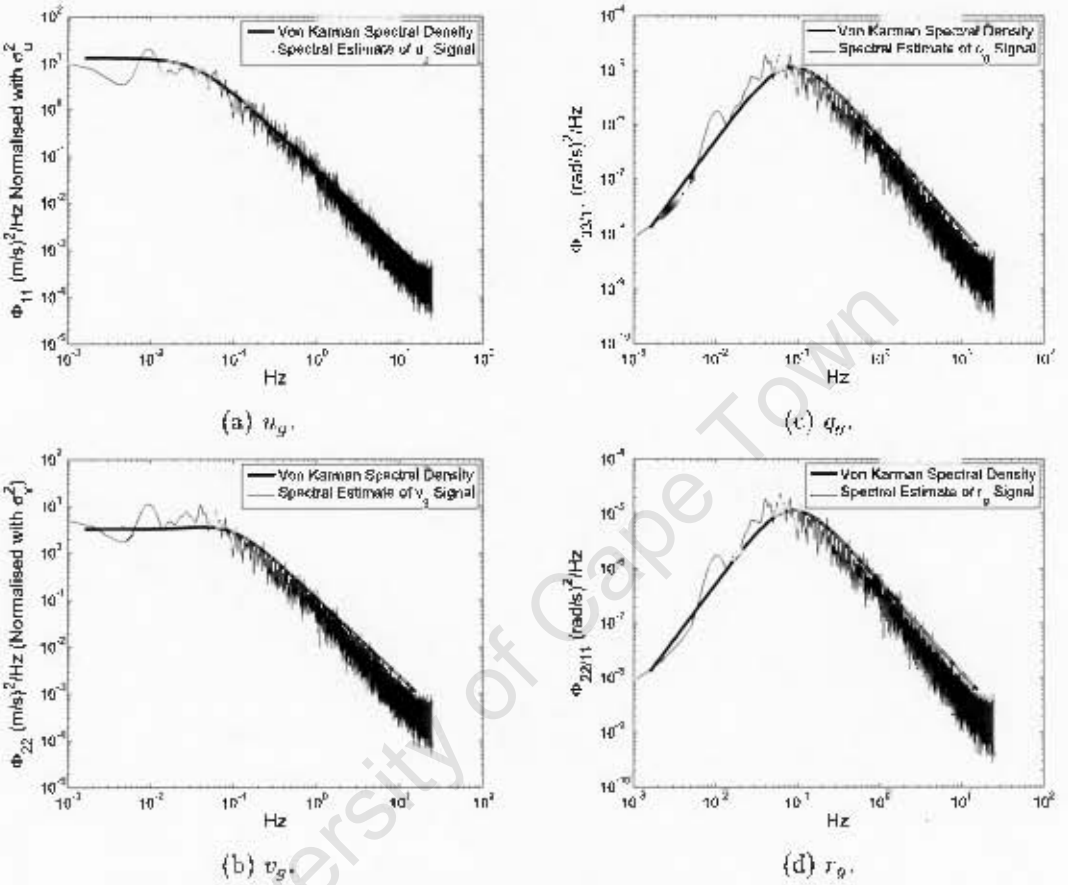

Figure 6.1: Spectral Density Estimations of the linear and angular turbulence velocity signals generated by passing white noise through the transfer functions (6.1) to (6.5). $\sigma = 1.3$, $L_u = 762$ m and $V_E = 236$ m/s (M = 0.8) at 40000 feet.

6.2 Simulation Flow

The gust velocities, generated by passing white noise through forming filters, together with the force and moment equations from chapter 3 are used to calculate the change in forces and moments due to the change in the induced flow of the trailing vortices by way of the gust velocities changing the effective separation. These changes in the forces and moments are transformed to the body frame and summed with forces and moments obtained via the equations of motion of chapter 5, due to the direct effect of the gust velocities, to

obtain the c.g. accelerations. The gust velocities are also transformed to the body frame prior to introduction into the equations of motion. As discussed earlier in this chapter, the disturbance state variables and control inputs remain zero. With the c.g. linear and angular accelerations, the passenger accelerations are obtained for the given offset from the c.g.. Since there is no control algorithm and the trailing aircraft is assumed to hold station, no feedback is necessary. The time history for the accelerations are built through looping over the random gust velocity samples. Figure 6.2 gives a high level overview of the simulation flow.

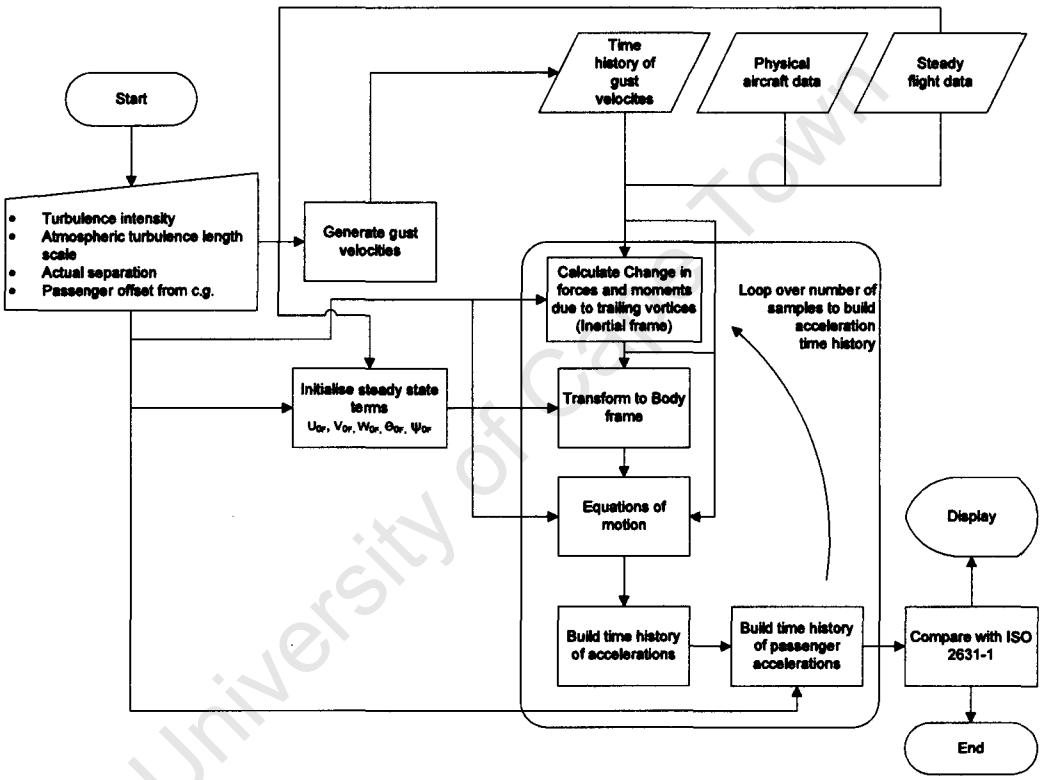

Figure 6.2: High level view of simulation flow.

6.3 Spectral Density Estimation

In order to obtain the spectral density of the output accelerations in the discreet time domain, a spectral density estimation is required. The Welch method has found wide application in engineering and experimental physics. This method finds the average spectral density of overlapping segments of window modified periodograms [80]: The time series is divided into overlapping segments before the discreet Fourier transform (DFT) of each

segment is found subsequent to a window function applied to the segments. The window function is required since the DFT implicitly assumes that the signal is periodic. The resulting outputs are then scaled and averaged to represent the power spectral density of the original signal. Appendix H provides a basic overview of spectral estimation. The Welch spectral estimation method with the 'Hamming' window function is employed in the current study.

6.4 Sampling

The Nyquist frequency is specified as half the sampling frequency, $\frac{1}{2\Delta t}$, and according to the sampling theorem avoids aliasing up to frequencies equal to the Nyquist frequency [81]. Aliasing results if a large sampling period is chosen and leads to confusion between the low and high frequency components in the original time history. Following from the data presented by Houbolt [70] that shows the von Karman spectrum agrees well with recorded flight data at high frequencies, up to 10^3 Hz, A sampling period of 0.01 s is chosen which provides reasonable computational speed and avoids aliasing up to 50 Hz. The frequency weighting curves in ISO 2631-1 [10],reprinted in Fig. 6.4, indicate that the critical frequency range with respect to human discomfort extends from 0.25 Hz to 40 Hz. The guidance in ISO 2631-1 which gives likely reactions to overall vibration is only considered applicable over a frequency range of 0.5 Hz to 80 Hz. The simulation is run over an extended period of 30 min which is deemed adequate to obtain reliable average values at frequencies greater than 0.1 Hz (180 samples) and inspection of values less than 0.1 Hz and greater than 0.01 Hz.

6.5 Analysis of Passenger Comfort

Table 6.1: Seat location co-ordinates from c.g. in Boeing 747-100 (See Fig. 6.3)

Location	x	y	z
A	0	0	-0.7
B	0	3	-0.7
C	0	-3	-0.7
D	-21	0	-0.7
E	30.5	0	-0.7
F	21	-1.7	-3.4

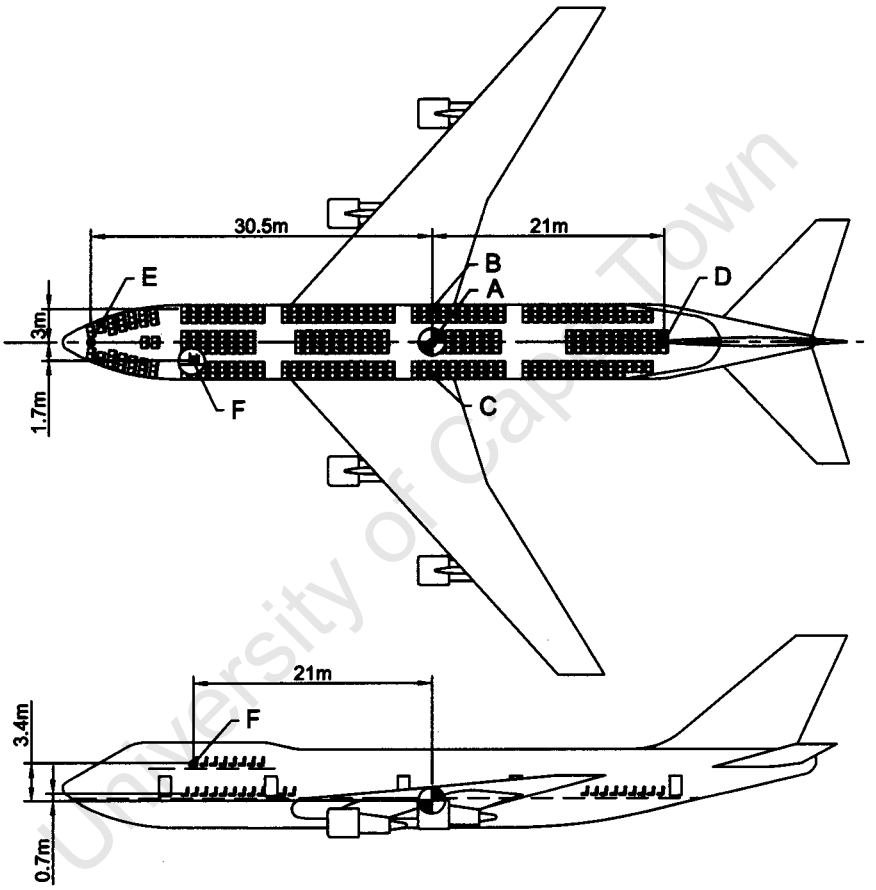

Figure 6.3: Interior seating arrangement of Boeing 747-100 for international all economy seating. Adapted from [82].

Figure 6.3 shows the maximum seating displacements from the c.g. of a Boeing 747 class aircraft, listed in table 6.1. The linear accelerations are determined by:

$$\boldsymbol{a}_p = \boldsymbol{a}_{cg} + \dot{\boldsymbol{\omega}} \times \boldsymbol{r}_{p/cg} + \boldsymbol{\omega} \times (\boldsymbol{\omega} \times \boldsymbol{r}_{p/cg}) + 2\boldsymbol{\omega} \times \boldsymbol{v}_{rel} + \boldsymbol{a}_{rel} \tag{6.6}$$

The aircraft fuselage is considered a rigid body and thus both $\boldsymbol{v}_{rel}$ and $\boldsymbol{a}_{rel}$ terms fall away. Furthermore, in the current simplified study, the aircraft is assumed to hold station without incurring any linear or angular velocity disturbances (implying ideal control as was alluded to before), thus equation (6.6) becomes:

$$\boldsymbol{a}_p = \boldsymbol{a}_{cg} + \dot{\boldsymbol{\omega}} \times \boldsymbol{r}_{p/cg} \tag{6.7}$$

Angular accelerations remain unchanged in a rigid body.

The method to determine passenger comfort as prescribed by ISO 2631-1 [10] is used. ISO 2631-1 gives the frequency weightings for one third octave bands (Fig. 6.4). In order to weight the accelerations according to frequency, the spectral density estimations for the accelerations are calculated. The standard deviation for each one third octave frequency band is calculated and then weighted according to ISO 2631-1. These weightings vary according to the orientation of the accelerations and the posture of the passenger. Different weightings are applied to accelerations in the vertical orientation and accelerations in the lateral orientation. The current study only considers the seated passenger. These weighted accelerations are then summed according to equation (9) in ISO 2631-1.

$$a_w = \left[\sum_i (W_i a_i)^2\right]^{1/2} \tag{6.8}$$

The lower and upper frequency limits for use in ISO 2631-1 extend from 0.5 Hz to 80 Hz. As discussed in Section 6.4 an upper limit of 50 Hz is chosen to retain reasonable computational speed but still consider frequency components critical to human comfort. The upper and lower bounds of the one third octave bands are obtained via the centre frequencies which are given. The centre frequencies are known to be the geometric mean between the upper and lower limits, hence:

$$f_{i_{n+1}} = f_i \times (\sqrt{2})^{\frac{1}{3}} \tag{6.9}$$

$$f_{i_n} = f_i / (\sqrt{2})^{\frac{1}{3}} \tag{6.10}$$

since

$$\frac{f_{i_{n+1}}}{f_{i_n}} = 2^{\frac{1}{3}}$$

where f_i is the centre frequency, $f_{i_{n+1}}$ is the upper bound and f_{i_n} is the lower bound. Figure 6.5 shows the orientation of the acceleration components relative to the subject in

Figure 6.4: Frequency weighting curves for principle weightings. In the seated posture, W_k is applied to vertical accelerations, W_d is applied to lateral accelerations and W_f is used for motion sickness evaluation. Reprinted from ISO 2631-1 [10].

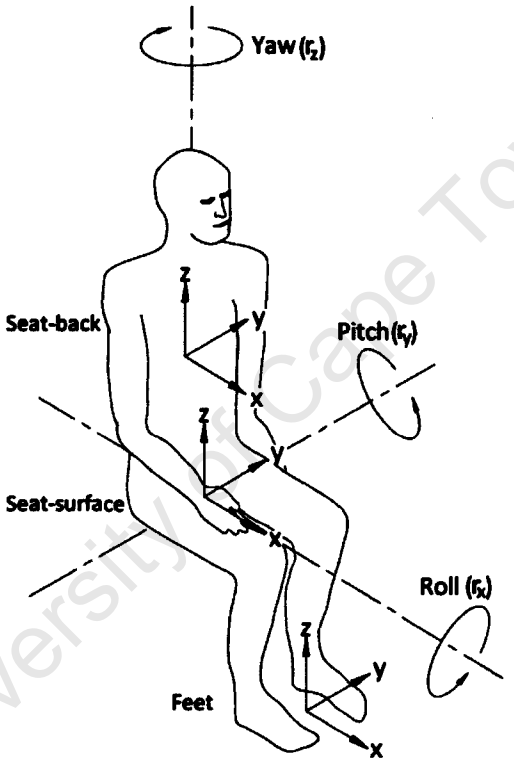

Figure 6.5: Orientation of acceleration components relative to subject in seated posture. Reprinted from ISO 2631-1 [10].

a seated posture. For seated persons, the total weighted linear acceleration value is simply calculated as the rms of the weighted components. ISO 2631-1 provides for the inclusion of accelerations at the seat, back-rest and feet where the weighting of the back-rest and feet locations are reduced compared to the seat location. The linear accelerations along with the angular accelerations at the seat alone are applied. The rms of weighted angular acceleration are combined with the linear accelerations vibration value via an additional root sum of squares to obtain an overall vibration total value. The weightings for the angular accelerations are provided in units of m/rad thus converting them to units of linear acceleration.

$$\begin{aligned} a_{v_s} &= \left(k_u^2 \dot{u}_w^2 + k_v^2 \dot{v}_w^2 + k_w^2 \dot{w}_w^2\right)^{\frac{1}{2}} \\ a_{v_r} &= \left(k_p^2 \dot{p}_w^2 + k_q^2 \dot{q}_w^2 + k_r^2 \dot{r}_w^2\right)^{\frac{1}{2}} \\ a_v &= \left(a_{v_s}^2 + a_{v_r}^2\right)^{\frac{1}{2}} \end{aligned} \tag{6.11}$$

7 Results and Discussion

7.1 Accelerations of CG

In Appendix E.1, Figs. E.1 to E.12 show the acceleration spectral density estimations of the mass centre and the aircraft angular accelerations for flight in isolation and in formation flight. All simulations assume longitudinal geometric separation of ten wingspans, $\xi = -10$, and zero geometric vertical separation, $\zeta = 0$, with $V_E = 236$ m/s at 40000 feet in atmospheric turbulence with length scale, $L_u = 762$ m. Four different lateral separations together with three levels of atmospheric turbulence intensity, $\sigma = 0.2$, 1.3 and 4.7 m/s, representing light, moderate and severe turbulence respectively are considered. The lateral separations were chosen after preliminary simulation runs showed a maximum increase in variance, of selected acceleration components, due to formation flight, at $\eta = 0.7$ in moderate turbulence and $\eta = 0.76$ in light turbulence. A third and fourth lateral separation, $\eta = 0.9$ and $\eta = 1.2$, are considered to investigate the decrease in acceleration magnitudes by shifting outboard of optimum lateral separation. The variance of the accelerations in formation flight and in isolation are indicated by σ^2_{form} and σ^2_{isol} on the graphs. These variances are calculated over a frequency band of 0.1 to 50 Hz. A factor representing the ratio of the standard deviation of acceleration in formation to the standard deviation in isolation is introduced. This factor is indicated by κ_i where i represents $\dot{u}, \dot{v}, \dot{w}, \dot{p}, \dot{q}, \dot{r}$ respectively. The spectral densities for the case of $\eta = 0.76$ in moderate turbulence are reprinted here in Fig. 7.1 for convenience.

A brief scan of these results immediately indicates a marked increase in acceleration magnitudes for four of the components: Longitudinal, vertical, roll and yaw acceleration magnitudes all show an increase due to formation flight at $\eta = 0.7$ and 0.76 over the frequency band indicated, 0.01 to 50 Hz. At $\eta = 0.9$ and 1.2, this increase is reduced significantly. As expected, the roll acceleration magnitudes show the most significant increase. These results can be explained by studying the gradients of the graphs on Figs. B.1 and B.2 and the last two terms of equation (5.18). For flight in isolation subjected to a varying lateral gust, little change in C_L is expected. However, for an aircraft in formation stationed at $\eta = 0.7$ behind the lead, the significant slope, $\frac{\partial C_L}{\partial \eta}$, on Fig. B.1c suggests considerable change in C_L for lateral gusts. The aircraft in formation hence, experiences increased vertical vibration. Figure B.1 will be often referred to when interpreting results. It is useful to note, from equation (4.7), that for $\xi = 10$ and $V_E = 236$ m/s, the following relationship

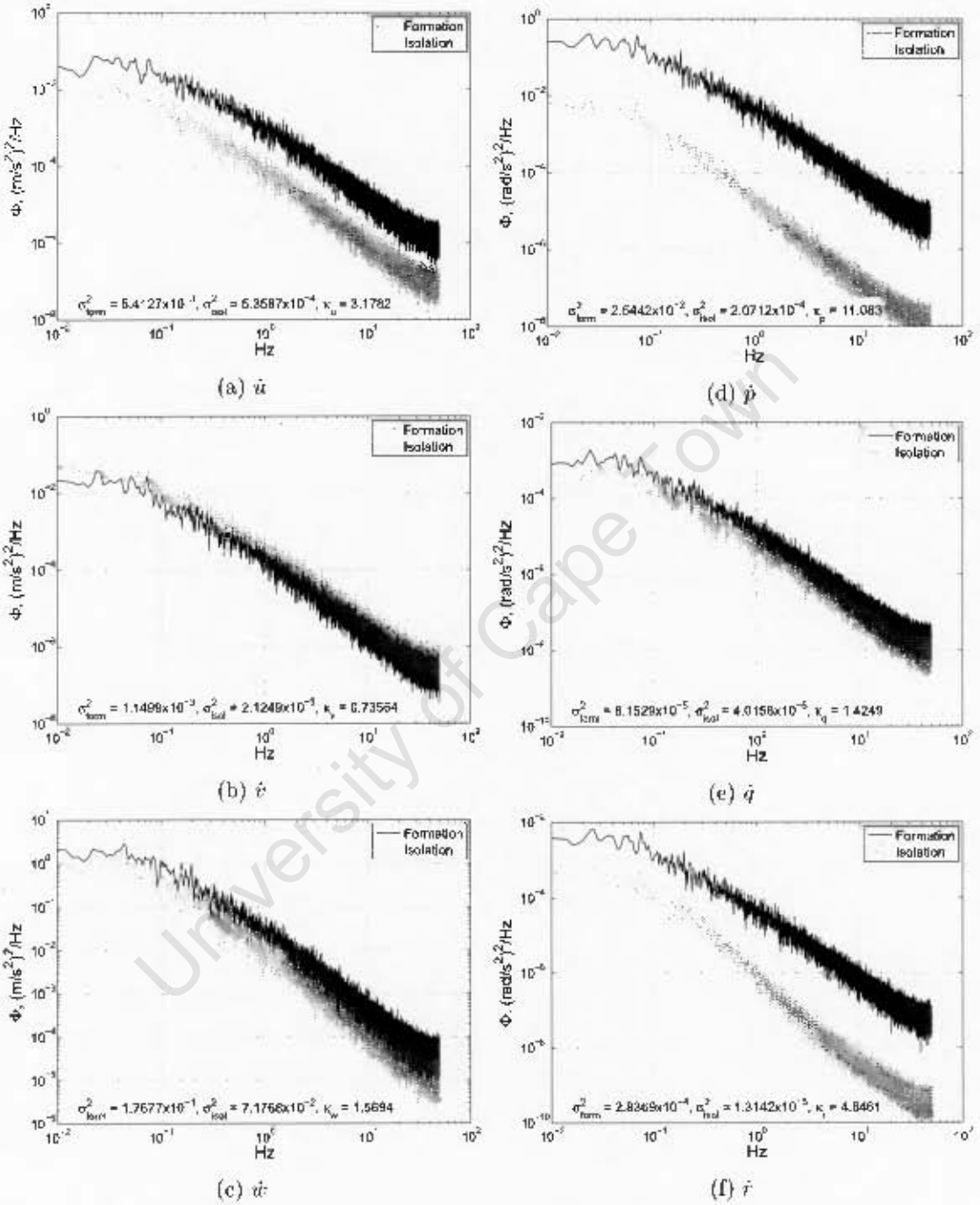

Figure 7.1: Spectral Density Estimations of the mass centre linear accelerations and angular accelerations about the mass centre in moderate turbulence, $\sigma = 1.3$ m/s, for flight in isolation and for formation flight at $\eta = 0.76$. From Appendix E.1.

between gust strength and changes in η_{eff} can be calculated:

Table 7.1: Useful data for lateral gust in formation.

v_g (m/s)	$\Delta\beta$ (rad)	η_{eff} at $\eta =$			
		0.7	0.76	0.9	1.2
+0.2	-0.00085	0.69	0.75	0.89	1.19
+1.3	-0.0055	0.65	0.7	0.85	1.15
+4.7	-0.02	0.5	0.56	0.7	1.0

From equations (5.16)

$$\begin{aligned}\frac{\partial \eta_{eff}}{\partial \beta} &= \frac{\eta_{eff} - \eta}{\Delta\beta} \\ &\approx \frac{-\xi \frac{v_g}{V_E}}{-\frac{v_g}{V_E}} \\ &\approx \xi\end{aligned}$$

Similarly from equation (5.17), $\frac{\partial \zeta_{eff}}{\partial \alpha} \approx \xi$. The gradients of tables B.1 and B.2 can be converted to gradients with respect to β and α and compared with the aircraft's stability derivatives in isolation.

Table 7.2: Induced force and moment gradients for small lateral gust velocities at lateral separations, $\eta = 0.7, 0.76, 0.9$ and 1.2, and zero vertical separation, $\zeta = 0$.

η	$\frac{\partial \Delta C_{Di}}{\partial \beta}$	$\frac{\partial \Delta C_S}{\partial \beta}$	$\frac{\partial \Delta C_L}{\partial \beta}$	$\frac{\partial \Delta C_l}{\partial \beta}$	$\frac{\partial \Delta C_m}{\partial \beta}$	$\frac{\partial \Delta C_n}{\partial \beta}$
0.7	-0.996	0.436	7.196	3.228	1.784	0.237
0.76	-1.416	0.293	10.225	5	1.141	0.551
0.9	0.517	0.13	-3.735	-0.899	0.523	-0.187
1.2	0.098	0.034	-0.705	-0.107	0.173	-0.031
Isolation	$\frac{\partial C_D}{\partial \beta}$	$\frac{\partial C_S}{\partial \beta}$	$\frac{\partial C_L}{\partial \beta}$	$\frac{\partial C_l}{\partial \beta}$	$\frac{\partial C_m}{\partial \beta}$	$\frac{\partial C_n}{\partial \beta}$
-	0	-0.879	0	-0.254	0	0.195

One should also note that the gradients, $\frac{\partial \Delta C_{Di}}{\partial \alpha}$, $\frac{\partial \Delta C_L}{\partial \alpha}$, $\frac{\partial \Delta C_l}{\partial \alpha}$ and $\frac{\partial \Delta C_m}{\partial \alpha}$ are non-zero for non-zero vertical separation, which is not considered in this study, as shown in Figs. B.2. The gradients in Tables 7.2 and 7.3 give a very good indication of the change in induced forces and moments due to small gusts in formation (less than 0.5 m/s). With increasing gust velocities the curves of Figs. B.1 and B.2 can no longer be linearised, particularly at $\eta = 0.7$ and 0.76 and the gradients can only be used as a guide.

Table 7.3: Induced force and moment gradients for small vertical gust velocities at lateral separations, $\eta = 0.7$, 0.76, 0.9 and 1.2, and zero vertical separation, $\zeta = 0$.

η	$\frac{\partial \Delta C_{Di}}{\partial \alpha}$	$\frac{\partial \Delta C_S}{\partial \alpha}$	$\frac{\partial \Delta C_L}{\partial \alpha}$	$\frac{\partial \Delta C_l}{\partial \alpha}$	$\frac{\partial \Delta C_m}{\partial \alpha}$	$\frac{\partial \Delta C_n}{\partial \alpha}$
0.7	0	0.264	0	0	0	-0.127
0.76	0	0.233	0	0	0	-0.112
0.9	0	0.156	0	0	0	-0.075
1.2	0	0.067	0	0	0	-0.032
Isolation	$\frac{\partial C_D}{\partial \alpha}$	$\frac{\partial C_S}{\partial \alpha}$	$\frac{\partial C_L}{\partial \alpha}$	$\frac{\partial C_l}{\partial \alpha}$	$\frac{\partial C_m}{\partial \alpha}$	$\frac{\partial C_n}{\partial \alpha}$
-	0.426	0	4.93	0	-1.04	0

Closer inspection of Figs. E.1 to E.12 reveals some interesting features. The lateral acceleration magnitudes at the mass centre are reduced in formation flight for all lateral separation cases and atmospheric turbulence intensity $\sigma = 0.2$ m/s and 1.3 m/s. This decrease is more pronounced with smaller lateral separations with the biggest drop experienced at $\eta = 0.7$. This is not the case for severe turbulence where the lateral acceleration magnitudes are greater in formation flight. If one considers a lateral gust in the positive 'y' direction, an aircraft in isolation will experience a resulting force due to the lateral velocity component on the tailfin and fuselage hence, experience acceleration in the positive 'y' direction. Now, if one considers the same effect on a trailing aircraft in a right-echelon formation with zero vertical separation (Fig. B.1b), the lateral gust will disturb the trailing vortices shifting them closer to the trailing aircraft centerline i.e. decreasing the effective lateral separation. Excluding the effects of vertical gusts, the trailing vortices induce a greater average sidewash on the tailfin in the negative 'y' direction effectively reducing or even reversing the local lateral velocity as shown in Fig. 7.2. This result is also supported by observing that $\frac{\partial \Delta C_S}{\partial \beta} > 0$.

One should, however, note that vertical gusts will induce lateral accelerations in formation flight as shown by $\frac{\partial \Delta C_S}{\partial \alpha}$ in Table 7.3 but not in isolation. The gradients $\frac{\partial \Delta C_S}{\partial \beta}$ in Table 7.2 at $\eta = 0.7$ and 0.76 are steeper than $\frac{\partial \Delta C_S}{\partial \alpha}$ in Table 7.3. Thus, at these lateral separations, lateral gusts will have a more prominent effect on the induced sideforce.

The pitch acceleration magnitudes show negligible change for lateral stations, $\eta = 0.9$ and 1.2 while an increase due to formation flight is shown at $\eta = 0.7$ and 0.76, particularly at low frequencies. This can be explained by studying the slope, $\frac{\partial \Delta C_m}{\partial \eta}$ on Fig. B.1e and $\frac{\partial \Delta C_m}{\partial \beta}$ in Table 7.2. For the η values considered, the slope is largest at $\eta = 0.7$, resulting in the largest sensitivity to lateral gusts.

Figures E.1...E.12(d) show a significant increase in the roll acceleration magnitudes at

$\eta = 0.7$, 0.76 and 0.9 while at $\eta = 1.2$ the increase in magnitude is less pronounced. For an aircraft statically stable in roll, $\frac{\partial C_l}{\partial \beta} < 0$. In formation flight:

$$\frac{\partial C_l}{\partial \beta}_{form} = \frac{\partial C_l}{\partial \beta}_{isol} + \frac{\partial \Delta C_l}{\partial \beta} \tag{7.1}$$

If $\frac{\partial \Delta C_l}{\partial \beta} < 0$, roll stability decreases and vice versa. From Fig. B.1d and Table 7.2 it can be seen that at $\eta = 0.7$ and 0.76, roll stability is highly unstable in formation flight while at $\eta = 0.9$ and 1.2, roll stability is highly stable. The vortices, hence, have a large influence on roll stability. The bigger magnitude of $\frac{\partial C_l}{\partial \beta}_{form}$ at $\eta = 0.7$ compared to $\eta = 0.9$ explains the difference between Figs. E.1d and E.3d. The fact that both these magnitudes are much bigger than the magnitude of $\frac{\partial C_l}{\partial \beta}_{isol}$ explains why the roll vibrations in formation are larger.

For a given turbulence intensity at $\eta = 0.9$, a distinct difference between high and low frequency content is shown in the yaw acceleration spectral density estimation shown in Figs. E.3f, E.7f and E.11f reprinted in Fig. 7.3 for convenience. An increase in acceleration magnitudes is evident over high frequencies while at low frequencies (less than 0.5 Hz) in light and moderate turbulence cases, the spectral density shows a decrease in acceleration magnitudes due to formation flight. In severe turbulence a small increase in the yaw acceleration magnitudes is shown at low frequencies for all lateral separation cases between isolated and formation flight (Figs. E.9f, E.10f, E.11f and E.12f). For an aircraft statically stable in yaw, $\frac{\partial C_n}{\partial \beta} > 0$. Now if the aircraft flies in formation:

$$\frac{\partial C_n}{\partial \beta}_{form} = \frac{\partial C_n}{\partial \beta}_{isol} + \frac{\partial \Delta C_n}{\partial \beta} \tag{7.2}$$

Hence, if $\frac{\partial \Delta C_n}{\partial \beta} > 0$, stability increases, however, if $\frac{\partial \Delta C_n}{\partial \beta} < 0$ then stability decreases. If yaw stability increases, the response to gusts increases and thus yaw vibration will increase. The opposite is true for decreasing stability. From Fig. B.1f and Table 7.3, $\frac{\partial \Delta C_n}{\partial \beta} > 0$ at $\eta = 0.7$ but $\frac{\partial \Delta C_n}{\partial \beta} < 0$ at $\eta = 0.9$. This explains the difference between Fig. E.1f, which has increased stability and responsiveness, and Fig. E.3f, which has decreased stability and responsiveness.

From Fig. 7.4, both the sidewash on the tailfin and drag distribution along the wing induce a yawing moment of similar magnitude at $\eta = 0.9$ and $\zeta = 0$. Changes in the effective vertical separation induce yaw moments in formation flight but vertical gusts do not have any effect on the yaw moment in isolated flight. This results in an increase of the yaw moment acceleration magnitudes in formation flight. From Tables 7.2, 7.3 and equation (7.2), $\frac{\partial C_n}{\partial \beta}_{form}$ at $\eta = 0.9$ is greater than $\frac{\partial C_n}{\partial \alpha}_{form}$ at $\eta = 0.9$ ($\frac{\partial C_n}{\partial \alpha}_{isol} \approx 0$) suggesting that lateral gusts will have a more significant effect on the yaw moment than vertical gusts. Further investigation found that application of the lateral gust velocities alone reduced the yaw moment acceleration magnitudes over all frequencies in formation flight confirming the

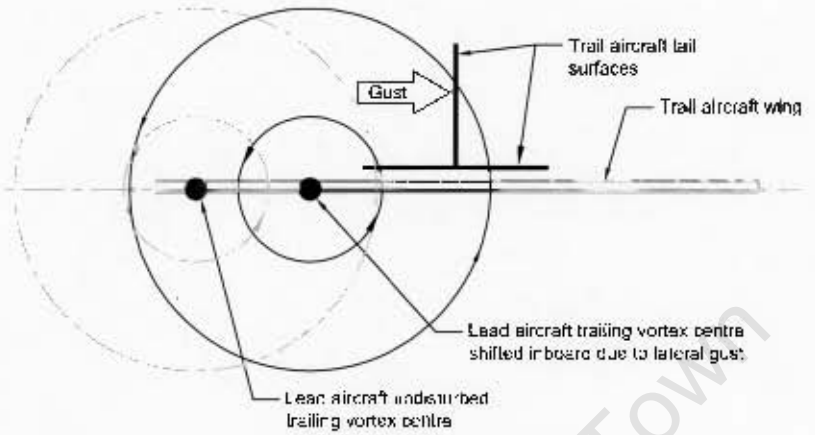

Figure 7.2: Illustration depicting change of induced flow over trailing wing and tail surfaces due to disturbed vortex.

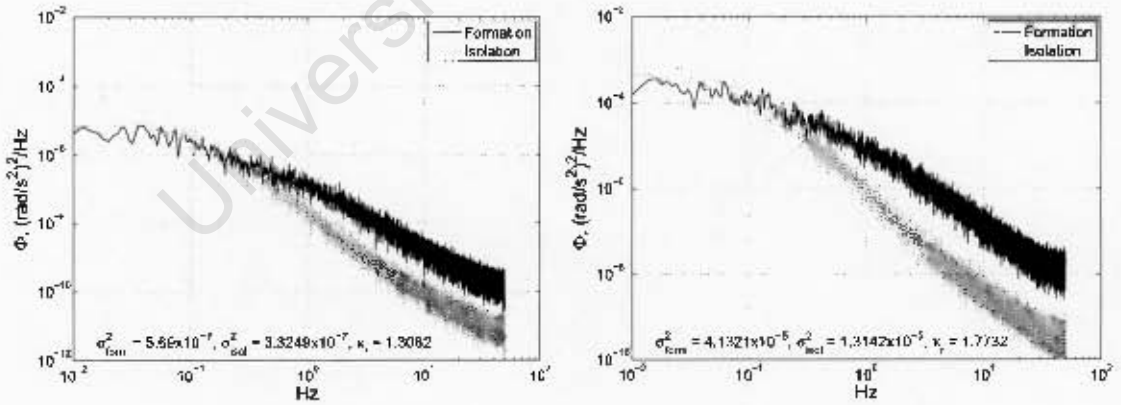

(a) $\sigma = 0.2$ (b) $\sigma = 1.3$

Figure 7.3: Spectral Density Estimations of the yaw accelerations in light and moderate turbulence, $\sigma = 0.2$ m/s and 1.3 m/s, for flight in isolation and in formation flight at $\eta = 0.90$. From Appendix E.

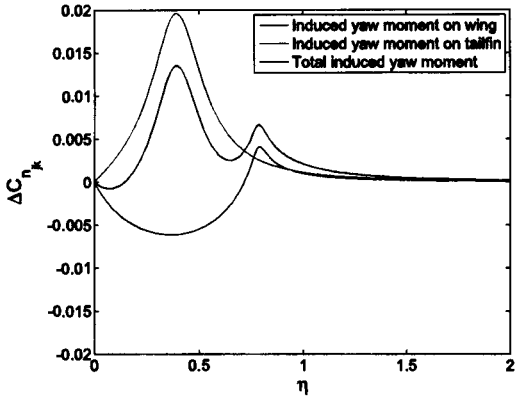

(a) Induced yaw moment for lateral separation and zero vertical separation. From Section 3.6.

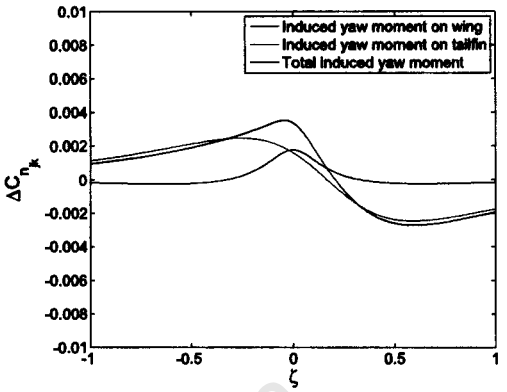

(b) Induced yaw moment for vertical separation and $\eta = 0.9$.

Figure 7.4: Induced yawing moments for changes in lateral and vertical separation about $\zeta = 0$ and $\eta = 0.9$ respectively.

aforementioned explanation. Introduction of the vertical gusts resulted in a small increase in the magnitudes of the formation flight yaw accelerations at high frequencies but not to the full extent shown in Figs. E.3 and E.7 where all gust velocities and gust velocity gradients are applied. The introduction of the lateral gust velocity gradient with respect to the longitudinal direction produced a significant increase in acceleration magnitudes at high frequencies in formation flight. Investigation of the yaw acceleration magnitude at $\eta = 1.2$ revealed that this effect was no longer prevalent. The acceleration magnitudes in formation flight at this lateral station are less than those in isolation for the entire frequency range following the reasoning described above. No suitable explanation could be found to explain the increased yaw acceleration magnitudes over high frequencies at $\eta = 0.9$ due to the lateral gust velocity gradient.

Plotting kappa values, $\frac{\sigma_{form}}{\sigma_{isol}}$, in Fig. 7.5 for the 6 DOF mass centre accelerations shows the multiplying effects due to formation flight as a function of turbulence intensity and lateral separation.

Large kappa values are found on the angular accelerations, indicating that the angular accelerations are much greater in formation flight than in isolated flight. The same is true for the linear accelerations except for lateral acceleration magnitudes, $\dot{v}$, which show a reduction due formation flight as discussed earlier. Figure 7.5 shows that the biggest differences occur in light to moderate turbulence while the smallest differences occur in severe turbulence. The κ values in severe turbulence are still significant, however, and

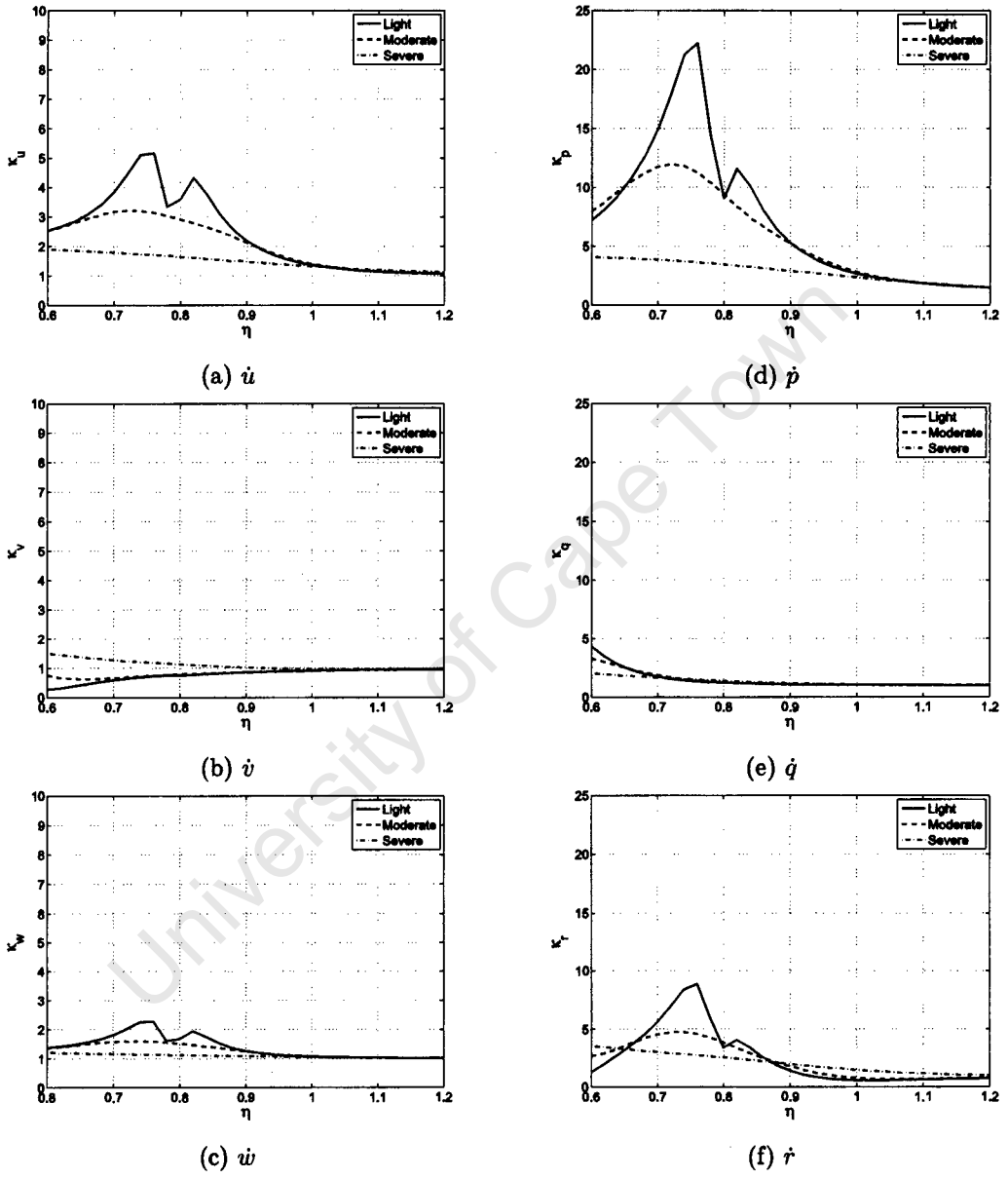

(a) $\dot{u}$ (d) $\dot{p}$

(b) $\dot{v}$ (e) $\dot{q}$

(c) $\dot{w}$ (f) $\dot{r}$

Figure 7.5: κ distribution of mass centre as a function of turbulence intensity and lateral separation, η. Reprinted from Fig. F.1.

cannot be ignored particularly in roll accelerations, $\dot{p}$.

A further interesting observation is the local minima found near $\eta = 0.79$, in light turbulence, which is marginally outboard of optimum lateral separation for performance benefit, predicted by the approximate model, suggesting that there may be a coupled optimum lateral separation for performance benefit and passenger comfort. This local minimum, however, may be the result of the approximate method used to calculate the induced forces and moments which yield peaks at $\eta = \frac{\pi}{4}$ exactly.

7.2 Accelerations of Passenger Offset from CG

In the preceding section, accelerations of the mass centre were considered. The accelerations of a passenger at a position removed from the mass centre may be significantly different as the angular accelerations show large increases due to formation flight.

From Fig. 6.3, different locations are identified for investigation. The benchmark location, 'A', is chosen directly above the mass centre where the z displacement from the mass centre is -0.7 m inferred from data in D6-58326 [82] and Heffley and Jewell [83].

The linear acceleration component spectral density estimations for each seat location specified in table 6.1 are shown in Figs. E.13 to E.24. Following from the rigid body assumption, the angular accelerations of a location offset from the mass centre are identical to the mass centre angular accelerations and are therefore not shown. The passenger acceleration spectral density estimations are shown for a lateral relative separation of $\eta = 0.76$ in moderate turbulence intensity, σ =0.2 m/s (Figs. E.13 to E.18), as well as the case for lateral separation of $\eta = 0.7$ in moderate turbulence, σ=1.3 m/s (Figs. E.19 to E.24). These are chosen following preliminary tests identifying the worst case. A severe turbulence case is not shown since the variance ratio, κ, indicates that there is less difference found in acceleration magnitudes between formation flight and isolated flight at this level of turbulence.

Figures 7.6 and 7.7, representing the accelerations at seat location 'A' and 'F', are displayed here for convenience. Comparing Figs. 7.1 and 7.6, it is seen that the longitudinal and vertical acceleration magnitudes for position 'A' are similar to those at the mass centre. In contrast, the lateral acceleration magnitudes show a distinct increase in formation flight for a location raised in the negative z direction from the mass centre. This is due to the large roll accelerations coupled with the vertical displacement.

Figure 7.8 shows that there is very little difference in longitudinal and vertical acceleration magnitudes between seat locations 'A', 'B' and 'C' in isolated flight. In formation flight, results of seating locations A, B and C in Figs. 7.9, E.13, E.15, E.16, E.19, E.21 and E.22 indicate that the vertical and longitudinal acceleration magnitudes increase with

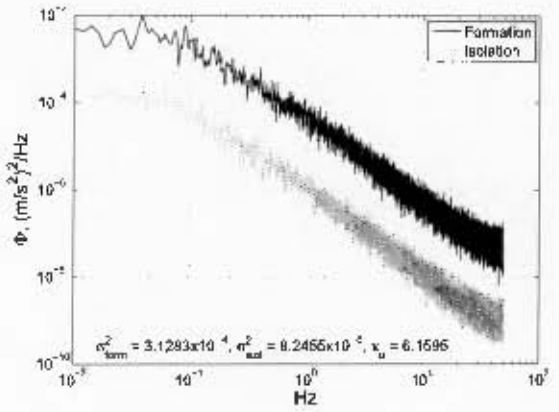

(a) $\dot{u}$

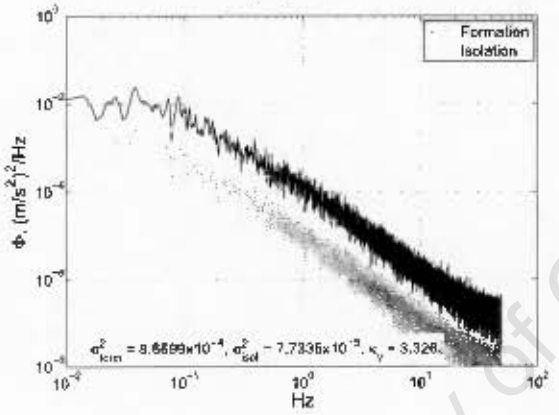

(b) $\dot{v}$

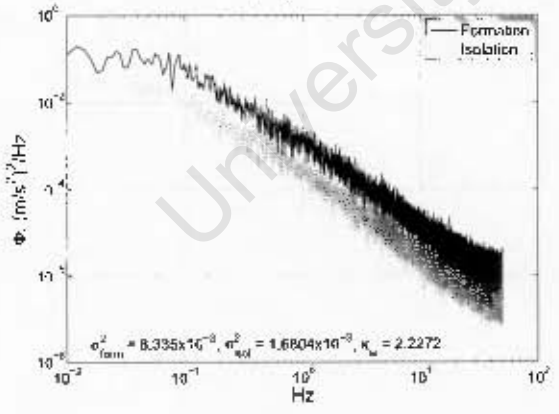

(c) $\dot{w}$

Figure 7.6: Passenger linear acceleration spectral densities at seat location 'A' in light turbulence, $\sigma = 0.2$ m/s, at $\eta = 0.76$. From Appendix E.

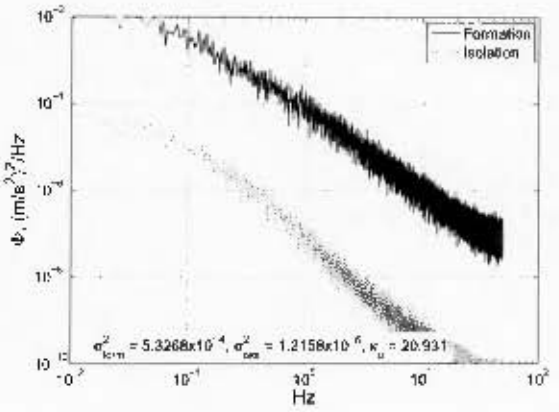

(a) $\dot{u}$

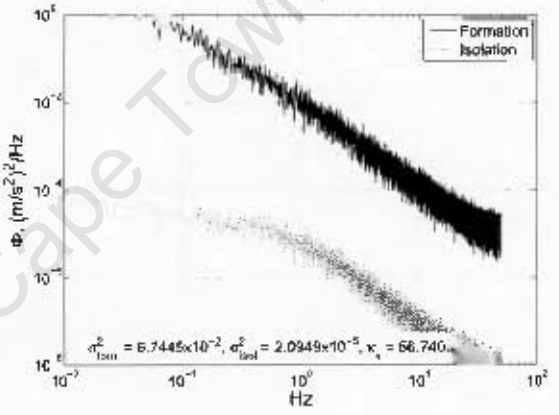

(b) $\dot{v}$

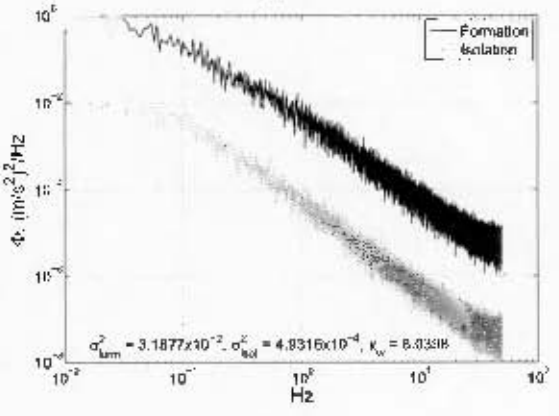

(c) $\dot{w}$

Figure 7.7: Passenger linear acceleration spectral densities at seat location 'F' in light turbulence, $\sigma = 0.2$ m/s, at $\eta = 0.76$. From Appendix E.

a shift from location 'A' to location 'C', on the same side as the lead aircraft, while decreasing with a shift from location 'A' to 'B'. The difference in these acceleration magnitudes between location 'B' and 'C' is significant. To explain this, consider the lateral and vertical

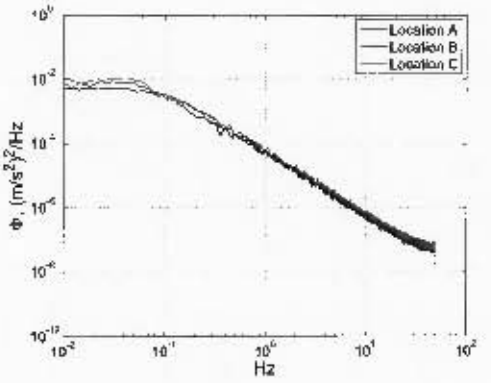

(a) $\dot{u}$

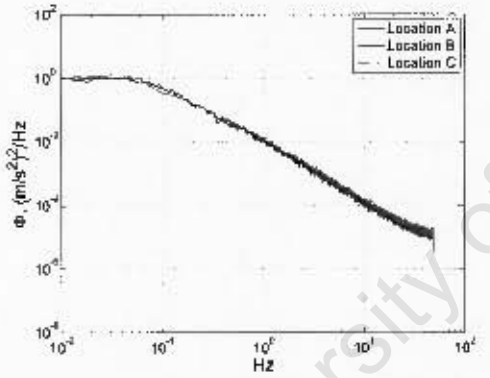

(b) $\dot{w}$

Figure 7.8: Spectral density of passenger accelerations in isolated flight at seat locations 'A', 'B' and 'C'. Moving average smoothing filter applied to improve clarity. Moderate turbulence, $\sigma = 1.3$ m/s, at $\eta = 0.70$.

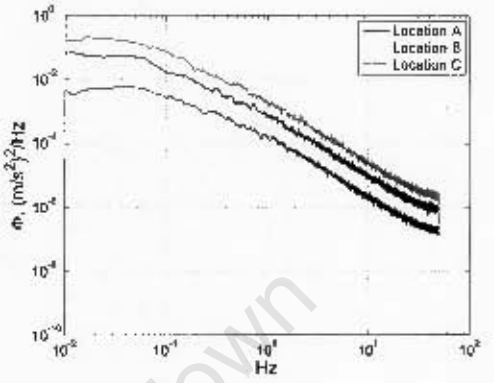

(a) $\dot{u}$

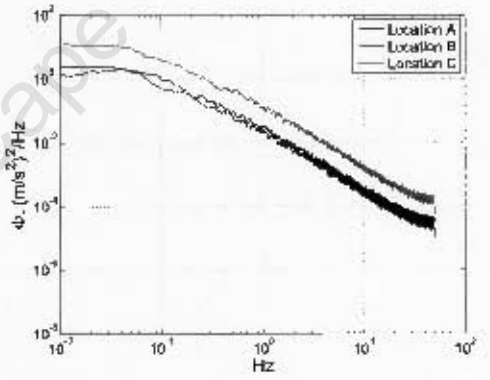

(b) $\dot{w}$

Figure 7.9: Spectral density of passenger accelerations in formation flight at seat locations 'A', 'B' and 'C'. Moving average smoothing filter applied to improve clarity. Moderate turbulence, $\sigma = 1.3$ m/s, at $\eta = 0.70$.

gusts which result in a change in the induced lift created by the trailing vortices (Fig. B.1c). Along with this change in induced lift, there is a corresponding change in induced rolling moment (Fig. B.1d) which generates vertical acceleration, via the lateral displacement, at location 'C' in the same sense as the acceleration due to the change in induced lift, but in the opposite sense at location 'B'. A similar effect is observed with the accelerations due to the change in induced drag and the change in induced yawing moment (Figs. B.1a and B.1f) which accumulate at location 'C' but are opposed at location 'B'.

A longitudinal displacement from the mass centre also has a significant impact on the acceleration magnitudes (Locations 'D' and 'E') in isolation and in formation flight. In isolation, Location 'D' exhibits increased acceleration magnitudes while at location 'E', fore fuselage, the acceleration magnitudes are significantly reduced with respect to location 'A'. If an aircraft in isolation experiences a lateral gust, a sideforce and stabilizing yawing moment results (Fig. 7.10). At the rear of the aircraft, the sideforce and yawing moment generate a

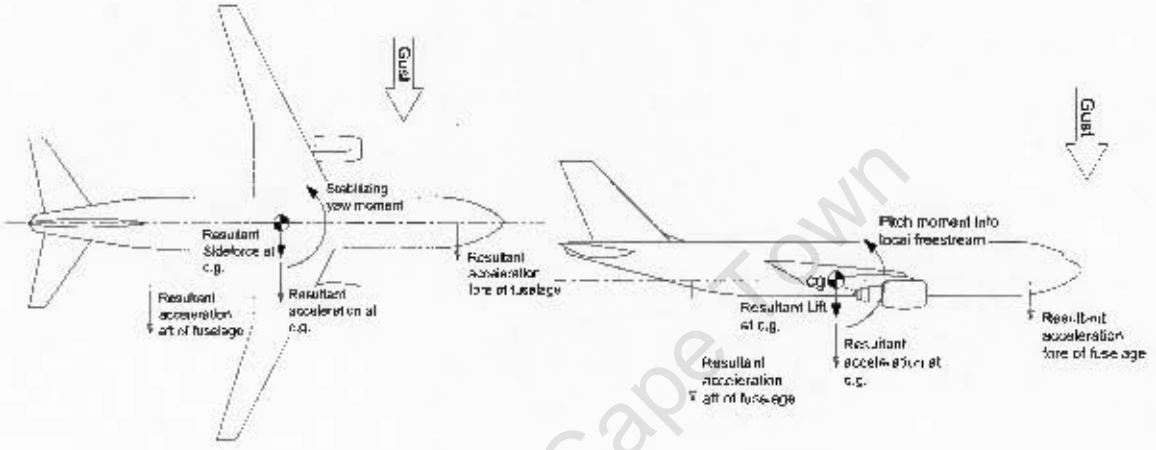

(a) Lateral gust (b) Vertical gust

Figure 7.10: Illustration of resultant accelerations due to lateral and vertical gusts in isolation

lateral acceleration in the same direction as the gust, with increasing magnitude from the mass centre toward the rear and decreasing magnitude from the mass centre toward the front, as shown by Figs. E.17, E.18 and Figs. E.23, E.24 for the case of flight in isolation.

Figures 7.11 and 7.12 show the variation in spectral density across selected seat locations fore, aft and at the mass centre.

The difference in vertical acceleration magnitudes at fore and aft fuselage locations in isolated flight is accounted for by the same reasoning, as shown in Fig. 7.10b. A vertical gust results in loss of lift and positive pitching moment generating a larger acceleration at the rear and reduced acceleration forward of the fuselage compared with the mass centre. Fig. 7.11a shows how a negative vertical displacement from the mass centre results in reduced longitudinal acceleration magnitudes. This is due to the interaction of drag and pitching moment in vertical gusts. The results of Fig. 7.11 for isolated flight in turbulence indicate that sitting in the front of the aircraft results in more comfortable flight than sitting in the rear.

The reduction in lateral acceleration magnitudes toward the front of the aircraft is

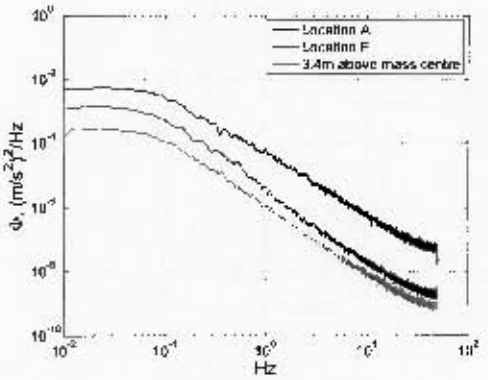

(a) $\dot{u}$

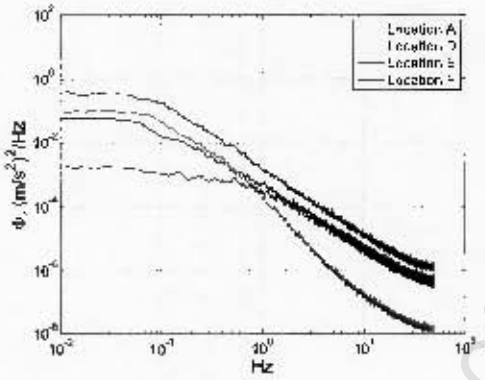

(b) $\dot{v}$

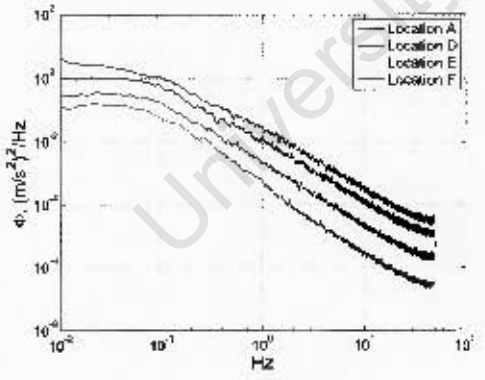

(c) $\dot{w}$

Figure 7.11: Spectral density of passenger accelerations in isolated flight at selected seat locations. Moving average smoothing filter applied to improve clarity. Moderate turbulence, $\sigma = 1.3$ m/s, at $\eta = 0.70$.

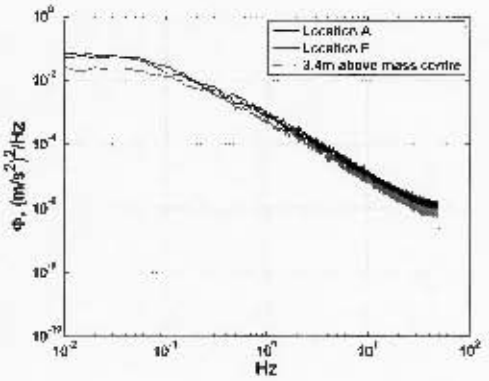

(a) $\dot{u}$

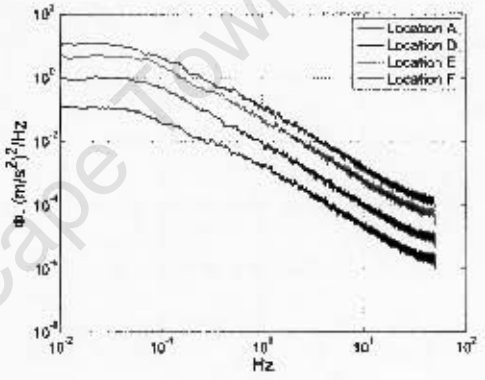

(b) $\dot{v}$

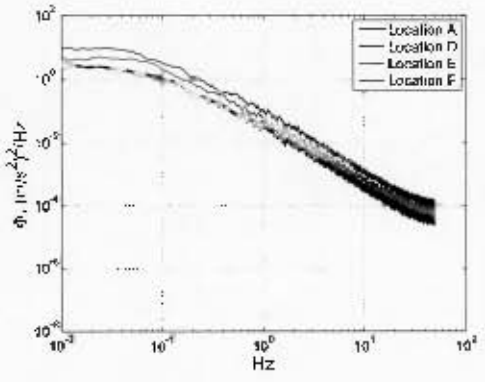

(c) $\dot{w}$

Figure 7.12: Spectral density of passenger accelerations in formation flight at selected seat locations. Moving average smoothing filter applied to improve clarity. Moderate turbulence, $\sigma = 1.3$ m/s, at $\eta = 0.70$.

reversed in formation flight (Fig. 7.12) due to the change in the induced yawing moments created by the disturbed trailing vortices (Fig. B.1f). At $\eta = 0.7$ and 0.76, a large increase in the yaw accelerations is evident over the entire frequency range investigated (Figs. E.5f and E.6f). Vertical gusts, which do not affect the yawing moment of an aircraft in isolation, also change the induced yawing moments due to formation flight. Greater vertical acceleration magnitudes are also evident at location 'E' (Figs. E.18 and E.24) due to increases in the pitching acceleration magnitudes (Fig. B.1e). Larger acceleration magnitudes are found at location 'E' compared with location 'D', particularly in the lateral and vertical orientations (Figs. 7.12, E.17, E.18, E.23 and E.24). This is the opposite effect to that experienced in isolation. The linear acceleration magnitudes at location 'D', aft of the fuselage, show very little difference compared with location 'A'. A small increase in the lateral acceleration magnitudes is, however, evident.

Location 'F', with displacement: $x = 21$, $y = -1.7$ and $z = -3.4$ m from the mass centre, was selected for investigation as a worst case seating location. Results do show large increases of the acceleration magnitudes in formation flight compared to flight in isolation at the same location (Figs. 7.12, 7.11, E.14 and E.20). However inspection of the results for flight in isolation at location 'F' show marked reductions in the acceleration magnitudes compared with location 'A' (Figs. E.13, E.14, E.19 and E.20). Comparison of the acceleration magnitudes at location 'F' with those at locations 'C' and 'E' in formation flight are in fact similar in terms of magnitude and frequency distribution. Location 'C', however, shows a smaller increase in the lateral acceleration magnitudes and a larger increase in the longitudinal acceleration magnitudes.

The results discussed suggest that the worst affected seat locations within an aircraft flying in a right echelon formation are found toward the front of the aircraft and to port (inboard side closer to lead aircraft).

The somewhat surprising result that forward fuselage seating locations will be less comfortable in formation flight than in isolated flight may conveniently be explained by reference to the gradients of the various graphs on Fig. B.1. For lateral separation of $\eta = 0.7$ and a small positive lateral gust as shown in Fig. 7.13. $\Delta C_n < 0$ resulting in a nose down accel-

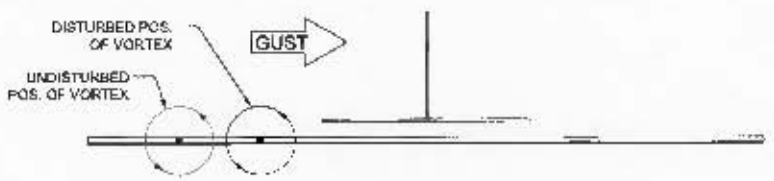

Figure 7.13: Rear view of trailing aircraft with position of disturbed vortex in positive lateral gust.

eration about the mass centre (Fig. B.1e), $\Delta C_L < 0$ resulting in a downward acceleration of the mass centre (Fig. B.1c) and $\Delta C_l < 0$ resulting in an anticlockwise acceleration about the mass centre (Fig. B.1d). From these results, seat location 'E' would be worse than 'D' and seat location 'C' would be worse than 'B'.

For a small negative lateral gust at $\eta = 0.7$ as shown in Fig. 7.14. $\Delta C_m > 0$ resulting in

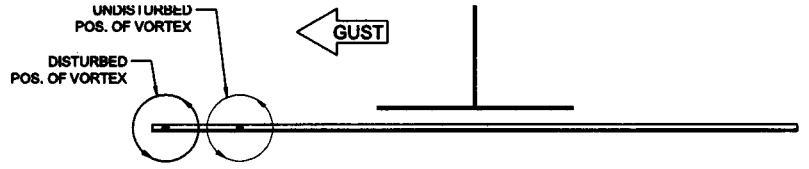

Figure 7.14: Rear view of trailing aircraft with position of disturbed vortex in negative lateral gust.

a nose up acceleration about the mass centre (Fig. B.1e), $\Delta C_L > 0$ resulting in an upward acceleration of the mass centre (Fig. B.1c) and $\Delta C_l > 0$ resulting in a clockwise acceleration about the mass centre (Fig. B.1d). From these results, once again seat location 'E' would be worse than 'D' and seat location 'C' would be worse than 'B'.

The κ values for the seating locations 'A' to 'F' are given in Figs. F.2 to F.7 (κ values for seat locations 'A' and 'F' are reprinted in Figs. 7.15 and 7.16 for convenience). These values provide a condensed summary of the spectra by dropping the frequency content and comparing the variance relationships between isolated and formation flight.

The passenger linear and angular acceleration spectra are transformed into overall vibration values as per the method prescribed by ISO 2631-1 [10]. These overall vibration values, a_{v_i}, where i represents 'A' to 'F', are displayed for $\eta = 0.6$ to 1.2 in Figs. 7.17 to 7.22. In each figure, the straight dashed lines indicate the comfort level of a passenger at the same seat location in an aircraft flying in isolation through identical atmospheric turbulence. The regions between the straight light gray lines indicate the expected comfort levels for a given overall vibration value adapted from ISO 2631-1 [10] suggesting likely reactions in public transport. Inspection of the overall vibration values for cases in isolation indicates reasonable comfort levels, even in severe atmospheric turbulence. This, however, may be due to the method applied which does not consider low frequency vibration (less than 0.5 Hz) which peak values exhibit as shown in all spectra less than 0.5 Hz.

It is immediately apparent that there are vastly different characteristics at different seat locations. For cases in isolated flight, locations 'A', 'B' and 'C' all show similar vibration values suggesting that atmospheric turbulence does not induce significant roll accelerations. Location 'D' shows the highest vibration values for all turbulence intensities while locations

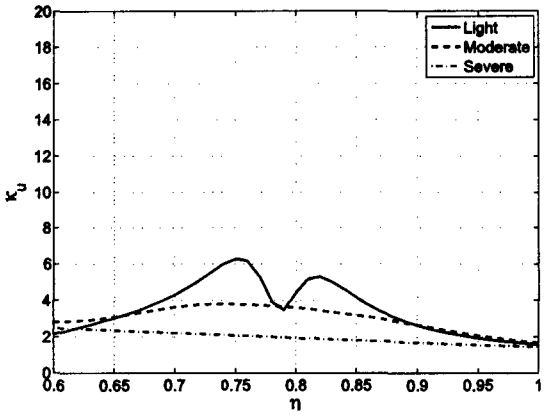

(a) $\kappa_{\dot{u}}$

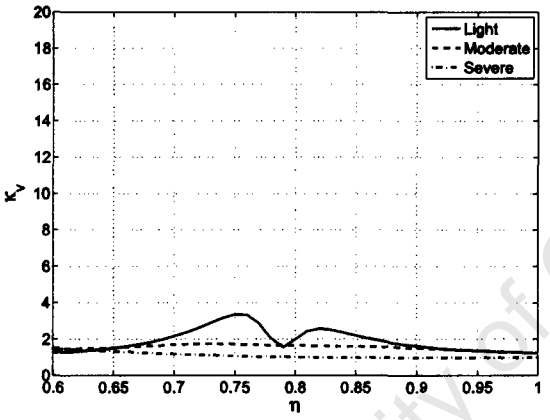

(b) $\kappa_{\dot{v}}$

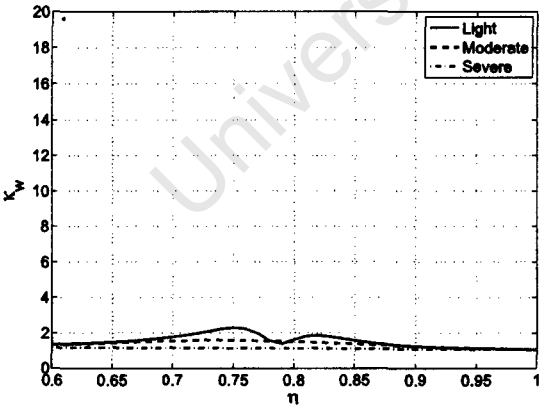

(c) $\kappa_{\dot{w}}$

Figure 7.15: Variance ratio κ distribution of passenger at location 'A' as a function of turbulence intensity and lateral separation, η.

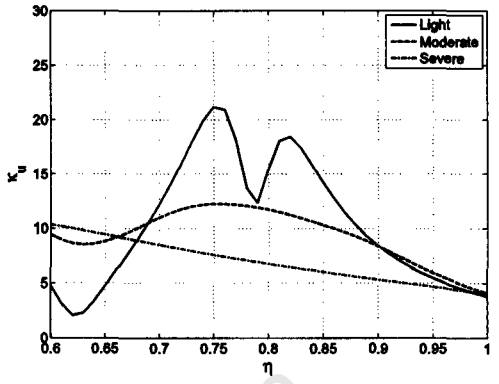

(a) $\kappa_{\dot{u}}$

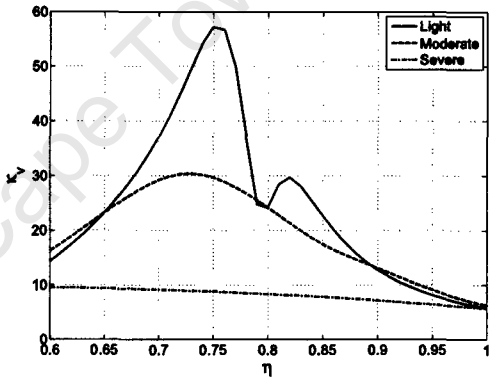

(b) $\kappa_{\dot{v}}$

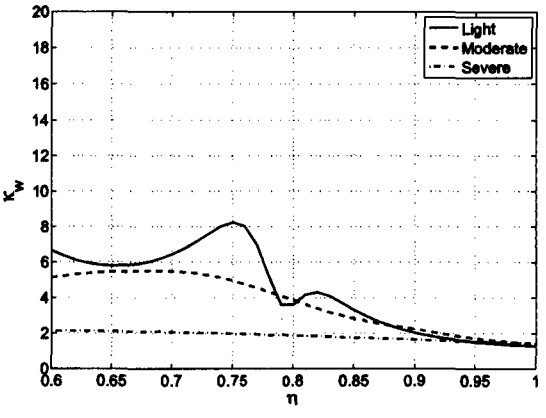

(c) $\kappa_{\dot{w}}$

Figure 7.16: Variance ratio κ distribution of passenger at location 'F' as a function of turbulence intensity and lateral separation, η.

'E' and 'F' show the minimum vibration values indicating that pitch and yaw accelerations are the dominant angular components acting on an isolated aircraft in atmospheric turbulence.

In formation flight, the vibration values calculated for seat locations 'A' to 'F' in light atmospheric turbulence, $\sigma = 0.2$ m/s, show two distinct peaks at $\eta \approx 0.75$ and $\eta \approx 0.82$. These lateral separations represent the trailing aircraft marginally inboard and outboard of optimum lateral separation for performance benefit as predicted by the horseshoe vortex model. The trough between these two peaks, as eluded to earlier, is a very interesting result and warrants further investigation. However, this could simply be an artefact of the simplified model predicting peaks at a lateral separation of exactly $\eta = \frac{\pi}{4}$. Seat locations 'A', 'B' and 'D' show very little difference to the equivalent isolated cases for all three atmospheric turbulence intensities considered, aside from location 'D' in severe atmospheric turbulence which shows a significant increase in the vibration value with decreasing lateral separation. Following from the discussion of the spectra results, locations 'C', 'E' and 'F' show very large vibration values compared with the isolated cases. These locations are all forward and inboard (closer to the lead aircraft) within the fuselage. In moderate atmospheric turbulence, the vibration values of these locations show a steep increase for $\eta < 0.82$ toward $\eta \approx 0.7$ where the vibration values drop off slightly toward $\eta = 0.6$ while a gentle decrease is observed with increasing lateral separations for $\eta > 0.85$. This is a consistent trend at locations 'C', 'E' and 'F' in moderate atmospheric turbulence. The vibration values for both light and moderate atmospheric turbulence conditions suggest that the favoured lateral separation for passenger comfort is found greater than 0.1 spans outboard of optimum lateral separation for performance benefit. In severe turbulence at all seat locations, there is a consistent increase in the vibration values for decreasing lateral separation.

Results of the vibration values at seat location 'F' predicted with an atmospheric turbulence of a shorter length scale (152 m) are compared with vibration values using a 762 m length scale, as applied to all previous simulations shown in Figs. 7.23 and 7.24.

It is immediately evident that turbulence with shorter wavelengths of greater amplitude increases the predicted discomfort. With the uncertainty related to the wavelengths and amplitudes expected in wake turbulence, smaller turbulence length scales may not be excluded.

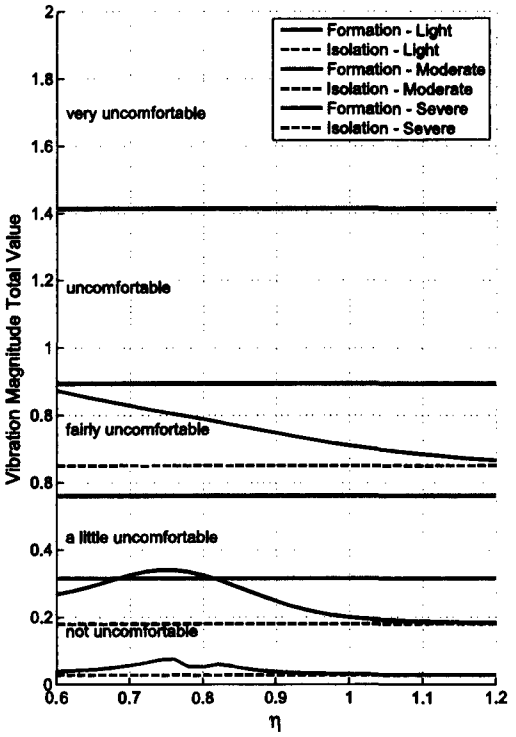

Figure 7.17: a_{v_A}

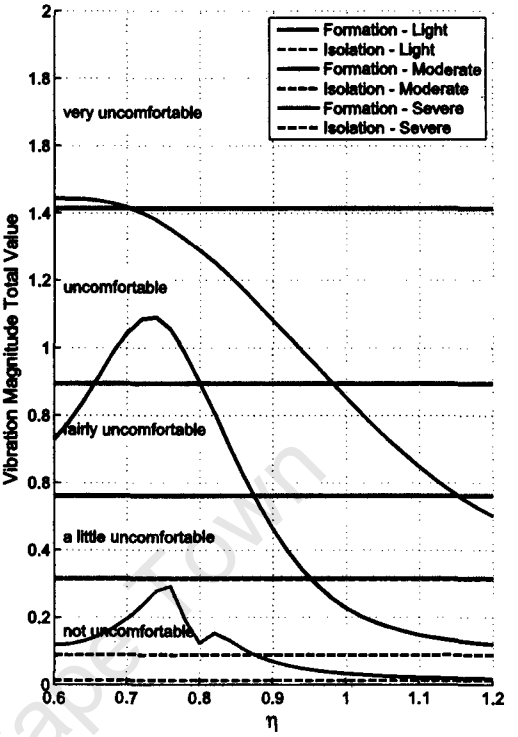

Figure 7.18: a_{v_F}

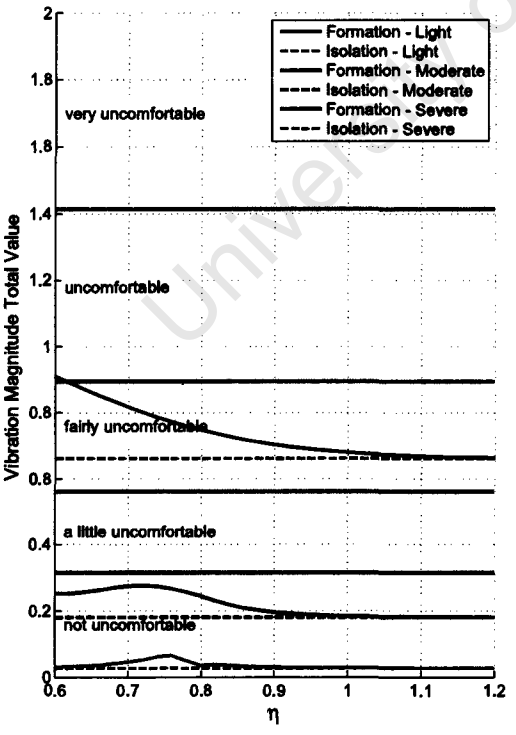

Figure 7.19: a_{v_B}

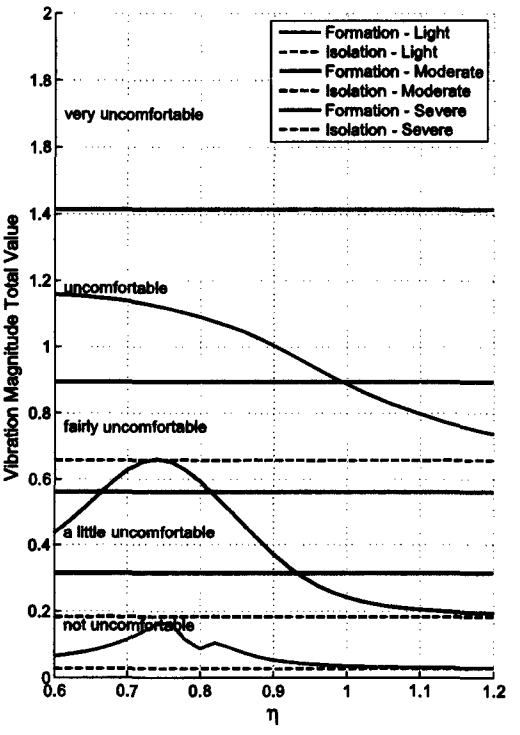

Figure 7.20: a_{v_C}

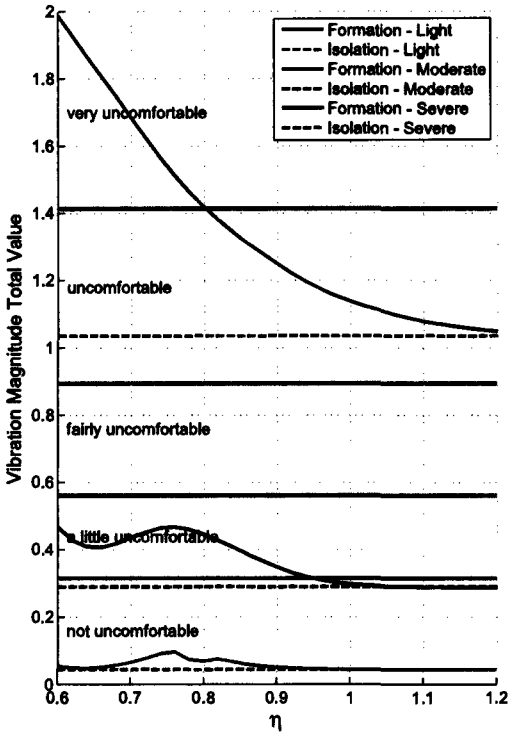

Figure 7.21: a_{v_D}

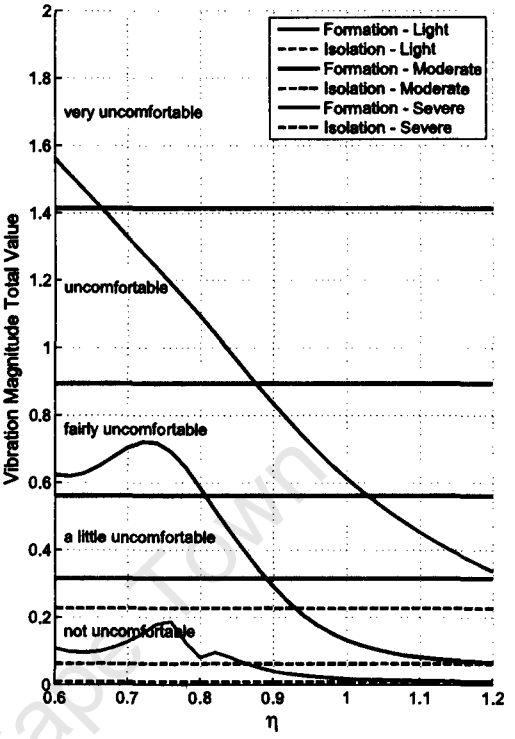

Figure 7.22: a_{v_E}

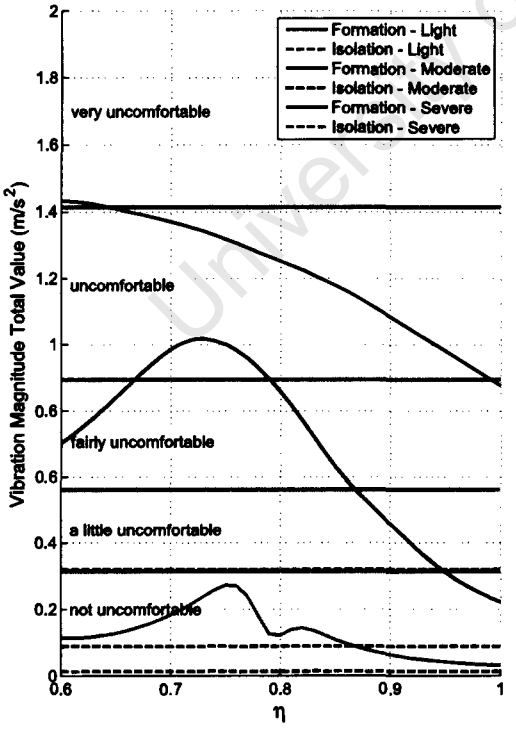

Figure 7.23: a_{v_F}, $L_u = 762$ m

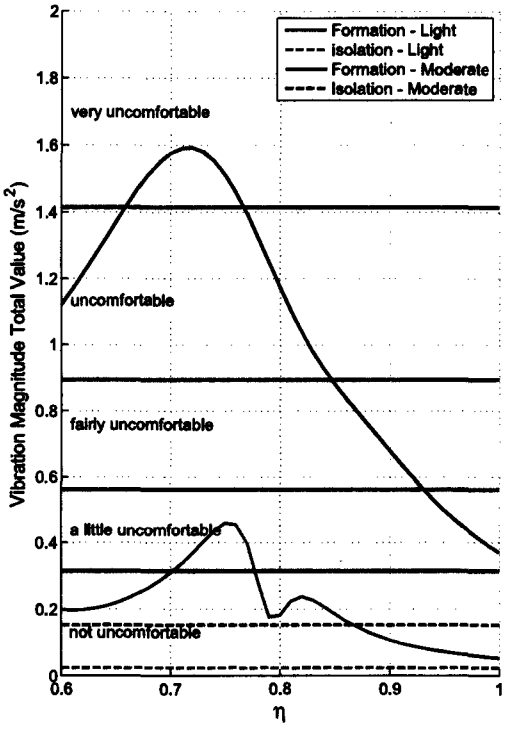

Figure 7.24: a_{v_F}, $L_u = 152$ m

8 Conclusions

The passenger comfort levels on board a trailing aircraft in a two ship formation, were predicted using a basic rms method prescribed by ISO 2631-1 [10], which provides guidance as to the likely reactions in public transport. Comparison with comfort levels in isolated flight were made, using the same simplifying assumptions and method of prediction. The accelerations due to formation flight were generated via a rudimentary aerodynamic model and both aircraft were considered to maintain station without any state perturbations. Aeroelastic effects were not included. This allowed investigation of the accelerations without the need for a complex control algorithm. Within the assumptions of the current study, the following conclusions were drawn.

A significant increase in discomfort due to formation flight was predicted. The results were highly dependent on lateral separation, variations in turbulence intensity and passenger seat displacement from the aircraft mass centre.

Increasing levels of turbulence generally resulted in less difference in comfort levels between isolated and formation flight. In moderate turbulence, results suggest that greater lateral separations offer increasing levels of comfort. In all cases of moderate turbulence, the peak in discomfort was found between 0.7 and 0.8 spans (around the predicted optimum lateral separation for performance benefit equal to 0.785 spans). At one wingspan separation (wing-tip to wing-tip), the results predict that in most cases, there is little increase in discomfort. The same can be said for light turbulence, however, simulations with light turbulence revealed a narrow trough in the comfort-separation curve about 0.01 spans outboard of optimum separation with a second smaller peak outboard of this lateral separation. The application of severe turbulence generated a monotonic increase in discomfort for decreasing lateral separation.

Formation flight results showed significant differences in passenger comfort for different seat locations (different displacements from mass centre). Seat locations on the inboard side (closer to the lead aircraft) of the fuselage produced significantly higher vibration values than seat locations on the outboard side of the fuselage and vibration values at seat locations in the front of the fuselage were considerably higher than the rear of the fuselage. In general, moving from rear, outboard seat locations toward the lead aircraft (front, inboard) within the fuselage yielded increasing overall vibration compared with isolated flight. The unexpected result obtained here, of less relative comfort for forward seating, is explained by considering the influence of the lead aircraft trailing vortex, moving in the presence of

atmospheric turbulence, on the trailing aircraft.

Large increases in roll and yaw acceleration magnitudes due to formation flight were identified. Coupling between these two angular components as well as the linear components may cause increased discomfort.

These conclusions could be invalidated by incorporating an autopilot within the control laws.

9 Recommendations

In order to simulate more realistic aircraft motion, a practical formation flight control algorithm should be implemented which would allow the simulation of non-zero perturbed state variables. A preliminary investigation could implement only the roll and yaw parameters which would offer better understanding of the effects of seat displacement from the mass centre. Aeroelastic effects, especially with respect to the main wing, would also increase the fidelity of the model.

There is scope for considerable improvement of the aerodynamic model:

- Realistic linear lift distributions which are analytically integrable should be modelled, i.e. triangular lift distribution.
- The sidewash on the fuselage will generate a significant contribution to the induced yaw moment and should be included.
- Including the effect of wing sweep will improve the fidelity of the induced pitching moment due to the changing centre of pressure.
- The induced flow over the tail lifting surface may be largely disturbed by the wing and fuselage and further investigation is required to ascertain the degree of influence.
- The effects of compressibility on the vortex flow and increased local velocities due to the trailing vortex need to be investigated.

One should consider approximating the non-uniform vortex induced flow impinging on the trailing aircraft with effective uniform wind and wind gradients as proposed by Dogan et al. [60]. This method allows the linear approximations to be applied directly to the standard equations of motion.

Further investigation of the turbulence structure within the vortex wake should be highly sought, particularly with regard to the expected wavelengths and amplitudes. The existence of short wavelength instabilities (aircraft generated), as noted in literature [16], would result in higher frequency vibration which may significantly increase the discomfort experienced by a passenger.

The vortex model used in the current study is a basic model and assumes no diffusion. Although some literature suggests that very little diffusion occurs [12, 16, 32], this may still be modelled while applying a more complex vortex velocity profile. The VM2 profile

as proposed by Jacquin and Fabre [42] or the combined Lamb-Oseen/potential flow profile by van Jaarsveld et al. [40] should be considered. The Lamb-Oseen/potential flow model allows for diffusion up to an outer core radius.

The approximation that the trailing vortices shift in an ideal manner due to the gust velocities requires validation. Particular emphasis should be placed on whether these vortices exhibit shorter wavelengths than those of atmospheric turbulence, especially with waveforms of 0.5 to 80 Hz.

It is the opinion of the author that the comfort levels, predicted using ISO 2631-1 [10], were under predicted, for example, psychological effects may play a dominant role in the perception of comfort in air travel. An alternative evaluation specific to air transport may offer comfort predictions which are more likely.

It would be valuable to examine the validity of the current approximate approach by means of flight tests. One conceivable test could entail measuring onboard vibrations on three aircraft; two of which fly in formation and the third some distance away to represent flight in isolation.

References

[1] J. H. Myatt and W. Blake. Aerodynamic database issues for modelling close formation flight. AIAA, 1999. paper 99-4194.

[2] D. R. Gingras. Experimental investigation of a multi-aircraft formation. In *AIAA 17th Applied Aerodynamics Conference*, Norfolk, VA, June-July 1999. paper 99-3143.

[3] W. Blake and D. R. Gingras. Comparison of predicted and measured formation flight interference effects. In *Journal of Aircraft*, volume 41, pages 201–207, March-April 2004.

[4] M. Beukenberg and D. Hummel. Aerodynamics, performance and control of airplanes in formation flight. ICAS, 1990. paper 90-5.9.3.

[5] W. Blake and D. Multhopp. Design, performance and modelling considerations for close formation flight. AIAA, 1998. paper 98–4343.

[6] W. Blake. An aerodynamic model for simulation of close formation flight. In *AIAA 2000 Modelling and Simulation Technologies Conference and Exhibit, Denver, USA*, 2000.

[7] J. Bradley. The handling and performance trials needed to clear an aircraft to act as a receiver during air-to-air refueling. AGARD, July 1984. CP 373: Flight Test Techniques, paper 9.

[8] G. Bower, T. Flanzer, and I. Kroo. Formation geometries and route optimization for commercial formation flight. AIAA, June 2009. Paper 2009-3615.

[9] S. A. Ning, T. C. Flanzer, and I. M. Kroo. Aerodynamic performance of extended formation flight. In *Journal of Aircraft*, volume 48, pages 855–865, 2011.

[10] ISO 2631-1. *Mechanical vibration and shock - Evaluation of human exposure to whole-body vibration - General requirements.* International Organization for Standardization, Geneva, Switzerland, 1997.

[11] C. Breitsamter. Wake vortex characteristics of transport aircraft. In *Progress in Aerospace Sciences*, volume 47, pages 89–134, 2011.

[12] L. Jacquin, D. Fabre, P. Geffroy, and E. Coustols. The properties of a transport aircraft wake in the extended near field: an experimental study. AIAA, 2001. paper 2001-1038.

[13] P. R. Spalart. Airplane trailing vortices. In *Annu. Rev. Fluid Mech.*, volume 30, pages 107–138, 1998.

[14] S. E. Widnall. The structure and dynamics of vortex filaments. In *Annual Review of Fluid Mechanics*, volume 7, pages 141–165, 1975.

[15] L. Jacquin, D. Fabre, D. Sipp, V. Theofilis, and H. Vollmers. Instability and unsteadiness of aircraft wake vortices. In *Aerospace Science and Technology*, volume 7, pages 577–593, 2003.

[16] F. Holzapfel, T. Gerz, and R. Baumann. The turbulent decay of trailing vortex pairs in stably stratified environments. In *Aerospace Science and Technology*, volume 5, pages 95–108, 2001.

[17] S. I. Green and A. J. Acosta. Unsteady flow in trailing vortices. In *J. Fluid Mech.*, volume 227, pages 107–134, 1991.

[18] J. S. Chow, G. G. Zilliac, and P. Bradshaw. Measurements in the near field of a turbulent wing-tip vortex. In *Proceedings of the AIAA 31st Aerospace Sciences Meeting*, 1993.

[19] M. L. Beninati and J. S. Marshall. An experimental study of the effect of free-stream turbulence on a trailing vortex. In *Exp. Fluids*, volume 38, pages 244–257, 2005.

[20] A. Shekarriz, T. C. Fu, and T. T. Huang. Near field behaviour of a tip vortex. In *AIAA J.*, volume 31, pages 112–118, 1993.

[21] W. J. Devenport, M. C. Rife, S. I. Liapis, and G. J. Follin. The structure and development of a wing-tip vortex. In *J. Fluid Mech.*, volume 312, pages 67–106, 1996.

[22] V. R. Corsiglia and K. L. Orloff. Scanning laser-velocimeter surveys and analysis of multiple vortex wakes of an aircraft. NASA Ames Research Center, Moffett Field, CA, 1973.

[23] S. J. Beresh, J. F. Henfling, and R. W. Spillers. Meander of a fin trailing vortex and the origin of its turbulence. In *Exp. Fluids*, volume 49, pages 599–611, 2010.

[24] A. L. Heyes, R. F. Jones, and D. A. R. Smith. Wandering of wing-tip vortices. In *Proceedings of the 12th international symposium on applications of laser techniques to fluid mechanics*, Lisbon, Portugal, 2004. paper 35-3.

[25] T. Gerz and F. Holzapfel. Wing-tip vortices, turbulence, and the distribution of emissions. In *AIAA Journal*, volume 37, pages 1270–1276, 1999.

[26] H. Lamb. *Hydrodynamics.* Cambridge University Press, 1932.

[27] G. Kurylowich. A method for assessing the impact of wake vortices on USAF operations. US Air Force Flight Dynamics Laboratory, 1979. AFFDL-TR-79-3060.

[28] D. C. Burnham and J. N. Hallock. Chicago monostatic acoustic vortex sensor system. U.S. Department of Transportation, July 1982. DOT-TSC-FAA-79-103.IV.

[29] J. N. Hallock. Aircraft wake vortices: An assesment of the current situation. U.S. Department of Transportation, Jan 1991. DOT-FAA-RD-90-29.

[30] C. Donaldson. A brief review of the aircraft trailing vortex problem. U.S. Air Force Office of Scientific Research, May 1971. AFOSR-TR-71-1910.

[31] S.E. Widnall, D. Bliss, and A. Zalay. Theoretical and experimental study of the stability of a vortex pair. In *Aircraft wake turbulence and its detection.* Plenum press, 1971.

[32] S. C. C. Bailey and S. Tavoularis. Measurements of the velocity field of a wing-tip vortex, wandering in grid turbulence. In *J. Fluid Mech.*, volume 601, pages 281–315, 2008.

[33] MIL-F-8785C. *US Department of Defence Specification - Flying Qualities of Piloted Airplanes.* US Department of Defence, 1980.

[34] D.A. Hinton and C. R. Tatnall. A candidate wake vortex strength definition for application to the NASA aircraft vortex spacing system (AVOSS). Langley Research Center, 1997.

[35] T. Gerz, F. Holzapfel, and D. Darracq. Commercial aircraft wake vortices. In *Progress in Aerospace Sciences*, volume 38, pages 181–208, 2002.

[36] D. Fabre and L. Jacquin. Short wave cooperative instabilities in representative aircraft vortices. In *Physics of Fluids*, volume 16, pages 1366–1378, 2004.

[37] S. C. Crow and E. R. Bate, Jr. Lifespan of trailing vortices in a turbulent atmosphere. In *Journal of Aircraft*, volume 13, pages 476–482, 1976.

[38] F. Holzapfel. Probabilistic two-phase aircraft wake-vortex decay and transport model. In *Journal of Aircraft*, volume 40, pages 323–331, March-April 2003.

[39] B. Cantwell and N. Rott. The decay of a viscous vortex pair. In *Physics of Fluids*, volume 31, pages 3213–3224, 1988.

[40] J. P. J van Jaarsveld, A. P .C Holten, A. Elsenaar, R. R. Trieling, and G. J. F. van Heijst. An experimental study of the effect of external turbulence on the decay of a single vortex and a vortex pair. In *Journal of Fluid Mechanics*, volume 670, pages 214–239, 2011.

[41] S. C. Crow. Stability theory for a pair of trailing vortices. In *AIAA Journal*, volume 8, pages 2172–2179, 1970.

[42] L. Jacquin and D. Fabre. Short wave cooperative instabilities in representative aircraft vortices. In *Physics of Fluids*, volume 16, pages 1366–1378, May 2004.

[43] L. J. Garodz. FAA full scale aircraft vortex wake turbulence flight test investigations: Past, present, future. National Aviation Facilities Experimental Center, January 1971. AIAA paper 71-97.

[44] J. N. Hallock, editor. *Proceedings of the Aircraft Wake Vortex Conference*, June 1977. FAA-RD-77-68.

[45] J. N. Hallock, editor. *Proceedings of the Aircraft Wake Vortex Conference*, June 1992. DOT-VNTSC-FAA-92-07.

[46] J. J. O'Callaghan. Flight control and wake turbulence effects on american airlines flight 587. In *AIAA Modeling and Simulation Technologies Conference and Exhibit*, San Francisco, Aug 2005. paper 2005-6110.

[47] T. Misaka, T. Ogasawara, and S. Obayashi. Measurement integrated simulation of wake turbulence. In *AIAA Aerospace Sciences Meeting and Exhibit*, Reno, Nevada, Jan 2008. paper 2008-466.

[48] J. L. Hansen and B. R. Cobleigh. Induced moment effects of formation flight using two F/A-18 aircraft. In *AIAA Atmospheric Flight Mechanics Conference and Exhibit*, 2002. TM-2002-210732.

[49] M. J. Vachon, R. J. Ray, K. R. Walsh, and K. Ennix. F/A-18 performance benefits measured during the autonomous formation flight project. NASA Dryden Flight Research Center, 2003. TM-2003-210734.

[50] A. W. Bloy, P. J. Lamont, H. A. Abu-Assaf, and K. A. M. Ali. The lateral dynamic stability and control of a large receiver aircraft during air-to-air refuelling. In *Aeronautical Journal*, volume 90, pages 237–243, June-July 1986.

[51] A. W. Bloy, K. A. M. Ali, and V. Trochalidis. The longitudinal dynamic stability and control of a large receiver aircraft during air-to-air refuelling. In *Aeronautical Journal*, volume 91, pages 64–71, Feb 1987.

[52] D. Kuchemann. A simple method for calculating the span and chordwise loading on straight and swept wings of any given aspect ratio at subsonic speeds. Aeronautical Research Council, 1956. Reports and Memoranda No. 2935.

[53] A. W. Bloy and V. Trochalidis. The performance and longitudinal stability and control of a large receiver aircraft during air-to-air refuelling. In *Aeronautical Journal*, volume 93, pages 367–378, Dec 1989.

[54] A. W. Bloy and V. Trochalidis. The aerodynamic interference between tanker and receiver aircraft during air-to-air refuelling. In *Aeronautical Journal*, volume 94, pages 165–171, May 1990.

[55] A. W. Bloy, V. Trochalidis, and M. G. West. The aerodynamic interference between a flapped tanker aircraft and a receiver aircraft during air-to-air refuelling. In *Aeronautical Journal*, volume 95, pages 274–282, Oct 1991.

[56] A. W. Bloy, M. G. West, K. A. Lea, and M. Jouma'a. Lateral aerodynamic interference between tanker receiver in air-to-air refuelling. In *Journal of Aircraft*, volume 30, pages 705–710, Sept-Oct 1993.

[57] A. W. Bloy and M. Jouma'a. Trailing vortex effects on large receiver aircraft. In *Journal of Aircraft*, volume 32, pages 1198–1204, Nov-Dec 1995.

[58] A. E. Albright, C. J. Dixon, and M. C. Hegedus. Modification and validation of conceptual design aerodynamic prediction method hasc95 with vtxchn. NASA Langley Research Center, 1996. Contractor Report 4712.

[59] E. H. Hoganson. A study of aerodynamic interference effects during aerial refuelling. Master's thesis, US Air Force Institute of Technology, 1983.

[60] A. Dogan, S. Venkataramanan, and W. Blake. Modeling of aerodynamic coupling between aircraft in close proximity. In *Journal of Aircraft*, volume 42, pages 941–955, July-Aug 2005.

[61] I. D. Jacobson and M. Lapins. Application of active controls technology to aircraft ride smoothing. In *Journal of Aircraft*, volume 14, pages 775–781, Aug 1977.

[62] A. Brindisi and A. Concilio. Passengers comfort modeling inside aircraft. In *Journal of Aircraft*, volume 45, pages 2001–2008, Nov-Dec 2008.

[63] I. D. Jacobson, A. R. Kuhlthau, and L. G. Richards. Application of ride quality technology to predict ride satisfaction for commuter-type aircraft. In *1975 Ride Quality Symposium*, pages 45–64, 1975.

[64] S. S. Stevens. On the psychophysical law. In *Psychological Review*, volume 64, pages 153–181, 1957.

[65] K. Hiramatsu and M. J. Griffin. Predicting the subjective response to nonsteady vibration based on the summation of subjective magnitude. In *Journal of the Acoustical Society of America*, volume 76, pages 1080–1089, Oct 1984.

[66] H. V. C. Howarth and M. J. Griffin. The frequency dependence of subjective reaction to vertical and horizontal whole-body vibration at low magnitudes. In *Journal of the Acoustical Society of America*, volume 83, pages 1406–1413, April 1988.

[67] F. Kubica and B. Madelaine. Passenger comfort improvement by integrated control law design. Aerospatiale Matra Airbus, 1999. ADP010491.

[68] E. W. Turner. An exposition on aircraft response to atmospheric turbulence using power spectral density analysis techniques. US Air Force Flight Dynamics Laboratory, 1977. AFFDL-TR-76-162.

[69] C. J. Houbolt, R. Steiner, and K. G. Pratt. Dynamic response of airplanes to atmospheric turbulence including flight data on input and response. Langley Research Center, 1964.

[70] J. C. Houbolt. Atmospheric turbulence. In *AIAA Journal*, volume 11, pages 421–437, April 1973.

[71] D.E. Newland. *An introduction to random vibrations, spectral and wavelet analysis.* John Wiley and Sons, Inc., 3 edition, 1993.

[72] B. Etkin. *Dynamics of Atmospheric Flight*, chapter 13. John Wiley and Sons, Inc., 1972.

[73] S. T. Wang and W. Frost. Aerospace turbulence simulation techniques with application to flight analysis. University of Tennessee Space Institute, 1980.

[74] G. D. Nastrom and K. S. Gage. A climatology of atmospheric wavenumber spectra of wind and temperature oserved by commercial aircraft. In *Journal of the Atmospheric Sciences*, volume 42, pages 950–960, 1985.

[75] D. R. Schaeffer, N. M. Barr, and D. Gangsaas. Wind models for flight simulator certification of landing and approach guidance and control systems. In *Proceedings of the First Annual Workshop on Meteorological Inputs to Aviation Systems.* NASA, Mar 1977.

[76] J. D. Anderson. *Fundamentals of Aerodynamics.* McGraw-Hill, Boston, 4th. edition, 2007.

[77] B. Etkin. Theory of flight of airplanes in isotropic turbulence - review and extension. NATO advisory group for aeronautical research and development, April 1961. AD445597.

[78] MIL-HDBK-1797. *US Department of Defence Handbook - Flying Qualities of Piloted Airplanes.* US Department of Defence, 1997.

[79] B. Etkin and L. Reid. *Dynamics of Flight: Stability and Control.* John Wiley and Sons, Inc., 3 edition, 1996.

[80] G. Heinzel, A Rudiger, and R. Schilling. Spectrum and spectral density estimation by the discrete fourier transform (DFT), including a comprehensive list of window functions and some new flat-top windows. Max-Planck-Institut fur Gravitationsphysik, 2002.

[81] R. K. Otnes. *Digital Time Series Analysis.* Wiley, 1972.

[82] D6-58326. *747 Airplane Characteristics - Airport Planning.* Boeing Commercial Airplane Company, 1984.

[83] R. K. Heffley and W. F. Jewell. Aircraft handling qualities data. NASA, 1972.

[84] J. Stewart. *Calculus, Concepts and Contexts.* Brooks/Cole, CA, USA, 2001.

[85] A. W. Bloy and K. A. Lea. Directional stability of a large receiver aircraft in air-to-air refueling. In *Journal of Aircraft*, volume 32, pages 453–455, 1995.

[86] J. D. Iverson. Correlation of turbulent trailing vortex decay data. NASA Ames Research Center, 1974. NASA-CR-146282.

[87] J. Hansen, B. Cobleigh, R. Ray, J. Vachon, and K. Ennix. Vortex-induced aerodynamic effects on a trailing F-18 aircraft flying in close formation. In *1st Technical Conference and Workshop on Unmanned Aerospace Vehicles*, 2002.

[88] C. R. Hanke and D. R. Nordwall. The simulation of a jumbo jet transport aircraft - volume 2: Modelling data. The Boeing Company, Wichita, Kansas, 1970. D6-30643.

Appendix A: Derivations of the Influence Factors

A.1 Derivation of $\sigma_{jk\,full_H}$

A.1.1 Derivation of $\sigma_{bound\,k_H}$

From equation (3.2), the downwash due to the lead aircraft's bound vortex at a point on the trailing aircraft's bound vortex using the Helmholtz potential flow velocity profile is (see Fig. A.1a):

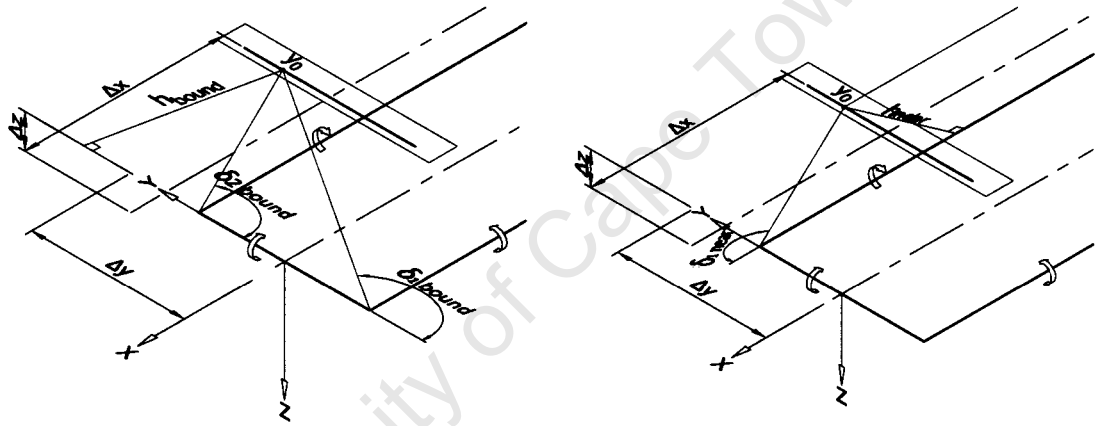

(a) Angles and perpendicular length from bound vortex

(b) Angles and perpendicular length from near trailing vortex

Figure A.1: Graphic illustrating angles and perpendicular lengths to vortex filaments

$$\left(\frac{4\pi}{\Gamma_j}\right) w_{bound\,k_H} = \frac{1}{\sqrt{\Delta x^2+\Delta z^2}}\left(\frac{y+\Delta y+\frac{b_w}{2}}{\sqrt{\Delta x^2+(y+\Delta y+\frac{b_w}{2})^2+\Delta z^2}} - \frac{y+\Delta y-\frac{b_w}{2}}{\sqrt{\Delta x^2+(y+\Delta y-\frac{b_w}{2})^2+\Delta z^2}}\right)\cdots \tag{A.1}$$

$$\left(\frac{-\Delta x}{\sqrt{\Delta x^2+\Delta z^2}}\right) \tag{A.2}$$

as

$$h = \sqrt{\Delta x^2+\Delta z^2}$$

$$\cos\delta_1 = -\frac{y+\Delta y+\frac{b_w}{2}}{\sqrt{\Delta x^2+(y+\Delta y+\frac{b_w}{2})^2+\Delta z^2}}\,,\quad \cos\delta_2 = -\frac{y+\Delta y-\frac{b_w}{2}}{\sqrt{\Delta x^2+(y+\Delta y-\frac{b_w}{2})^2+\Delta z^2}}$$

and $\cos\gamma = \dfrac{-\Delta x}{\sqrt{\Delta x^2+\Delta z^2}}$ i.e. determines the vertical component (Fig. A.2).

Subscript $bound\,k_H$ indicates the influence due to the bound portion of the vortex, *bound*, on the trailing aircraft, k, using the Helmholtz profile, H. Figure A.2 illustrates the effect of a vertical separation. Introducing the σ influence factor:

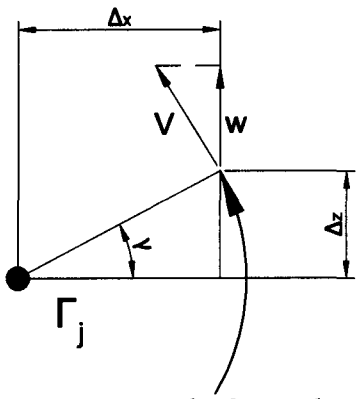

Figure A.2: Depiction of vertical component of velocity due to vortex with Δz separation

$$\sigma_{bound\,k_H} = \left(\frac{4\pi}{\Gamma_j}\right) \int_{-\frac{b_v}{2}}^{\frac{b_v}{2}} w_{bound\,k_H}\, dy$$

$$\sigma_{bound\,k_H} = \int_{-\frac{b_v}{2}}^{\frac{b_v}{2}} \frac{1}{\sqrt{\Delta x^2+\Delta z^2}} \left(\frac{y+\Delta y+\frac{b_v}{2}}{\sqrt{\Delta x^2+(y+\Delta y+\frac{b_v}{2})^2+\Delta z^2}} - \frac{y+\Delta y-\frac{b_v}{2}}{\sqrt{\Delta x^2+(y+\Delta y-\frac{b_v}{2})^2+\Delta z^2}} \right) \ldots$$
$$\left(\frac{-\Delta x}{\sqrt{\Delta x^2+\Delta z^2}}\right) dy$$

The terms are seperated and in the first term $y+\Delta y+\frac{b_v}{2} = p$ and $dp = dy$. In the second term, $y+\Delta y-\frac{b_v}{2} = r$ and $dr = dy$

$$\sigma_{bound\,k_H} = \int_{\Delta y}^{\Delta y+b_v} \frac{1}{\sqrt{\Delta x^2+\Delta z^2}} \left(\frac{p}{\sqrt{\Delta x^2+(p)^2+\Delta z^2}}\right)\left(\frac{-\Delta x}{\sqrt{\Delta x^2+\Delta z^2}}\right) dp \ldots$$
$$- \int_{\Delta y-b_v}^{\Delta y} \frac{1}{\sqrt{\Delta x^2+\Delta z^2}} \left(\frac{r}{\sqrt{\Delta x^2+(r)^2+\Delta z^2}}\right)\left(\frac{-\Delta x}{\sqrt{\Delta x^2+\Delta z^2}}\right) dr$$

Set $\Delta x^2+p^2+\Delta z^2 = m$ in the first term where $dm = 2p\,dp$ and set $\Delta x^2+r^2+\Delta z^2 = n$ in the second term where $dn = 2p\,dp$. We can also factor out constants:

$$\sigma_{bound\,k_H} = \frac{-\Delta x}{\Delta x^2+\Delta z^2} \int_{\Delta x^2+\Delta y^2+\Delta z^2}^{\Delta x^2+(\Delta y+b_v)^2+\Delta z^2} \left(\frac{1}{2\sqrt{m}}\right) dm \ldots$$
$$+ \frac{\Delta x}{\Delta x^2+\Delta z^2} \int_{\Delta x^2+(\Delta y-b_v)^2+\Delta z^2}^{\Delta x^2+\Delta y^2+\Delta z^2} \left(\frac{1}{2\sqrt{n}}\right) dm$$

The integral of $\frac{1}{2\sqrt{x}} = \sqrt{x}$ hence the equation becomes:

$$\sigma_{bound\,k_H} = \frac{-\Delta x}{\Delta x^2+\Delta z^2} \left(\sqrt{m}\right)_{\Delta x^2+\Delta y^2+\Delta z^2}^{\Delta x^2+(\Delta y+b_v)^2+\Delta z^2} + \frac{\Delta x}{\Delta x^2+\Delta z^2} \left(\sqrt{n}\right)_{\Delta x^2+(\Delta y-b_v)^2+\Delta z^2}^{\Delta x^2+\Delta y^2+\Delta z^2}$$

We therefore obtain:

$$\sigma_{bound\,k_H} = \frac{\Delta x}{\Delta x^2 + \Delta z^2}\left(2\sqrt{\Delta x^2 + \Delta y^2 + \Delta z^2} - \sqrt{\Delta x^2 + (\Delta y + b_v)^2 + \Delta z^2} - \sqrt{\Delta x^2 + (\Delta y - b_v)^2 + \Delta z^2}\right)$$

Setting $\Delta x = \xi b$, $\Delta y = \eta b$, $\Delta z = \zeta b$ and $b_v = \frac{\pi}{4} b$, the following is obtained:

$$\sigma_{bound\,k_H} = \frac{b\xi}{b^2(\xi^2 + \zeta^2)}\left(2b\sqrt{\xi^2 + \eta^2 + \zeta^2} - b\sqrt{\xi^2 + (\eta + \frac{\pi}{4})^2 + \zeta^2} - b\sqrt{\xi^2 + (\eta - \frac{\pi}{4})^2 + \zeta^2}\right)$$

Notice that the b's cancel and we're left with:

$$\sigma_{bound\,k_H} = \frac{\xi}{\xi^2 + \zeta^2}\left(2\sqrt{\xi^2 + \eta^2 + \zeta^2} - \sqrt{\xi^2 + (\eta + \frac{\pi}{4})^2 + \zeta^2} - \sqrt{\xi^2 + (\eta - \frac{\pi}{4})^2 + \zeta^2}\right)$$

A.1.2 Derivation of $\sigma_{near\,k_H}$

The downwash at a point on the trailing aircraft's bound vortex due to the near trailing vortex is (see Fig. A.1b):

$$\left(\frac{4\pi}{\Gamma_j}\right) w_{near\,k_H} = -\frac{1}{\sqrt{(y + \Delta y - \frac{b_v}{2})^2 + \Delta z^2}}\left(1 - \frac{\Delta x}{\sqrt{\Delta x^2 + (y + \Delta y - \frac{b_v}{2})^2 + \Delta z^2}}\right) \ldots \quad \text{(A.3)}$$

$$\left(\frac{y + \Delta y - \frac{b_v}{2}}{\sqrt{(y + \Delta y - \frac{b_v}{2})^2 + \Delta z^2}}\right) \quad \text{(A.4)}$$

as

$$h = \sqrt{(y + \Delta y - \frac{b_v}{2})^2 + \Delta z^2}$$

$$\cos\delta_1 = \frac{\Delta x}{\sqrt{\Delta x^2 + (y + \Delta y - \frac{b_v}{2})^2 + \Delta z^2}}, \quad \cos\delta_2 = 1$$

$$\text{and } \cos\gamma = \frac{y + \Delta y - \frac{b_v}{2}}{\sqrt{(y + \Delta y - \frac{b_v}{2})^2 + \Delta z^2}}$$

Introducing $\sigma_{near\,k_H}$:

$$\sigma_{near\,k_H} = \left(\frac{4\pi}{\Gamma_j}\right)\int_{-\frac{b_v}{2}}^{\frac{b_v}{2}} w_{near\,k_H}\, dy$$

$$\sigma_{near\,k_H} = -\int_{-\frac{b_v}{2}}^{\frac{b_v}{2}} \frac{y + \Delta y - \frac{b_v}{2}}{(y + \Delta y - \frac{b_v}{2})^2 + \Delta z^2}\left(1 - \frac{\Delta x}{\sqrt{\Delta x^2 + (y + \Delta y - \frac{b_v}{2})^2 + \Delta z^2}}\right) dy$$

Set $y + \Delta y - \frac{b_v}{2} = p$ where $dp = dy$ and seperate terms:

$$\sigma_{near\,k_H} = -\int_{\Delta y - b_v}^{\Delta y} \frac{p}{p^2 + \Delta z^2} + \int_{\Delta y - b_v}^{\Delta y} \frac{p}{p^2 + \Delta z^2}\left(\frac{\Delta x}{\sqrt{\Delta x^2 + p^2 + \Delta z^2}}\right) dp$$

The first term is integrated after setting $p^2 + \Delta z^2 = m$ where $dm = 2pdp$. This results in $\int \frac{1}{2}\frac{dm}{m}$ with limtis from $(\Delta y - b_v)^2 + \Delta z^2$ to $\Delta y^2 + \Delta z^2$. In the second term, set $\Delta x^2 + p^2 + \Delta z^2 = n$, then $dn = 2p\,dp$:

$$\sigma_{near\,k_H} = -\frac{1}{2}\ln\left|\frac{\Delta y^2 + \Delta z^2}{(\Delta y - b_v)^2 + \Delta z^2}\right| + \frac{\Delta x}{2}\int_{\Delta x^2+(\Delta y-b_v)^2+\Delta z^2}^{\Delta x^2+\Delta y^2+\Delta z^2} \frac{dn}{(n-\Delta x^2)\sqrt{n}}$$

Now set $r = \sqrt{n}$ and $dr = \frac{dn}{2\sqrt{n}}$:

$$\sigma_{near\,k_H} = -\frac{1}{2}\ln\left|\frac{\Delta y^2 + \Delta z^2}{(\Delta y - b_v)^2 + \Delta z^2}\right| + \frac{\Delta x}{2}\int_{\sqrt{\Delta x^2+(\Delta y-b_v)^2+\Delta z^2}}^{\sqrt{\Delta x^2+\Delta y^2+\Delta z^2}} \frac{dr}{(r^2-\Delta x^2)}$$

Using the table of integrals from [84], the second term is now easily integrated to yield:

$$\sigma_{near\,k_H} = -\frac{1}{2}\ln\left|\frac{\Delta y^2 + \Delta z^2}{(\Delta y - b_v)^2 + \Delta z^2}\right| + \frac{1}{2}\ln\left|\frac{\sqrt{\Delta x^2+\Delta y^2+\Delta z^2}-\Delta x}{\sqrt{\Delta x^2+\Delta y^2+\Delta z^2}+\Delta x}\right| \ldots$$
$$-\frac{1}{2}\ln\left|\frac{\sqrt{\Delta x^2+(\Delta y-b_v)^2+\Delta z^2}-\Delta x}{\sqrt{\Delta x^2+(\Delta y-b_v)^2+\Delta z^2}+\Delta x}\right|$$

Setting $\Delta x = \xi b$, $\Delta y = \eta b$, $\Delta z = \zeta b$ and $b_v = \frac{\pi}{4}b$, the dimensionless form is obtained:

$$\sigma_{near\,k_H} = -\frac{1}{2}\ln\left|\frac{\eta^2+\zeta^2}{(\eta-\frac{\pi}{4})^2+\zeta^2}\right| + \frac{1}{2}\ln\left|\frac{\sqrt{\xi^2+\eta^2+\zeta^2}-\xi}{\sqrt{\xi^2+\eta^2+\zeta^2}+\xi}\right| - \frac{1}{2}\ln\left|\frac{\sqrt{\xi^2+(\eta-\frac{\pi}{4})^2+\zeta^2}-\xi}{\sqrt{\xi^2+(\eta-\frac{\pi}{4})^2+\zeta^2}+\xi}\right| \tag{A.5}$$

A.1.3 Derivation of $\sigma_{far\,k_H}$

The downwash at a point on the trailing aircraft's bound vortex due to the far trailing vortex follows the same derivation as per the near trailing vortex:

$$\left(\frac{4\pi}{\Gamma_j}\right) w_{far\,k_H} = \frac{1}{\sqrt{(y+\Delta y+\frac{b_v}{2})^2+\Delta z^2}}\left(1 - \frac{\Delta x}{\sqrt{\Delta x^2+(y+\Delta y+\frac{b_v}{2})^2+\Delta z^2}}\right)\ldots \tag{A.6}$$

$$\left(\frac{y+\Delta y+\frac{b_v}{2}}{\sqrt{(y+\Delta y+\frac{b_v}{2})^2+\Delta z^2}}\right) \tag{A.7}$$

as

$$h = \sqrt{(y+\Delta y+\frac{b_v}{2})^2+\Delta z^2}$$
$$\cos\delta_1 = -1 \;\; \cos\delta_2 = -\frac{\Delta x}{\sqrt{\Delta x^2+(y+\Delta y+\frac{b_v}{2})^2+\Delta z^2}}$$
$$\text{and } \cos\gamma = \frac{y+\Delta y+\frac{b_v}{2}}{\sqrt{(y+\Delta y+\frac{b_v}{2})^2+\Delta z^2}}$$

Introducing $\sigma_{far\,k_H}$:

$$\sigma_{far\,k_H} = \int_{-\frac{b_v}{2}}^{\frac{b_v}{2}} \frac{y+\Delta y+\frac{b_v}{2}}{(y+\Delta y+\frac{b_v}{2})^2+\Delta z^2}\left(1 - \frac{\Delta x}{\sqrt{\Delta x^2+(y+\Delta y+\frac{b_v}{2})^2+\Delta z^2}}\right) dy$$

Setting $y + \Delta y + \frac{b_v}{2} = p$, we get:

$$\sigma_{far\,k_H} = \int_{\Delta y}^{\Delta y + b_v} \frac{p}{p^2 + \Delta z^2} - \int_{\Delta y}^{\Delta y + b_v} \frac{p}{p^2 + \Delta z^2} \left(\frac{\Delta x}{\sqrt{\Delta x^2 + p^2 + \Delta z^2}} \right) dp$$

The derivation follows that of $\sigma_{near\,k_H}$ where $r = \sqrt{\Delta x^2 + p^2 + \Delta z^2}$:

$$\sigma_{far\,k_H} = \frac{1}{2} \ln \left| \frac{(\Delta y + b_v)^2 + \Delta z^2}{\Delta y^2 + \Delta z^2} \right| - \frac{\Delta x}{2} \int_{\sqrt{\Delta x^2 + \Delta y^2 + \Delta z^2}}^{\sqrt{\Delta x^2 + (\Delta y + b_v)^2 + \Delta z^2}} \frac{dr}{(r^2 - \Delta x^2)}$$

The dimensionless form is thus:

$$\sigma_{far\,k_H} = \frac{1}{2} \ln \left| \frac{(\eta + \frac{\pi}{4})^2 + \zeta^2}{\eta^2 + \zeta^2} \right| - \frac{1}{2} \ln \left| \frac{\sqrt{\xi^2 + (\eta + \frac{\pi}{4})^2 + \zeta^2} - \xi}{\sqrt{\xi^2 + (\eta + \frac{\pi}{4})^2 + \zeta^2} + \xi} \right| + \frac{1}{2} \ln \left| \frac{\sqrt{\xi^2 + \eta^2 + \zeta^2} - \xi}{\sqrt{\xi^2 + \eta^2 + \zeta^2} + \xi} \right| \quad \text{(A.8)}$$

The influence factor representing the effect of the full lead aircraft wing horseshoe vortex is the sum of the influence factors (A.3), (A.5) and (A.8):

$$\sigma_{jk\,full_H} = (\sigma_{bound\,k_H} + \sigma_{near\,k_H} + \sigma_{far\,k_H}) \quad \text{(A.9)}$$

$\sigma_{jk\,full_H}$ represents the effects due to the full lead horseshoe vortex as a function of the separation alone. The following section reveals how this equation can be simplified while maintaining a very close approximation.

A.1.4 Simplification

A.2 Derivation of $\sigma_{jk\,approx_H}$

In an effort to simplify the equations, the influence of the lead aircraft bound vortex is removed and only the influence of the trailing vortices are considered. In equations (A.2) to (A.7), let $\Delta x \to \infty$ and sum all the equations:

$$\left(\frac{4\pi}{\Gamma_j}\right) w_{jk\,approx_H} = - \frac{1}{\sqrt{(y + \Delta y - \frac{b_v}{2})^2 + \Delta z^2}} (1 + 1) \left(\frac{y + \Delta y - \frac{b_v}{2}}{\sqrt{(y + \Delta y - \frac{b_v}{2})^2 + \Delta z^2}} \right) \ldots \quad \text{(A.10)}$$

$$+ \frac{1}{\sqrt{(y + \Delta y + \frac{b_v}{2})^2 + \Delta z^2}} (1 + 1) \left(\frac{y + \Delta y + \frac{b_v}{2}}{\sqrt{(y + \Delta y + \frac{b_v}{2})^2 + \Delta z^2}} \right) \quad \text{(A.11)}$$

Simplifying:

$$\left(\frac{4\pi}{\Gamma_j}\right) w_{jk\,approx_H} = - \frac{2\,(y + \Delta y - \frac{b_v}{2})}{(y + \Delta y - \frac{b_v}{2})^2 + \Delta z^2} + \frac{2\,(y + \Delta y + \frac{b_v}{2})}{(y + \Delta y + \frac{b_v}{2})^2 + \Delta z^2} \quad \text{(A.12)}$$

Introducing $\sigma_{jk\,approx_H}$:

$$\sigma_{jk\,approx_H} = - \left(\frac{4\pi}{\Gamma_j}\right) \int_{-\frac{b_v}{2}}^{\frac{b_v}{2}} w_{jk\,approx_H}\, dy$$

Set $y + \Delta y - \frac{b_v}{2} = p$ and $y + \Delta y + \frac{b_v}{2} = r$, separate terms and take out constants:

$$\sigma_{jk\,approx_H} = -2\int_{\Delta y - b_v}^{\Delta y} \frac{p}{p^2 + \Delta z^2}\,dp + 2\int_{\Delta y}^{\Delta y + b_v} \frac{r}{r^2 + \Delta z^2}\,dr$$

Set $p^2 + \Delta z^2 = m$ where $dm = 2dp$ and $r^2 + \Delta z^2 = n$ where $dn = 2dr$:

$$\sigma_{jk\,approx_H} = -\int_{(\Delta y - b_v)^2 + \Delta z^2}^{\Delta y^2 + \Delta z^2} \frac{dm}{m} + \int_{\Delta y^2 + \Delta z^2}^{(\Delta y + b_v)^2 + \Delta z^2} \frac{dn}{n}$$

$$\sigma_{jk\,approx_H} = -\ln\left|\frac{\Delta y^2 + \Delta z^2}{(\Delta y - b_v)^2 + \Delta z^2}\right| + \ln\left|\frac{(\Delta y + b_v)^2 + \Delta z^2}{\Delta y^2 + \Delta z^2}\right|$$

$$\sigma_{jk\,approx_H} = \ln\left|\frac{\left((\Delta y - b_v)^2 + \Delta z^2\right)\left((\Delta y + b_v)^2 + \Delta z^2\right)}{\left(\Delta y^2 + \Delta z^2\right)^2}\right|$$

Convert to dimensionless units:

$$\sigma_{jk\,approx_H} = \ln\left|\frac{\left((\eta - \frac{\pi}{4})^2 + \zeta^2\right)\left((\eta + \frac{\pi}{4})^2 + \zeta^2\right)}{\left(\eta^2 + \zeta^2\right)^2}\right| \tag{A.13}$$

which is far simpler than equation (A.9). Comparison of equations (A.9) and (A.13) reveals that the difference between them is negligible for ξ greater than 1 (see Fig. A.3). The current study is interested in longitudinal separation of 10 to 40 spans. Therefore $\sigma_{jk\,full_H}$ can be approximated by $\sigma_{jk\,approx_H}$.

A.3 Derivation of $\sigma_{jk\,approx_B}$

Introducing a viscous core, r_c, into equation (A.12) using the Burnham Hallock profile yields:

$$\left(\frac{4\pi}{\Gamma_j}\right) w_{jk\,approx_B} = -\frac{y + \Delta y - \frac{b_v}{2}}{(y + \Delta y - \frac{b_v}{2})^2 + \Delta z^2 + r_c^2}(2) + \frac{y + \Delta y + \frac{b_v}{2}}{(y + \Delta y + \frac{b_v}{2})^2 + \Delta z^2 + r_c^2}(2) \tag{A.14}$$

where subscript $jk\,approx_B$ indicates the influence of the lead aircraft horseshoe vortex, j, on the trailing aircraft wing, k, using the effect of the trailing vortices only, i.e. approximate method, *approx*, and the Burnham Hallock profile, B.

$$\sigma_{jk\,approx_B} = -\left(\frac{4\pi}{\Gamma_j}\right)\int_{-\frac{b_v}{2}}^{\frac{b_v}{2}} w_{jk\,approx_B}\,dy$$

$$\sigma_{jk\,approx_B} = -2\int_{-\frac{b_v}{2}}^{\frac{b_v}{2}} \frac{y + \Delta y - \frac{b_v}{2}}{(y + \Delta y - \frac{b_v}{2})^2 + \Delta z^2 + r_c^2}\,dy + 2\int_{-\frac{b_v}{2}}^{\frac{b_v}{2}} \frac{y + \Delta y + \frac{b_v}{2}}{(y + \Delta y + \frac{b_v}{2})^2 + \Delta z^2 + r_c^2}\,dy$$

The method of integration is identical to that of $\sigma_{jk\,approx_H}$ where the extra term r_c^2 is consumed through the substitutions $(y + \Delta y - \frac{b_v}{2})^2 + \Delta z^2 + r_c^2 = m$ and $(y + \Delta y + \frac{b_v}{2})^2 + \Delta z^2 + r_c^2 = n$ so we get:

$$\sigma_{jk\,approx_B} = -\int_{(\Delta y - b_v)^2 + \Delta z^2 + r_c^2}^{\Delta y^2 + \Delta z^2 + r_c^2} \frac{dm}{m} + \int_{\Delta y^2 + \Delta z^2 + r_c^2}^{(\Delta y + b_v)^2 + \Delta z^2 + r_c^2} \frac{dn}{n}$$

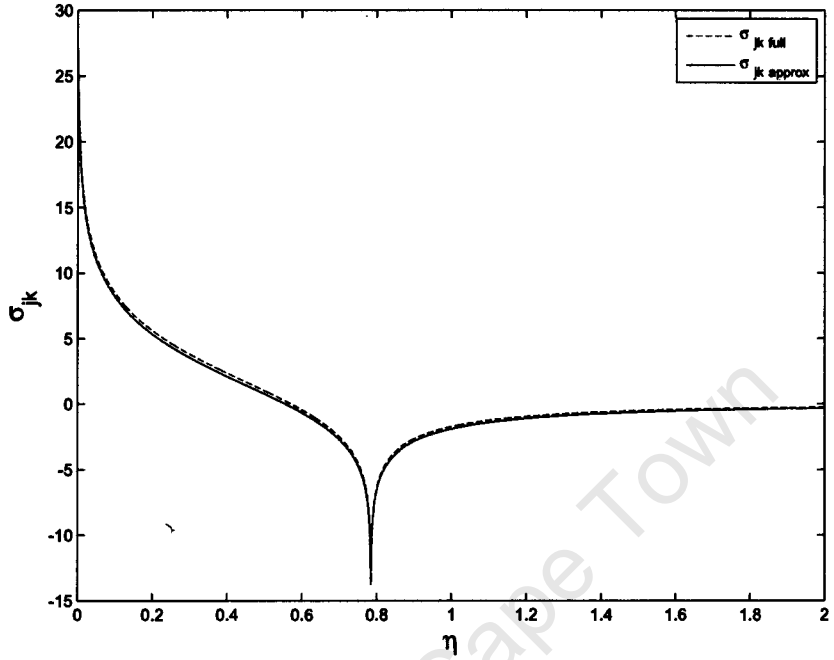

Figure A.3: Comparison of the 'full' and 'approximate' methods to solve σ_{jk} where $\xi = -1$ and $\zeta = 0$

The dimensionless unit of r_c is given as $\mu = \frac{r_c}{b}$, the equation therefore becomes:

$$\sigma_{jk\,approx_B} = \ln \left| \frac{\left((\eta - \frac{\pi}{4})^2 + \zeta^2 + \mu^2\right)\left((\eta + \frac{\pi}{4})^2 + \zeta^2 + \mu^2\right)}{\left(\eta^2 + \zeta^2 + \mu^2\right)^2} \right|$$

The current study applies the approximate method and Burnham Hallock profile to all influence factors, hence, aside from the derivation shown above, subscript jk infers the use of the approximate method and Burnham Hallock profile.

A.4 Derivation of $\sigma_{jk\,wh}$

The downwash on the wing is given in equation (A.14).

$$\left(\frac{4\pi}{\Gamma_j}\right) w_{jk\,wh} = -\frac{2\left(y + \Delta y - \frac{b_v}{2}\right)}{(y + \Delta y - \frac{b_v}{2})^2 + \Delta z^2 + r_c^2} + \frac{2\left(y + \Delta y + \frac{b_v}{2}\right)}{(y + \Delta y + \frac{b_v}{2})^2 + \Delta z^2 + r_c^2}$$

The integration however, extends along a portion of the wing of which the span is equal to the span of the tailfin bound vortex, $-b_{h_v}$ to b_{h_v}.

$$\sigma_{jk\,wh} = -2\int_{-\frac{b_{h_v}}{2}}^{\frac{b_{h_v}}{2}} \frac{y + \Delta y - \frac{b_v}{2}}{(y + \Delta y - \frac{b_v}{2})^2 + \Delta z^2 + r_c^2} + 2\int_{-\frac{b_{h_v}}{2}}^{\frac{b_{h_v}}{2}} \frac{y + \Delta y + \frac{b_v}{2}}{(y + \Delta y + \frac{b_v}{2})^2 + \Delta z^2 + r_c^2}\, dy$$

Using the substitutions, $(y+\Delta y-\frac{b_v}{2})^2+\Delta z^2+r_c^2=m$ and $(y+\Delta y+\frac{b_v}{2})^2+\Delta z^2+r_c^2=n$, we get:

$$\sigma_{jk\,wh}=-\int_{(\Delta y-\frac{b_v}{2}-\frac{b_{h_v}}{2})^2+\Delta z^2+r_c^2}^{(\Delta y-\frac{b_v}{2}+\frac{b_{h_v}}{2})^2+\Delta z^2+r_c^2}\frac{dm}{m}+\int_{(\Delta y+\frac{b_v}{2}-\frac{b_{h_v}}{2})^2+\Delta z^2+r_c^2}^{(\Delta y+\frac{b_v}{2}+\frac{b_{h_v}}{2})^2+\Delta z^2+r_c^2}\frac{dn}{n}$$

Resolving and converting to dimensionless units:

$$\sigma_{jk\,wh}=\ln\left|\frac{\left(\zeta^2+\left(\eta-\frac{\pi}{8}-\frac{\pi}{8}\eta_h\right)^2+\mu^2\right)\left(\zeta^2+\left(\eta+\frac{\pi}{8}+\frac{\pi}{8}\eta_h\right)^2+\mu^2\right)}{\left(\zeta^2+\left(\eta-\frac{\pi}{8}+\frac{\pi}{8}\eta_h\right)^2+\mu^2\right)\left(\zeta^2+\left(\eta+\frac{\pi}{8}-\frac{\pi}{8}\eta_h\right)^2+\mu^2\right)}\right| \tag{A.15}$$

A.5 Derivation of τ_{jk}

The distribution of downwash along the wing is obtained by multiplying the downwash by the moment arm from the c.g.:

$$\left(\frac{4\pi}{\Gamma_j}\right)w_{jk}y=-\frac{2y\left(y+\Delta y-\frac{b_v}{2}\right)}{(y+\Delta y-\frac{b_v}{2})^2+\Delta z^2+r_c^2}+\frac{2y\left(y+\Delta y+\frac{b_v}{2}\right)}{(y+\Delta y+\frac{b_v}{2})^2+\Delta z^2+r_c^2} \tag{A.16}$$

Introducing τ_{jk}:

$$\tau_{jk_{ab}}\equiv\frac{4\pi}{\Gamma_j b}\int_{-\frac{b_v}{2}}^{\frac{b_v}{2}}w_{jk}y\,dy$$

$$\tau_{jk}=-\frac{2}{b}\int_{-\frac{b_v}{2}}^{\frac{b_v}{2}}\frac{y\left(y+\Delta y-\frac{b_v}{2}\right)}{(y+\Delta y-\frac{b_v}{2})^2+\Delta z^2+r_c^2}dy+\frac{2}{b}\int_{-\frac{b_v}{2}}^{\frac{b_v}{2}}\frac{y\left(y+\Delta y+\frac{b_v}{2}\right)}{(y+\Delta y+\frac{b_v}{2})^2+\Delta z^2+r_c^2}dy$$

Set $y+\Delta y-\frac{b_v}{2}=p$ and $y+\Delta y+\frac{b_v}{2}=r$:

$$\tau_{jk}=-\frac{2}{b}\int_{\Delta y-b_v}^{\Delta y}\frac{\left(p-\Delta y+\frac{b_v}{2}\right)p}{p^2+\Delta z^2+r_c^2}dp+\frac{2}{b}\int_{\Delta y}^{\Delta y+b_v}\frac{\left(r-\Delta y-\frac{b_v}{2}\right)r}{r^2+\Delta z^2+r_c^2}dr$$

Separate terms:

$$\begin{aligned}\tau_{jk}=&-\frac{2}{b}\int_{\Delta y-b_v}^{\Delta y}\frac{p^2}{p^2+\Delta z^2+r_c^2}dp+\frac{2}{b}\int_{\Delta y-b_v}^{\Delta y}\frac{p\left(\Delta y-\frac{b_v}{2}\right)}{p^2+\Delta z^2+r_c^2}dp\ldots\\&+\frac{2}{b}\int_{\Delta y}^{\Delta y+b_v}\frac{r^2}{r^2+\Delta z^2+r_c^2}dr-\frac{2}{b}\int_{\Delta y}^{\Delta y+b_v}\frac{r\left(\Delta y+\frac{b_v}{2}\right)}{r^2+\Delta z^2+r_c^2}dr\end{aligned}$$

Focusing on the first term alone, the integrand can be rewritten as follows:

$$\begin{aligned}\frac{p^2}{p^2+\Delta z^2+r_c^2}=&\frac{p^2+\Delta z^2+r_c^2}{p^2+\Delta z^2+r_c^2}-\frac{\Delta z^2+r_c^2}{p^2+\Delta z^2+r_c^2}\\=&1-\frac{\Delta z^2+r_c^2}{p^2+\Delta z^2+r_c^2}\end{aligned}$$

The third term can also be written in the form above and we therefore have:

$$\begin{aligned}\tau_{jk}=&-\frac{2}{b}\int_{\Delta y-b_v}^{\Delta y}dp+\frac{2}{b}\int_{\Delta y-b_v}^{\Delta y}\frac{\Delta z^2+r_c^2}{p^2+\Delta z^2+r_c^2}dp+\frac{2}{b}\int_{\Delta y-b_v}^{\Delta y}\frac{p\left(\Delta y-\frac{b_v}{2}\right)}{p^2+\Delta z^2+r_c^2}dp\ldots\\&+\frac{2}{b}\int_{\Delta y}^{\Delta y+b_v}dr-\frac{2}{b}\int_{\Delta y}^{\Delta y+b_v}\frac{\Delta z^2+r_c^2}{r^2+\Delta z^2+r_c^2}dr-\frac{2}{b}\int_{\Delta y}^{\Delta y+b_v}\frac{r\left(\Delta y+\frac{b_v}{2}\right)}{r^2+\Delta z^2+r_c^2}dr\end{aligned}$$

Resolving the first and fourth terms along with the the second and fifth terms using the table of integrals from [84]:

$$\begin{aligned}\tau_{jk} = &-\frac{2}{b}\left(\Delta y - \Delta y + b_v\right) + \frac{2}{b}\frac{\Delta z^2 + r_c^2}{\sqrt{\Delta z^2 + r_c^2}}\left(\tan^{-1}\left(\frac{\Delta y}{\sqrt{\Delta z^2 + r_c^2}}\right) - \tan^{-1}\left(\frac{\Delta y - b_v}{\sqrt{\Delta z^2 + r_c^2}}\right)\right)\ldots \\ &+ \frac{2}{b}\int_{\Delta y - b_v}^{\Delta y}\frac{p\left(\Delta y - \frac{b_v}{2}\right)}{p^2 + \Delta z^2 + r_c^2}dp\ldots \\ &+ \frac{2}{b}\left(\Delta y + b_v - \Delta y\right) - \frac{2}{b}\frac{\Delta z^2 + r_c^2}{\sqrt{\Delta z^2 + r_c^2}}\left(\tan^{-1}\left(\frac{\Delta y + b_v}{\sqrt{\Delta z^2 + r_c^2}}\right) - \tan^{-1}\left(\frac{\Delta y}{\sqrt{\Delta z^2 + r_c^2}}\right)\right)\ldots \\ &- \frac{2}{b}\int_{\Delta y}^{\Delta y + b_v}\frac{r\left(\Delta y + \frac{b_v}{2}\right)}{r^2 + \Delta z^2 + r_c^2}dr\end{aligned}$$

Simplifying:

$$\begin{aligned}\tau_{jk} = &-2\frac{b_v}{b} + \frac{2}{b}\sqrt{\Delta z^2 + r_c^2}\left(\tan^{-1}\left(\frac{\Delta y}{\sqrt{\Delta z^2 + r_c^2}}\right) - \tan^{-1}\left(\frac{\Delta y - b_v}{\sqrt{\Delta z^2 + r_c^2}}\right)\right)\ldots \\ &+ \frac{2}{b}\int_{\Delta y - b_v}^{\Delta y}\frac{p\left(\Delta y - \frac{b_v}{2}\right)}{p^2 + \Delta z^2 + r_c^2}dp\ldots \\ &+ 2\frac{b_v}{b} - \frac{2}{b}\sqrt{\Delta z^2 + r_c^2}\left(\tan^{-1}\left(\frac{\Delta y + b_v}{\sqrt{\Delta z^2 + r_c^2}}\right) - \tan^{-1}\left(\frac{\Delta y}{\sqrt{\Delta z^2 + r_c^2}}\right)\right)\ldots \\ &- \frac{2}{b}\int_{\Delta y}^{\Delta y + b_v}\frac{r\left(\Delta y + \frac{b_v}{2}\right)}{r^2 + \Delta z^2 + r_c^2}dr\end{aligned}$$

Simplifying further:

$$\begin{aligned}\tau_{jk} = &-\frac{2}{b}\sqrt{\Delta z^2 + r_c^2}\left(\tan^{-1}\left(\frac{\Delta y - b_v}{\sqrt{\Delta z^2 + r_c^2}}\right) + \tan^{-1}\left(\frac{\Delta y + b_v}{\sqrt{\Delta z^2 + r_c^2}}\right) - 2\tan^{-1}\left(\frac{\Delta y}{\sqrt{\Delta z^2 + r_c^2}}\right)\right)\ldots \\ &+ \frac{2}{b}\int_{\Delta y - b_v}^{\Delta y}\frac{p\left(\Delta y - \frac{b_v}{2}\right)}{p^2 + \Delta z^2 + r_c^2}dp - \frac{2}{b}\int_{\Delta y}^{\Delta y + b_v}\frac{r\left(\Delta y + \frac{b_v}{2}\right)}{r^2 + \Delta z^2 + r_c^2}dr\end{aligned}$$

Set $p^2 + \Delta z^2 + r_c^2 = m$ and $r^2 + \Delta z^2 + r_c^2 = n$:

$$\begin{aligned}\tau_{jk} = &-\frac{2}{b}\sqrt{\Delta z^2 + r_c^2}\left(\tan^{-1}\left(\frac{\Delta y - b_v}{\sqrt{\Delta z^2 + r_c^2}}\right) + \tan^{-1}\left(\frac{\Delta y + b_v}{\sqrt{\Delta z^2 + r_c^2}}\right) - 2\tan^{-1}\left(\frac{\Delta y}{\sqrt{\Delta z^2 + r_c^2}}\right)\right)\ldots \\ &+ \frac{1}{b}\left(\Delta y - \frac{b_v}{2}\right)\int_{(\Delta y - b_v)^2 + \Delta z^2 + r_c^2}^{\Delta y^2 + \Delta z^2 + r_c^2}\frac{dm}{m} - \frac{1}{b}\left(\Delta y + \frac{b_v}{2}\right)\int_{\Delta y^2 + \Delta z^2 + r_c^2}^{(\Delta y + b_v)^2 + \Delta z^2 + r_c^2}\frac{dn}{n}\end{aligned}$$

$$\begin{aligned}\tau_{jk} = &-\frac{2}{b}\sqrt{\Delta z^2 + r_c^2}\left(\tan^{-1}\left(\frac{\Delta y - b_v}{\sqrt{\Delta z^2 + r_c^2}}\right) + \tan^{-1}\left(\frac{\Delta y + b_v}{\sqrt{\Delta z^2 + r_c^2}}\right) - 2\tan^{-1}\left(\frac{\Delta y}{\sqrt{\Delta z^2 + r_c^2}}\right)\right)\ldots \\ &+ \frac{1}{b}\left(\Delta y - \frac{b_v}{2}\right)\ln\left|\frac{\Delta y^2 + \Delta z^2 + r_c^2}{(\Delta y - b_v)^2 + \Delta z^2 + r_c^2}\right| - \frac{1}{b}\left(\Delta y + \frac{b_v}{2}\right)\ln\left|\frac{(\Delta y + b_v)^2 + \Delta z^2 + r_c^2}{\Delta y^2 + \Delta z^2 + r_c^2}\right|\end{aligned}$$

Simplify and convert to dimensionless units:

$$\begin{aligned}\tau_{jk} = &-2\sqrt{\zeta^2 + \mu^2}\left(\tan^{-1}\left(\frac{\eta - \frac{\pi}{4}}{\sqrt{\zeta^2 + \mu^2}}\right) + \tan^{-1}\left(\frac{\eta + \frac{\pi}{4}}{\sqrt{\zeta^2 + \mu^2}}\right) - 2\tan^{-1}\left(\frac{\eta}{\sqrt{\zeta^2 + \mu^2}}\right)\right)\ldots \\ &- \eta\ln\left|\frac{\left((\eta - \frac{\pi}{4})^2 + \zeta^2 + \mu^2\right)\left((\eta + \frac{\pi}{4})^2 + \zeta^2 + \mu^2\right)}{\left(\eta^2 + \zeta^2 + \mu^2\right)^2}\right| - \frac{\pi}{8}\ln\left|\frac{(\eta + \frac{\pi}{4})^2 + \zeta^2 + \mu^2}{(\eta - \frac{\pi}{4})^2 + \zeta^2 + \mu^2}\right|\end{aligned}$$

A.6 Derivation of σ_{jk_f}

The sidewash at the tailfin due to the near and far trailing vortices is:

$$\left(\frac{4\pi}{\Gamma_j}\right) v_{near\,k_f} = \frac{\sqrt{(\Delta y - \frac{b_v}{2})^2 + (\Delta z + z_v + z)^2}}{(\Delta y - \frac{b_v}{2})^2 + (\Delta z + z_v + z)^2 + r_c^2} \left(1 + \frac{\Delta x}{\sqrt{\Delta x^2 + (\Delta y - \frac{b_v}{2})^2 + (\Delta z + z_v + z)^2 + r_c^2}}\right) \ldots$$
$$\left(\frac{\Delta z + z_v + z}{\sqrt{(\Delta y - \frac{b_v}{2})^2 + (\Delta z + z_v + z)^2}}\right)$$

$$\left(\frac{4\pi}{\Gamma_j}\right) v_{far\,k_f} = \frac{-\sqrt{(\Delta y + \frac{b_v}{2})^2 + (\Delta z + z_v + z)^2}}{(\Delta y + \frac{b_v}{2})^2 + (\Delta z + z_v + z)^2 + r_c^2} \left(\frac{\Delta x}{\sqrt{\Delta x^2 + (\Delta y + \frac{b_v}{2})^2 + (\Delta z + z_v + z)^2 + r_c^2}} + 1\right) \ldots$$
$$\left(\frac{\Delta z + z_v + z}{\sqrt{(\Delta y + \frac{b_v}{2})^2 + (\Delta z + z_v + z)^2}}\right)$$

Let $\Delta x \to \infty$ and the sum of $\left(\frac{4\pi}{\Gamma_j}\right) v_{near\,k_f} + \left(\frac{4\pi}{\Gamma_j}\right) v_{far\,k_f}$ becomes:

$$\left(\frac{4\pi}{\Gamma_j}\right) v_{jk_f} = \frac{2(\Delta z + z_v + z)}{(\Delta y - \frac{b_v}{2})^2 + (\Delta z + z_v + z)^2 + r_c^2} - \frac{2(\Delta z + z_v + z)}{(\Delta y + \frac{b_v}{2})^2 + (\Delta z + z_v + z)^2 + r_c^2}$$

Where z_v is the vertical distance from the plane of the wing to the bottom of the tailfin. Introducing σ_{jk_f}:

$$\sigma_{jk_f} \equiv \frac{4\pi}{\Gamma_j} \int_{-\frac{b_{f_v}}{2}}^{0} v_{jk_f}\, dz$$

$$\sigma_{jk_f} = \int_{-\frac{b_{f_v}}{2}}^{0} \frac{2(\Delta z + z_v + z)}{(\Delta y - \frac{b_v}{2})^2 + (\Delta z + z_v + z)^2 + r_c^2} - \frac{2(\Delta z + z_v + z)}{(\Delta y + \frac{b_v}{2})^2 + (\Delta z + z_v + z)^2 + r_c^2}\, dz$$

Set $(\Delta y - \frac{b_v}{2})^2 + (\Delta z + z_f + z)^2 + r_c^2 = p$, set $(\Delta y + \frac{b_v}{2})^2 + (\Delta z + z_f + z)^2 + r_c^2 = r$ and separate terms:

$$\sigma_{jk_f} = \int_{(\Delta y - \frac{b_v}{2})^2 + (\Delta z + z_v - \frac{b_{f_v}}{2})^2 + r_c^2}^{(\Delta y - \frac{b_v}{2})^2 + (\Delta z + z_v)^2 + r_c^2} \frac{dp}{p} - \int_{(\Delta y - \frac{b_v}{2})^2 + (\Delta z + z_v - \frac{b_{f_v}}{2})^2 + r_c^2}^{(\Delta y + \frac{b_v}{2})^2 + (\Delta z + z_v)^2 + r_c^2} \frac{dr}{r}$$

Hence the equation becomes:

$$\sigma_{jk_f} = \ln\left|\frac{(\Delta y - \frac{b_v}{2})^2 + (\Delta z + z_v)^2 + r_c^2}{(\Delta y - \frac{b_v}{2})^2 + (\Delta z + z_v - \frac{b_{f_v}}{2})^2 + r_c^2}\right| - \ln\left|\frac{(\Delta y + \frac{b_v}{2})^2 + (\Delta z + z_v)^2 + r_c^2}{(\Delta y + \frac{b_v}{2})^2 + (\Delta z + z_v - \frac{b_{f_v}}{2})^2 + r_c^2}\right|$$

Converting to dimensionless units:

$$\sigma_{jk_f} = \ln\left|\frac{(\eta - \frac{\pi}{8})^2 + (\zeta + \zeta_v)^2 + \mu^2}{(\eta - \frac{\pi}{8})^2 + (\zeta + \zeta_v - \frac{\pi}{8}\zeta_f)^2 + \mu^2}\right| - \ln\left|\frac{(\eta + \frac{\pi}{8})^2 + (\zeta + \zeta_v)^2 + \mu^2}{(\eta + \frac{\pi}{8})^2 + (\zeta + \zeta_v - \frac{\pi}{8}\zeta_f)^2 + \mu^2}\right|$$

Where $\zeta_v = \frac{z_v}{b}$ and $\zeta_f = \frac{b_f}{b}$ since $b_{f_v} = \frac{\pi}{4} b_f$.

A.6.1 Derivation of τ_{jk_f}

The distribution of sidewash along the tailfin is obtained by multiplying the sidewash by the moment arm from the c.g.:

$$\left(\frac{4\pi}{\Gamma_j}\right) v_{jk_f}(z_v+z) = \frac{2(z_v+z)(\Delta z+z_v+z)}{(\Delta y-\frac{b_v}{2})^2+(\Delta z+z_v+z)^2+r_c^2} - \frac{2(z_v+z)(\Delta z+z_v+z)}{(\Delta y+\frac{b_v}{2})^2+(\Delta z+z_v+z)^2+r_c^2}$$

Introducing τ_{jk_f}:

$$\tau_{jk_f} \equiv \frac{4\pi}{\Gamma_j b}\int_{\frac{-b_{f_v}}{2}}^{0} v_{jk} z\, dz$$

Set $\Delta z + z_v + z = p$:

$$\tau_{jk_f} = \frac{1}{b}\int_{\Delta z+z_v-\frac{b_{f_v}}{2}}^{\Delta z+z_v} \frac{2(p-\Delta z)p}{(\Delta y-\frac{b_v}{2})^2+p^2+r_c^2} - \frac{2(p-\Delta z)p}{(\Delta y+\frac{b_v}{2})^2+p^2+r_c^2}\, dp$$

Rearranging the equation:

$$\begin{aligned}\tau_{jk_f} =& \frac{2}{b}\int_{\Delta z+z_v-\frac{b_{f_v}}{2}}^{\Delta z+z_v} dp - \frac{2}{b}\int_{\Delta z+z_v-\frac{b_{f_v}}{2}}^{\Delta z+z_v} \frac{\Delta z^2+z_v^2}{(\Delta y-\frac{b_v}{2})^2+p^2+r_c^2} - \frac{2}{b}\int_{\Delta z+z_v-\frac{b_{f_v}}{2}}^{\Delta z+z_v} \frac{p(\Delta z)}{(\Delta y-\frac{b_v}{2})^2+p^2+r_c^2}\cdots \\ & - \frac{2}{b}\int_{\Delta z+z_v-\frac{b_{f_v}}{2}}^{\Delta z+z_v} dp + \frac{2}{b}\int_{\Delta z+z_v-\frac{b_{f_v}}{2}}^{\Delta z+z_v} \frac{\Delta z^2+z_v^2}{(\Delta y+\frac{b_v}{2})^2+p^2+r_c^2} + \frac{2}{b}\int_{\Delta z+z_v-\frac{b_{f_v}}{2}}^{\Delta z+z_v} \frac{p(\Delta z)}{(\Delta y+\frac{b_v}{2})^2+p^2+r_c^2}\end{aligned}$$

Resolving the integrals:

$$\begin{aligned}\tau_{jk_f} =& -\frac{b_{f_v}}{b} - \frac{2}{b}\sqrt{(\Delta y-\frac{b_v}{2})^2+r_c^2}\left(\tan^{-1}\left(\frac{\Delta z+z_v-\frac{b_{f_v}}{2}}{\sqrt{(\Delta y-\frac{b_v}{2})^2+r_c^2}}\right)-\tan^{-1}\left(\frac{\Delta z+z_v}{\sqrt{(\Delta y-\frac{b_v}{2})^2+r_c^2}}\right)\right)\cdots \\ & - \frac{\Delta z}{b}\ln\left|\frac{(\Delta y-\frac{b_v}{2})^2+(\Delta z+z_v-\frac{b_{f_v}}{2})^2+r_c^2}{(\Delta y-\frac{b_v}{2})^2+(\Delta z+z_v)^2+r_c^2}\right|\cdots \\ & + \frac{b_{f_v}}{b} + \frac{2}{b}\sqrt{(\Delta y+\frac{b_v}{2})^2+r_c^2}\left(\tan^{-1}\left(\frac{\Delta z+z_v-\frac{b_{f_v}}{2}}{\sqrt{(\Delta y+\frac{b_v}{2})^2+r_c^2}}\right)-\tan^{-1}\left(\frac{\Delta z+z_v}{\sqrt{(\Delta y+\frac{b_v}{2})^2+r_c^2}}\right)\right)\cdots \\ & + \frac{\Delta z}{b}\ln\left|\frac{(\Delta y+\frac{b_v}{2})^2+(\Delta z+z_v-\frac{b_{f_v}}{2})^2+r_c^2}{(\Delta y+\frac{b_v}{2})^2+(\Delta z+z_v)^2+r_c^2}\right|\end{aligned}$$

Simplifying and converting to dimensionless units:

$$\begin{aligned}\tau_{jk_f} =& -2\sqrt{(\eta-\frac{\pi}{8})^2+\mu^2}\left(\tan^{-1}\left(\frac{\zeta+\zeta_v-\frac{\pi}{8}\zeta_f}{\sqrt{(\eta-\frac{\pi}{8})^2+\mu^2}}\right)-\tan^{-1}\left(\frac{\zeta+\zeta_v}{\sqrt{(\eta-\frac{\pi}{8})^2+\mu^2}}\right)\right)\cdots \\ & + 2\sqrt{(\eta+\frac{\pi}{8})^2+\mu^2}\left(\tan^{-1}\left(\frac{\zeta+\zeta_v-\frac{\pi}{8}\zeta_f}{\sqrt{(\eta+\frac{\pi}{8})^2+\mu^2}}\right)-\tan^{-1}\left(\frac{\zeta+\zeta_v}{\sqrt{(\eta+\frac{\pi}{8})^2+\mu^2}}\right)\right)\cdots \\ & + \zeta\ln\left|\frac{\left((\eta-\frac{\pi}{8})^2+(\zeta+\zeta_v)^2+\mu^2\right)\left((\eta+\frac{\pi}{8})^2+(\zeta+\zeta_v-\frac{\pi}{8}\zeta_f)^2+\mu^2\right)}{\left((\eta-\frac{\pi}{8})^2+(\zeta+z_v-\frac{\pi}{8}\zeta_f)^2+\mu^2\right)\left((\eta+\frac{\pi}{8})^2+(\zeta+\zeta_v)^2+\mu^2\right)}\right|\end{aligned}$$

Appendix B: Force and Moment Derivations

B.1 Induced Lift

The resulting local reduction in the coefficient of lift is:

$$\delta C_{L,k} = -c_{l\alpha}\left(\frac{w}{V}\right)$$

Subscript k refers to the trailing aircraft. Converting to dimensional lift:

$$\delta L_k = -\bar{q}\bar{c}c_{l\alpha}\left(\frac{w}{V_E}\right)dy$$

Integration along the bound vortex yields an approximation of the total change in lift.

$$\Delta L_k = -\bar{q}\bar{c}\int_{-b_v/2}^{b_v/2} c_{l\alpha}\left(\frac{w}{V_E}\right)dy$$

Converting back to coefficient $\Delta C_{L,k} = \frac{\Delta L_k}{q\bar{c}b}$:

$$\Delta C_{L,k} = -\frac{1}{b}\int_{-b_v/2}^{b_v/2} c_{l\alpha}\left(\frac{w}{V_E}\right)dy \tag{B.1}$$

From basic aerodynamic relationships, the circulation of the lead horseshoe vortex can be converted to a function of the lead aircraft coefficient of lift $C_{L,j}$.

$$\Gamma_j = \frac{L_j}{\rho V_E b_v} = \frac{2V_E b}{\pi AR}C_{L,j} \tag{B.2}$$

With the dimensionless influence factor σ_{jk} given from equation (3.5), (B.1) becomes:

$$\Delta C_{L,k} = \frac{-c_{l_\alpha}\Gamma_j\sigma_{jk}}{b4\pi V_E} \tag{B.3}$$

Substituting equation (B.2) into equation (B.3), we have:

$$\Delta C_{L,k} = \frac{-c_{l_\alpha}C_{L,j}}{2\pi^2 AR}\sigma_{jk} \tag{B.4}$$

From thin airfoil theory, $c_{l_\alpha} = 2\pi$.

$$\Delta C_{L,k} = \frac{-C_{L,j}}{\pi AR}\sigma_{jk} \tag{B.5}$$

B.2 Induced Drag

From the Kutta-Joukowski theorem, the downwash will induce a change in drag at any spanwise position given by:

$$\delta D_{i,k} = \rho w(y)\Gamma_k dy$$

or

$$\delta C_{Di,k} = \frac{2w(y)\Gamma_k dy}{V^2 S}$$

Integrating along the bound vortex filament gives:

$$\Delta C_{Di,k} = \frac{2\Gamma_k}{V^2 S} \int_{-b_v/2}^{b_v/2} w\langle y\rangle \, dy$$

and using equations (B.2) and (3.4) yields:

$$\begin{aligned} \Delta C_{Di,k} =& \frac{4C_{L,k}}{\pi b} \int_{-b_v/2}^{b_v/2} \left(\frac{w}{V_E}\right) dy \\ =& \frac{2C_{L,j}C_{L,k}}{\pi^3 AR}\sigma_{jk} \end{aligned} \tag{B.6}$$

Both $\Delta C_{L,k}$ and $\Delta C_{Di,k}$ are hence directly proportional to σ_{jk}.

B.3 Induced Sideforce

The lead trailing vortex generates a local sidewash on the trailing aircraft tailfin and therefore a local sideslip angle $\beta = \frac{v}{V}$. The sideforce coefficient created by the tailfin due to this local sideslip is:

$$\delta C_{y\,k_f} = c_{l_{\alpha_f}} \frac{v}{V_E}$$

Converting to dimensional sideforce:

$$\delta Y_{k_f} = q c_f c_{l_{\alpha_f}} \frac{v}{V_E} dz$$

Assuming the tailfin to be a semi-wing as shown in Fig. 3.9, integration along the upper half of the tailfin bound vortex gives:

$$\Delta Y_{k_f} = q c_f \int_{\frac{-b_{f_v}}{2}}^{0} c_{l\alpha_f} \left(\frac{v}{V_E}\right) dz$$

Conversion to dimensionless coefficient $C_{y\,k_f} = \frac{Y_{k_f}}{q c_f \frac{b_f}{2}}$ yields

$$\Delta C_{y\,k_f} = \frac{2}{b_f} \int_{\frac{-b_{f_v}}{2}}^{0} c_{l\alpha_f} \left(\frac{v}{V_E}\right) dz \tag{B.7}$$

where b_f is twice the tailfin span, symmetric about an axis at the bottom of the tailfin and $\Delta C_{y\,k_f}$ is referred to the tailfin area $c_f \frac{b_f}{2}$. Introducing a dimensionless influence factor σ_{jk_f} defined as

$$\sigma_{jk_f} \equiv \frac{4\pi}{\Gamma_j} \int_{-\frac{b_{f_v}}{2}}^{0} v(z) \, dz \tag{B.8}$$

equation B.7 becomes:

$$\Delta C_{y\,k_f} = \frac{2c_{l\alpha_f}}{b_f} \frac{\Gamma_j}{4\pi} \frac{\sigma_{jk_f}}{V_E}$$

A dimensionless term, $\zeta_f = \frac{b_f}{b}$, is introduced from which $b_{f_v} = \frac{\pi}{4}\zeta_f b$. Γ_j is converted to C_{L_j} using equation (B.2). Apply the result of airfoil theory, $c_{l\alpha_f} = 2\pi$, to the tailfin, the solution for the change in sideforce coefficient is therefore:

$$\Delta C_{y\,k_f} = \frac{2C_{L,j}}{\pi AR\zeta_f}\sigma_{jk_f} \tag{B.9}$$

Referring $\Delta C_{y\,k_f}$ to the wing area S, the coefficient for the total sideforce is found:

$$\Delta C_{y\,k} = \Delta C_{y\,k_f}{}' = \frac{S_f}{S}\frac{2C_{L,j}}{\pi AR\zeta_f}\sigma_{jk_f} \tag{B.10}$$

where $S_f = c_f\frac{b_f}{2}$

B.4 Induced Rolling Moment

The rolling moment due to a wing section is:

$$\delta\widetilde{L}_k = \delta L_k y = \bar{q}\bar{c}c_{l_\alpha}\frac{w}{V_E}y dy$$

Here, $\widetilde{L}$ represents rolling moment and L represents lift. Integration along the trailing wing bound vortex yields:

$$\Delta\widetilde{L}_k = \bar{q}\bar{c}\,c_{l_\alpha}\int_{-\frac{b_y}{2}}^{\frac{b_y}{2}}\frac{w}{V_E}y\,dy$$

Conversion to dimensionless coefficient $\delta C_{l\,k} = \frac{\delta\widetilde{L}_k}{qSb}$ yields:

$$\Delta C_{l\,k} = \frac{c_{l_\alpha}}{b^2}\int_{-\frac{b_y}{2}}^{\frac{b_y}{2}}\frac{w}{V_E}y\,dy \tag{B.11}$$

The moment influence factor τ_{jk} is introduced:

$$\tau_{jk} \equiv \frac{4\pi}{\Gamma_j b}\int_{-\frac{b_y}{2}}^{\frac{b_y}{2}} w_{jk}y\;dy \tag{B.12}$$

From equations (B.2) and (B.12), equation (B.11) becomes:

$$\Delta C_{l\,k} = \frac{c_{l_\alpha}C_{L,j}}{2\pi^2 AR}\tau_{jk} \tag{B.13}$$

Applying the result of thin airfoil theory, $c_{l_\alpha} = 2\pi$:

$$\Delta C_{l\,k} = \frac{C_{L,j}}{\pi AR}\tau_{jk} \tag{B.14}$$

The rolling moment due to the sidewash along the tailfin is found to be negligible compared with the rolling moment due to the downwash along the wing. The derivation follows the same method described above.

$$\delta\widetilde{L}_{k_f} = -\delta Y_{k_f}z = -\bar{q}c_f c_{l\,\alpha_f}\frac{v}{V_E}z dz$$

Integration along the upper half of the tailfin bound vortex produces:

$$\Delta\widetilde{L}_{k_f} = -\bar{q}c_f c_{l\,\alpha_f} \int_{-\frac{b_{f_v}}{2}}^{0} \frac{v}{V_E} z\, dz$$

Conversion to dimensionless coefficient $\Delta C_{l\,k_f} = \frac{\Delta\widetilde{L}_{k_f}}{\bar{q}c_f\left(\frac{b_f}{2}\right)^2}$ yields:

$$\Delta C_{l\,k_f} = -\frac{4c_{l\,\alpha_f}}{b_f^2} \int_{-\frac{b_{f_v}}{2}}^{0} \frac{v}{V_E} z\, dz \tag{B.15}$$

Equation (B.15) can be reduced using the same approach as that followed in the derivation of the sideforce where b_f which is twice the span of the tailfin is equal to $\zeta_f b$. Another influence factor is introduced, however, which accounts for the integration of $v_{jk_f}\langle z\rangle z$ along the tailfin bound vortex semi-span:

$$\tau_{jk_f} \equiv \frac{4\pi}{\Gamma_j b} \int_{-\frac{b_{f_v}}{2}}^{0} v_{jk_f} z\, dz \tag{B.16}$$

Equation (B.15) becomes:

$$\Delta C_{l\,k_f} = -\frac{4C_{L,j}}{\pi AR\zeta_f^2}\tau_{jk_f} \tag{B.17}$$

Referring equation (B.17) to wing area and wing span, requires multiplying by $\frac{S_f}{S}$ and $\frac{(z_v+\frac{b_{f_v}}{4})}{b}$. $z_v + \frac{b_{f_v}}{4}$ is the distance from the wing longitudinal axis to the tailfin centre of pressure.

$$\Delta C_{l\,k_f}{}' = -\frac{S_f}{S}\frac{(z_v+\frac{b_{f_v}}{4})}{b}\frac{4C_{L,j}}{\pi AR\zeta_f^2}\tau_{jk_f} \tag{B.18}$$

B.5 Induced Pitching Moment

The angle of attack on the tailplane is:

$$\alpha_T = \bar{\alpha} + \delta\alpha_i - \varepsilon + \eta_T$$
$$\text{and } \bar{\alpha} + \delta\alpha_i - \varepsilon = (\bar{\alpha} + \delta\alpha_i)\left(1 - \frac{d\varepsilon}{d\alpha}\right)$$

For steady flight in isolation, $\bar{\alpha} = \frac{C_{L\,k_w}}{a}$ where a is the wing lift coefficient slope. The effect due to the lead trailing vortices, $\delta\alpha_i = -\frac{w'}{V}$, where w' represents the downwash along a portion of the wing span equal to the span of the tailplane bound vortex. The tailplane angle of attack is thus approximated as:

$$\alpha_T = \left(\frac{C_{L\,k_w}}{a} - \frac{w'}{V}\right)\left(1 - \frac{d\varepsilon}{d\alpha}\right) + \eta_T \tag{B.19}$$

The change in aircraft pitching moment coefficient due to the presence of the lead aircraft trailing vortices is:

$$\begin{aligned}\Delta C_{m\,k} &= \Delta C_{L,k}(h - h_0) + \overline{V}_T a_1 \frac{w'}{V_E}\left(1 - \frac{d\varepsilon}{d\alpha}\right)\\ &= \Delta C_{L,k}(h - h_0) - \overline{V}_T \Delta C_{L\,w_h}\left(1 - \frac{d\varepsilon}{d\alpha}\right)\end{aligned} \tag{B.20}$$

Where $\Delta C_{L\,w_h} = -a_1 \frac{w'}{V_E}$. a_1 is the tailplane lift coefficient slope. The derivation of $\Delta C_{L\,w_h}$ follows:

$$\Delta C_{L\,w_h} = -\,a_1 \frac{w'}{V} = -\frac{a_1}{b_{h_v}} \int_{\frac{-b_{h_v}}{2}}^{\frac{b_{h_v}}{2}} \frac{w}{V} dy \tag{B.21}$$

Introducing the influence factor $\sigma_{jk\,wh}$

$$\sigma_{jk\,wh} \equiv \frac{4\pi}{\Gamma_j} \int_{\frac{-b_{h_v}}{2}}^{\frac{b_{h_v}}{2}} w\, dy$$

and following the same approach used to obtain equation (B.4), equation (B.21) becomes

$$\begin{aligned} \Delta C_{L\,w_h} &= -\frac{a_1}{b_{h_v}} \frac{\Gamma_j}{4\pi} \frac{\sigma_{jk\,wh}}{V} \\ &= -\frac{4a_1}{\pi b_h} \frac{2bC_{L,j}}{4\pi^2 AR} \sigma_{jk\,wh} \\ \Delta C_{L\,wh} &= \frac{-2a_1 C_{L,j}}{\pi^3 AR\eta_h} \sigma_{jk\,wh} \end{aligned} \tag{B.22}$$

where $\eta_h = \frac{b_h}{b}$. $\sigma_{jk_{wh}}$ is given as (see Appendix A.4 and Fig. 3.15):

$$\sigma_{jk_{wh}} = \ln \left| \frac{\left(\zeta^2 + \left(\eta - \frac{\pi}{8} - \frac{\pi}{8}\eta_h\right)^2 + \mu^2\right)\left(\zeta^2 + \left(\eta + \frac{\pi}{8} + \frac{\pi}{8}\eta_h\right)^2 + \mu^2\right)}{\left(\zeta^2 + \left(\eta - \frac{\pi}{8} + \frac{\pi}{8}\eta_h\right)^2 + \mu^2\right)\left(\zeta^2 + \left(\eta + \frac{\pi}{8} - \frac{\pi}{8}\eta_h\right)^2 + \mu^2\right)} \right| \tag{B.23}$$

B.6 Induced Yawing Moment

The yawing moment due to the local drag at a spanwise position, y, is given by:

$$\delta N_{k_w} = \delta D_{i\,k}\, y = \rho w\langle y\rangle \Gamma_k y dy$$

$$\text{and } \delta C_{n\,k_w} = \frac{\rho w\langle y\rangle \Gamma_k y dy}{\bar{q} S b}$$

Integrating along the wing bound vortex gives:

$$\Delta C_{n\,k_w} = \frac{2\Gamma_k}{V_E^2 S b} \int_{-b_v/2}^{b_v/2} w\langle y\rangle\, dy$$

Using τ_{jk} as defined by equation (B.12) and converting Γ_k to $C_{L,k}$ using equation (B.2), the above equation is reduced to:

$$\Delta C_{n\,k_w} = \frac{4C_{L,k}}{\pi V_E b^2} \frac{\Gamma_j}{4\pi} \tau_{jk}$$

Converting Γ_j to C_{L_j}, again using equation (B.2), we arrive at the equation to describe the change in yaw coefficient due to the induced drag distribution along the wing:

$$\Delta C_{n\,k_w} = \frac{2C_{L,k} C_{L,j}}{\pi^3 AR} \tau_{jk} \tag{B.24}$$

The yaw moment coefficient due to the tailfin is simply taking the sideforce on the tailfin and multiplying by the moment arm. Recalling equation (B.9),

$$\Delta C_{y\,k_f} = \frac{2C_{L,j}}{\pi AR\zeta_f}\sigma_{jk_f}$$

and introducing the tailfin volume ratio, $\bar{V}_f = \frac{S_f l_f}{Sb}$:

$$\Delta C_{n\,k_f}{}' = -\bar{V}_f \frac{2C_{L,j}}{\pi AR\zeta_f}\sigma_{jk_f} \tag{B.25}$$

The total yaw moment coefficient is hence after summing equations (B.24) and (B.25):

$$\Delta C_{n,k} = \frac{2C_{L,j}C_{L,k}}{\pi^3 AR}\tau_{jk_{ab}} - \bar{V}_f \frac{2C_{L,j}}{\pi AR\zeta_f}\sigma_{jk_f} \tag{B.26}$$

B.7 Graphical Comparison of Forces and Moments Calculation Methods

Experimental data of formation flight for performance benefits is limited. NASA has conducted the most extensive research during its Autonomous Formation Flight Program where two F-18 aircraft were employed [49, 48]. A number of wind tunnel experiments have been conducted, however, these are predominantly focused on aerial refueling where the separations are commensurate with the application [53, 54, 55, 56, 57, 85]. The wind tunnel tests which have explored formation flight have generally used F-18 models or tailless delta wing models, both of which are not representative of a typical large airliner configuration [1, 3]. The rolling moment coefficient and lift coefficient increments have, however, been used for comparison since it is believed that these measured coefficients still provide adequate representation of the expected trend. The forces and moments dependent on the tailfin and tailplane are not considered from the wind tunnel tests of Myatt and Blake [1] and Blake and Gingras [3]. The tailless delta wing model is certainly not adequate while the slanted twin tail fin of the F-18 is also considered inadequate. Furthermore, the tailplane or stabilators of the F-18 rotate independently for additional roll control and the flight test data is therefore considered inadequate. The F-18 pitching moment data by Myatt and Blake is too sparse to indicate any trend. Iverson [86] conducted wind tunnel tests of two Hercules transport aircraft but did not provide any usable data for the required range of relative separation.

Figure B.1 compares the approximate method to calculate induced forces and moments with numerical integration over an elliptical wing for $\zeta = 0$. The approximate method assumes a rectangular planform with span, $\frac{\pi}{4}b$, and chord, $\bar{c}$, with constant $c_{l_\alpha} = 2\pi$. An elliptical wing of equivalent circulation has maximum chord, $\bar{c}$, at wing centerline, span b, and constant c_{l_α}. Figure B.2 shows contour plots of the changes in induced forces and moments with respect to lateral and vertical separation using the approximate method while B.3 compares the induced lift and roll coefficients of the approximate method and numerical integration over an elliptical wing for $\zeta = 0$ with flight test data, experimental data and data from vortex lattice methods from other sources. Tables B.1 and B.2 show the gradients of the induced forces and moments for small changes in vertical separation at specific lateral and vertical separations using the approximate method. Where necessary data from appendix G is used.

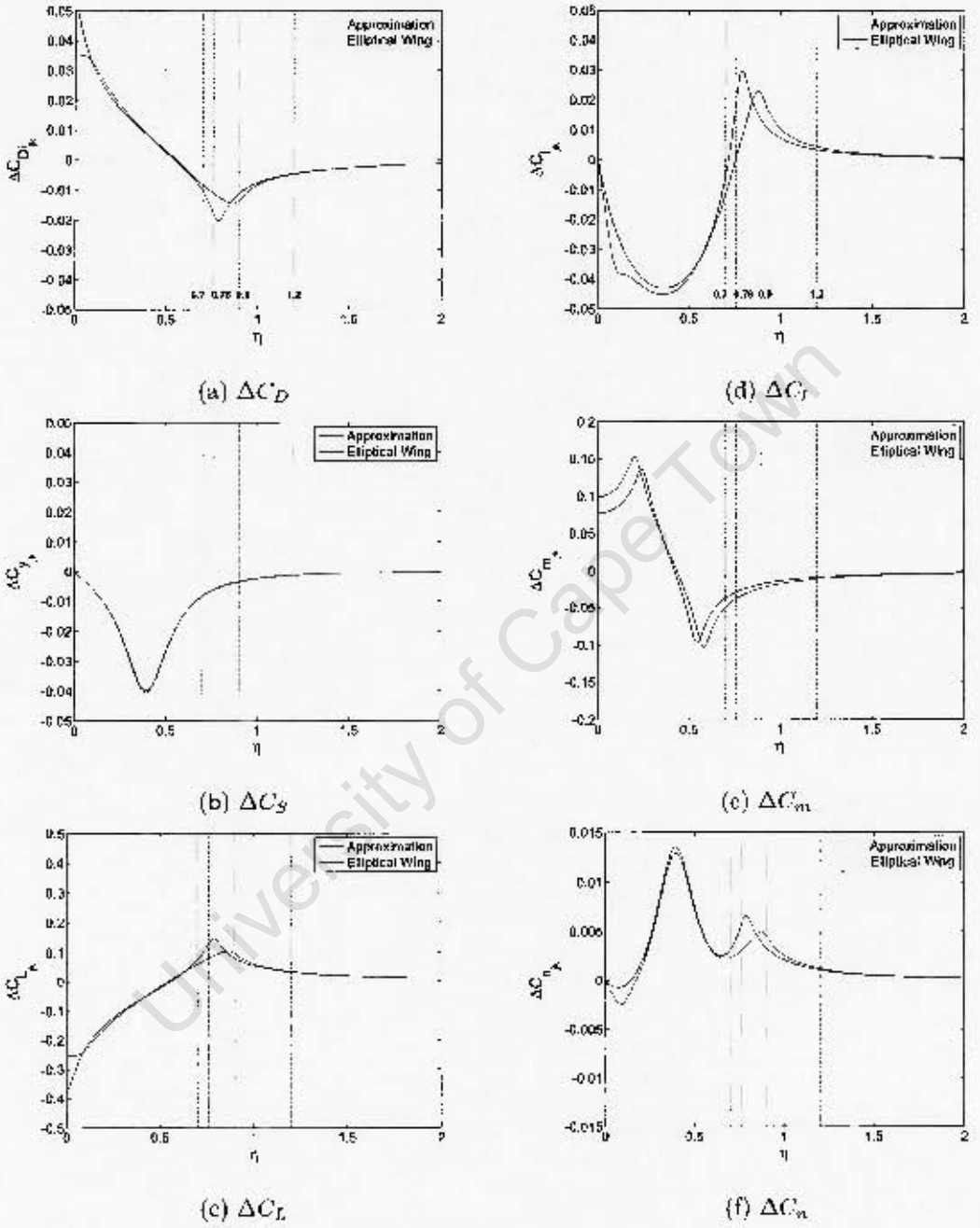

(a) ΔC_D (d) ΔC_l

(b) ΔC_S (e) ΔC_m

(c) ΔC_L (f) ΔC_n

Figure B.1: Comparison of the approximate method to calculate induced forces and moments with numerical integration over an elliptical wing for $\zeta = 0$. Vertical dashed lines represent lateral separations of $\eta = 0.7, 0.76, 0.9$ and 1.2.

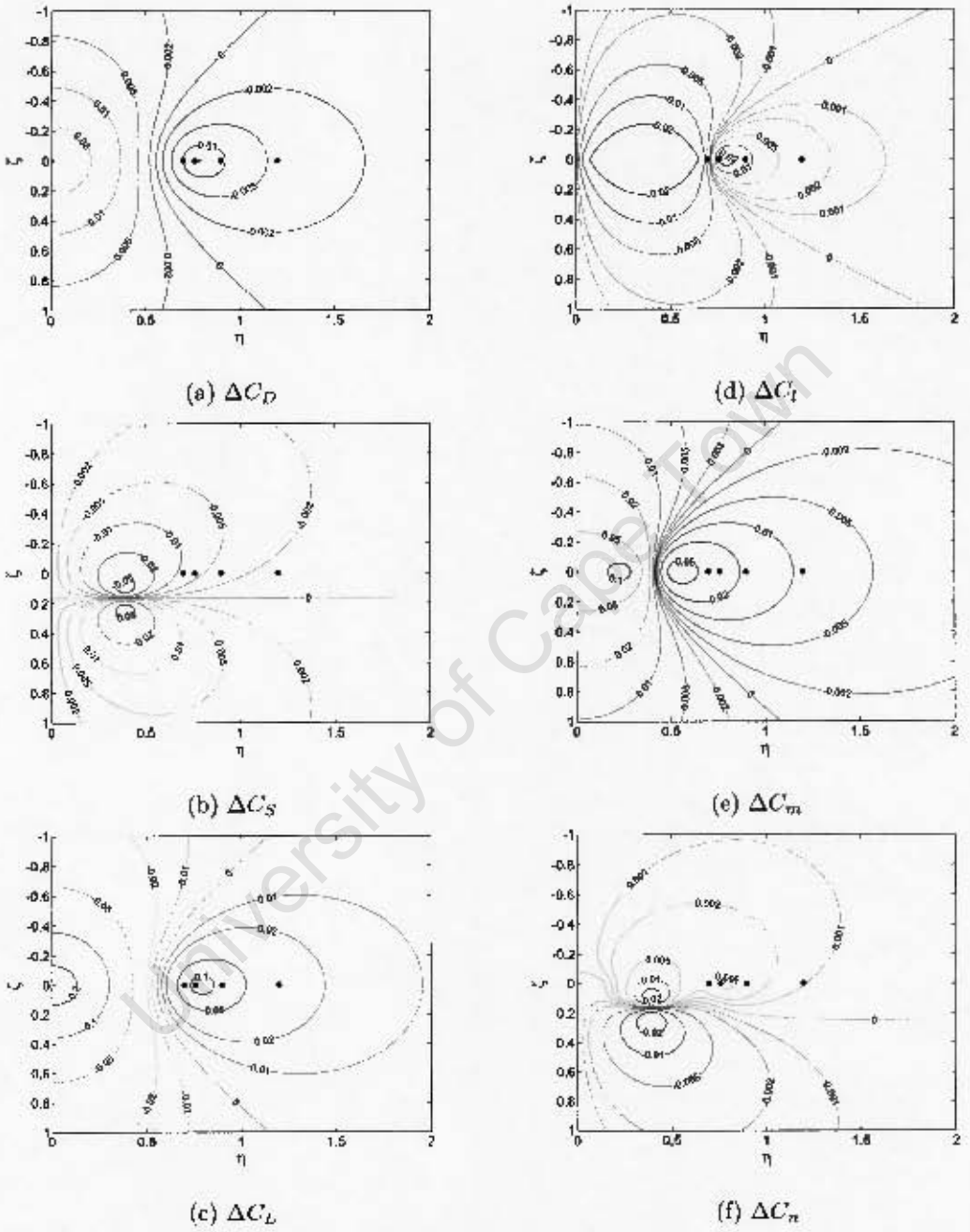

Figure B.2: Contour plots of the changes in induced forces and moments with respect to lateral and vertical separation using the approximate method. Black markers represent lateral separations of $\eta - 0.7, 0.76, 0.9$ and 1.2 and vertical separation of $\zeta - 0$.

Table B.1: Induced force and moment gradients for small changes in lateral separation, η, at lateral separations, $\eta = 0.7, 0.76, 0.9$ and 1.2, and zero vertical separation, $\zeta = 0$.

η	$\frac{\partial \Delta C_{Di}}{\partial \eta}$	$\frac{\partial \Delta C_S}{\partial \eta}$	$\frac{\partial \Delta C_L}{\partial \eta}$	$\frac{\partial \Delta C_l}{\partial \eta}$	$\frac{\partial \Delta C_m}{\partial \eta}$	$\frac{\partial \Delta C_n}{\partial \eta}$
0.7	-0.0996	0.0436	0.7196	0.3228	0.1784	0.0237
0.76	-0.1416	0.0293	1.0225	0.5	0.1141	0.0551
0.9	0.0517	0.013	-0.3735	-0.0899	0.0523	-0.0187
1.2	0.0098	0.0034	-0.0705	-0.0107	0.0173	-0.0031

Table B.2: Induced force and moment gradients for small changes in vertical separation at lateral separations, $\eta = 0.7, 0.76, 0.9$ and 1.2, and zero vertical separation, $\zeta = 0$.

η	$\frac{\partial \Delta C_{Di}}{\partial \eta}$	$\frac{\partial \Delta C_S}{\partial \eta}$	$\frac{\partial \Delta C_L}{\partial \eta}$	$\frac{\partial \Delta C_l}{\partial \eta}$	$\frac{\partial \Delta C_m}{\partial \eta}$	$\frac{\partial \Delta C_n}{\partial \eta}$
0.7	0	0.0264	0	0	0	-0.0127
0.76	0	0.0233	0	0	0	-0.0112
0.9	0	0.0156	0	0	0	-0.0075
1.2	0	0.0067	0	0	0	-0.0032

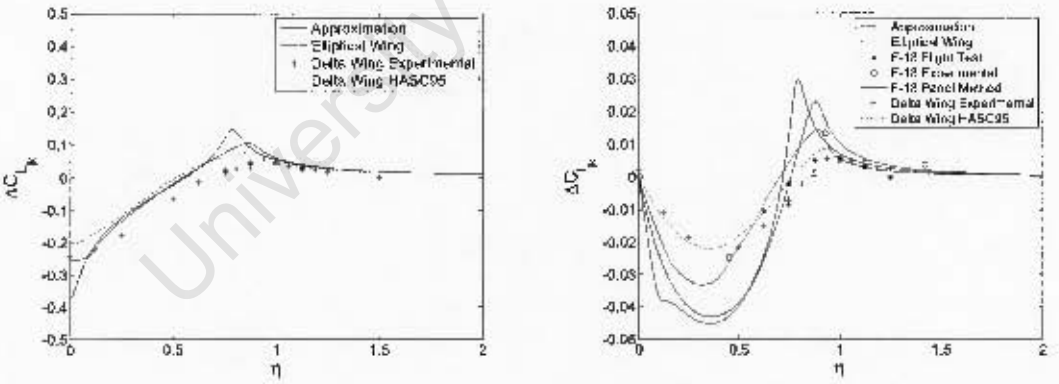

(a) ΔC_L (b) ΔC_l

Figure B.3: Induced lift and roll coefficients of the approximate method, numerical integration over an elliptical wing for $\zeta = 0$ along with flight test data, experimental data and data from vortex lattice methods from other sources. F-18 flight test data from Hansen et al. [87] and Vachon et al. [49]. F-18 panel method results and wind tunnel tests (experiment) from Myatt and Blake [1]. Tailless delta wing wind tunnel tests (experiment) and HASC95 results from Blake and Gingras [3].

Appendix C: Steady State Orientation and Deflection Angle Changes

To solve the change in trim angle of attack $\delta\alpha$ and trim deflection $\delta\delta_e$ at constant η and zero gust velocity, consider the coefficients, $C_{L_{trim}}$ and $C_{m_{trim}}$.

$$C_{L_{trim}} = \frac{mg}{qS} = C_{L_\alpha}(\bar{\alpha} + \delta\alpha) + \Delta C_L < \eta, \zeta > + C_{L_{\delta_e}}(\delta_{e_0} + \delta\delta_e)$$
$$C_{m_{trim}} = 0 = C_{m_0} + C_{m_\alpha}(\alpha_0 + \delta\alpha) + \Delta C_m < \eta, \zeta > + C_{m_{\delta_e}}(\delta_{e_0} + \delta\delta_e)$$

In isolated flight, i.e. no influence due to trailing vortices, and in equilibrium:

$$C_L = \frac{mg}{qS} = C_{L_\alpha}\bar{\alpha} + C_{L_{\delta_e}}\delta_{e_0}$$
$$C_m = 0 = C_{m_0} + C_{m_\alpha}\alpha_0 + C_{m_{\delta_e}}\delta_{e_0}$$

Due to the influence of the trailing vortices, $\Delta C_L < \eta, \zeta >$ and $\Delta C_m < \eta, \zeta >$ are generated and require changes in $\delta\alpha$ and $\delta\delta_e$, Hence:

$$0 = C_{L_\alpha}(\delta\alpha) + \Delta C_L < \eta, \zeta > + C_{L_{\delta_e}}(\delta\delta_e)$$
$$0 = C_{m_\alpha}(\delta\alpha) + \Delta C_m < \eta, \zeta > + C_{m_{\delta_e}}(\delta\delta_e)$$

The above equation can be written in matrix form.

$$\begin{bmatrix} C_{L_\alpha} & C_{L_{\delta_e}} \\ C_{m_\alpha} & C_{m_{\delta_e}} \end{bmatrix} \begin{Bmatrix} \delta\alpha \\ \delta\delta_e \end{Bmatrix} = \begin{Bmatrix} -\Delta C_L < \eta, \zeta > \\ -\Delta C_m < \eta, \zeta > \end{Bmatrix} \tag{C.1}$$

Using Kramer's rule, we can solve $\delta\alpha$ and $\delta\delta_e$.

$$\delta\alpha = \frac{\begin{vmatrix} -\Delta C_L < \eta, \zeta > & C_{L_{\delta_e}} \\ -\Delta C_m < \eta, \zeta > & C_{m_{\delta_e}} \end{vmatrix}}{\begin{vmatrix} C_{L_\alpha} & C_{L_{\delta_e}} \\ C_{m_\alpha} & C_{m_{\delta_e}} \end{vmatrix}} \quad \delta\delta_e = \frac{\begin{vmatrix} C_{L_\alpha} & -\Delta C_L < \eta, \zeta > \\ C_{m_\alpha} & -\Delta C_m < \eta, \zeta > \end{vmatrix}}{\begin{vmatrix} C_{L_\alpha} & C_{L_{\delta_e}} \\ C_{m_\alpha} & C_{m_{\delta_e}} \end{vmatrix}} \tag{C.2}$$

To find $\delta\beta$, $\delta\delta_a$ and $\delta\delta_r$, consider $C_{y_{trim}}$, $C_{l_{trim}}$ and $C_{n_{trim}}$.

$$C_{y_{trim}} = 0 = C_{y_\beta}(\beta_0 + \delta\beta) + \Delta C_y < \eta, \zeta > + C_{y_{\delta_r}}(\delta_{r_0} + \delta\delta_r)$$
$$C_{l_{trim}} = 0 = C_{l_\beta}(\beta_0 + \delta\beta) + \Delta C_l < \eta, \zeta > + C_{l_{\delta_a}}(\delta_{a_0} + \delta\delta_a) + C_{l_{\delta_r}}(\delta_{r_0} + \delta\delta_r)$$
$$C_{n_{trim}} = 0 = C_{n_\beta}(\beta_0 + \delta\beta) + \Delta C_n < \eta, \zeta > + C_{n_{\delta_a}}(\delta_{a_0} + \delta\delta_a) + C_{n_{\delta_r}}(\delta_{r_0} + \delta\delta_r)$$

In isolated flight and in equilibrium, $\beta_0 = \delta_{a_0} = \delta_{r_0} = 0$. Hence:

$$
\begin{aligned}
0 &= C_{y_\beta}\delta\beta + \Delta C_y < \eta, \zeta > + C_{y_{\delta_r}}\delta\delta_r \\
0 &= C_{l_\beta}\delta\beta + \Delta C_l < \eta, \zeta > + C_{l_{\delta_a}}\delta\delta - a + C_{l_{\delta_r}}\delta\delta_r \\
0 &= C_{n_\beta}\delta\beta + \Delta C_n < \eta, \zeta > + C_{n_{\delta_a}}\delta\delta_a + C_{n_{\delta_r}}\delta\delta_r
\end{aligned}
$$

or

$$
\begin{bmatrix} C_{y_\beta} & 0 & C_{y_{\delta_r}} \\ C_{l_\beta} & C_{l_{\delta_a}} & C_{l_{\delta_r}} \\ C_{n_\beta} & C_{n_{\delta_a}} & C_{n_{\delta_r}} \end{bmatrix} \begin{Bmatrix} \delta\beta \\ \delta\delta_a \\ \delta\delta_r \end{Bmatrix} = \begin{Bmatrix} -\Delta C_y < \eta, \zeta > \\ -\Delta C_l < \eta, \zeta > \\ -\Delta C_n < \eta, \zeta > \end{Bmatrix} \tag{C.3}
$$

Once again we can solve using Kramer's rule.

$$
\delta\beta = \frac{\begin{vmatrix} -\Delta C_y < \eta, \zeta > & 0 & C_{y_{\delta_r}} \\ -\Delta C_l < \eta, \zeta > & C_{l_{\delta_a}} & C_{l_{\delta_r}} \\ -\Delta C_n < \eta, \zeta > & C_{n_{\delta_a}} & C_{n_{\delta_r}} \end{vmatrix}}{\begin{vmatrix} C_{y_\beta} & 0 & C_{y_{\delta_r}} \\ C_{l_\beta} & C_{l_{\delta_a}} & C_{l_{\delta_r}} \\ C_{n_\beta} & C_{n_{\delta_a}} & C_{n_{\delta_r}} \end{vmatrix}} \quad \delta\delta_a = \frac{\begin{vmatrix} C_{y_\beta} & -\Delta C_y < \eta, \zeta > & C_{y_{\delta_r}} \\ C_{l_\beta} & -\Delta C_l < \eta, \zeta > & C_{l_{\delta_r}} \\ C_{n_\beta} & -\Delta C_n < \eta, \zeta > & C_{n_{\delta_r}} \end{vmatrix}}{\begin{vmatrix} C_{y_\beta} & 0 & C_{y_{\delta_r}} \\ C_{l_\beta} & C_{l_{\delta_a}} & C_{l_{\delta_r}} \\ C_{n_\beta} & C_{n_{\delta_a}} & C_{n_{\delta_r}} \end{vmatrix}}
$$

$$
\delta\delta_r = \frac{\begin{vmatrix} C_{y_\beta} & 0 & -\Delta C_y < \eta, \zeta > \\ C_{l_\beta} & C_{l_{\delta_a}} & -\Delta C_l < \eta, \zeta > \\ C_{n_\beta} & C_{n_{\delta_a}} & -\Delta C_n < \eta, \zeta > \end{vmatrix}}{\begin{vmatrix} C_{y_\beta} & 0 & C_{y_{\delta_r}} \\ C_{l_\beta} & C_{l_{\delta_a}} & C_{l_{\delta_r}} \\ C_{n_\beta} & C_{n_{\delta_a}} & C_{n_{\delta_r}} \end{vmatrix}} \tag{C.4}
$$

Appendix D: Development of the Equations of Motion

The six-degree-of-freedom equations of motion for a rigid body, with origin at the CG are given by equations (D.1) to (D.6) where the body is symmetrical w.r.t. the xz plane Etkin and Reid [79].

$$m\left(\dot{u} - vr + wq\right) = -mg\sin\theta + X + T \tag{D.1}$$

$$m\left(\dot{v} + ur - wp\right) = mg\sin\phi\cos\theta + Y \tag{D.2}$$

$$m\left(\dot{w} - uq + vp\right) = mg\cos\phi\cos\theta + Z \tag{D.3}$$

$$I_x\dot{p} - \left(I_y - I_z\right)qr - I_{xz}\left(pq + \dot{r}\right) = \tilde{L} \tag{D.4}$$

$$I_y\dot{q} - \left(I_z - I_x\right)pr - I_{xz}\left(r^2 - p^2\right) = M \tag{D.5}$$

$$I_z\dot{r} - \left(I_x - I_y\right)pq - I_{xz}\left(\dot{p} - qr\right) = N \tag{D.6}$$

The velocity transformation from the inertial frame to the body frame through orientation angles θ_{0_f} and ψ_{0_f} due to steady formation flight are:

$$\mathbf{u}^B_{0_f} = \mathbf{R}_{BI}\mathbf{u}^I_{0_f}$$

$$\begin{Bmatrix} u_{0_f} \\ v_{0_f} \\ w_{0_f} \end{Bmatrix}^B = \begin{bmatrix} \cos\theta^{BI}_{0_f}\cos\psi^{BI}_{0_f} & \cos\theta^{BI}_{0_f}\sin\psi^{BI}_{0_f} & -\sin\theta^{BI}_{0_f} \\ -\sin\psi^{BI}_{0_f} & \cos\psi^{BI}_{0_f} & 0 \\ \sin\theta^{BI}_{0_f}\cos\psi^{BI}_{0_f} & \sin\theta^{BI}_{0_f}\sin\psi^{BI}_{0_f} & \cos\theta^{BI}_{0_f} \end{bmatrix} \begin{Bmatrix} u_{0_f} \\ v_{0_f} \\ w_{0_f} \end{Bmatrix}^I \tag{D.7}$$

Small perturbations from the trimmed state are defined as:

$$\begin{aligned} u &= u_{0_f} + u_d\langle t\rangle & p &= p_{0_f} + p_d\langle t\rangle & \phi &= \phi_{0_f} + \phi_d\langle t\rangle \\ v &= v_{0_f} + v_d\langle t\rangle & q &= q_{0_f} + q_d\langle t\rangle & \theta &= \theta_{0_f} + \theta_d\langle t\rangle \\ w &= w_{0_f} + w_d\langle t\rangle & r &= r_{0_f} + r_d\langle t\rangle & \psi &= \psi_{0_f} + \psi_d\langle t\rangle \end{aligned}$$

The perturbed equations of motion are generated by substituting the above relationships into equa-

tions (D.1) to (D.6):

$$m\left(-v_{0_f}r_{0_f}+w_{0_f}q_{0_f}\right)+m\left(\dot{u}-v_{0_f}r_d\langle t\rangle-r_{0_f}v_d\langle t\rangle+w_{0_f}q_d\langle t\rangle+q_{0_f}w_d\langle t\rangle\right)\ldots$$
$$+m\left(-v_d\langle t\rangle r_d\langle t\rangle+w_d\langle t\rangle q_d\langle t\rangle\right)=-mg\sin\theta_{0_f}-mg\theta_d\langle t\rangle\cos\theta_{0_f}+X_{0_f}+X_d\langle t\rangle+T_{0_f} \quad \text{(D.8)}$$

$$m\left(u_{0_f}r_{0_f}-w_{0_f}p_{0_f}\right)+m\left(\dot{v}+u_{0_f}r_d\langle t\rangle+r_{0_f}u_d\langle t\rangle-w_{0_f}p_d\langle t\rangle-p_{0_f}w_d\langle t\rangle\right)\ldots$$
$$+m\left(u_d\langle t\rangle r_d\langle t\rangle-w_d\langle t\rangle p_d\langle t\rangle\right)=mg\sin\phi_{0_f}\cos\theta_{0_f}-mg\theta_d\langle t\rangle\sin\phi_{0_f}\sin\theta_{0_f}+mg\phi_d\langle t\rangle\cos\phi_{0_f}\cos\theta_{0_f}\ldots$$
$$-mg\phi_d\langle t\rangle\theta_d\langle t\rangle\cos\phi_{0_f}\sin\theta_{0_f}+Y_{0_f}+Y_d\langle t\rangle \quad \text{(D.9)}$$

$$m\left(-u_{0_f}q_{0_f}+v_{0_f}p_{0_f}\right)+m\left(\dot{w}-u_{0_f}q_d\langle t\rangle-q_{0_f}u_d\langle t\rangle+v_{0_f}p_d\langle t\rangle+p_{0_f}v_d\langle t\rangle\right)\ldots$$
$$+m\left(-u_d\langle t\rangle q_d\langle t\rangle+v_d\langle t\rangle p_d\langle t\rangle\right)=mg\cos\phi_{0_f}\cos\theta_{0_f}-mg\theta_d\langle t\rangle\cos\phi_{0_f}\sin\theta_{0_f}-mg\phi_d\langle t\rangle\sin\phi_{0_f}\cos\theta_{0_f}\ldots$$
$$+mg\phi_d\langle t\rangle\theta_d\langle t\rangle\sin\phi_{0_f}\cos\theta_{0_f}+Z_{0_f}+Z_d\langle t\rangle \quad \text{(D.10)}$$

$$I_x\dot{p}-(I_y-I_z)r_{0_f}q_{0_f}+I_{xz}p_{0_f}q_{0_f}-I_{xz}\dot{r}-I_{xz}\left(p_{0_f}q_d\langle t\rangle+q_{0_f}p_d\langle t\rangle\right)\ldots$$
$$-(I_y-I_z)\left(r_{0_f}q_d\langle t\rangle+q_{0_f}r_d\langle t\rangle\right)-I_{xz}p_d\langle t\rangle q_d\langle t\rangle-(I_y-I_z)r_d\langle t\rangle q_d\langle t\rangle=\tilde{L}_{0_f}+\tilde{L}_d\langle t\rangle \quad \text{(D.11)}$$

$$I_y\dot{q}-(I_z-I_x)p_{0_f}p_{0_f}+I_{xz}\left(p_{0_f}^2-r_{0_f}^2\right)-(I_z-I_x)\left(p_{0_f}r_d\langle t\rangle+r_{0_f}p_d\langle t\rangle\right)\ldots$$
$$+I_{xz}\left(2p_{0_f}p_d\langle t\rangle+2r_{0_f}r_d\langle t\rangle\right)-(I_z-I_x)p_d\langle t\rangle r_d\langle t\rangle+I_{xz}\left(p_d\langle t\rangle^2-r_d\langle t\rangle^2\right)=M_{0_f}+M_d\langle t\rangle \quad \text{(D.12)}$$

$$I_z\dot{r}-(I_x-I_y)p_{0_f}q_{0_f}+I_{xz}q_{0_f}r_{0_f}-I_{xz}\dot{p}+I_{xz}\left(q_{0_f}r_d\langle t\rangle+r_{0_f}q_d\langle t\rangle\right)\ldots$$
$$-(I_x-I_y)\left(p_{0_f}q_d\langle t\rangle+q_{0_f}p_d\langle t\rangle\right)+I_{xz}q_d\langle t\rangle r_d\langle t\rangle-(I_x-I_y)p_d\langle t\rangle q_d\langle t\rangle=N_{0_f}+N_d\langle t\rangle \quad \text{(D.13)}$$

All 'small' second order terms (All perturbation terms, v_{0_f}, ψ_{0_f},) are considered negligible while $\phi_{0_f}=p_{0_f}=q_{0_f}=r_{0_f}=0$. Reference state terms which are not functions of time fallout without losing generality.

$$m\left(\dot{u}_d\langle t\rangle+w_{0_f}q_d\langle t\rangle\right)=-mg\theta_d\langle t\rangle+X_d\langle t\rangle \quad \text{(D.14)}$$
$$m\left(\dot{v}_d\langle t\rangle+u_{0_f}r_d\langle t\rangle-w_{0_f}p_d\langle t\rangle\right)=mg\phi_d\langle t\rangle+Y_d\langle t\rangle \quad \text{(D.15)}$$
$$m\left(\dot{w}_d\langle t\rangle-u_{0_f}q_d\langle t\rangle\right)=Z_d\langle t\rangle \quad \text{(D.16)}$$
$$I_x\dot{p}_d\langle t\rangle-I_{xz}\dot{r}_d\langle t\rangle=\tilde{L}_d\langle t\rangle \quad \text{(D.17)}$$
$$I_y\dot{q}_d\langle t\rangle=M_d\langle t\rangle \quad \text{(D.18)}$$
$$I_z\dot{r}_d\langle t\rangle-I_{xz}\dot{p}_d\langle t\rangle=N_d\langle t\rangle \quad \text{(D.19)}$$

The aerodynamic force and moment coefficients for steady flight in isolation can be represented

as [6]:

$$C^I_{D_0} = C^I_D \langle \alpha, \beta, M \rangle + \sum C^I_D \langle \delta_k, \alpha, M \rangle \tag{D.20}$$

$$C^I_{S_0} = C^I_S \langle \alpha, \beta, M \rangle + \sum C^I_S \langle \delta_k, \alpha, M \rangle \tag{D.21}$$

$$C^I_{L_0} = C^I_L \langle \alpha, \beta, M \rangle + \sum C^I_L \langle \delta_k, \alpha, M \rangle \tag{D.22}$$

$$C^I_{l_0} = C^I_l \langle \alpha, \beta, M \rangle + \sum C^I_l \langle \delta_k, \alpha, M \rangle \tag{D.23}$$

$$C^I_{m_0} = C^I_m \langle \alpha, \beta, M \rangle + \sum C^I_m \langle \delta_k, \alpha, M \rangle \tag{D.24}$$

$$C^I_{n_0} = C^I_n \langle \alpha, \beta, M \rangle + \sum C^I_n \langle \delta_k, \alpha, M \rangle \tag{D.25}$$

Equations (D.20) to (D.25) are expanded to include force and moment coefficients due to formation flight in zero wind.

$$C^I_{D_{0_f}} = C^I_{D_0} + \Delta C^I_D \langle \eta, \zeta \rangle + C^I_D \langle \delta\alpha, \delta\beta, M \rangle + \sum C^I_D \langle \delta\delta_k, \alpha, M \rangle \tag{D.26}$$

$$C^I_{S_{0_f}} = C^I_{S_0} + \Delta C^I_S \langle \eta, \zeta \rangle + C^I_S \langle \delta\alpha, \delta\beta, M \rangle + \sum C^I_S \langle \delta\delta_k, \alpha, M \rangle \tag{D.27}$$

$$C^I_{L_{0_f}} = C^I_{L_0} + \Delta C^I_L \langle \eta, \zeta \rangle + C_L \langle \delta\alpha, \delta\beta, M \rangle + \sum C^I_L \langle \delta\delta_k, \alpha, M \rangle \tag{D.28}$$

$$C^I_{l_{0_f}} = C^I_{l_0} + \Delta C^I_l \langle \eta, \zeta \rangle + C_l \langle \delta\alpha, \delta\beta, M \rangle + \sum C^I_l \langle \delta\delta_k, \alpha, M \rangle \tag{D.29}$$

$$C^I_{m_{0_f}} = C^I_{m_0} + \Delta C^I_m \langle \eta, \zeta \rangle + C_m \langle \delta\alpha, \delta\beta, M \rangle + \sum C^I_m \langle \delta\delta_k, \alpha, M \rangle \tag{D.30}$$

$$C^I_{n_{0_f}} = C^I_{n_0} + \Delta C^I_n \langle \eta, \zeta \rangle + C_n \langle \delta\alpha, \delta\beta, M \rangle + \sum C^I_n \langle \delta\delta_k, \alpha, M \rangle \tag{D.31}$$

Solving the orientation angles, $\delta\alpha$ and $\delta\beta$, from equations C.2 and C.4 due to steady formation flight.

$$\delta\alpha = \frac{\begin{vmatrix} -\Delta C_L < \eta, \zeta > & C_{L_{\delta_e}} \\ -\Delta C_m < \eta, \zeta > & C_{m_{\delta_e}} \end{vmatrix}}{\begin{vmatrix} C_{L_\alpha} & C_{L_{\delta_e}} \\ C_{m_\alpha} & C_{m_{\delta_e}} \end{vmatrix}} \qquad \delta\delta_e = \frac{\begin{vmatrix} C_{L_\alpha} & -\Delta C_L < \eta, \zeta > \\ C_{m_\alpha} & -\Delta C_m < \eta, \zeta > \end{vmatrix}}{\begin{vmatrix} C_{L_\alpha} & C_{L_{\delta_e}} \\ C_{m_\alpha} & C_{m_{\delta_e}} \end{vmatrix}}$$

$$\delta\beta = \frac{\begin{vmatrix} -\Delta C_y < \eta, \zeta > & 0 & C_{y_{\delta_r}} \\ -\Delta C_l < \eta, \zeta > & C_{l_{\delta_a}} & C_{l_{\delta_r}} \\ -\Delta C_n < \eta, \zeta > & C_{n_{\delta_a}} & C_{n_{\delta_r}} \end{vmatrix}}{\begin{vmatrix} C_{y_\beta} & 0 & C_{y_{\delta_r}} \\ C_{l_\beta} & C_{l_{\delta_a}} & C_{l_{\delta_r}} \\ C_{n_\beta} & C_{n_{\delta_a}} & C_{n_{\delta_r}} \end{vmatrix}} \qquad \delta\delta_a = \frac{\begin{vmatrix} C_{y_\beta} & -\Delta C_y < \eta, \zeta > & C_{y_{\delta_r}} \\ C_{l_\beta} & -\Delta C_l < \eta, \zeta > & C_{l_{\delta_r}} \\ C_{n_\beta} & -\Delta C_n < \eta, \zeta > & C_{n_{\delta_r}} \end{vmatrix}}{\begin{vmatrix} C_{y_\beta} & 0 & C_{y_{\delta_r}} \\ C_{l_\beta} & C_{l_{\delta_a}} & C_{l_{\delta_r}} \\ C_{n_\beta} & C_{n_{\delta_a}} & C_{n_{\delta_r}} \end{vmatrix}}$$

$$\delta\delta_r = \frac{\begin{vmatrix} C_{y_\beta} & 0 & -\Delta C_y < \eta, \zeta > \\ C_{l_\beta} & C_{l_{\delta_a}} & -\Delta C_l < \eta, \zeta > \\ C_{n_\beta} & C_{n_{\delta_a}} & -\Delta C_n < \eta, \zeta > \end{vmatrix}}{\begin{vmatrix} C_{y_\beta} & 0 & C_{y_{\delta_r}} \\ C_{l_\beta} & C_{l_{\delta_a}} & C_{l_{\delta_r}} \\ C_{n_\beta} & C_{n_{\delta_a}} & C_{n_{\delta_r}} \end{vmatrix}}$$

$$\theta_{0_f} = \theta_0 + \delta\alpha$$
$$\psi_{0_f} = \psi_0 - \delta\beta$$

The force and moment coefficients are transformed to the body frame using $\mathbf{R}_{BI}$ from equation (D.7) where θ_{0_f} and ψ_{0_f} are considered to be small.

$$\begin{Bmatrix} C^B_{x_{0_f}} - C^B_{T_{0_f}} \\ C^B_{y_{0_f}} \\ C^B_{z_{0_f}} \end{Bmatrix} = \mathbf{R}_{BI} \begin{Bmatrix} -C^I_{D_{0_f}} \\ C^I_{S_{0_f}} \\ -C^I_{L_{0_f}} \end{Bmatrix} \tag{D.32}$$

$$C^B_{x_{0_f}} = C^I_{T_{0_f}} - C^I_{D_{0_f}} - C^I_{S_{0_f}}\psi_{0_f} - C^I_{L_{0_f}}\theta_{0_f} \tag{D.33}$$
$$C^B_{y_{0_f}} = -C^I_{D_{0_f}}\psi_{0_f} + C^I_{S_{0_f}} \tag{D.34}$$
$$C^B_{z_{0_f}} = C^I_{D_{0_f}}\theta_{0_f} - C^I_{L_{0_f}} \tag{D.35}$$

$$\begin{Bmatrix} C^B_{l_{0_f}} \\ C^B_{m_{0_f}} \\ C^B_{n_{0_f}} \end{Bmatrix} = \mathbf{R}_{BI} \begin{Bmatrix} C^I_{l_{0_f}} \\ C^I_{m_{0_f}} \\ C^I_{n_{0_f}} \end{Bmatrix} \tag{D.36}$$

$$C^B_{l_{0_f}} = -C^I_{l_{0_f}} - C^I_{m_{0_f}}\psi_{0_f} - C^I_{n_{0_f}}\theta_{0_f} \tag{D.37}$$
$$C^B_{m_{0_f}} = -C^I_{n_{0_f}}\psi_{0_f} + C^I_{m_{0_f}} \tag{D.38}$$
$$C^B_{n_{0_f}} = C^I_{l_{0_f}}\theta_{0_f} - C^I_{n_{0_f}} \tag{D.39}$$

Due to atmospheric turbulence, the aircraft experiences a disturbance angle of attack and sideslip angle.

$$\alpha_d\langle t\rangle = \frac{w_d\langle t\rangle - w^B_g\langle t\rangle}{u_{0_f} + u_d\langle t\rangle - u^B_g\langle t\rangle}$$
$$\beta_d\langle t\rangle = \frac{v_d\langle t\rangle - v^B_g\langle t\rangle}{u_{0_f} + u_d\langle t\rangle - u^B_g\langle t\rangle}$$

The longitudinal component, $u_{0_f} + u_d\langle t\rangle - u_g\langle t\rangle^B$, is approximated as the free stream velocity V_E. The gust velocities, specified in the inertial frame, are transformed to the body frame with the direction cosine matrix where all angles are considered small:

$$\mathbf{u}^B_g = \mathbf{R}_{B_dI}\mathbf{u}^I_g$$
$$\mathbf{u}^B_g = \begin{bmatrix} 1 & \psi_{0_f} + \psi_d & -\theta_{0_f} - \theta_d \\ -\psi_{0_f} - \psi_d & 1 & \phi_d \\ \theta_{0_f} + \theta_d & -\phi_d & 1 \end{bmatrix} \mathbf{u}^I_g$$

The effective separation is determined as per section 4.3.

$$\eta_{eff}\langle t\rangle = \sqrt{\xi^2+\eta^2}\sin\left(\tan^{-1}\left(\frac{\eta}{-\xi}\right)-\left(\frac{v_g\langle t\rangle}{V}\right)\right)$$
$$\zeta_{eff}\langle t\rangle = \sqrt{\xi^2+\zeta^2}\sin\left(\tan^{-1}\left(\frac{\zeta}{-\xi}\right)-\left(\frac{w_g\langle t\rangle}{V}\right)\right)$$

Assuming $\xi >> |\eta|$ and v_g to be small compared to V_E

$$\eta_{eff}\langle t\rangle = \eta + \xi\left(\frac{v_g\langle t\rangle}{V_E}\right) \tag{D.40}$$
$$\zeta_{eff}\langle t\rangle = \zeta + \xi\left(\frac{w_g\langle t\rangle}{V_E}\right) \tag{D.41}$$

Representing $C_x, C_y, C_z, C_l, C_m, C_n$ as C_i and $\delta\delta_k$ as the disturbance control inputs while noting that, to first order, $\Delta V\langle t\rangle^2 = 2u_{0_f}\left(u_d\langle t\rangle - u_g\langle t\rangle\right)$, the first order approximations of the aerodynamic loads combined with the non-linear functions due to formation flight, defined in chapter 3, are given below.

$$\begin{aligned}
C_i\langle t\rangle =& C_{i_{0_f}} + C_{i_d}\langle t\rangle \\
C_{i_d}\langle t\rangle =& C_i|_r\frac{2\left(u_d\langle t\rangle - u_g\langle t\rangle\right)}{V} + \frac{\partial C_i}{\partial\alpha}|_r\left\{\frac{w_d\langle t\rangle - w_g^B\langle t\rangle}{V_E}\right\} + \frac{\partial C_i}{\partial\beta}|_r\left\{\frac{v_d\langle t\rangle - v_g^B\langle t\rangle}{V_E}\right\}\cdots \\
&+ \frac{\partial C_i}{\partial\hat{p}}|_r\frac{pb}{2V_E} + \frac{\partial C_i}{\partial\hat{q}}|_r\frac{q\bar{c}}{2V_E} + \frac{\partial C_i}{\partial\hat{r}}|_r\frac{rb}{2V_E} + \frac{\partial C_i}{\partial\delta\delta_k}|_r\delta\delta_k\cdots \\
&+ C_i\langle\eta_{eff},\zeta_{eff}\rangle
\end{aligned} \tag{D.42}$$

The first term on the RHS of equation (D.42) is only considered in the x and z components. For small disturbances:

$$p_d\langle t\rangle = \dot{\phi}_d\langle t\rangle$$
$$q_d\langle t\rangle = \dot{\theta}_d\langle t\rangle$$
$$r_d\langle t\rangle = \dot{\psi}_d\langle t\rangle$$

The perturbation forces and moments are incorporated into equations (D.14) to (D.19) as shown:

$$X_d = \frac{1}{2}\rho V^2 C_{x_d}$$
$$Y_d = \frac{1}{2}\rho V^2 C_{y_d}$$
$$Z_d = \frac{1}{2}\rho V^2 C_{z_d}$$
$$\tilde{L}_d = \frac{1}{2}\rho V^2 b C_{l_d}$$
$$M_d = \frac{1}{2}\rho V^2 \bar{c} C_{m_d}$$
$$N_d = \frac{1}{2}\rho V^2 b C_{n_d}$$

where V is approximated by V_E. Rearranging into matrix form gives the set of equations used for modelling the accelerations of a trailing aircraft of a two ship formation flying through turbulence.

$$
\begin{bmatrix}
m & 0 & 0 & 0 & 0 & 0 & 0 & 0 & 0 \\
0 & m & 0 & 0 & 0 & 0 & 0 & 0 & 0 \\
0 & 0 & m & 0 & 0 & 0 & 0 & 0 & 0 \\
0 & 0 & 0 & I_x & 0 & -I_{xz} & 0 & 0 & 0 \\
0 & 0 & 0 & 0 & I_y & 0 & 0 & 0 & 0 \\
0 & 0 & 0 & -I_{xz} & 0 & I_z & 0 & 0 & 0 \\
0 & 0 & 0 & 0 & 0 & 0 & 1 & 0 & 0 \\
0 & 0 & 0 & 0 & 0 & 0 & 0 & 1 & 0 \\
0 & 0 & 0 & 0 & 0 & 0 & 0 & 0 & 1
\end{bmatrix}
\begin{Bmatrix}
\dot{u} \\ \dot{v} \\ \dot{w} \\ \dot{p} \\ \dot{q} \\ \dot{r} \\ \dot{\phi} \\ \dot{\theta} \\ \dot{\psi}
\end{Bmatrix} \cdots
$$

$$
= \begin{bmatrix}
\frac{2C_x\bar{q}S}{V_E} & \frac{\bar{q}S}{V_E}\frac{\partial C_x}{\partial \beta} & \frac{\bar{q}S}{V_E}\frac{\partial C_x}{\partial \alpha} & 0 & \frac{\bar{q}S\bar{c}}{2V_E}\frac{\partial C_x}{\partial \hat{q}} - mw_{0_f} & 0 & 0 & -mg & 0 \\
0 & \frac{\bar{q}S}{V_E}\frac{\partial C_y}{\partial \beta} & 0 & \frac{\bar{q}Sb}{2V_E}\frac{\partial C_y}{\partial \hat{p}} + mw_{0_f} & 0 & \frac{\bar{q}Sb}{2V_E}\frac{\partial C_y}{\partial \hat{r}} + mu_{0_f} & mg & 0 & 0 \\
\frac{2C_x\bar{q}S}{V_E} + \frac{\bar{q}S}{V_E}\frac{\partial C_x}{\partial \hat{u}} & \frac{\bar{q}S}{V_E}\frac{\partial C_x}{\partial \beta} & \frac{\bar{q}S}{V_E}\frac{\partial C_x}{\partial \alpha} & 0 & \frac{\bar{q}S\bar{c}}{2V_E}\frac{\partial C_x}{\partial \hat{q}} + mu_{0_f} & 0 & 0 & 0 & 0 \\
0 & \frac{\bar{q}Sb}{V_E}\frac{\partial C_l}{\partial \beta} & 0 & \frac{\bar{q}Sb^2}{2V_E}\frac{\partial C_l}{\partial \hat{p}} & 0 & \frac{\bar{q}Sb^2}{2V_E}\frac{\partial C_l}{\partial \hat{r}} & 0 & 0 & 0 \\
\frac{\bar{q}S\bar{c}}{V_E}\frac{\partial C_m}{\partial \hat{u}} & 0 & \frac{\bar{q}S\bar{c}}{V_E}\frac{\partial C_m}{\partial \alpha} & 0 & \frac{\bar{q}S\bar{c}^2}{2V_E}\frac{\partial C_m}{\partial \hat{q}} & 0 & 0 & 0 & 0 \\
0 & \frac{\bar{q}Sb}{V_E}\frac{\partial C_n}{\partial \beta} & 0 & \frac{\bar{q}Sb^2}{2V_E}\frac{\partial C_n}{\partial \hat{p}} & 0 & \frac{\bar{q}Sb^2}{2V_E}\frac{\partial C_n}{\partial \hat{r}} & 0 & 0 & 0 \\
0 & 0 & 0 & 1 & 0 & 0 & 0 & 0 & 0 \\
0 & 0 & 0 & 0 & 1 & 0 & 0 & 0 & 0 \\
0 & 0 & 0 & 0 & 0 & 1 & 0 & 0 & 0
\end{bmatrix}
\begin{Bmatrix}
u \\ v \\ w \\ p \\ q \\ r \\ \phi \\ \theta \\ \psi
\end{Bmatrix} \cdots
$$

$$
- \begin{bmatrix}
\frac{2C_x\bar{q}S}{V_E} & 0 & \frac{\bar{q}S}{V_E}\frac{\partial C_x}{\partial \alpha} & 0 & \frac{\bar{q}S\bar{c}}{2V_E}\frac{\partial C_x}{\partial \hat{q}} & 0 \\
0 & \frac{\bar{q}S}{V_E}\frac{\partial C_y}{\partial \beta} & 0 & \frac{\bar{q}Sb}{2V_E}\frac{\partial C_y}{\partial \hat{p}} & 0 & \frac{\bar{q}Sb}{2V_E}\frac{\partial C_y}{\partial \hat{r}} \\
\frac{2C_x\bar{q}S}{V_E} + \frac{\bar{q}S}{V_E}\frac{\partial C_x}{\partial \hat{u}} & 0 & \frac{\bar{q}S}{V_E}\frac{\partial C_x}{\partial \alpha} & 0 & \frac{QS\bar{c}}{2V_E}\frac{\partial C_x}{\partial \hat{q}} & 0 \\
0 & \frac{\bar{q}Sb}{V_E}\frac{\partial C_l}{\partial \beta} & 0 & \frac{\bar{q}Sb^2}{2V_E}\frac{\partial C_l}{\partial \hat{p}} & 0 & \frac{\bar{q}Sb^2}{2V_E}\frac{\partial C_l}{\partial \hat{r}} \\
\frac{\bar{q}S\bar{c}}{V_E}\frac{\partial C_m}{\partial \hat{u}} & 0 & \frac{\bar{q}S\bar{c}}{V_E}\frac{\partial C_m}{\partial \alpha} & 0 & \frac{\bar{q}S\bar{c}^2}{2V_E}\frac{\partial C_m}{\partial \hat{q}} & 0 \\
0 & \frac{\bar{q}Sb}{V_E}\frac{\partial C_n}{\partial \beta} & 0 & \frac{\bar{q}Sb^2}{2V_E}\frac{\partial C_n}{\partial \hat{p}} & 0 & \frac{\bar{q}Sb^2}{2V_E}\frac{\partial C_n}{\partial \hat{r}}
\end{bmatrix}
\begin{Bmatrix}
u_g \\ v_g \\ w_g \\ p_g \\ q_g \\ r_g
\end{Bmatrix}^B \cdots
$$

$$
+ \begin{bmatrix}
\frac{\partial C_x}{\partial \delta\delta_{th}} & 0 & 0 & 0 \\
0 & \frac{\partial C_y}{\partial \delta\delta_a} & 0 & \frac{\partial C_y}{\partial \delta\delta_r} \\
\frac{\partial C_x}{\partial \delta\delta_{th}} & 0 & \frac{\partial C_x}{\partial \delta\delta_e} & 0 \\
0 & \frac{\partial C_l}{\partial \delta\delta_a} & 0 & \frac{\partial C_l}{\partial \delta\delta_r} \\
\frac{\partial C_m}{\partial \delta\delta_{th}} & 0 & \frac{\partial C_m}{\partial \delta\delta_e} & 0 \\
0 & \frac{\partial C_l}{\partial \delta\delta_a} & 0 & \frac{\partial C_l}{\partial \delta\delta_r}
\end{bmatrix}
\cdot
\begin{Bmatrix}
\delta\delta_{th} \\ \delta\delta_a \\ \delta\delta_e \\ \delta\delta_r
\end{Bmatrix}
+ \mathbf{R}_{BI}
\begin{Bmatrix}
\bar{q}S\left(\Delta C_D\langle \eta_{eff}, \zeta_{eff}\rangle - \Delta C_D\langle \eta, \zeta\rangle\right) \\
\bar{q}S\left(\Delta C_S\langle \eta_{eff}, \zeta_{eff}\rangle - \Delta C_S\langle \eta, \zeta\rangle\right) \\
\bar{q}S\left(\Delta C_L\langle \eta_{eff}, \zeta_{eff}\rangle - \Delta C_L\langle \eta, \zeta\rangle\right) \\
\bar{q}Sb\left(\Delta C_l\langle \eta_{eff}, \zeta_{eff}\rangle - \Delta C_l\langle \eta, \zeta\rangle\right) \\
\bar{q}S\bar{c}\left(\Delta C_m\langle \eta_{eff}, \zeta_{eff}\rangle - \Delta C_m\langle \eta, \zeta\rangle\right) \\
\bar{q}Sb\left(\Delta C_n\langle \eta_{eff}, \zeta_{eff}\rangle - \Delta C_n\langle \eta, \zeta\rangle\right)
\end{Bmatrix}
\tag{D.43}
$$

Appendix E: Acceleration Spectral Densities

E.1 CG Accelerations for Different Turbulence Intensities and Separations

In all cases, zero vertical separation is assumed while three lateral separations are identified for investigation. These lateral separations were chosen based on preliminary runs which showed the maximum increase in variance ratio, κ, at $\eta = 0.7$ for moderate turbulence and $\eta = 0.76$ for light turbulence. A third lateral separation of $\eta = 0.9$ was also chosen to identify the decrease in severity for a small outboard shift in lateral separation. The graphs are arranged in ascending order of turbulence intensity while grouping the results for the three different relative separations for each level of turbulence intensity. This aids comparison of the graphs since the range in each component's log graph of identical turbulence intensity has the same scale.

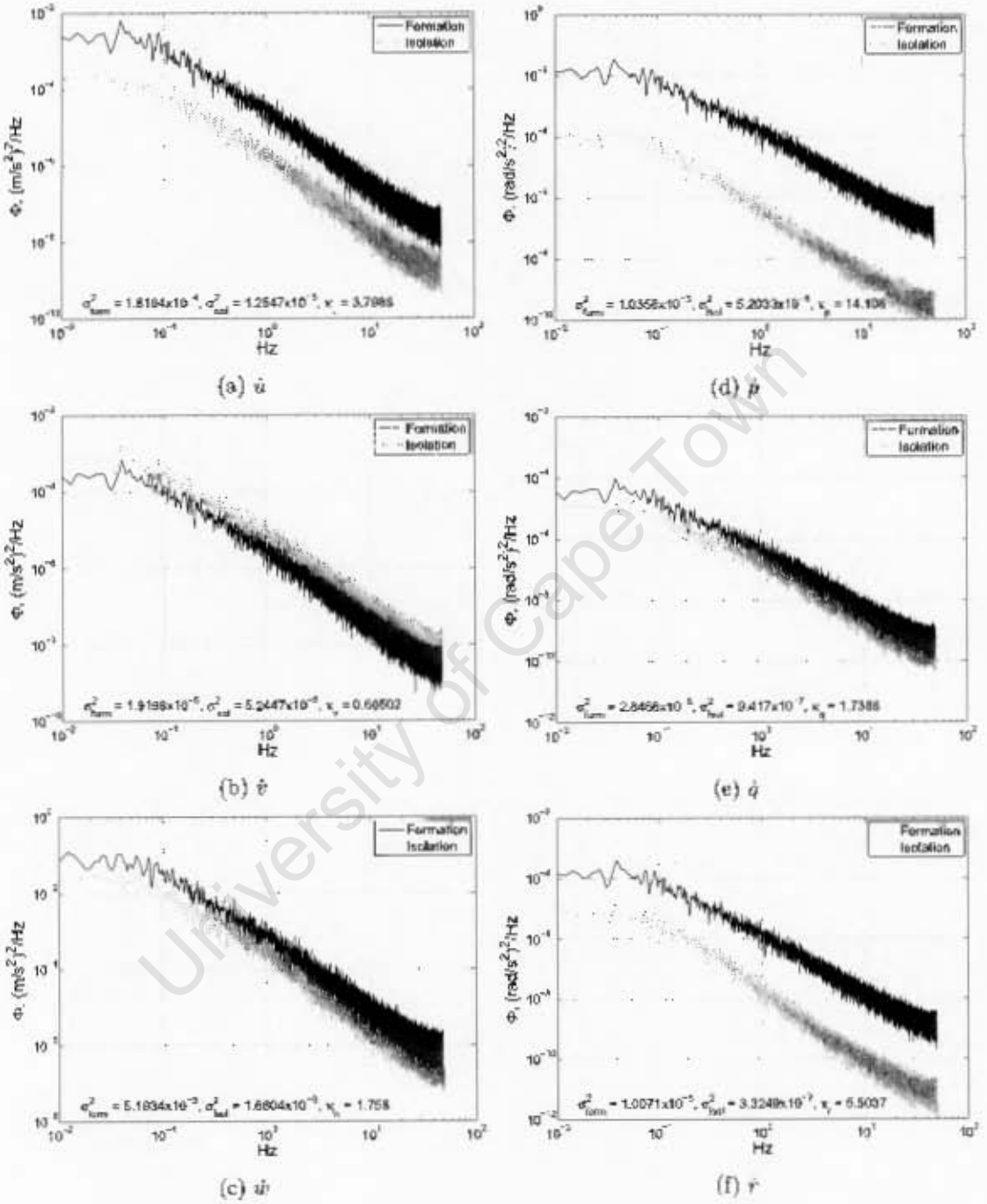

Figure E.1: Spectral Density Estimations of the c.g. linear accelerations and angular accelerations about the c.g. in light turbulence, $\sigma = 0.2$ m/s, for flight in isolation and for formation flight at $\eta = 0.7$

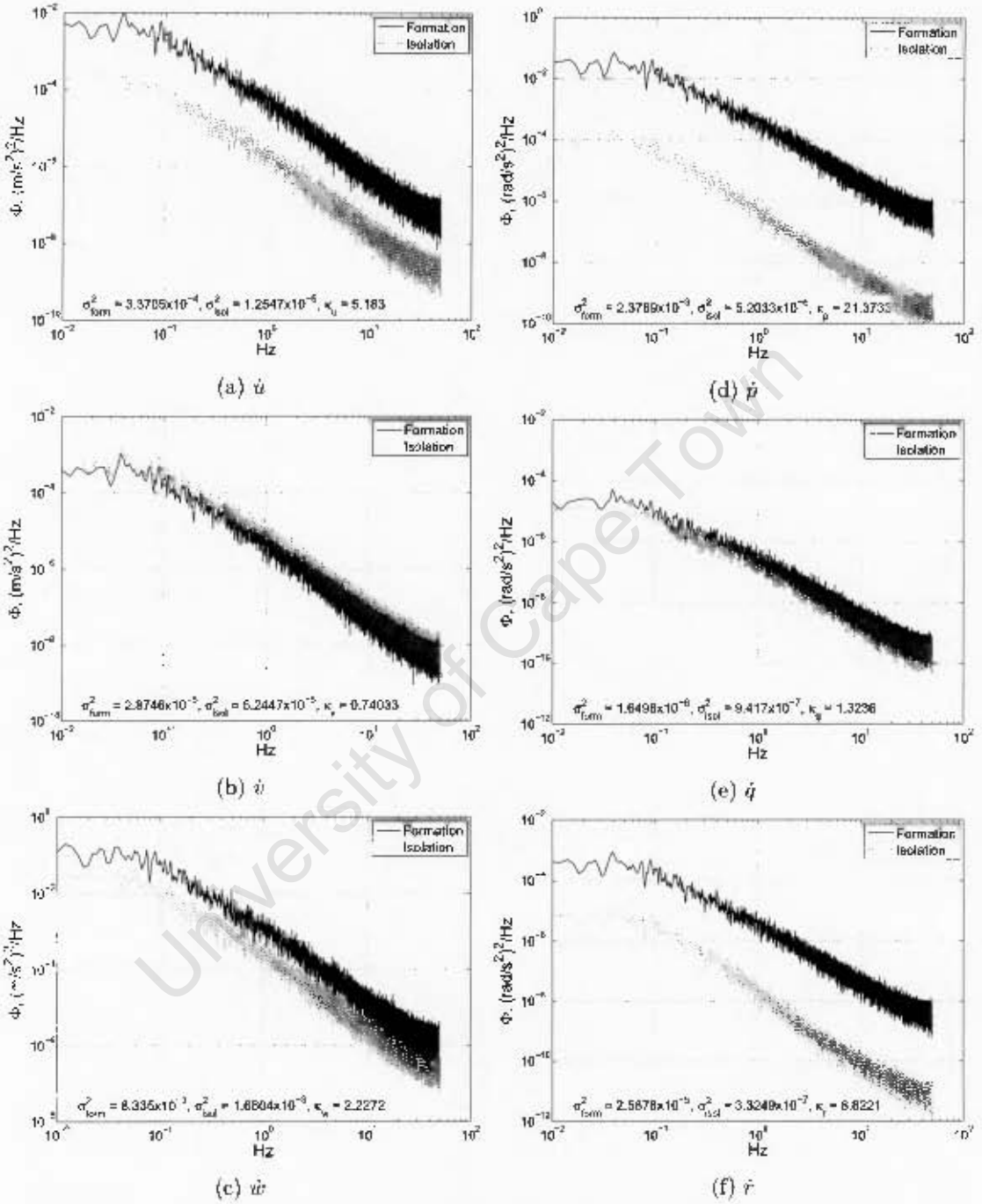

Figure E.2: Spectral Density Estimations of the c.g. linear accelerations and angular accelerations about the c.g. in light turbulence, $\sigma = 0.2$ m/s, for flight in isolation and for formation flight at $\eta = 0.76$.

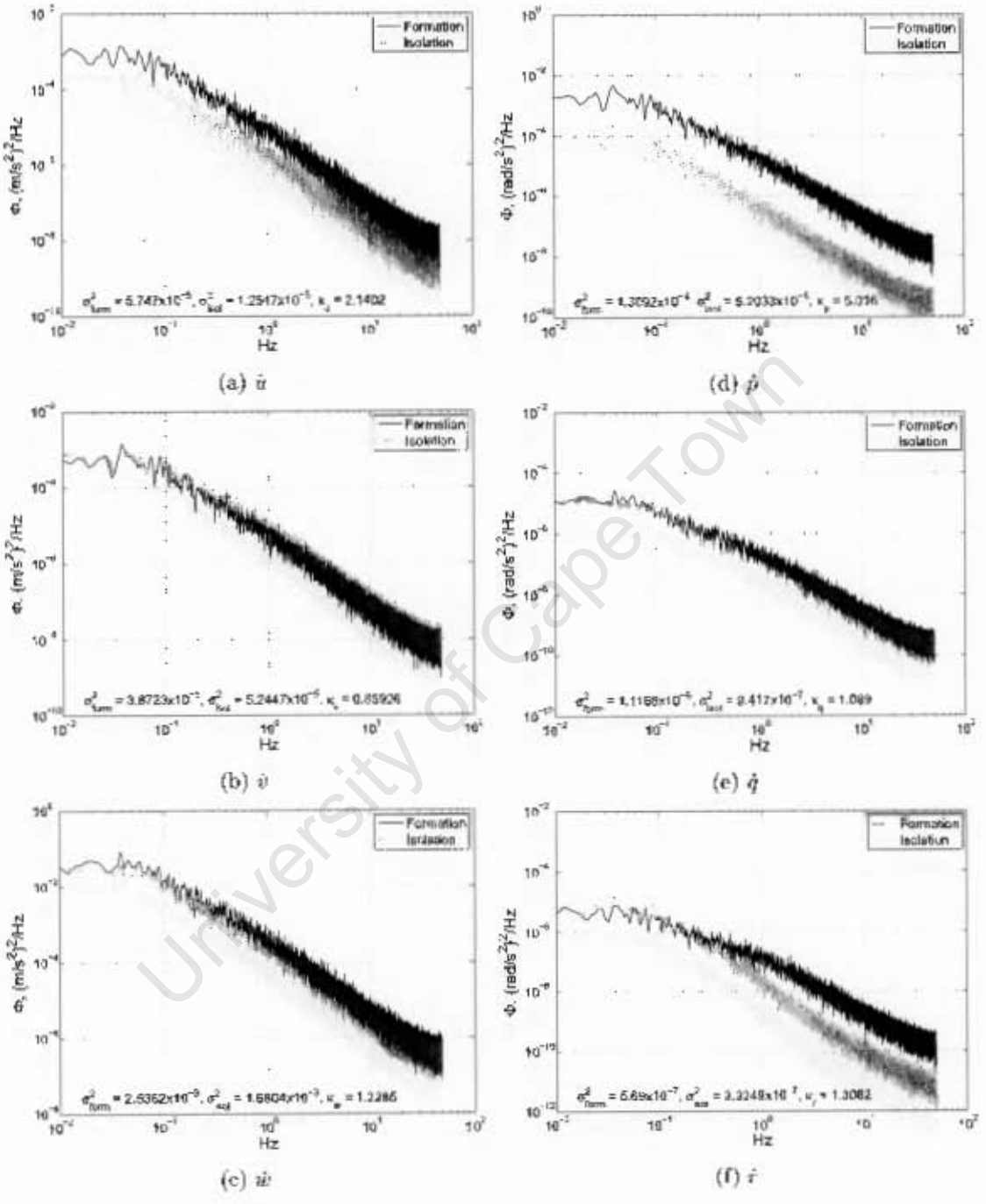

Figure E.3: Spectral Density Estimations of the c.g. linear accelerations and angular accelerations about the c.g. in light turbulence, $\sigma = 0.2$ m/s, for flight in isolation and for formation flight at $\eta = 0.90$.

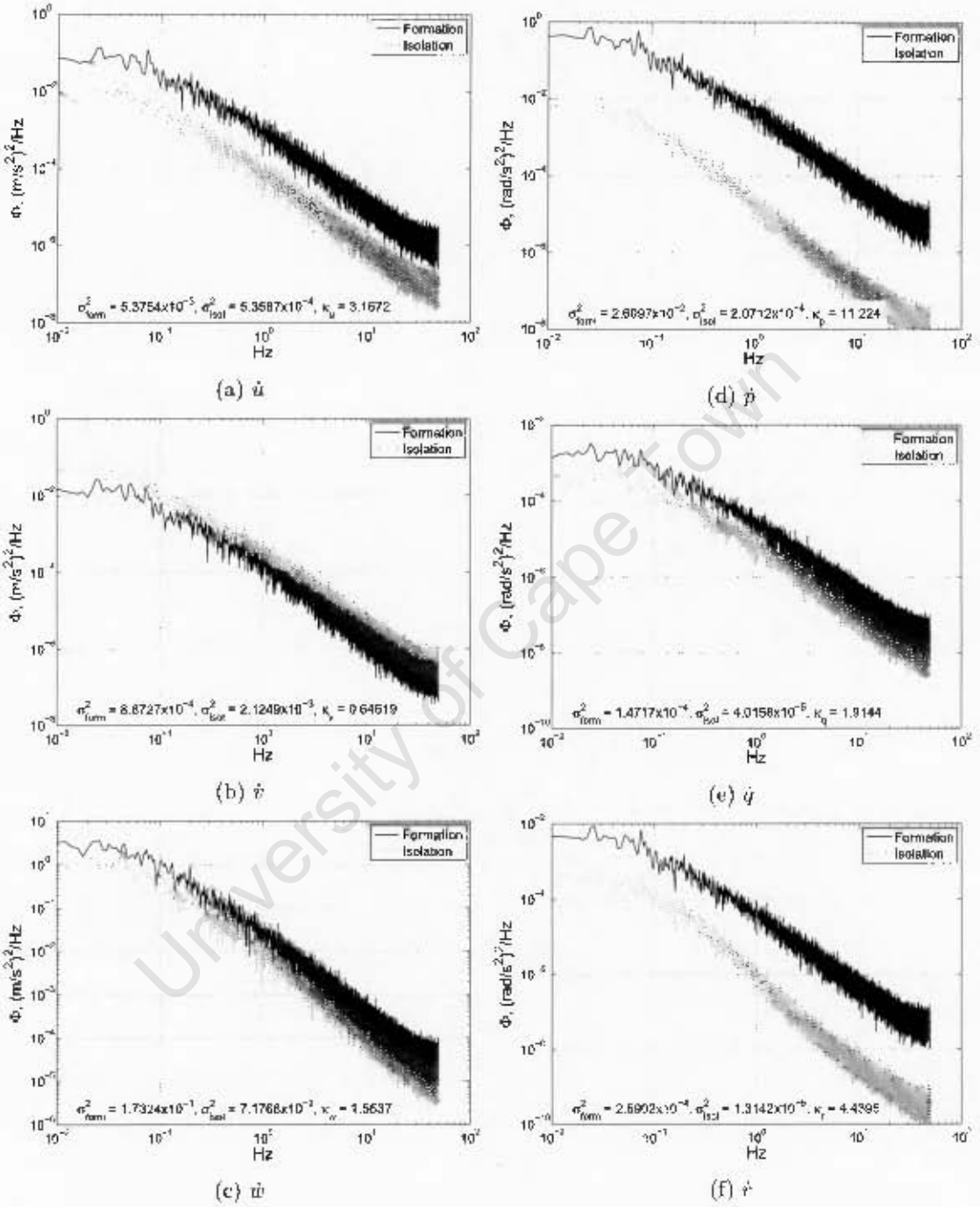

Figure E.5: Spectral Density Estimations of the c.g. linear accelerations and angular accelerations about the c.g. in moderate turbulence, $\sigma = 1.3$ m/s, for flight in isolation and for formation flight at $\eta = 0.7$

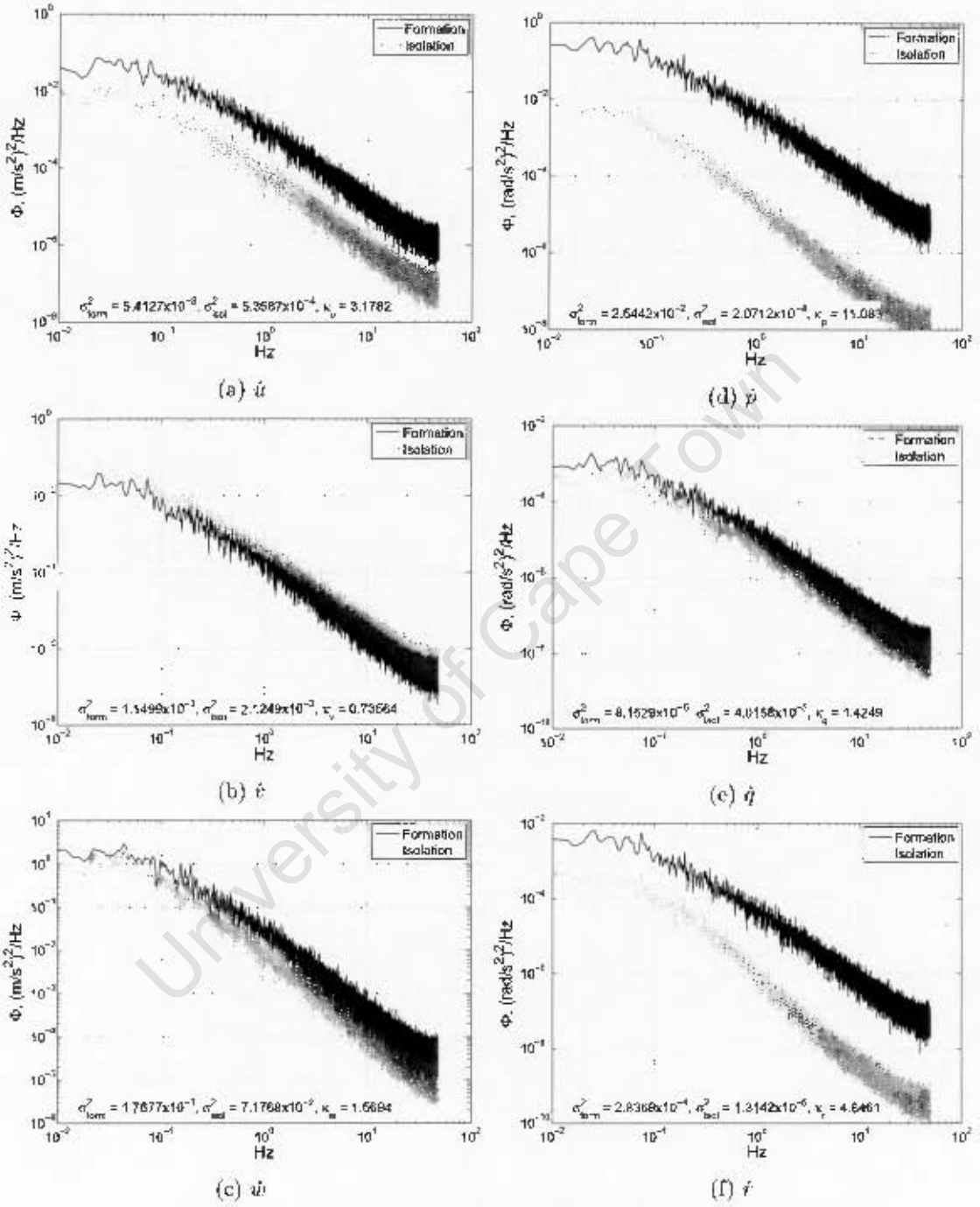

Figure E.6: Spectral Density Estimations of the c.g. linear accelerations and angular accelerations about the c.g. in moderate turbulence, $\sigma = 1.3$ m/s, for flight in isolation and for formation flight at $\eta = 0.76$.

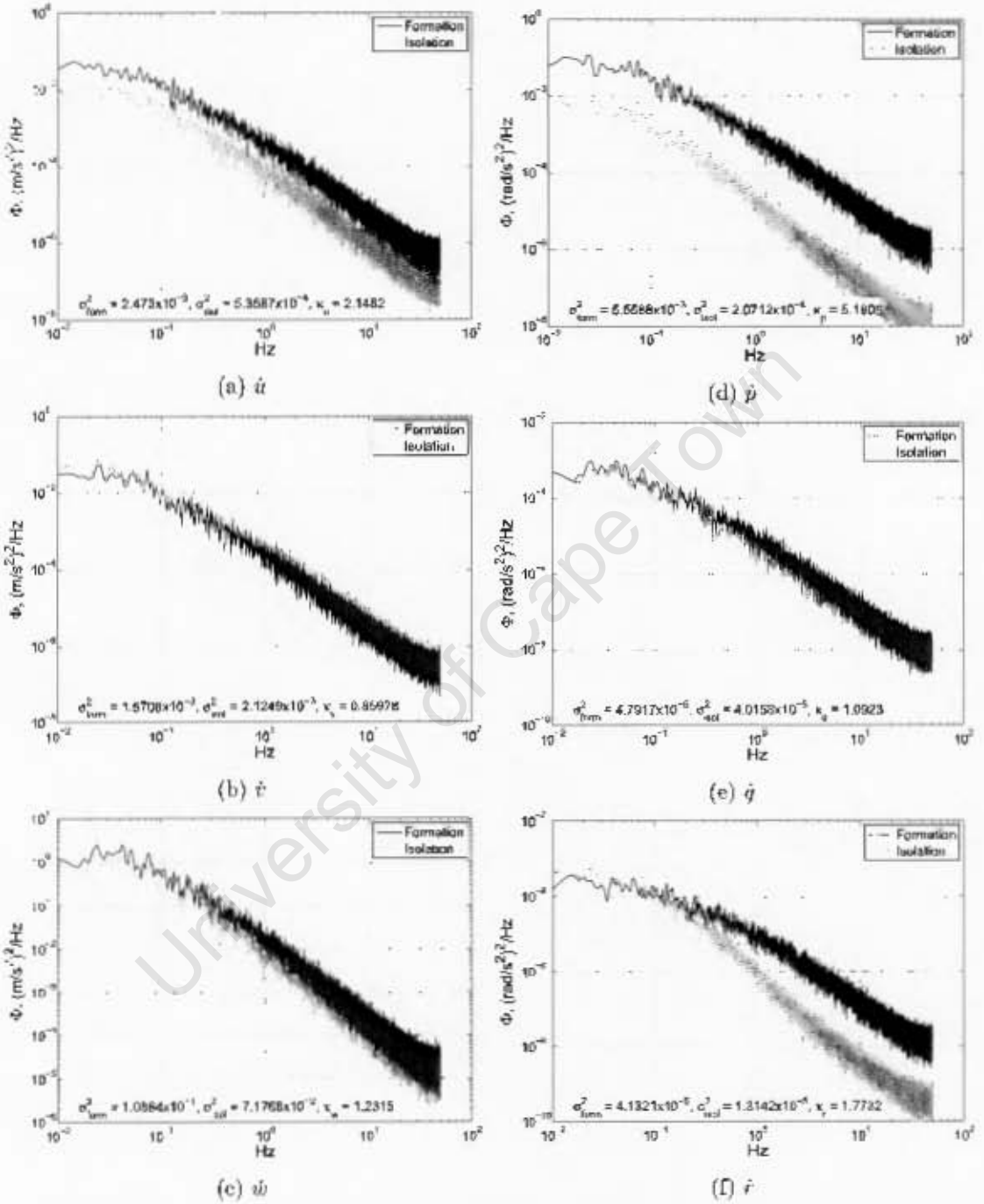

(a) $\dot{u}$ (d) $\dot{p}$

(b) $\dot{v}$ (e) $\dot{q}$

(c) $\dot{w}$ (f) $\dot{r}$

Figure E.7: Spectral Density Estimations of the c.g. linear accelerations and angular accelerations about the c.g. in moderate turbulence, $\sigma = 1.3$ m/s, for flight in isolation and for formation flight at $\eta = 0.90$.

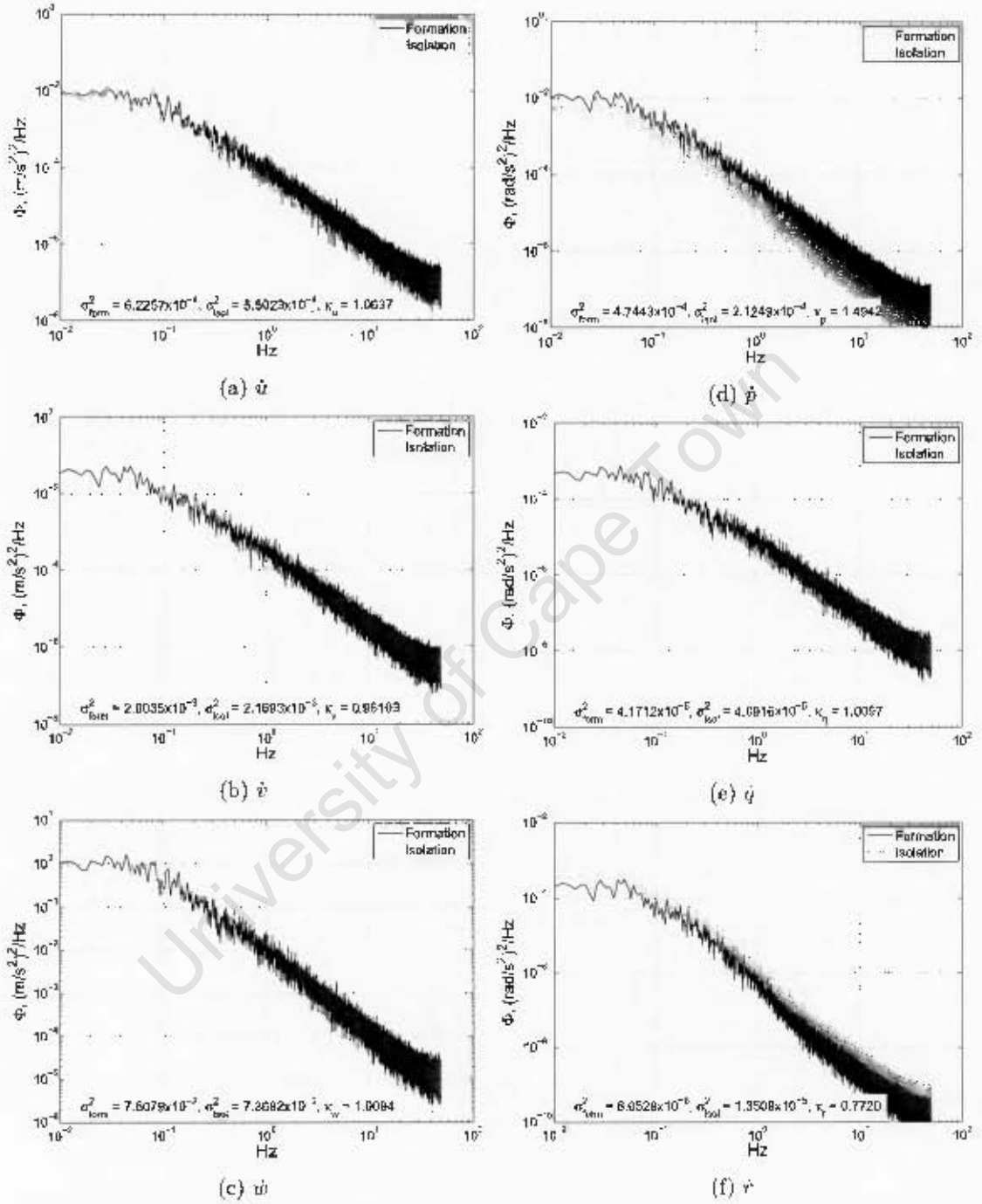

Figure E.8: Spectral Density Estimations of the c.g. linear accelerations and angular accelerations about the c.g. in moderate turbulence, $\sigma = 1.3$ m/s, for flight in isolation and for formation flight at $\eta = 1.20$.

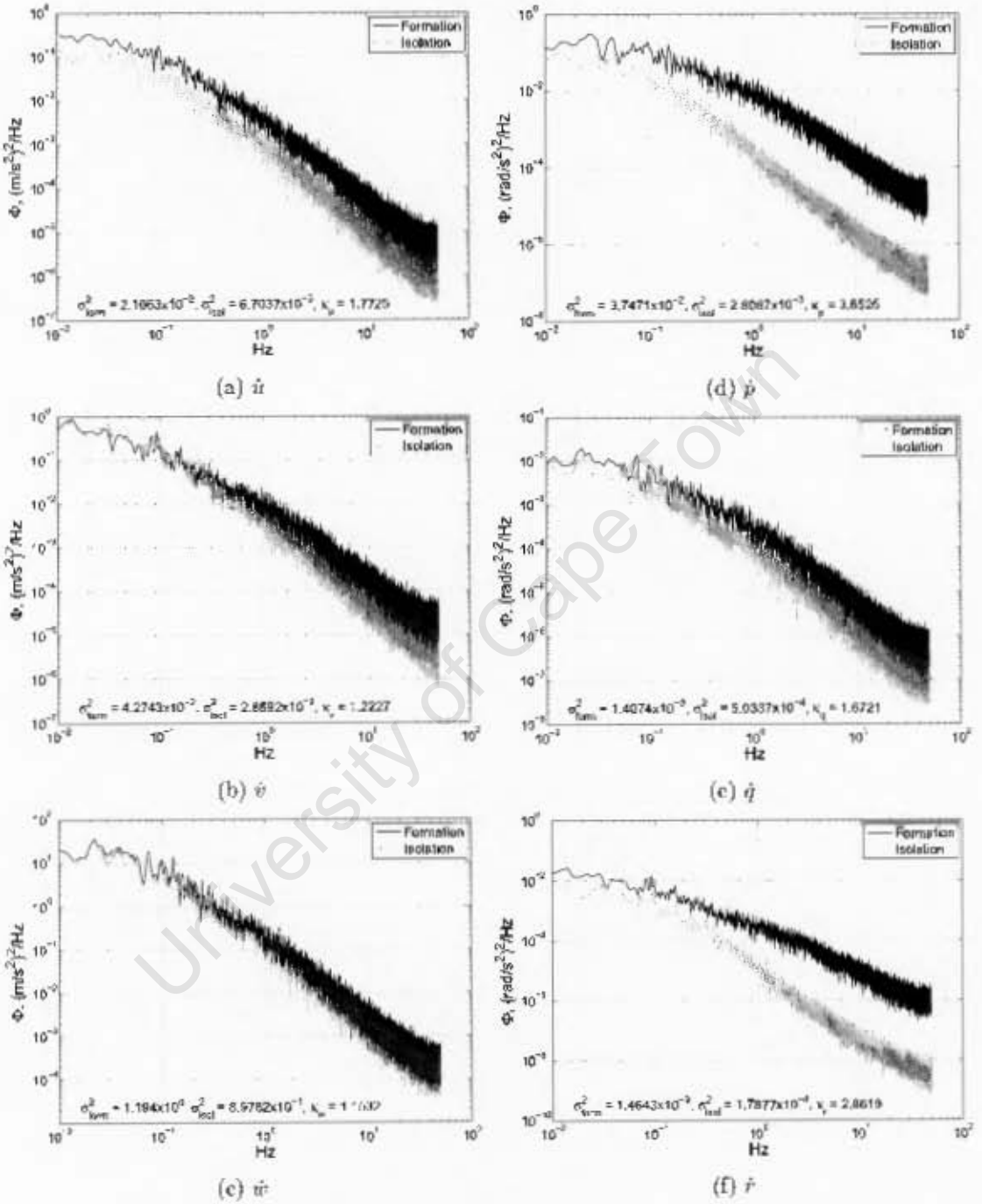

Figure E.9: Spectral Density Estimations of the c.g. linear accelerations and angular accelerations about the c.g. in severe turbulence, $\sigma = 4.7$ m/s, for flight in isolation and for formation flight at $\eta = 0.7$

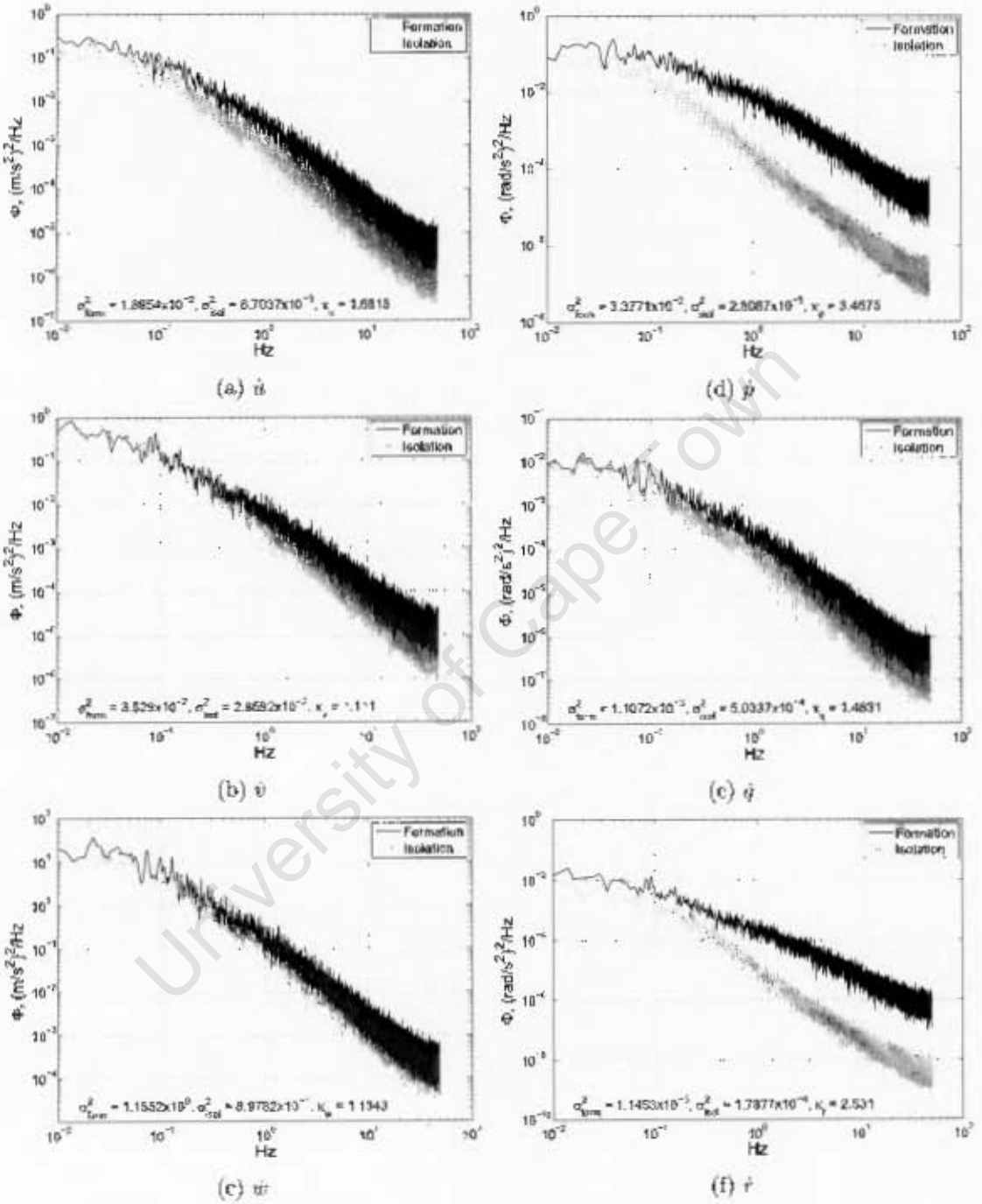

Figure E.10: Spectral Density Estimations of the c.g. linear accelerations and angular accelerations about the c.g. in severe turbulence, $\sigma = 4.7$ m/s, for flight in isolation and for formation flight at $\eta = 0.76$.

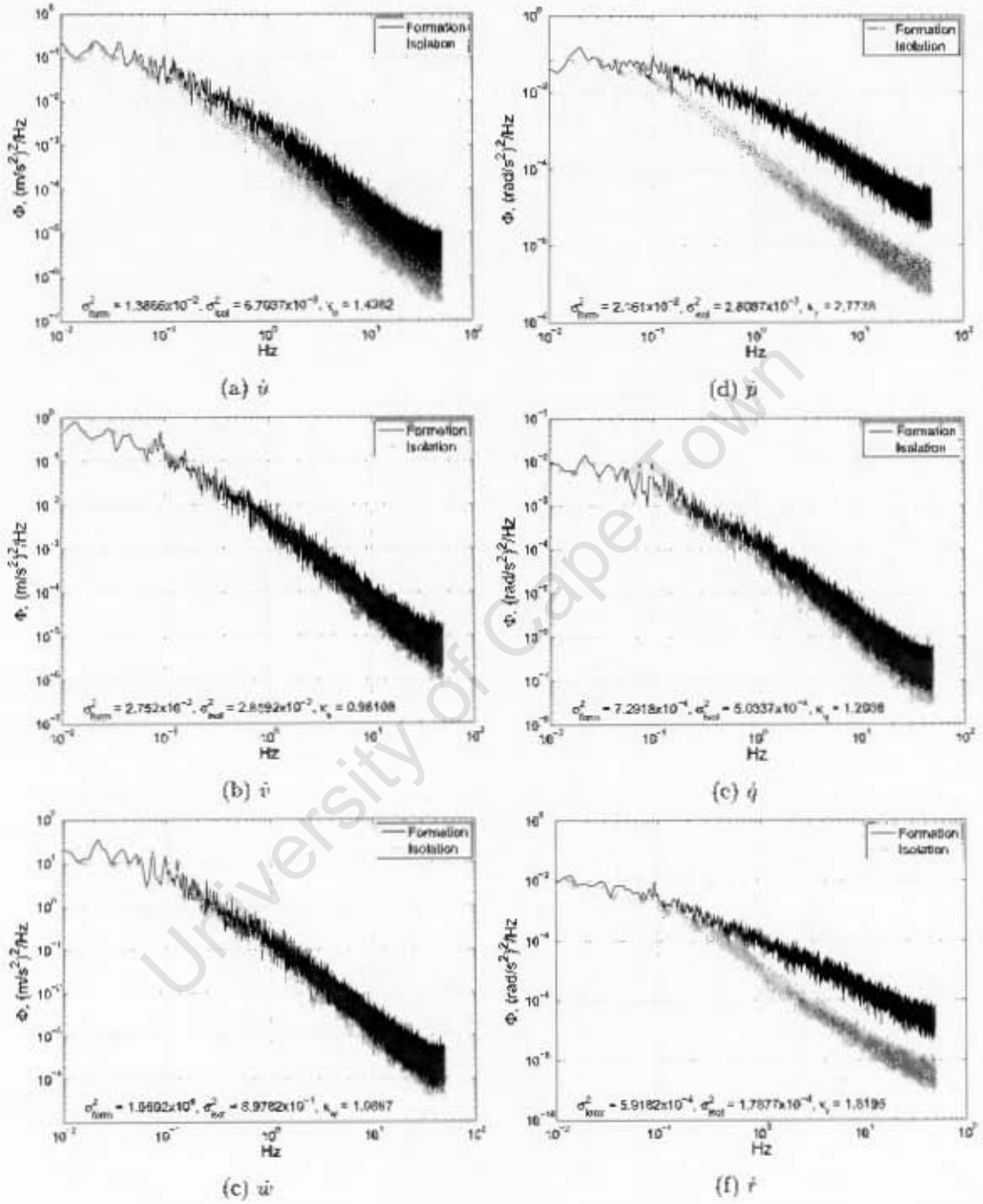

Figure E.11: Spectral Density Estimations of the c.g. linear accelerations and angular accelerations about the c.g. in severe turbulence, $\sigma = 4.7$ m/s, for flight in isolation and for formation flight at $\eta = 0.90$.

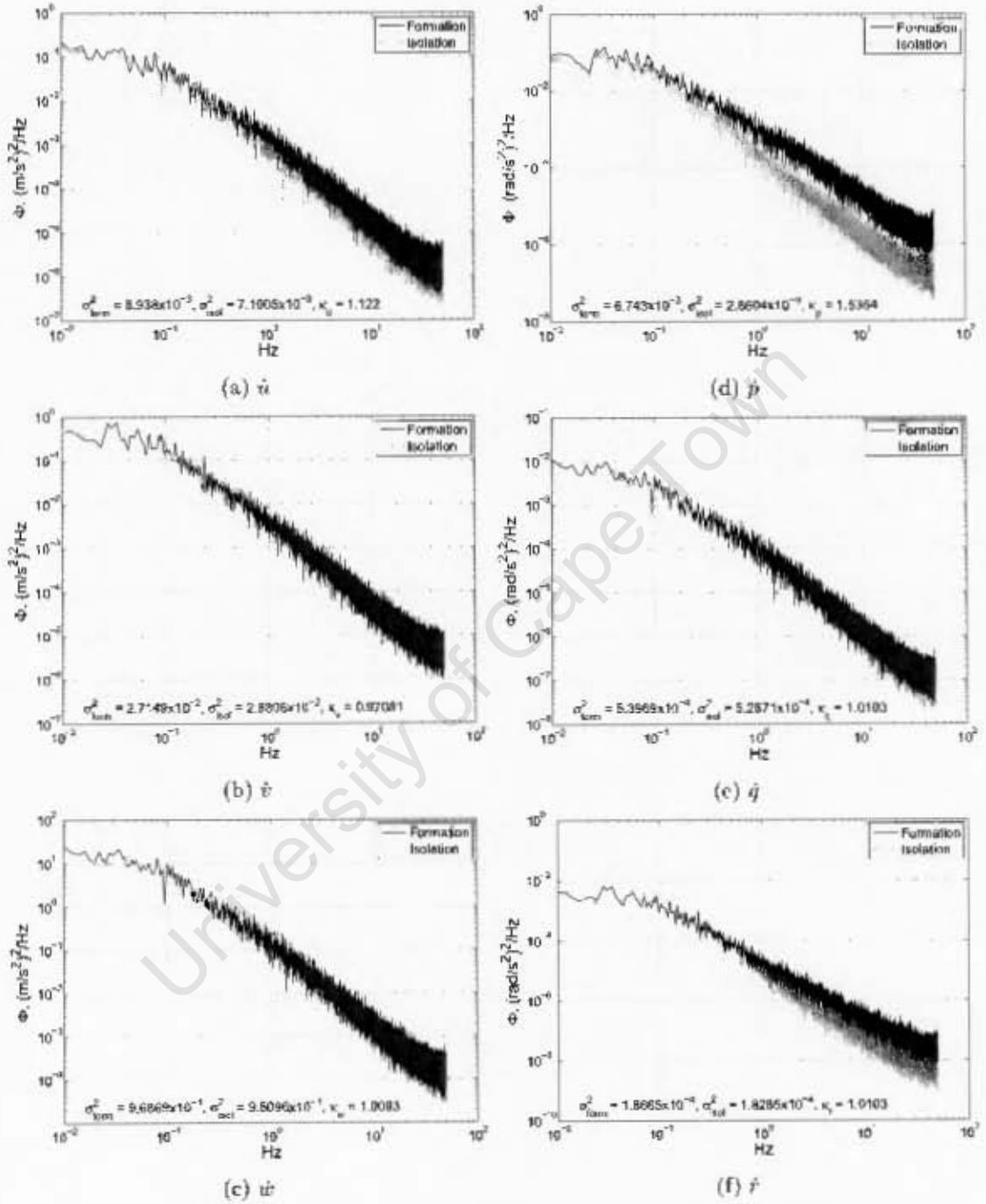

Figure E.12: Spectral Density Estimations of the c.g. linear accelerations and angular accelerations about the c.g. in severe turbulence, $\sigma = 4.7$ m/s, for flight in isolation and for formation flight at $\eta = 1.20$.

E.2 Passenger Accelerations for Different Turbulence Intensities, Separations and Seat Locations

The linear acceleration component spectral density estimations are displayed for each seat location specified in table 6.1. Angular accelerations are not shown as they do not differ from the c.g. angular accelerations (rigid body assumption). The passenger acceleration spectral density estimations for lateral relative separation of $\eta = 0.7$ in moderate turbulence intensity, σ =1.3 m/s, and lateral separation of $\eta = 0.76$ in light turbulence intensity, σ=0.2 m/s is shown. A severe turbulence case is not shown since the variance ratio, κ, indicates that there is less difference found in acceleration magnitudes between formation flight and isolated flight at this level of turbulence. The spectral density estimations are grouped in pairs in the following order: 'A' and 'F', 'B' and 'C' and 'D' and 'E' are grouped together. This is simply to aid comparison between cases which are deemed most likely comparable.

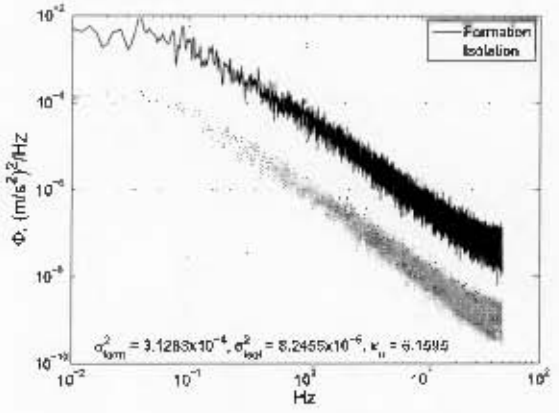

(a) $\dot{u}$

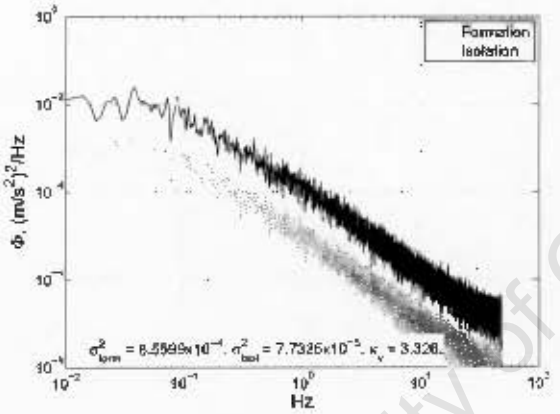

(b) $\dot{v}$

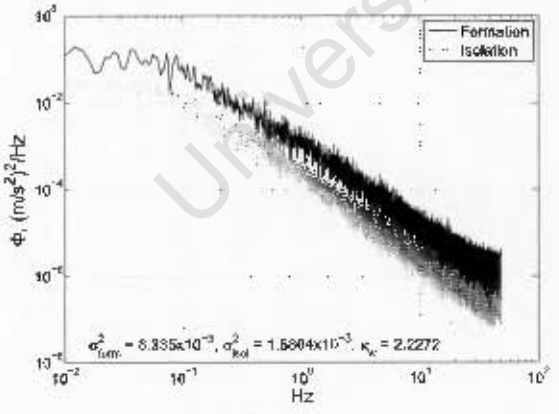

(c) $\dot{w}$

Figure E.13: Passenger linear acceleration spectral densities at seat location 'A' in light turbulence, $\sigma = 0.2$ m/s, at $\eta = 0.76$.

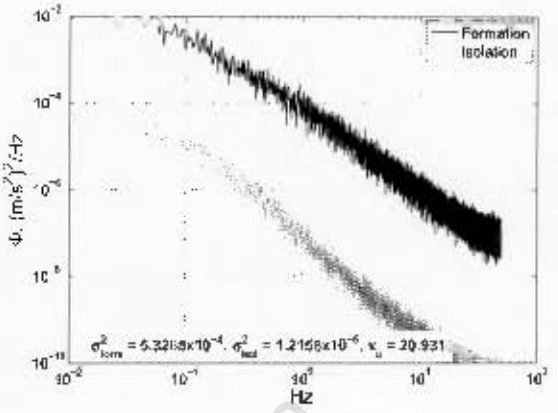

(a) $\dot{u}$

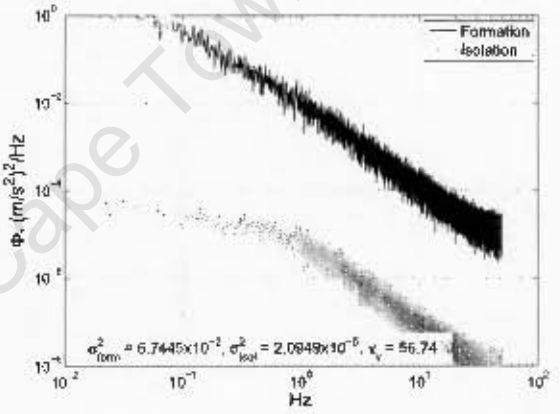

(b) $\dot{v}$

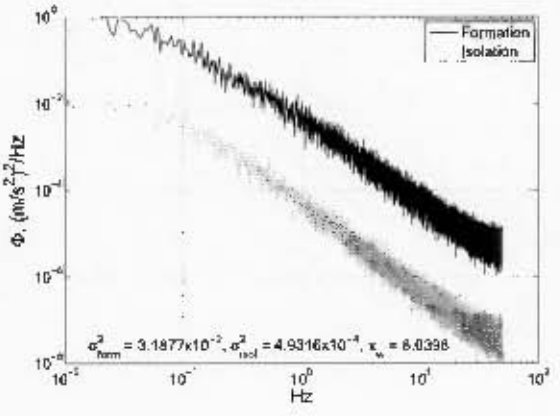

(c) $\dot{w}$

Figure E.14: Passenger linear acceleration spectral densities at seat location 'I' in light turbulence, $\sigma = 0.2$ m/s, at $\eta = 0.76$.

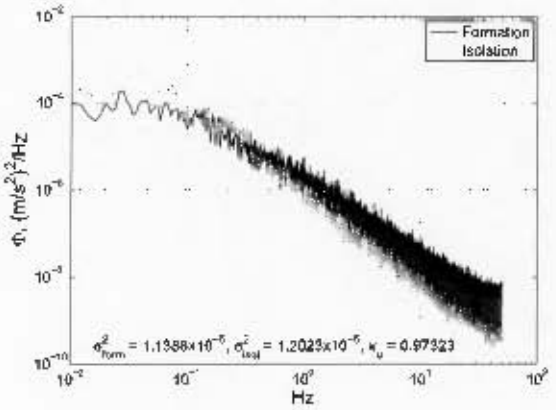

(a) $\ddot{u}$

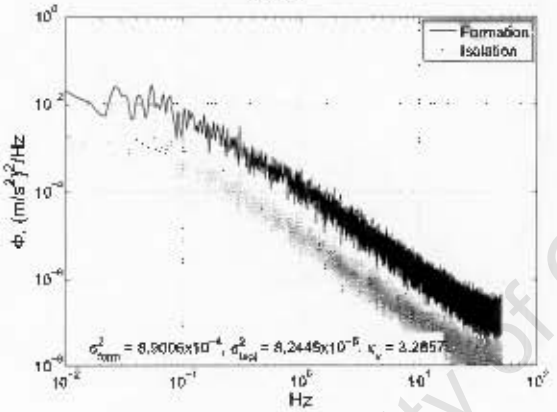

(b) $\ddot{v}$

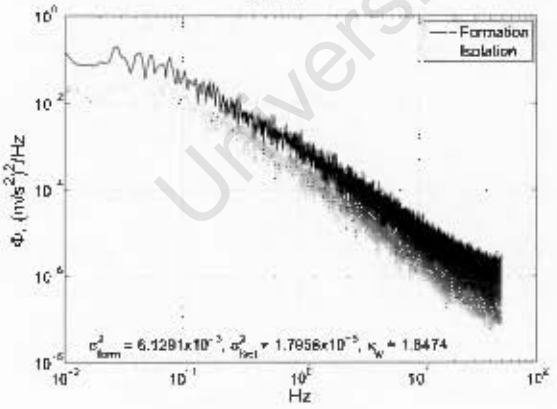

(c) $\ddot{w}$

Figure E.15: Passenger linear acceleration spectral densities at seat location 'B' in light turbulence, $\sigma = 0.2$ m/s, at $\eta = 0.76$.

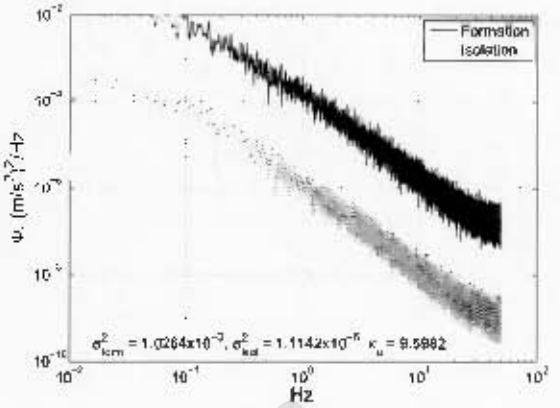

(a) $\ddot{u}$

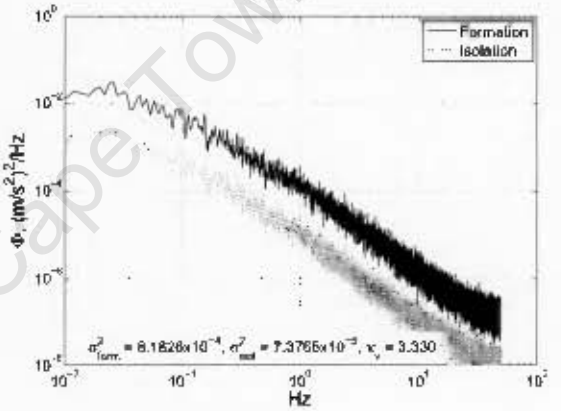

(b) $\ddot{v}$

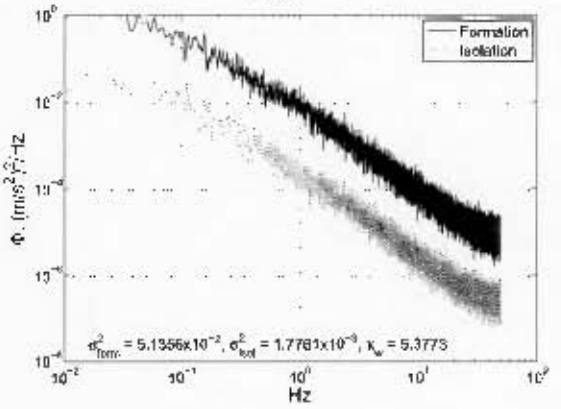

(c) $\ddot{w}$

Figure E.16: Passenger linear acceleration spectral densities at seat location 'C' in light turbulence, $\sigma = 0.2$ m/s, at $\eta = 0.76$.

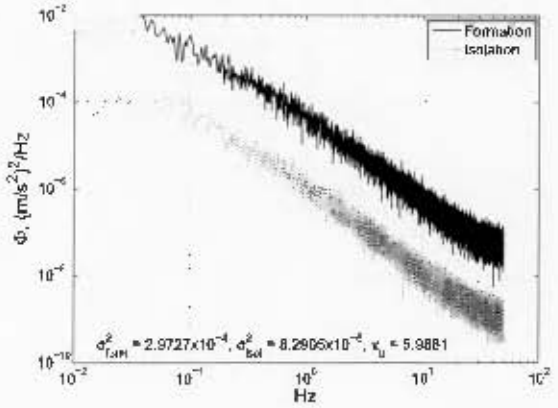

(a) $\dot{u}$

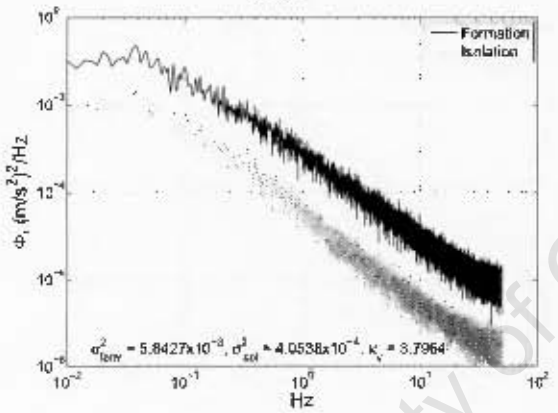

(b) $\dot{v}$

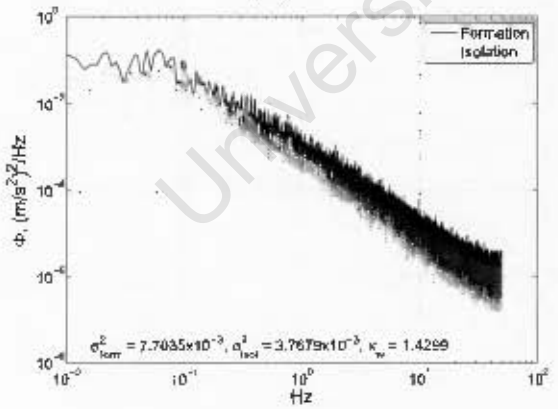

(c) $\dot{w}$

Figure E.17: Passenger linear acceleration spectral densities at seat location 'D' in light turbulence, $\sigma = 0.2$ m/s, at $\eta = 0.76$.

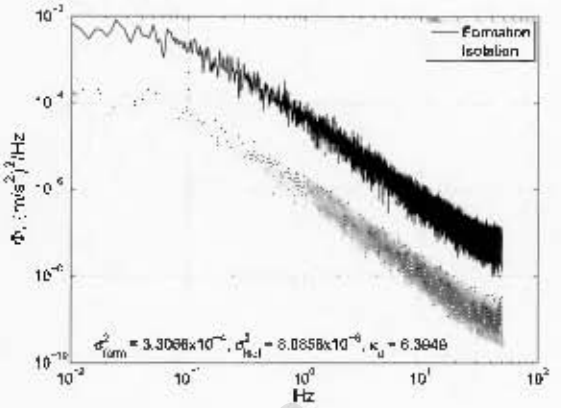

(a) $\dot{u}$

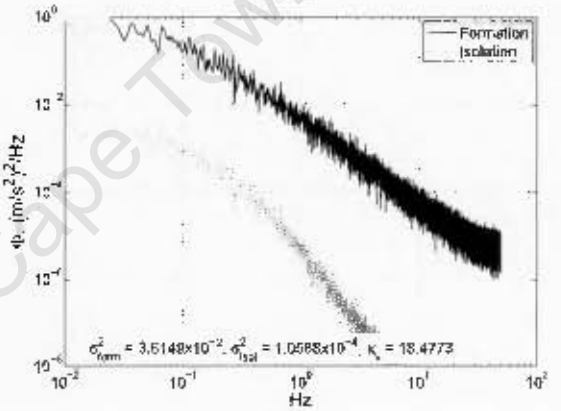

(b) $\dot{v}$

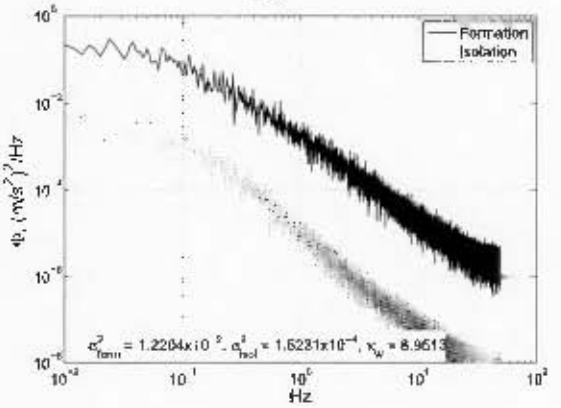

(c) $\dot{w}$

Figure E.18: Passenger linear acceleration spectral densities at seat location 'E' in light turbulence, $\sigma = 0.2$ m/s, at $\eta = 0.76$.

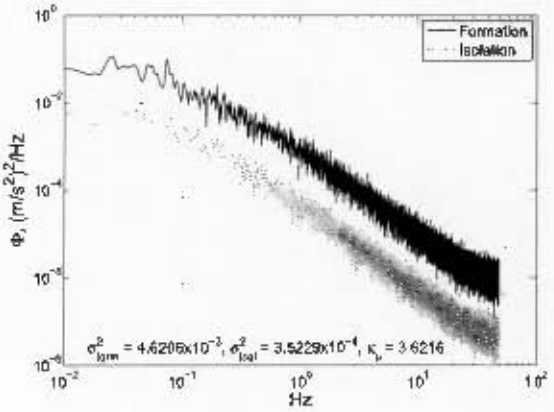

(a) $\dot{u}$

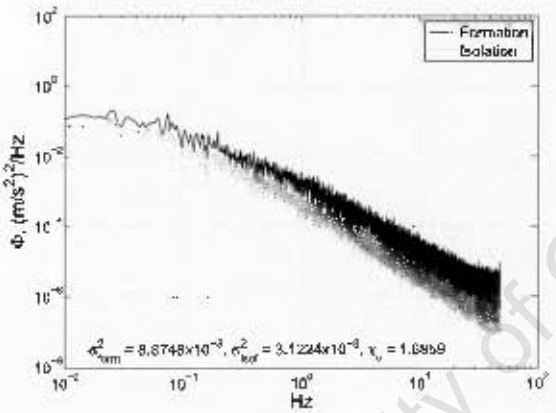

(b) $\dot{v}$

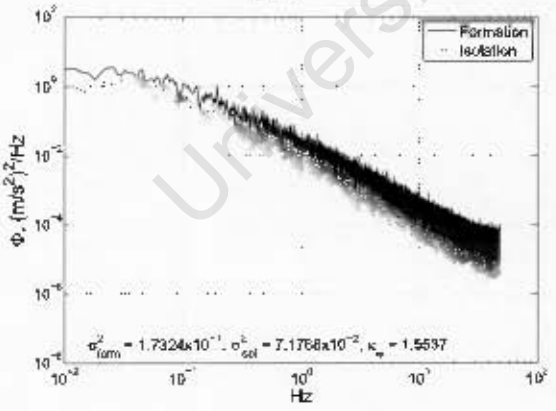

(c) $\dot{w}$

Figure E.19: Passenger linear acceleration spectral densities at seat location 'A' in moderate turbulence, $\sigma = 1.3$ m/s, at $\eta = 0.7$.

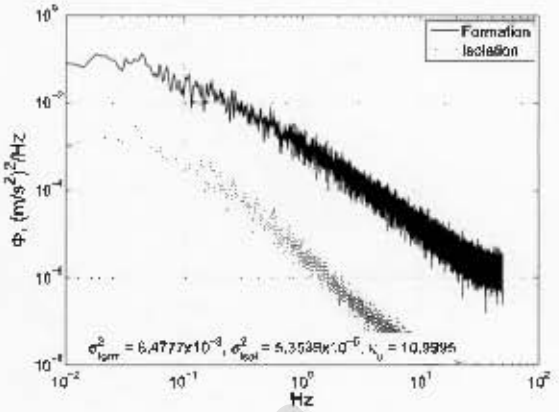

(a) $\dot{u}$

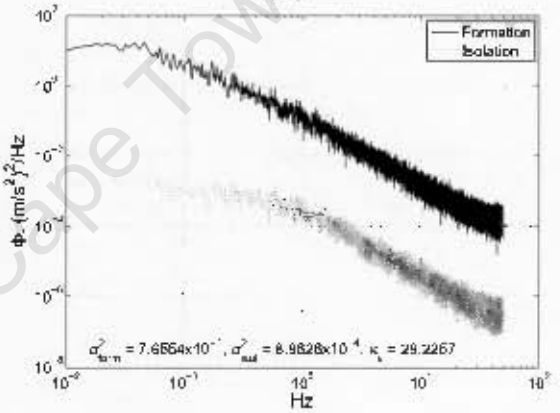

(b) $\dot{v}$

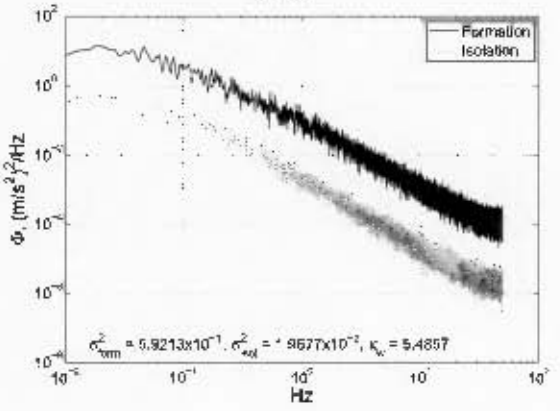

(c) $\dot{w}$

Figure E.20: Passenger linear acceleration spectral densities at seat location 'F' in moderate turbulence, $\sigma = 1.3$ m/s, at $\eta = 0.7$.

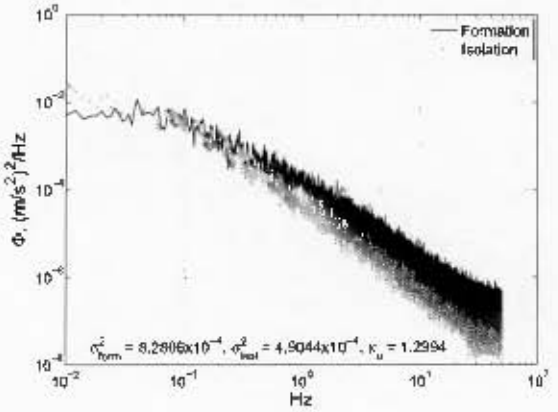

(a) $\dot{u}$

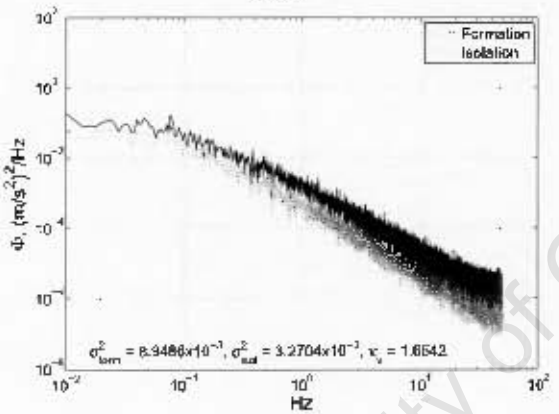

(b) $\dot{v}$

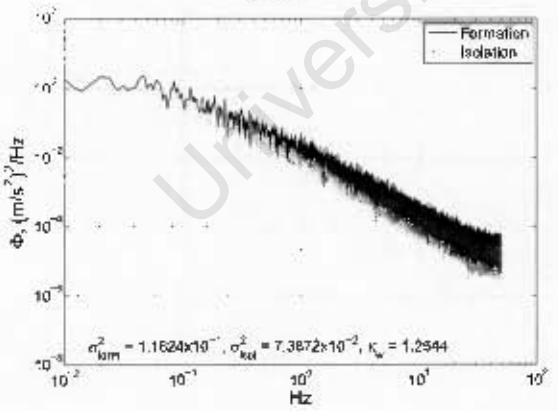

(c) $\dot{w}$

Figure E.21: Passenger linear acceleration spectral densities at seat location 'B' in moderate turbulence, $\sigma = 1.3$ m/s, at $\eta = 0.7$.

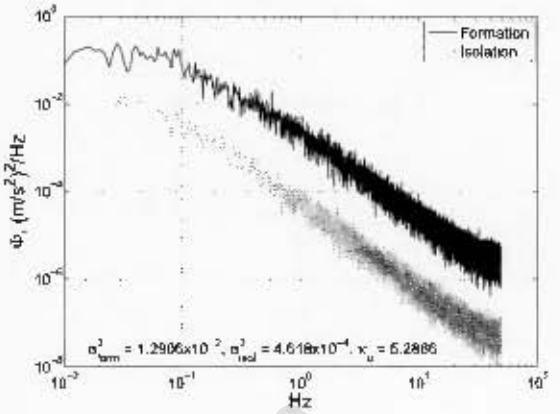

(a) $\dot{u}$

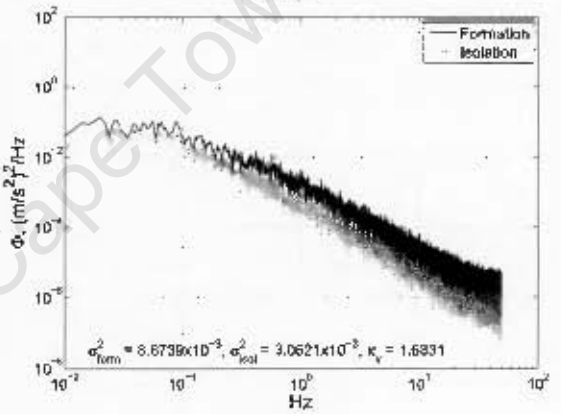

(b) $\dot{v}$

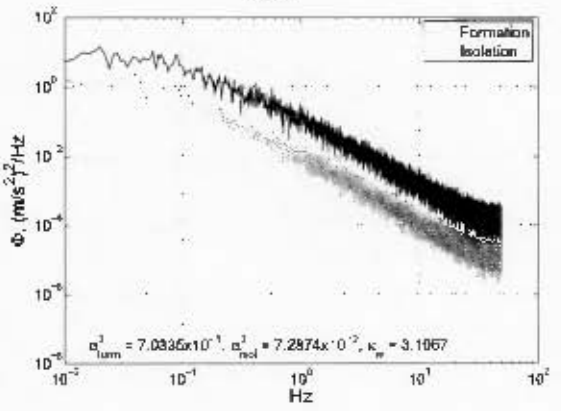

(c) $\dot{w}$

Figure E.22: Passenger linear acceleration spectral densities at seat location 'C' in moderate turbulence, $\sigma = 1.3$ m/s, at $\eta = 0.7$.

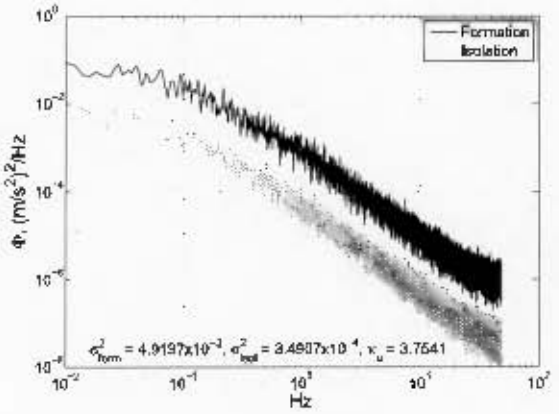

(a) $\dot{u}$

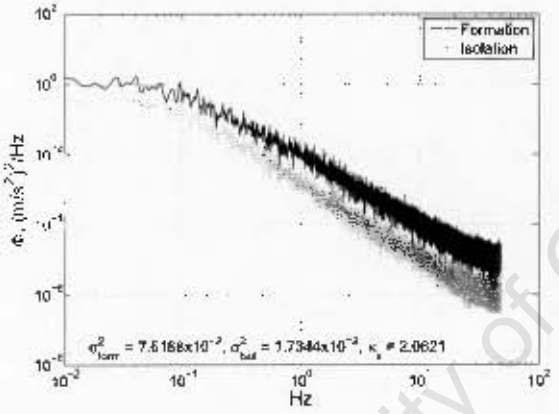

(b) $\dot{v}$

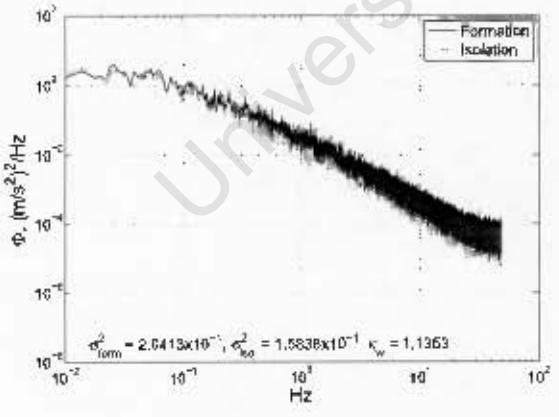

(c) $\dot{w}$

Figure E.23: Passenger linear acceleration spectral densities at seat location 'D' in moderate turbulence, $\sigma = 1.3$ m/s, at $\eta = 0.7$.

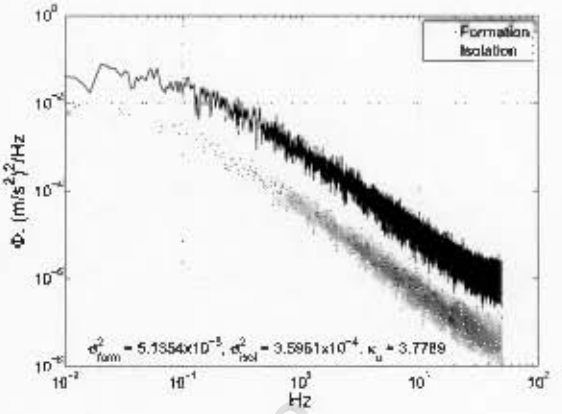

(a) $\dot{u}$

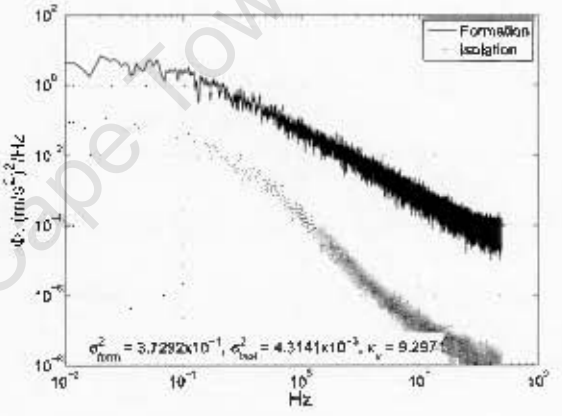

(b) $\dot{v}$

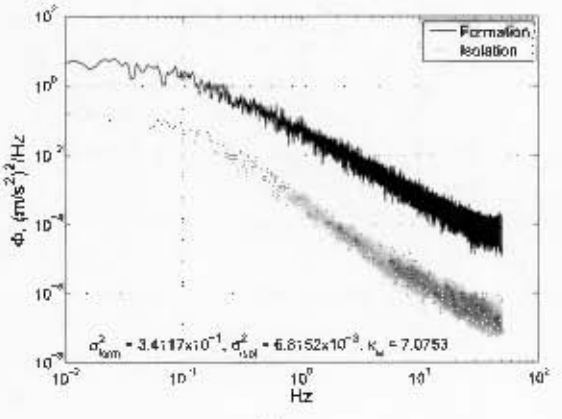

(c) $\dot{w}$

Figure E.24: Passenger linear acceleration spectral densities at seat location 'E' in moderate turbulence, $\sigma = 1.3$ m/s, at $\eta = 0.7$.

Appendix F: Variance Ratio's, κ, Between Isolated and Formation Flight

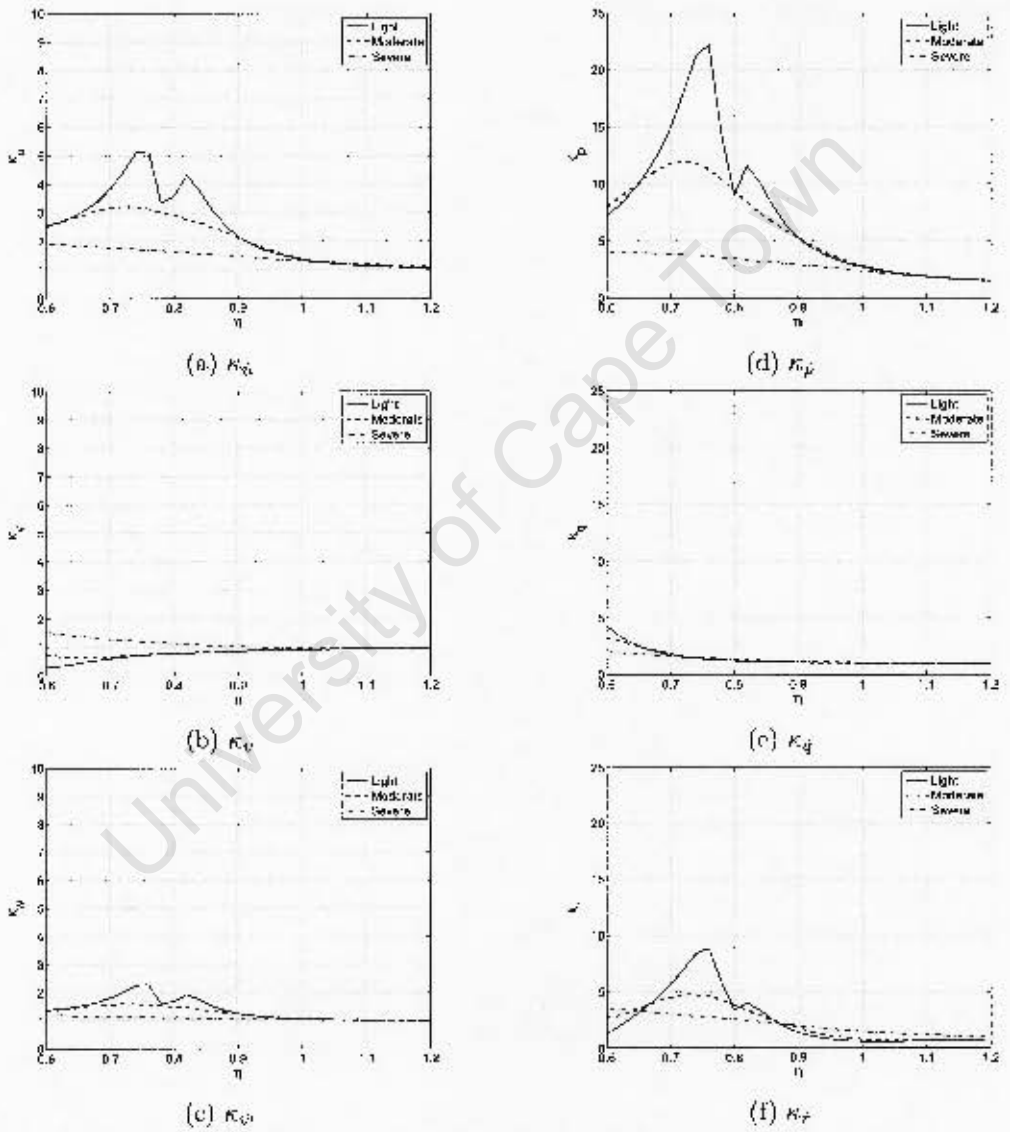

(a) $\kappa_{\dot{q}_i}$ (d) $\kappa_{\dot{p}}$

(b) $\kappa_{\dot{v}}$ (c) $\kappa_{\dot{q}}$

(e) $\kappa_{\dot{w}}$ (f) $\kappa_{\dot{r}}$

Figure F.1: Variance ratio, κ, distribution of e.g. as a function of turbulence intensity and lateral separation, η.

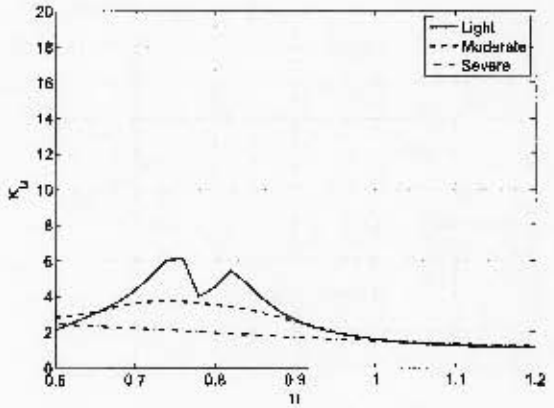

(a) κ_u

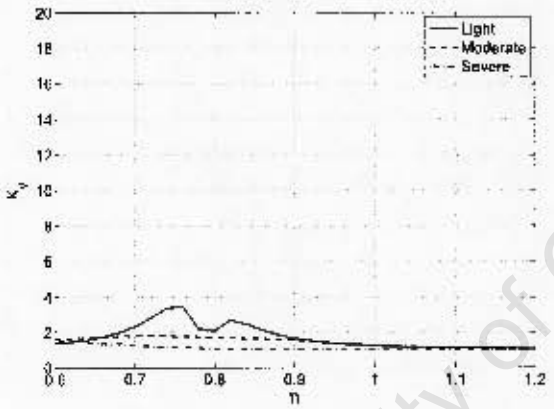

(b) κ_v

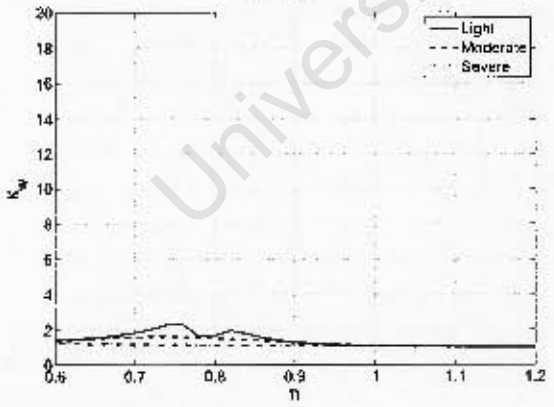

(c) κ_w

Figure F.2: Variance ratio, κ, distribution of passenger at location A as a function of turbulence intensity and lateral separation, η.

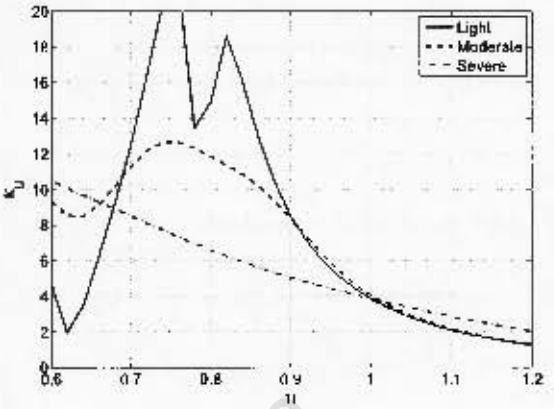

(a) κ_u

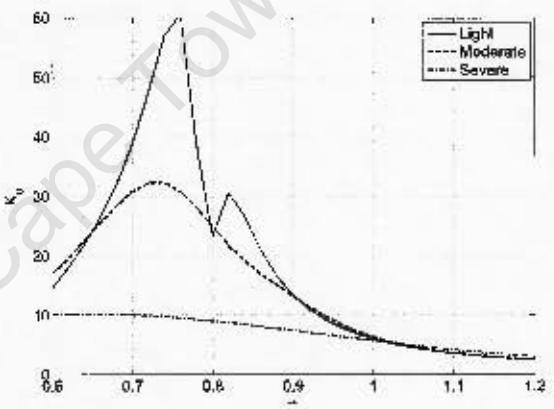

(b) κ_v

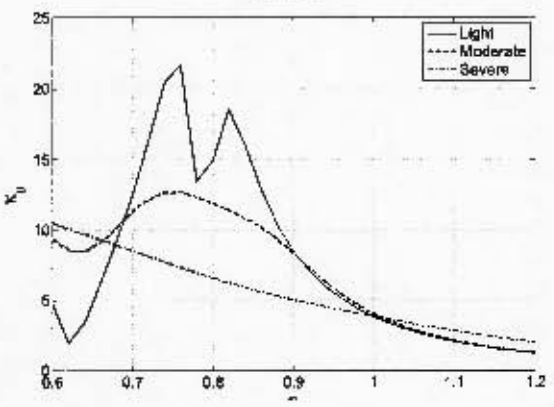

(c) κ_w

Figure F.3: Variance ratio, κ, distribution of passenger at location F as a function of turbulence intensity and lateral separation, η.

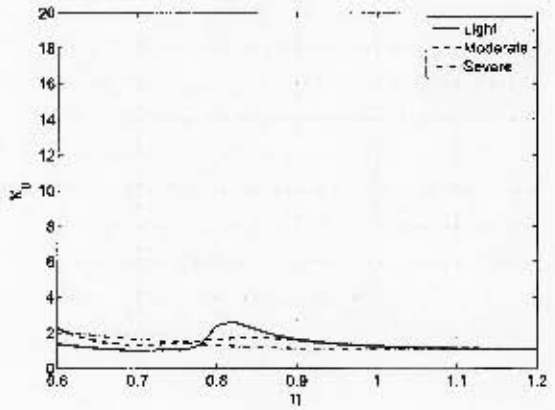

(a) $\kappa_{\dot{u}}$

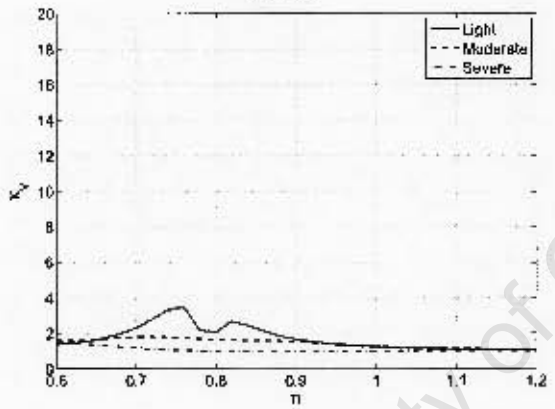

(b) $\kappa_{\dot{v}}$

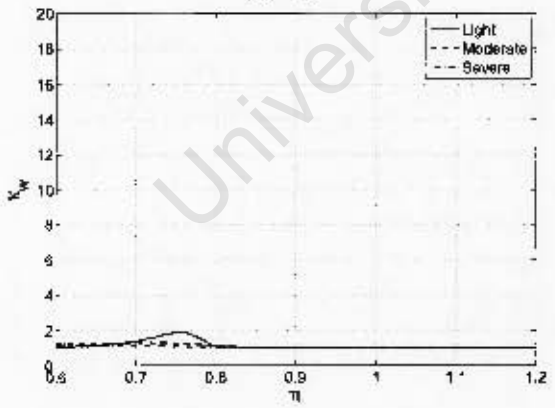

(c) $\kappa_{\dot{w}}$

Figure F.4: Variance ratio, κ, distribution of passenger at location B as a function of turbulence intensity and lateral separation, η.

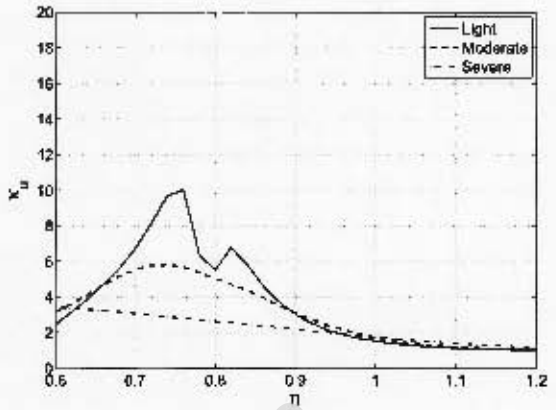

(a) $\kappa_{\dot{u}}$

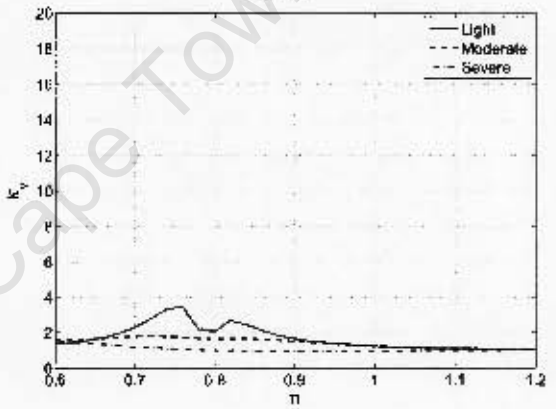

(b) $\kappa_{\dot{v}}$

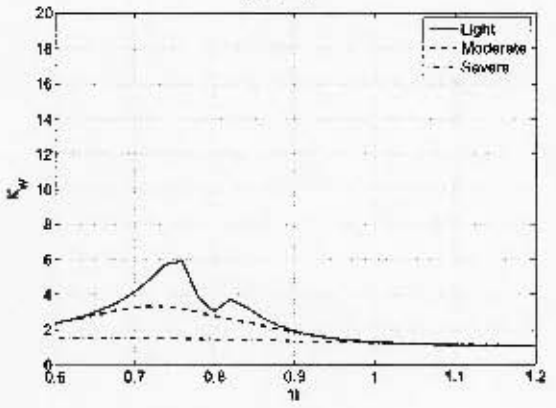

(c) $\kappa_{\dot{w}}$

Figure F.5: Variance ratio, κ, distribution of passenger at location C as a function of turbulence intensity and lateral separation, η.

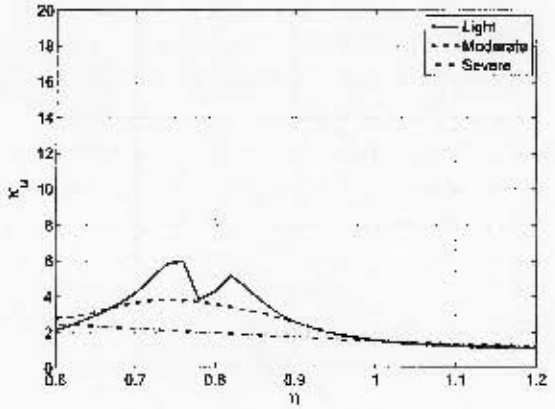

(a) κ_u

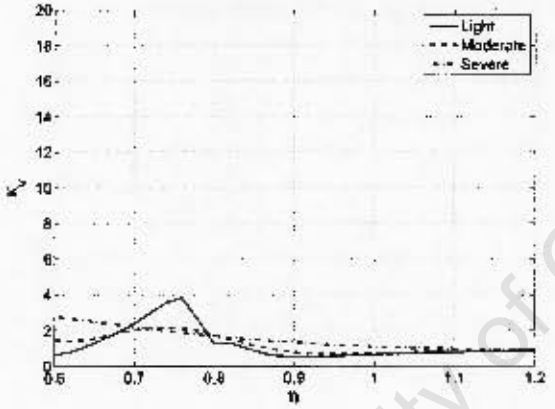

(b) κ_v

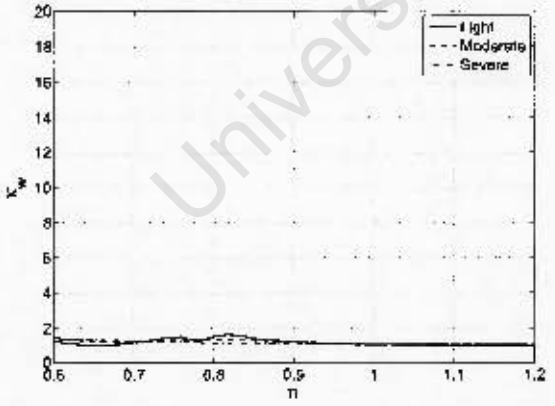

(c) κ_w

Figure F.6: Variance ratio, κ, distribution of passenger at location D as a function of turbulence intensity and lateral separation, η.

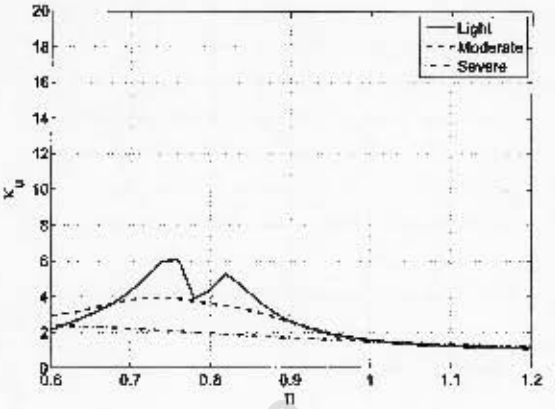

(a) κ_u

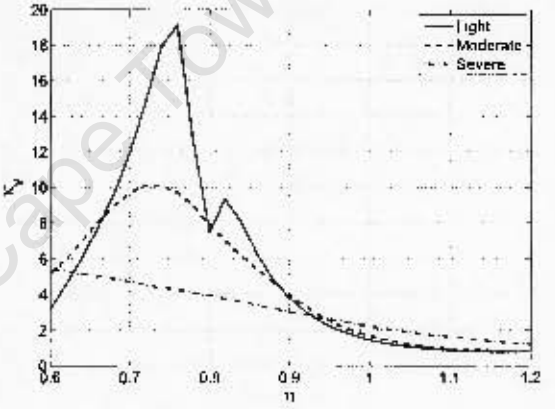

(b) κ_v

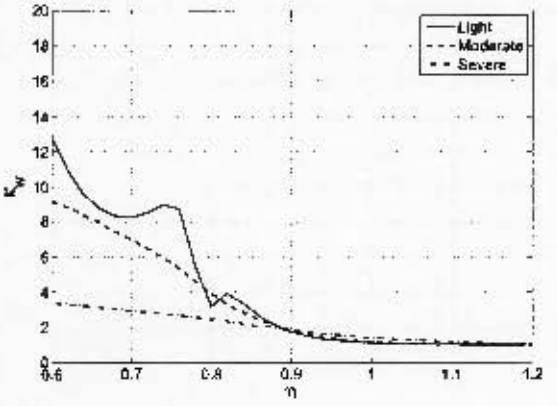

(c) κ_w

Figure F.7: Variance ratio, κ, distribution of passenger at location E as a function of turbulence intensity and lateral separation, η.

Appendix G: Selected Aircraft Data and Representation of a Typical Large Passenger Airliner

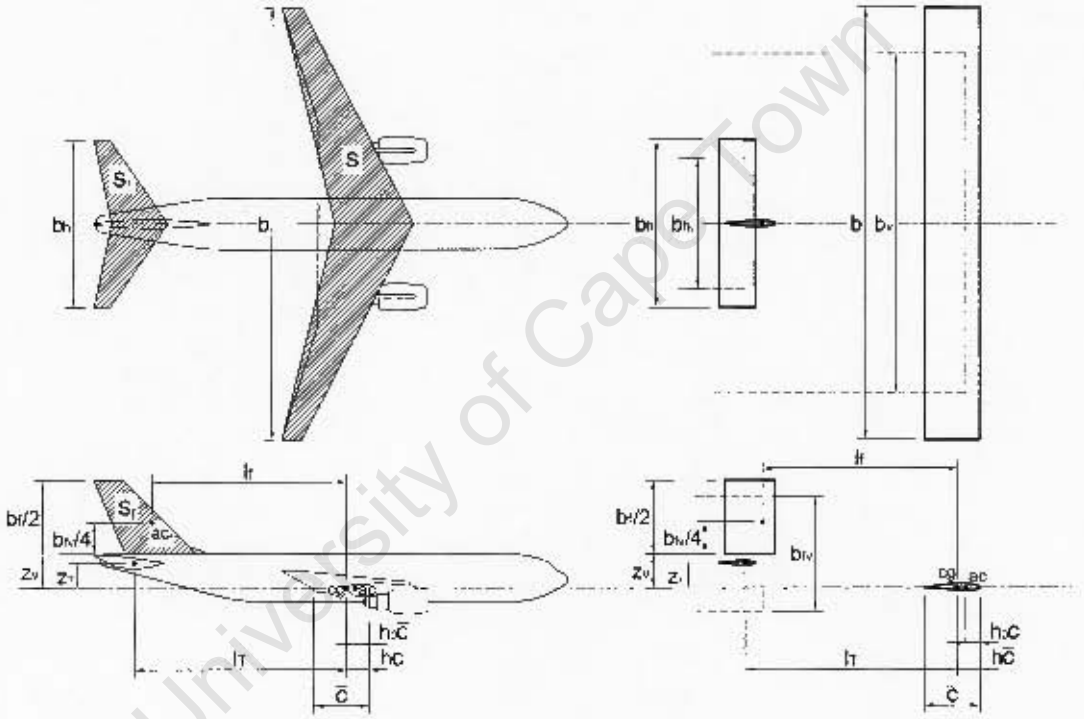

Figure G.1: Model representation of typical passenger airliner.

Selected data of Boeing 747-100 collected for simple application: Spoilers not considered, outboard ailerons not considered (flaps up operations), stabilizer not considered (trim maintained with elevator, aileron and rudder), upper and lower rudders considered as one, inboard and outboard elevators considered as one, aeroelastic modes not considered, control response considered immediate.

Table G.1: Selected B-747 data from Heffley & Jewell [83]

Flight Data			Tailfin Data			Selected Handling Data		
Alt	40000	ft	$\frac{b_f}{2}$	10.3	m	C_{L_α}	4.93	rad^{-1}
ρ	0.305	kg/m^3	l_f	28.7	m	C_{D_α}	0.426	rad^{-1}
V	236	m/s	S_f	79.6	m^2	C_{m_α}	-1.04	rad^{-1}
M	0.8		z_v	-5.9	m	$C_{L_{\delta_e}}$	0.366	rad^{-1}
						$C_{m_{\delta_e}}$	-1.44	rad^{-1}
Physical Data			Tailplane Data			C_{y_β}	-0.879	rad^{-1}
m	290000	kg	b_h	22.4	m	C_{n_β}	0.195	rad^{-1}
$\bar{c}$	8.3	m	l_T	29.6	m	C_{l_β}	-0.254	rad^{-1}
b	59.7	m	S_T	141	m^2	$C_{l_{\delta_a}}$	0.014	rad^{-1}
S	511	m^2	z_T	-5.1	m	$C_{n_{\delta_a}}$	0.0002	rad^{-1}
h_0	0.25					$C_{y_{\delta_r}}$	0.117	rad^{-1}
h	0.25					$C_{n_{\delta_r}}$	-0.124	rad^{-1}
						$C_{l_{\delta_r}}$	0.007	rad^{-1}

Table G.2: Maximum control surface deflections from Hanke and Nordwall [88]

Control surface	Maximum deflection	Notes
Aileron	40°	Max. differential deflection of both inboard ailerons
Elevator	17°	Nose down
Elevator	23°	Nose up
Rudder	25°	

Appendix H: Spectral Density Estimation

The following brief outline follows directly from Heinzel et al. [80] who provides a practical overview of the implementation of spectral density estimation using the approach of the 'Welch' method.

This method finds the average spectral density of overlapping segments of window modified periodograms. The time series is divided into overlapping segments before a window function is applied to the segments after which the Discreet Fourier Transform (DFT) is applied to each window modified segment. The resulting outputs are then scaled and averaged to represent the power spectral density of the entire signal.

The sampling frequency is the inverse of the sampling period. Assuming that the sampling frequency f_s is fixed, then from the Nyquist theorem, the maximum useful frequency is $f_{Ny} = \frac{1}{2\Delta t}$ [81]. The kth element in the frequency domain is referred to as a frequency bin. The frequency of bin k can be related to the frequency of the input signal using, $f_k = \frac{kf_s}{N}$. The width of a frequency bin (also called frequency resolution) is given by $f_{res} = \frac{f_s}{N}$.

The DFT will produce only $\frac{N}{2} + 1$ distinct complex numbers corresponding to:

$$f_m = mf_{res} \quad m = 0 \ldots \frac{N}{2}$$

Hence, in a practical approximation, we obtain $\frac{N}{2}$ frequency bins of width $\frac{f_s}{N}$ in the output. If a DFT is performed on a stretch, length N, of a time series containing a sinusoidal signal, The likely expectation is that the result will show a sharp peak in only one frequency bin. This is, however, rarely the case and will instead show up as decreasing magnitudes spread across many frequency components. Figure H.1 shows the likely spectral response of a DFT applied to a stretch of samples of a sinusoidal signal.

Heinzel et al. [80] provides a succinct explanation of the effect of applying a DFT to a non periodic signal. "The DFT implicitly assumes that the signal is periodic, i.e. that the time series of length N repeats itself infinitely in a cyclic manner. If the frequency of the sinusoidal input signal is not an exact multiple of the frequency resolution f_{res}, i.e. does not fall in the exact center of a frequency bin, this assumption is not true, and the DFT will 'see' a discontinuity between the last sample and the first sample due to the cyclic continuation. That discontinuity spreads power all across the spectrum". This spread of power over many frequency bins is known as spectral leakage.

A Window function can be applied to shape the samples of the measured signal into a curve that tapers to zero (or near zero) at the end points. In this way the measured samples

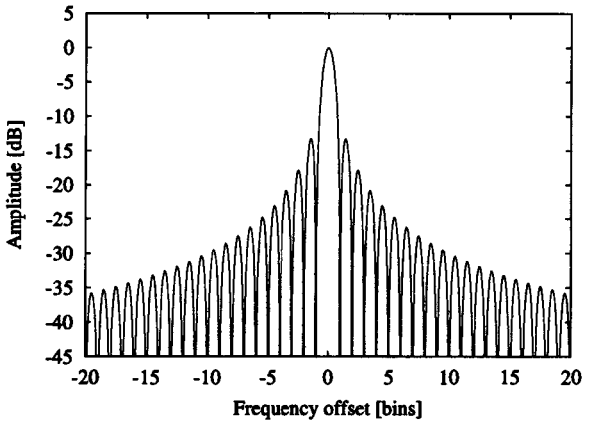

Figure H.1: The spectral response of a rectangular window. Reprinted from Heinzel et al. [80]

are attenuated at the end points to ensure that the signal is continuous. A rectangular window is the equivalent of no shaping and a DFT of this window (sinc function) produces very wide spreading of low amplitude frequency components. Many non-rectangular window functions have been developed which usually involve some compromise between the width of the resulting peak in the frequency domain, the amplitude accuracy and the rate of decrease of the spectral leakage into other frequency bins. The choice of window depends on the application. In general, lower spectral leakage in the near vicinity increases the bandwidth around the original component.

A complex vector, y_m, of length $\frac{N}{2}+1$ results from a real-to-complex DFT applied to a set of segments which has been modified with a window function. The power spectral density is obtained by scaling the result:

$$\Phi\langle f_m = m f_{res}\rangle = \frac{2|y_m|^2}{f_s S}$$

where S is the area of the window modified amplitudes of the set of segments given by (see Fig. H.2):

$$S = \sum_{j=0}^{N-1} w_j^2$$

For stationary signals, a number of spectral density estimates can be averaged to improve the standard deviation. If M estimates are considered, the standard deviation of the averaged result reduces by a factor of $\frac{1}{\sqrt{M}}$.

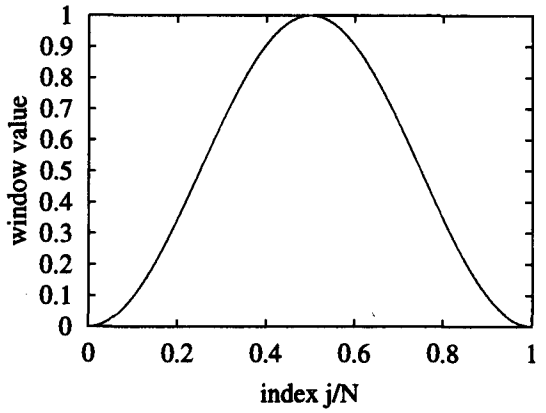

Figure H.2: The Hanning window divided into N segments. Reprinted from Heinzel et al. [80]

One of the disadvantages of windowing functions is that the data at the beginning and end of the window is attenuated in the calculation of the spectrum. This requires more averages to get a reasonable statistical representation. Overlap processing is a measure to recover the lost data by recovering a portion of each previous frame and reducing the measurement time. Figure H.3 illustrates this method. The 'pwelch' function in Matlab is

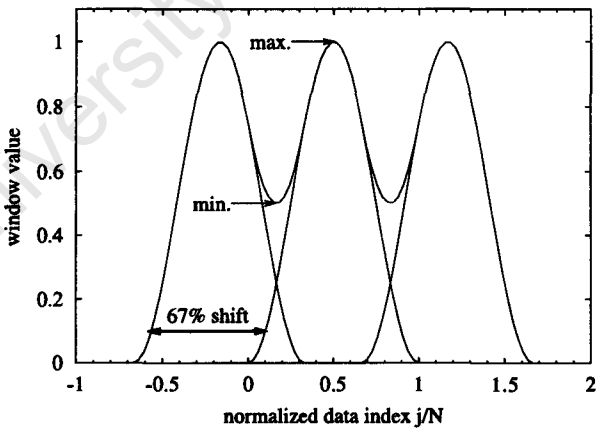

Figure H.3: Hanning windows with 33% overlap. Reprinted from Heinzel et al. [80]

used to estimate the spectral density of the accelerations which uses the 'Hamming' window by default. `[Pxx,f] = Pwelch(x,nwin,noverlap,nfft,fs)`. The vector `x` is the input, `nwin` determines the length of the Hamming window, `noverlap` indicates the amount of overlap desired, `nfft` defines the length, N, of the FFT. Heinzel et al. [80] notes that `nfft`

should be the same as the length of the window vector `nwin`.

Appendix I: Influence Factors Converted to Include Roll Disturbance Angle

To allow for large roll disturbance angles in the simulation code, the influence factors were converted to functions of the separation from the near and far trailing vortices. Figure I.1 shows the difference between the lateral and vertical separations from the near and far trailing vortices with a large non-zero roll angle, ϕ. The transformation is given by:

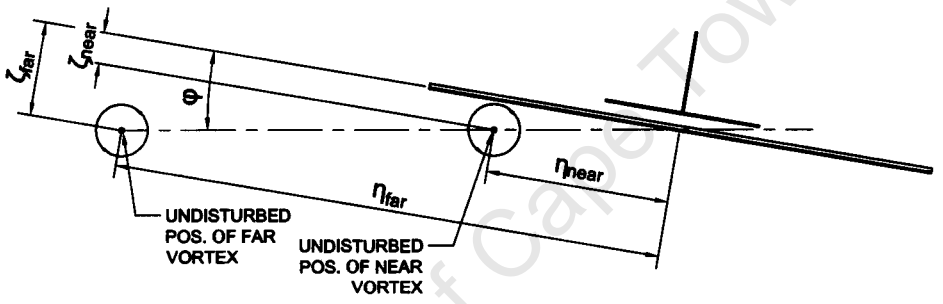

Figure I.1: Trailing aircraft separation from near and far trailing vortices with large roll disturbance angle.

$$\begin{Bmatrix} \eta_{near} \\ \zeta_{near} \end{Bmatrix} = \begin{bmatrix} \cos\phi & \sin\phi \\ -\sin\phi & \cos\phi \end{bmatrix} \begin{Bmatrix} \eta - \frac{\pi}{8} \\ \zeta \end{Bmatrix} \tag{I.1}$$

and

$$\begin{Bmatrix} \eta_{far} \\ \zeta_{far} \end{Bmatrix} = \begin{bmatrix} \cos\phi & \sin\phi \\ -\sin\phi & \cos\phi \end{bmatrix} \begin{Bmatrix} \eta + \frac{\pi}{8} \\ \zeta \end{Bmatrix} \tag{I.2}$$

The upwash influence factor, σ_{jk}, can be rewritten as follows:

$$\begin{aligned} \sigma_{jk} &= \ln \left| \frac{\left((\eta - \frac{\pi}{4})^2 + \zeta^2 + \mu^2\right)\left((\eta + \frac{\pi}{4})^2 + \zeta^2 + \mu^2\right)}{\left(\eta^2 + \zeta^2 + \mu^2\right)^2} \right| \\ &= \ln \left| \frac{\left((\eta_{near} - \frac{\pi}{8})^2 + \zeta_{near}^2 + \mu^2\right)\left((\eta_{far} + \frac{\pi}{8})^2 + \zeta_{far}^2 + \mu^2\right)}{\left((\eta_{near} + \frac{\pi}{8})^2 + \zeta_{near}^2 + \mu^2\right)\left((\eta_{far} - \frac{\pi}{8})^2 + \zeta_{far}^2 + \mu^2\right)} \right| \end{aligned} \tag{I.3}$$

The upwash influence factor σ_{jkwh}, over a span equal to the tailfin span is rewritten as shown:

$$\begin{aligned}\sigma_{jkwh} &= \ln\left|\frac{\left(\zeta^2+(\eta-\frac{\pi}{8}-\frac{\pi}{8}\eta_h)^2+\mu^2\right)\left(\zeta^2+(\eta+\frac{\pi}{8}+\frac{\pi}{8}\eta_h)^2+\mu^2\right)}{\left(\zeta^2+(\eta-\frac{\pi}{8}+\frac{\pi}{8}\eta_h)^2+\mu^2\right)\left(\zeta^2+(\eta+\frac{\pi}{8}-\frac{\pi}{8}\eta_h)^2+\mu^2\right)}\right| \\ &= \ln\left|\frac{\left(\zeta_{near}^2+(\eta_{near}-\frac{\pi}{8}\eta_h)^2+\mu^2\right)\left(\zeta_{far}^2+(\eta_{far}+\frac{\pi}{8}\eta_h)^2+\mu^2\right)}{\left(\zeta_{near}^2+(\eta_{near}+\frac{\pi}{8}\eta_h)^2+\mu^2\right)\left(\zeta_{far}^2+(\eta_{far}-\frac{\pi}{8}\eta_h)^2+\mu^2\right)}\right|\end{aligned} \tag{I.4}$$

The upwash distribution influence factor τ_{jk}, along the main wing:

$$\begin{aligned}\tau_{jk} =& -2\sqrt{\zeta^2+\mu^2}\left(\tan^{-1}\left(\frac{\eta-\frac{\pi}{4}}{\sqrt{\zeta^2+\mu^2}}\right)+\tan^{-1}\left(\frac{\eta+\frac{\pi}{4}}{\sqrt{\zeta^2+\mu^2}}\right)-2\tan^{-1}\left(\frac{\eta}{\sqrt{\zeta^2+\mu^2}}\right)\right)\cdots \\ &-\eta\ln\left|\frac{((\eta-\frac{\pi}{4})^2+\zeta^2+\mu^2)\,((\eta+\frac{\pi}{4})^2+\zeta^2+\mu^2)}{(\eta^2+\zeta^2+\mu^2)^2}\right|-\frac{\pi}{8}\ln\left|\frac{(\eta+\frac{\pi}{4})^2+\zeta^2+\mu^2}{(\eta-\frac{\pi}{4})^2+\zeta^2+\mu^2}\right| \\ =&2\sqrt{\zeta_{near}^2+\mu^2}\left(\tan^{-1}\left(\frac{\eta_{near}+\frac{\pi}{8}}{\sqrt{\zeta_{near}^2+\mu^2}}\right)-\tan^{-1}\left(\frac{\eta_{near}-\frac{\pi}{8}}{\sqrt{\zeta_{near}^2+\mu^2}}\right)\right)\cdots \\ &-\eta_{near}\ln\left|\frac{((\eta_{near}-\frac{\pi}{8})^2+\zeta_{near}^2+\mu^2)}{((\eta_{near}+\frac{\pi}{8})^2+\zeta_{near}^2+\mu^2)}\right|\cdots \\ &-2\sqrt{\zeta_{far}^2+\mu^2}\left(\tan^{-1}\left(\frac{\eta_{far}+\frac{\pi}{8}}{\sqrt{\zeta_{far}^2+\mu^2}}\right)-\tan^{-1}\left(\frac{\eta_{far}-\frac{\pi}{8}}{\sqrt{\zeta_{far}^2+\mu^2}}\right)\right)\cdots \\ &-\eta_{far}\ln\left|\frac{\left((\eta_{far}+\frac{\pi}{8})^2+\zeta_{far}^2+\mu^2\right)}{\left((\eta_{far}-\frac{\pi}{8})^2+\zeta_{far}^2+\mu^2\right)}\right|\end{aligned} \tag{I.5}$$

and the sidewash influence factor, σ_{jk_f}, on the tailfin:

$$\begin{aligned}\sigma_{jk_f} &= \ln\left|\frac{(\eta-\frac{\pi}{8})^2+(\zeta+\zeta_v)^2+\mu^2}{(\eta-\frac{\pi}{8})^2+(\zeta+\zeta_v-\frac{\pi}{8}\zeta_f)^2+\mu^2}\right|-\ln\left|\frac{(\eta+\frac{\pi}{8})^2+(\zeta+\zeta_v)^2+\mu^2}{(\eta+\frac{\pi}{8})^2+(\zeta+\zeta_v-\frac{\pi}{8}\zeta_f)^2+\mu^2}\right| \\ &= \ln\left|\frac{\eta_{near}^2+(\zeta_{near}+\zeta_v)^2+\mu^2}{\eta_{near}^2+(\zeta_{near}+\zeta_v-\frac{\pi}{8}\zeta_f)^2+\mu^2}\right|-\ln\left|\frac{\eta_{far}^2+(\zeta_{far}+\zeta_v)^2+\mu^2}{\eta_{far}^2+(\zeta+\zeta_v-\frac{\pi}{8}\zeta_f)^2+\mu^2}\right|\end{aligned} \tag{I.6}$$